Energy-based models for the design of cavities located in creeping media

Thomas John Birchall

Submitted as partial consideration towards
the degree of Doctor of Philosophy
at Durham University

Mechanics Group
School of Engineering & Computing Sciences
Durham University
United Kingdom

May 2013

Abstract

This thesis uses an energy-based approach to develop new analytical solutions for the time-dependent creep response of deeply embedded cavities. The new models developed here can be used for the initial design of tunnels and for other applications such as underground storage caverns and problems outside the field of geomechanics. The objective of using this energy-based approach is to develop models that can provide a quick estimate of cavity closure and that can be applied to different design situations and material behaviour.

For the first time a three-dimensional analytical solution has been developed for the time-dependent response of a cavity embedded in a viscoelastic medium. The cavity is excavated quasi-instantaneously from an infinite body with an initial isotropic stress field. The problem is three-dimensional due to the effect of a tunnel face. This new solution can predict the full interaction between the tunnel and the surrounding creeping rock and thus can be incorporated with field monitoring data in an expert system for tunnel design. The accuracy of this model is comparable with finite element analysis.

A new class of thermodynamically consistent constitutive models have been developed, which couple viscoplasticity and damage, describing both the secondary and tertiary stages of creep behaviour. Models were derived for both frictionless and frictional materials within the framework of hyperplasticity. The frictional model provided a good fit to data obtained from the triaxial compression testing of sandstone, illustrating its capability of describing creeping rock.

These new constitutive models were incorporated into the energy-based method for cavity analysis, using a two-dimensional plane strain cylindrical cavity for demonstration purposes. A parametric study was carried out and results were also compared with FE analysis. Findings show that the models successfully describe the secondary and tertiary stages of creep behaviour.

These new solutions only require a simple text file as an input and need minimal skill to operate. The formation of an initial geometry or finite element mesh is not necessary. This is shown through the creation of a standalone program for the three-dimensional model. The new solutions can take into account a wide range of different material behaviour, both two-dimensional and three-dimensional problems and due to their thermodynamic consistency are able to simulate other time-dependent processes, such as relaxation. This shows the flexibility of this approach and its applicability to different geomechanics problems.

Key words: cavity, creep, energy-based, viscoelasticity, viscoplasticity, damage.

Declaration

The work in this thesis is based on research carried out in the School of Engineering and Computing Sciences, Durham University. No part of this report has been submitted elsewhere for any other degree or qualification. All of the work shown here is my own unless referenced to the contrary in the text.

Acknowledgements

Firstly I would like to thank my supervisor Dr. Ashraf Osman for his great guidance and support throughout the course of this research. His knowledge of and enthusiasm for the subject have been a great help and encouragement, and have led to a number of very stimulating discussions.

I would not have been able to undertake this work without the financial support of EPSRC and Cleveland Potash Ltd. I would like to thank Allan Williams and Mike Keen at Cleveland Potash Ltd for allowing me to visit Boulby Potash Mine and for helpful discussions on the challenges faced in predicting the time-dependent creep closure of deeply embedded cavities.

I would like to thank Dr. William Coombs for his help in understanding plasticity theory and the stress integration of constitutive equations through sharing algorithms that he programmed in MATLAB.

I am grateful to my research colleagues, particularly Salma, Asem and Syazwan for their friendship over the last few years.

Special thanks go to my wife Lorna for her steadfast love, great patience and help in writing this thesis. I am grateful to my family, particularly my parents, John and Julia, my sister Helen and brother-in-law Adrian for their unfailing support.

Finally I would like to thank God for enabling me to complete this research and the great love that he has shown me through sending his son Jesus to die on the cross.

"You are worthy, our Lord and God to receive glory and honor and power, for you created all things, and by your will they were created and have their being." Revelation 4:11

Contents

List of Figures

List of Tables

Notation

Symbols (lowercase)

a_1, a_2, a_3, a_4, a_5	coefficients of governing equations
b	tunnel radius in Chapter 2
b_1, b_2	constants used to solve governing equations
$\{b\}$	residuals in stress integration scheme
c	cohesion
c_1, c_2, c_3, c_4, c_5, c_6, c_7, c_8	coefficients of boundary conditions in Chapter 4, frictional viscoplastic-damage constitutive model parameters in Chapter 6
c_k	frictional viscoplastic-damage constitutive model parameter
d	Drucker-Prager constitutive model parameter related to the cohesion
d_1, d_2, d_3, d_4	closed-form equation parameters in Chapter 3, coefficients of governing equation in Chapter 4
dX	controls the evolution of the loading process when simulating triaxial tests
$\{dY\}$	vector used to calculate the strain increment when simulating triaxial tests
$[e]$	deviatoric strain matrix
e_{ij}	deviatoric strain component
$[e^p]$	deviatoric plastic strain matrix
$\{e^p\}$	deviatoric plastic strain vector
f	yield function
g	plastic potential function
i	iteration number
j	previous load step
k	material stiffness in Chapter 2, Drucker-Prager constitutive model parameter in Chapter 3
m	closed-form equation parameter
m_1, m_2, m_3, m_4, m_5	coefficients of governing equations
n	viscoplastic constitutive model constant
p	mean stress
p_i	cavity internal pressure
p_o	cavity external pressure
p_{vo}	vertical component of cavity external pressure
p_{ho}	horizontal component of cavity external pressure
q	von Mises equivalent stress

q_1	closed-form equation parameter in Chapter 3, tunnel wall pressure in Chapter 4
q_2	tunnel face pressure
r	radial distance
r_d	viscoplastic-damage material constant
r_p	viscoplastic-damage material constant
r_0	cavity radius
r_c	cavity plastic radius
r_m	cavity external boundary
s	Laplace coordinate
$[s]$	deviatoric stress matrix
$\{s\}$	deviatoric stress vector
s_{ij}	deviatoric stress component
t	time
u	displacement
u_1	actual displacement
u_r	radial displacement
u_θ	circumferential displacement
u_z	longitudinal displacement
x	distance from tunnel face
x_1, x_2	parameters used to solve governing equations
z	longitudinal distance

Symbols (uppercase)

A	material constant in Chapter 2, constant in solution for governing equation in Chapter 3, total cross-sectional area of a surface within a unit cell in one of the three perpendicular directions in Chapter 5.
A_1	closed-form equation parameter
A_s	solid matrix area within A
$[A]$	Hessian matrix
B	constant appearing in solution for governing equation
B_1	closed-form equation parameter
C	constant appearing in solution for governing equation
C_1	closed-form equation parameter
C_2	closed-form equation parameter
$\dot{D}$	dissipation potential
$[D^e]$	elastic stiffness matrix
E	Young's modulus
E_s	slope of the approximately linear part of the stress-strain curve
E_{50}	slope of the line connecting the origin and half the peak strength of the stress-strain curve
$[Emat]$	matrix used to calculate the strain increment when simulating triaxial tests
G	shear modulus

H	constant hardening modulus
$\{H\}$	hardening modulus
K	material constant in Chapter 2, bulk modulus elsewhere
I_1	modified Bessel function of the first kind of order one
Q	activation energy
R	universal gas constant
$[Smat]$	matrix used to calculate the strain increment when simulating triaxial tests
T	absolute temperature
U	potential energy
V	gradient of secondary stage of creep curve
W	external work

Greek symbols (lowercase)

α	closed-form equation parameter in Chapter 3, softening/hardening parameter in Chapters 5 and 6
α_d	damage parameter
$\dot{\alpha}_s$	equivalent deviatoric plastic strain rate
$\dot{\alpha}_v$	volumetric plastic strain rate
β	Drucker-Prager constitutive model parameter related to the dilation angle
$\{\beta\}$	hardening variables
$\dot{\gamma}$	plastic consistency parameter
γ_1, γ_2, γ_3, γ_4, γ_5	coefficients of governing equations
δ_{ij}	Kronecker delta
ε	one-dimensional strain
ε^e	one-dimensional elastic strain
ε_1	primary creep strain in Chapter 2, first component of principal strain elsewhere
ε_3	tertiary creep strain
$[\varepsilon]$	strain matrix
$\{\varepsilon\}$	strain vector
$\{d\varepsilon\}$	strain vector increment
ε_{ij}	strain component
$\{\varepsilon^e\}$	elastic strain vector
$[\varepsilon^p]$	plastic strain matrix
$\{\varepsilon^p\}$	plastic strain vector
ε_q	equivalent strain
ε_v	volumetric strain
ε_{kk}	volumetric strain
ε_{rr}	radial strain
ε^e_{rr}	radial elastic strain
ε^p_{rr}	radial plastic strain
$\varepsilon_{\theta\theta}$	circumferential strain
$\varepsilon^e_{\theta\theta}$	circumferential elastic strain
$\varepsilon^p_{\theta\theta}$	circumferential plastic strain
ε_{zz}	longitudinal strain

ε^e_{zz}	longitudinal elastic strain
ε^p_{zz}	longitudinal plastic strain
$\varepsilon_{\Phi\Phi}$	component of strain in spherical coordinates
$\varepsilon_{r\theta}$	shear strain in polar coordinates
ε_{zr}	shear strain in polar coordinates
η	Drucker-Prager constitutive model parameter in Chapter 3, parameter describing the viscosity of a material elsewhere
$\bar{\eta}$	Drucker-Prager constitutive model parameter
θ	circumferential coordinate
λ	empirical parameter in Chapter 2, Lamé constant elsewhere
μ	Drucker-Prager constitutive model parameter related to the friction angle
μ^*	Drucker-Prager constitutive model parameter related to the friction angle
ν	material constant used in rate-dependent hyperplastic formulation in Chapter 5, Poisson's ratio elsewhere
ρ	used to define the dissipation potential in viscoplastic-damage constitutive models
σ	one-dimensional stress
σ_0	one-dimensional constant stress
σ_y	yield stress
σ_{y0}	initial yield stress
$\Delta\sigma$	change in deviatoric stress
σ_h	horizontal stress applied to external cavity boundary
σ_v	vertical stress applied to external cavity boundary
$[\sigma]$	stress matrix
$\{\sigma\}$	stress vector
σ_{ij}	stress component
σ_1, σ_2, σ_3	principal stresses
σ_{kk}	volumetric stress
σ_{rr}	radial stress
$\sigma_{\theta\theta}$	circumferential stress
σ_{zz}	longitudinal stress
$\sigma_{\Phi\Phi}$	component of stress in spherical coordinates
$\tau_{r\theta}$	shear stress in polar coordinates
τ_{zr}	shear stress in polar coordinates
ϕ	friction angle
ϕ_1,ϕ_2,ϕ_3	functions governing the attenuation of rock displacements away from the cavity wall in the r direction
χ_d	damage component of dissipative stress
$\bar{\chi}_d$	generalised damage stress
χ_p	volumetric component of dissipative stress
χ_q	deviatoric component of dissipative stress

$\{\chi\}$	dissipative stress vector
χ_{rr}	dissipative radial stress
$\chi_{\theta\theta}$	dissipative circumferential stress
χ_{zz}	dissipative longitudinal stress
ψ	free energy potential, dilation angle
ψ_{r1}, ψ_{r2}, ψ_{z1}, ψ_{z2}	functions describing the variation of the radial and longitudinal displacements in the z direction

Greek symbols (uppercase)

Λ	Lagrange multiplier
Π	softening/hardening function in Chapters 5 and 6, total energy of cavity system elsewhere
Φ	spherical coordinate

Acronyms

1D	one-dimensional
2D	two-dimensional
3D	three-dimensional
FE	finite element
FD	finite difference
bE	backward Euler
CDM	continuum damage mechanics

Chapter 1

Introduction

1.1 Statement of the problem

Removal of rock during the formation of an underground cavity induces changes in the local stress state of the rock surrounding the excavation, causing a disturbance in the stability of the rock mass. Readjustment of the rock mass towards a new equilibrium can take the form of slow creep-like movements, which can increase for months and years after the excavation has taken place. This involves closure of the cavity with time, which is often called ground squeezing. Ground squeezing is mainly related to the progressive yielding, time-dependent deformation and strength properties of the ground. It is initiated by the concentration of shear stresses in the cavity vicinity overcoming the limiting shear stress at which creep starts and has been described by Terzaghi [14] as displacement occurring under limited volume change.

The magnitude of time-dependent creep deformation depends on a number of factors such as the material properties and the loading conditions and thus is difficult to predict. Significant time-dependent deformation is found in evaporite rocks, such as salt rock and potash when located in a mining environment. The deformation of these weak rocks is dominated by creep [13]. Creep has also been identified as the prime mechanism causing ground squeezing in sheared or faulted rock masses containing mylonite or clay gouge [3, 11, 14] and has even been identified in hard rock [5].

Excessive ground squeezing has been observed at a number of different sites, such as in road and rail tunnels, mines, underground waste storage caverns and shafts. Kontogianni et al. [8] analysed two road tunnels located in Greece and acknowledged that more than 50% of total deformation of tunnels is due to the time-dependent response of the surrounding ground. Large deformations have also been observed at Boulby Potash Mine in North Yorkshire (Figure 1.1a) where tunnels are driven in evaporite rocks, located at depths of over 1 km at which these rocks are stressed to their limit. Other cases of squeezing behaviour include the Stillwater tunnel in USA and a number of tunnels running through the Alps, such as the Gotthard tunnel in Switzerland, the Fréjus tunnel in France and the Lyon-Turin tunnel (Figure 1.1b).

Such behaviour often leads to re-excavation of a tunnel, thus causing severe delays in the construction program and cost overruns.

(a)

(b)

Figure 1.1: Ground squeezing: (a) Boulby Mine (Cleveland Potash Ltd [4]); (b) Saint Martin La Porte access adit (Lyon-Turin Base Tunnel) (Barla et al. [1])

It is of great importance for the tunnel or mining engineer to obtain an understanding of this time-dependent behaviour in order to prevent a delay in construction and to ensure the stability and safety of an underground opening. Knowledge of the time-dependent behaviour of the ground is essential for the design of a stable support system, which more recently consist of ductile elements in combination with standard supports such as shotcrete or rockbolts [10] in creeping conditions. For the design of such systems [9] the development of the expected tunnel displacements must be predicted. Further benefits of understanding the time-dependent behaviour of the ground may include a more efficient design of mine workings and an increase in the quantity of extracted ore.

1.2 Current design practice

The efficient and accurate prediction of the time-dependent performance of cavities located in creeping rock is a main concern in the design. However, the full three-dimensional (3D) interaction between a tunnel and the surrounding creeping rock is complex. It is commonplace to conduct finite element (FE) analysis with advanced constitutive models to accurately predict the time-dependent response of a cavity (e.g. [6], [12]), but such analyses are computationally expensive for routine practice. Another approach is to use analytical solutions which often require simplifications regarding material behavior, the geometry of the problem and its boundary conditions and are sometimes difficult to apply to complex practical problems. However, they are very useful in the early cavity design process, often being able to provide solutions in a short period of time and may provide an insight into the effect of individual parameters on the solution.

However, many existing analytical solutions are viscoelastic and fail to take into account the failure of the rock surrounding a cavity, whilst few viscoplastic analytical solutions currently exist [17]. There is currently no general tool which can incorporate a wide range of different constitutive behaviour. Furthermore, current analytical solutions for tunnelling problems are 2D, using the assumption of plane strain. These solutions cannot describe the full 3D interaction between a tunnel and the surrounding rock in close proximity to the tunnel face. Currently a simplified approach is used where the analysis of stresses and displacements near the tunnel face is performed by regarding the face as providing a fictitious internal support pressure. The magnitude of this internal pressure is related to the face position by using empirical relations based on field measurements or 3D FE analyses. However, there are significant uncertainties in extrapolating these empirical relations to different design situations and rock behaviour.

Therefore there is a need for new models which are able to take into account a wide range of material behaviour and that can be applied to both 2D and 3D problems, providing a quick estimate of cavity closure.

1.3 Aims and objectives

The aims of this research are to develop new simple tools to aid the design of cavities located in creeping rock. Here we seek to develop models that could be used in the early stages of the cavity design process to conduct a parametric study or provide a validation to more complex FE analyses. The objective is to enable tunnelling and mining engineers to design safer and more stable cavities.

The proposed approach uses an energy-based formulation. Here we express the energy of the cavity system in terms of an assumed displacement field which is composed of a multiplication of 1D functions. The principle of virtual work is then used to obtain the differential equations

governing the ground deformation and the corresponding boundary conditions. This method is a powerful tool that can be used to obtain approximate solutions to a range of practical problems. This approach is based on that used by Vlasov and Leontiev [15] and has been used by a number of authors to analyse the 3D behaviour of piles (e.g. [2], [7]). Here we assume the cavity to be unsupported and cylindrical or spherical in shape. The surrounding material is assumed to be homogeneous, isotropic and the volumetric behaviour is time-independent with only deviatoric creep occuring.

The specific objectives of this research are:

1. to use the proposed energy-based method to develop models for cavity analysis which are able to accommodate a wide range of material behaviour.

2. to develop a 3D model which is able to take into account the effect of a tunnel face.

3. to develop new energy-based constitutive models which are able to describe the full range of creep behaviour.

1.4 Thesis layout

Chapter 2 reviews the literature on the creep behaviour of deeply embedded cavities, focusing on constitutive modelling and current methods for cavity analysis.

Chapter 3 introduces the energy-based method which is used throughout this thesis to develop new tools for cavity analysis. Simple 2D models for cylindrical and spherical cavities are derived here and viscoelastic and elasto-plastic material behaviour is incorporated. Results are successfully validated with existing closed-form solutions and FE analysis. These models are built upon throughout the remainder of the thesis where novel work is presented.

Chapter 4 presents for the first time a 3D analytical solution for the long term time-dependent response of a deeply embedded and unsupported tunnel of circular cross-section. This model takes into account the effect of a tunnel face. The tunnel is located in an infinite viscoelastic medium. Results are successfully validated with FE analysis and closed-form solutions.

Chapter 5 introduces time-dependent viscoplastic constitutive behaviour into the cavity equations, thus developing new models that can be used to analyse cavities located in creeping rock. An incremental loading procedure is adopted to enable different rates of loading to be modelled, thus being able to take into account the rate of cavity excavation. In this chapter we derive new viscoplastic constitutive models within the framework of hyperplasticity, therefore ensuring that thermodynamic principles are adhered to. A novel contribution

here is the development of a frictionless viscoplastic-damage constitutive model which is able to take into account both the secondary and tertiary stages of creep behaviour. This model is successfully incorporated into the energy-based method for cavity analysis. A parametric study is conducted and results are compared with FE analysis.

Chapter 6 presents a novel frictional viscoplastic-damage constitutive model within the framework of hyperplasticity. This model is compared with triaxial data obtained by Yang and Jiang [16] during the testing of sandstone, illustrating its capability of describing creeping rock. The model is also successfully incorporated into the energy-based method for cavity analysis and results are compared with FE analysis.

Chapter 7 draws conclusions, summarises the achievements and contains suggestions for future research.

1.5 References

1 Barla, G., Bonini, M. & Debernardi, D. (2008). Time Dependent Deformations in Squeezing Tunnels. *International Journal of Geoengineering Case Histories*, 2(1) p. 40-65.

2 Basu, D. & Salgado, R. (2007). Elastic analysis of laterally loaded pile in multi-layered soil. *Geomechanics and Geoengineering*, 2(3) p. 183-196.

3 Brekke, T.L. & Howard, T.R. (1973). Functional classification of gouge materials from seams and faults in relation to stability problem in underground openings. Rep. No. H0220022, U.S. Bureau of Mines (ARPA).

4 Cleveland Potash Ltd. (2008). Ground Control at Boulby Mine. Internal Report.

5 Dusseault, M. B. & Fordham, C. J. (1993). Time-dependent behaviour of rocks. In:*Comprehensive rock engineering*, 3 (edited by J.A. Hudson), Pergamon Press, p. 119-149.

6 Ghaboussi, J. & Gioda, G. (1977). On the time dependent effects in advancing tunnels. *International Journal for Numerical and Analytical Methods in Geomechanics*, 1 p. 249-269.

7 Guo, W.D., & Lee, F.H. (2001). Load transfer approach for laterally loaded piles. *International Journal for Numerical and Analytical Methods in Geomechanics*, 25(11) p. 1101-1129.

8 Kontogianni, V., Psimoulis, P. & Stiros, S. (2005). What is the contribution of time-dependent deformation in tunnel convergence? *Engineering Geology*, 82 p. 264-267.

9 Radoncic, N., Schubert, W. & Moritz, B. (2009). Ductile support design. Zur Auslegung duktiler Ausbauten. *Geomechanics and Tunnelling*, 2(5) p. 561-577.

10 Schubert, W. (2008). Design of Ductile Tunnel Linings. *42nd U.S. Rock Mechanics Symposium (USRMS)*, San Francisco, CA.

11 Semple, R.M. (1973). Effect of time-dependent properties of altered rocks on tunnel support requirements. Ph.D. Thesis, University of Illinois at Urbana Champaign, Urbana, III.

12 Sterpi, D. & Gioda, G. (2009). Visco-plastic behaviour around advancing tunnels in squeezing rock. *Rock Mechanics and Rock Engineering* 42, p. 319-339.

13 Swift, G.M. & Reddish, D.J. (2005). Underground excavations in rock salt. *Geotechnical and Geological Engineering*, 23 p. 17-42.

14 Terzaghi, K. (1946). Rock defects and loads on tunnel supports. *Rock tunneling with steel supports*, Proctor and White Ed., Commercial Shearing and Stamping Co., Youngstown, Ohio.

15 Vlasov, V.Z. & Leontiev, U.N. (1966). Beams, plates and shells on elastic foundations. In:*Israel Program for Scientific Translations*, Jerusalem, translated from Russian.

16 Yang, S. & Jiang, Y. (2010). Triaxial mechanical creep behaviour of sandstone. *Mining Science and Technology*, 20 p. 0339-0349.

17 Yu, H.S. (2000). *Cavity Expansion Methods in Geomechanics*. Kluwer, Dordrecht.

Chapter 2

Creep behaviour of deeply embedded cavities

Synopsis

This chapter provides an overview of different material models that are commonly used to describe time-dependent creep behaviour of geomaterials, as well as current methods for the creep analysis of deep cavities. Section 2.1 describes creep testing in the laboratory and alternative methods of obtaining creep behaviour, such as *in situ* testing. The issues concerned with deriving a constitutive model which is representative of *in situ* behaviour are discussed in Section 2.1.1. The different material models that are commonly used to describe creep behaviour are reviewed in Section 2.2. These include rheological models, empirical laws and laws based on physical processes. Analytical and numerical models for the creep analysis of deep cavities are reviewed in Section 2.3. The purpose of this chapter is to identify suitable material models for the creep analysis of deep cavities and identify areas in which new tools can be developed for cavity design.

2.1 Creep testing in the laboratory and *in situ*

According to Dusseault and Fordham [17] creep is defined as *continued deformation without a stress change*. Creep has been studied since about 1905, although such behaviour has been documented as early as 1833 [29]. Most early studies focused on the creep rupture of metals under tensile stress, however, later studies have been carried out on rocks, particularly salt rocks as these soft rocks creep under temperature and stress conditions easily simulated in the laboratory [61].

Determining the creep characteristics of rock is an important stage in developing a tool which is able to predict the time-dependent deformation of an underground cavity. Cristescu [14] states that *creep tests performed in the laboratory are very significant in mining and in improved design of underground structures, in order to ensure safety, to increase the amount of extracted ore, etc.*

Creep testing of rock in the laboratory has been carried out by a number of researchers (e.g. [29], [35], [36], [44], [50], [53], [57] and [66]), with many of these studies focusing on salt rock. The simplest creep tests are those during which the rock specimen is uniaxially loaded in compression. The testing procedure involves an increment of load applied quickly to the rock specimen and the stress is held constant while the gradually increasing strain is recorded regularly [28]. Triaxial tests have also been carried out in which the sample is confined by an all around pressure, more closely simulating *in situ* conditions. The duration of an individual creep test is generally several weeks or months. Tests lasting a number of years have also been reported [14].

Laboratory data from creep tests are mostly displayed in the form of strain-time curves of which the general form is displayed in Figure 2.1 (e.g. [28], [32] and [33]). An instantaneous elastic strain, ε^e is followed by primary or transient creep (region 1.) in which strain occurs at an ever decreasing rate. Secondary creep (region 2.) follows if the constant stress overcomes a given limit and is characterised by a constant strain rate. For higher constant stress levels tertiary creep (region 3.) is also observed, which is characterised by a strain rate increasing with time and leads eventually to failure. According to Jeremic [33], laboratory investigations have proved that removal of the applied load in region 1. at point P of Figure 2.1 caused the strain to decrease rapidly to point Q (change in strain equal to ε^e) and then asymptotically back to zero at point R. Thus region 1. can be classified as viscoelastic. Removal of stress in region 2. at point T will result in a permanent deformation (VO). Thus region 2. can be classified as viscoplastic. Despite the classification of these regions as viscoelastic and viscoplastic being an idealisation, it is reasonable to think that at low levels of stress the material behaviour is roughly viscoelastic and at high levels the behaviour is viscoplastic. Region 3. is due to material damage in the form of cracks developing in the rock.

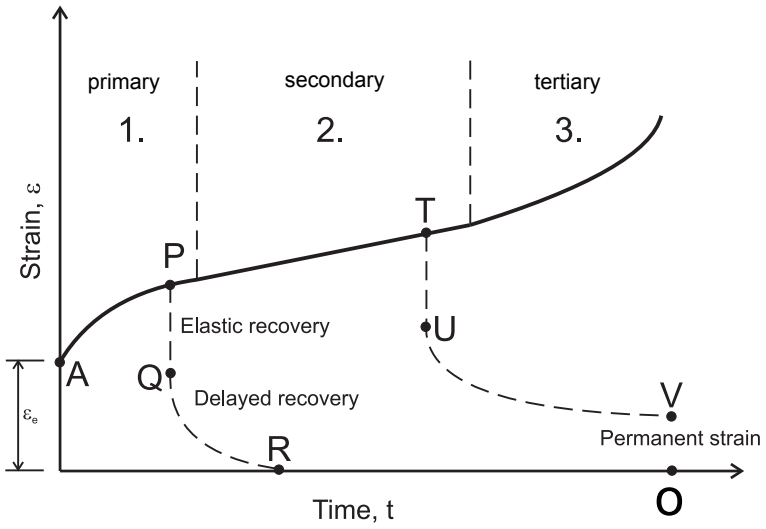

Figure 2.1: Typical deformation of creep materials as a function of time (after Jeremic [33])

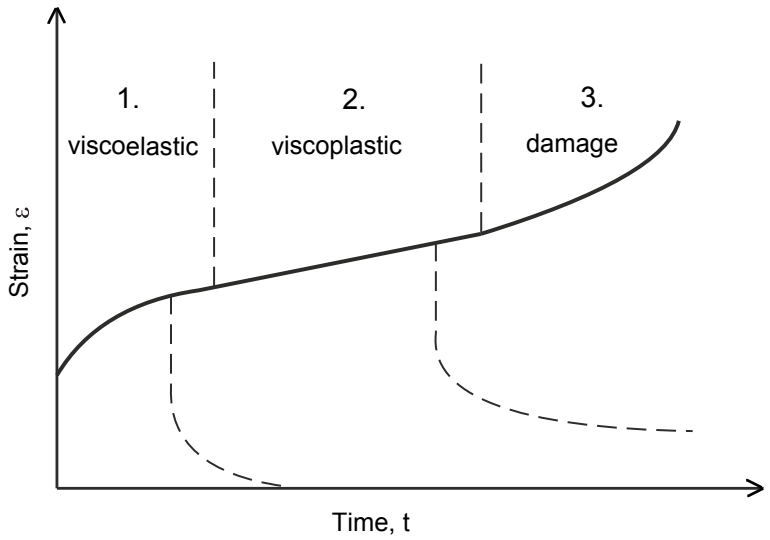

Figure 2.2: Behaviours associated with different stages of creep

Laboratory testing has shown that the creep behaviour of soft rocks, particularly evaporite rocks, is affected by many factors such as stress [31, 36, 44, 53], temperature [31, 36, 65], confining pressure [36, 65], grain size [36], humidity [53], mineral content [16], specimen size and loading history [55] and type of loading [50].

Le Comte [36] concluded that stress difference and temperature are the two factors that most influence the creep behaviour of salt rock with an increase in either stress or temperature giving rise to an increase in creep rate. Jeremic [33] states that the observed processes by which salt rock deforms are primarily a function of stress and temperature. The magnitude of the effect of these two parameters is shown in Figure 2.3 for an investigation by Hansen and Carter [31] on Avery Island domal salt.

2.1.1 Important implications in creep testing

In situ creep testing

It is evident that the creep deformation of rock is a complex process depending on many different factors. In order to determine the creep behaviour of the rock that is representative of *in situ* conditions it is necessary to replicate these conditions as closely as possible. This can be achieved by conducting *in situ* creep tests which overcome the problem of controlling temperature and humidity in the laboratory and reduce the effect of specimen size. Two commonly used field tests are the borehole dilatometer and plate loading tests [28]. The dilatometer test is simple and economic [67], involving the application of a constant pressure via a borehole probe to a certain borehole section. Radial displacement measurements are recorded with time enabling the deformation characteristic of the rock in the stressed region to be determined. The plate loading test is much more expensive, involving a constant load being applied to the surface of a circular plate resting against the wall of an underground opening. Deformation with time is then recorded.

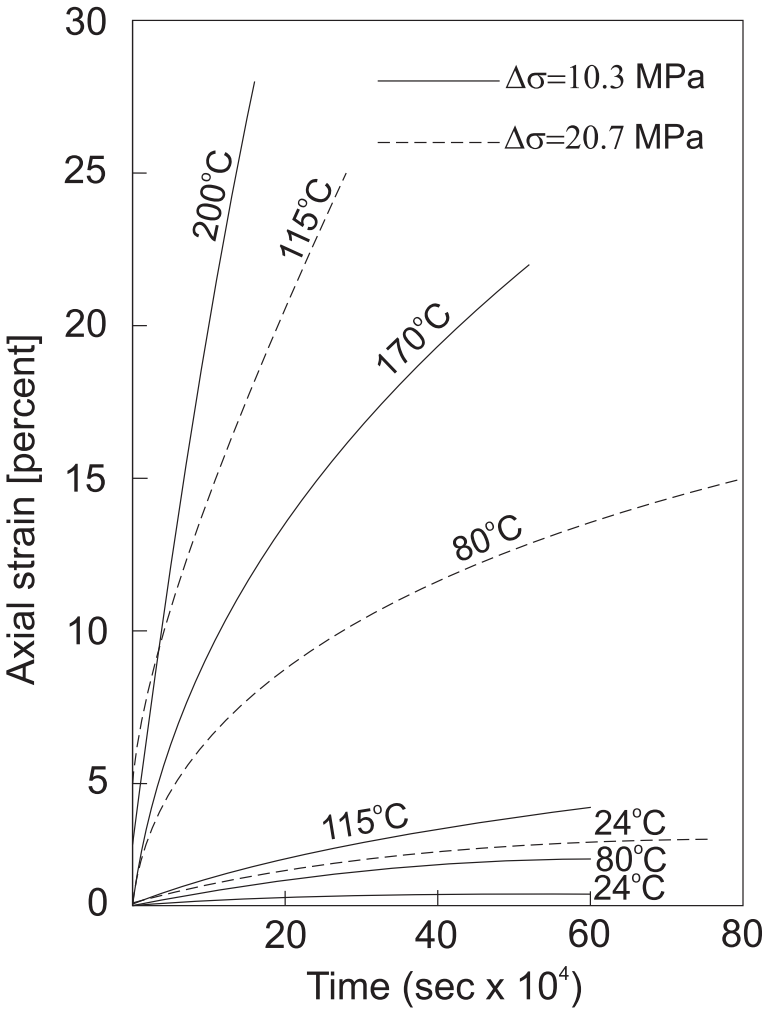

Figure 2.3: Creep curves for Avery Island domal salt deformed at a range of temperatures and two stress differences. The initial confining pressure was 3.5 MPa (after Hansen and Carter [31]).

However, these tests are often expensive, it is not always possible to undertake an extensive underground measurement program and *in situ* stresses are often difficult to measure. In such cases the creep properties can be estimated through laboratory creep testing on core samples. The benefit of laboratory tests is simple and well-controlled boundary conditions which make it easy to determine related parameters accurately. An overview of evaluating these creep properties in the laboratory for underground openings is provided by Aiyer [2]. Aiyer [2] states that a triaxial test cannot truly duplicate the state of stress existing in the medium surrounding a cylindrical opening as the circumferential stress, $\sigma_{\theta\theta}$, the longitudinal stress, σ_{zz} and the radial stress, σ_{rr} are such that $\sigma_{\theta\theta} \neq \sigma_{zz} \neq \sigma_{rr}$. This corresponds to a triaxial state of stress in which $\sigma_1 \neq \sigma_2 \neq \sigma_3$. Therefore, neither a triaxial compression test $\sigma_1 > \sigma_2 = \sigma_3$ or a triaxial extension test $\sigma_1 = \sigma_2 > \sigma_3$ can truly duplicate the stress state surrounding a cylindrical opening. However, due to the fact that the creep closure strains of interest are radial in the field, thus in the direction of the minor principal stress, σ_3, it is believed that the triaxial extension test represents a sufficiently close approximation to the

stress conditions existing around a cylindrical opening. This test involves keeping a constant axial stress on the specimen whilst the confining stress is increased. The US Army Corps of Engineers [64] found that uniaxial creep tests were too severe for use in predicting the time-dependent displacements around underground openings.

Testing to evaluate the creep properties of pillars may involve a different procedure. Uniaxial compressive creep testing of model salt pillars has been carried out by Obert [44] and Mirza [41]. Such experiments are intended to simulate the behaviour of *in situ* pillars by simulating the constraints provided by the roof and floor of a mine opening. These investigations included pillars of various width to height ratios and applied loads anticipated from mining development.

The stress pattern around an underground opening or the stress acting on a pillar continues to change due to material creep until equilibrium is reached. It is not possible to replicate this behaviour in the laboratory, therefore testing has to be carried out under a constant state of stress. Obert [44] states that the load on a pillar prior to reaching a constant value is less than that after the pillar has assumed its maximum load, therefore any design based on constant load conditions would be on the conservative side. However, it is important that the applied stresses in the laboratory are comparable to those existing in the field. For an underground opening the stress level of interest is the vertical stress at the centre of the opening which can be estimated based on unit weights of the overlying strata.

Core samples used in laboratory creep tests must be representative of the *in situ* material. Due to the high complexity and inhomogeneity of the rock mass *in situ* it is very difficult to determine representative material creep parameters. Cylindrical samples of length to diameter ratio of 2 are often used in triaxial creep tests.

Temperature and humidity should be closely controlled. Creep tests are commonly carried out in a climatologically controlled room [53].

Lastly, time is an important factor when carrying out creep testing. As shown in Figure 2.1 the nature of creep may change with time, from primary to secondary and even tertiary creep. In order to develop a constitutive creep model that can be incorporated into tools to predict opening deformation it is necessary to run creep tests for a significant period of time. Creep tests that have been run for only days and weeks are sometimes used to predict rates of deformation over periods of hundreds of years. This emphasises the need to run tests for longer periods of time.

Back analysis

An alternative method of obtaining representative creep behaviour is through the method of back analysis. This involves monitoring the displacements of an underground opening

and using these to determine the creep properties of the rock. These properties can then be used to predict the time-dependent closure at other underground locations. Examples of back analysis in calculating the time-dependent properties of weak rock surrounding tunnels are Phienwej et al. [49] and Zhifa et al. [68], amongst others. According to Sulem et al. [61] the time-dependent parameters can only be properly determined by back analysing the long term closure observations. Also, both the laboratory and field tests may have the shortcomings of scale effect as well as the difficulty of obtaining the stress-dependent creep characteristics. Zhifa et al. [69] states that it is not always necessary to establish another measuring system for back analysis as a measuring system is usually established anyway to ensure safety of construction. The only drawback of back analysis is the difficulty in finding the material parameters for complex constitutive models. In fact this proves to be impossible, thus simplifying assumptions have to be made concerning the rock mass, such as the mass being homogeneous and isotropic and the presence of a uniform stress field [69]. Therefore alternative, empirical methods are sometimes adopted, such as that proposed by Sulem et al. [61]. This involves analysing the tunnel convergence measurements themselves to determine a law for tunnel closure, rather than checking a constitutive behaviour law and determining ground parameters.

2.2 Modelling creep behaviour

Creep data obtained from testing in either the laboratory or *in situ* can be fitted using an appropriate mathematical model which will describe the relationship between strain, stress and time for a specific rock. Model parameters are obtained through analysing each section of the strain-time curves (e.g. [32] and [67]). This enables the practical use of creep test results to solve geotechnical problems. Two types of models are widely used, namely rheological models and empirical models, both of which are described here.

2.2.1 Rheological models

Rheological models consist of a combination of different components, such as springs, dashpots and sliders to describe the time-dependent creep behaviour of a material. The structure of these models is not related to a particular creep test and therefore only the model parameters change between tests in order to provide a fit for the strain-time data. It is important to note that these models can be easily extended to three-dimensions (3D) and are particularly suitable for engineering analyses carried out using the finite element (FE) method.

Viscoelastic models

It is possible to model creep associated with materials by assuming that the material in question has viscous, or fluid properties. Viscoelastic theory is an extension of elasticity theory with the addition of one or more viscous components thereby giving it a time-dependent nature. Linear viscoelastic theory consists of various combinations of two states of deformation, namely elastic behaviour (represented by a spring) and viscous behaviour (represented by a

dashpot) which are used to represent complex strain-time behaviour. Many different linear viscoelastic models have been proposed, such as the Maxwell, the Kelvin and the Burger's model. An overview of these viscoelastic models is provided by Jaeger et al. [32]. Each of these models is composed of spring and dashpot elements connected in series and/or parallel, which exhibit a time-dependent behaviour similar to that of the real material. Figure 2.4 shows these viscoelastic models in 1D form and the strain-time response of each when instantaneously subjected to a constant stress σ_0.

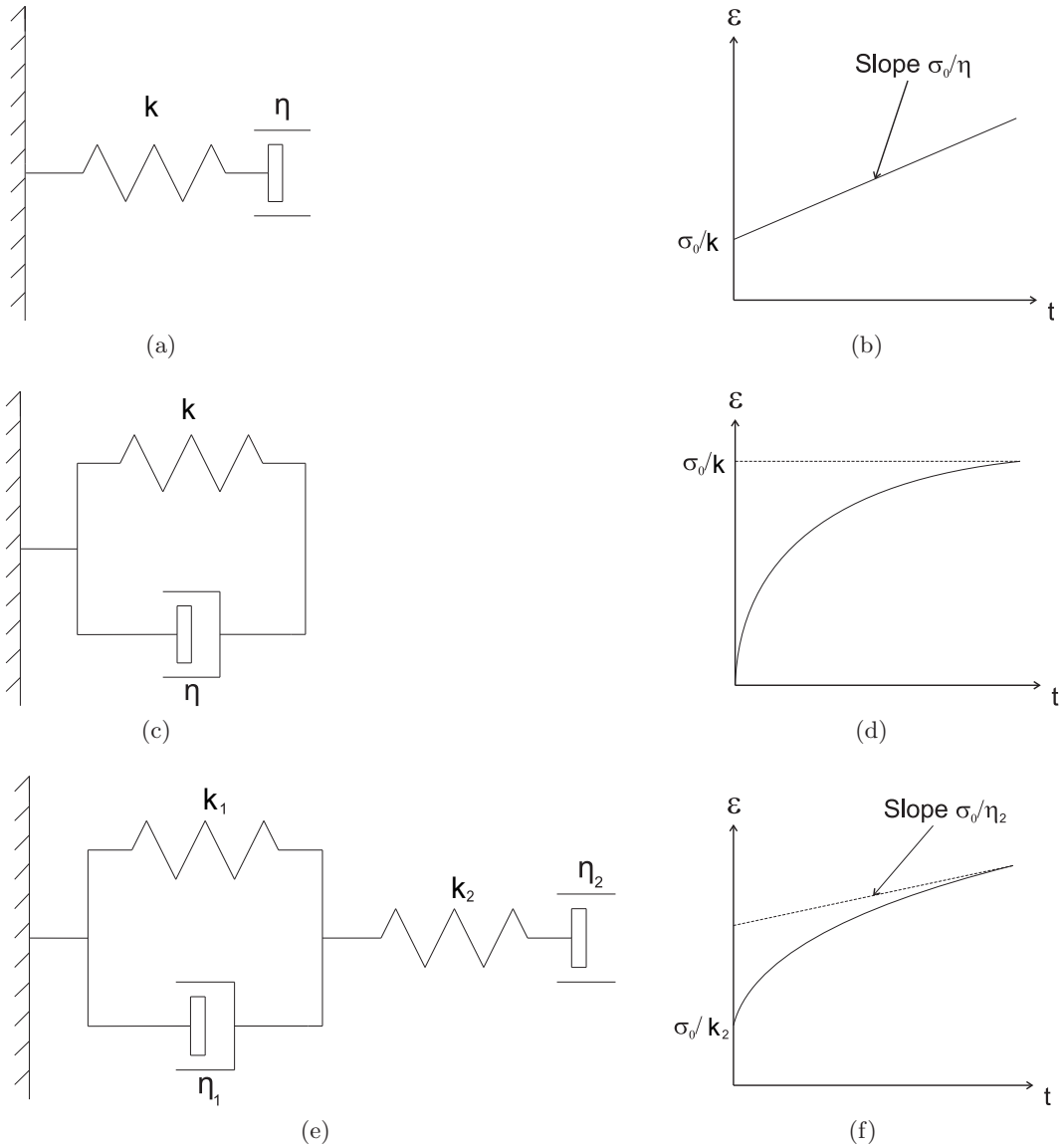

Figure 2.4: Viscoelastic creep models and their strain-time response to an instantaneous stress σ_0 (a) Maxwell model; (b) Maxwell response (c) Kelvin model; (d) Kelvin response (e) Burger's model; (f) Burger's response. (after Jaeger et al. [32]).

The spring element represents an elastic material in which stress and strain are related according to Hooke's law

$$\sigma = k\varepsilon, \tag{2.1}$$

where k represents the Young's modulus or shear modulus, depending on the context. The dashpot represents a Newtonian viscous material where the strain rate is dependent on the applied stress

$$\sigma = \eta \left(\frac{d\varepsilon}{dt} \right), \tag{2.2}$$

where η is a viscous parameter controlling the dashpot response and t is the time.

The Maxwell model comprises of a spring element in series with a dashpot element. This model represents a material flowing continuously at a constant rate when a stress is suddenly applied and held constant [28]. Therefore, the total strain is the sum of the strain in the spring and the dashpot, with an instantaneous elastic component and a long term viscous component. Two parameters are required to predict the creep response. The Maxwell model appears to be simple but proves to be insufficient at modelling creep data due to it postulating a constant rate of creep. Creep tests show that the creep rate decreases with time (Figure 2.1).

The Kelvin model has the same elements as the Maxwell model, but connected in parallel rather than in series. The sudden application of a stress causes strain to develop with time at an exponentially decreasing rate which approaches zero as t grows without bound [28]. As in the Maxwell model, two parameters are required to predict creep behaviour. However, this model fails to capture the instantaneous elastic response of a material and the secondary component of creep.

The simplest model that can be used to trace strain up to the onset of tertiary creep is Burger's model comprising of a Maxwell model and Kelvin model connected in series. Its response is a combination of the previous models and is the same as that of the general creep curve (Figure 2.1). Upon application of a sudden and constant stress an initial instantaneous response is followed by an exponential decay in strain (primary creep) over time eventually becoming asymptotic to a line representing a constant rate of creep (secondary creep). Four parameters are required to predict creep behaviour. The differential equation describing this model is

$$\eta_1 \frac{d^2\varepsilon}{dt^2} + k_1 \frac{d\varepsilon}{dt} = \left(\frac{\eta_1}{k_2} \right) \frac{d^2\sigma}{dt^2} + \left[1 + \left(\frac{k_1}{k_2} \right) + \left(\frac{\eta_1}{\eta_2} \right) \right] \frac{d\sigma}{dt} + \left(\frac{k_1}{\eta_2} \right) \sigma, \tag{2.3}$$

where k_1 and η_1 are the Kelvin parameters and k_2 and η_2 are the Maxwell parameters.

If a constant stress is applied at $t = 0$ when the model is unstrained the following closed-form equation can be written for the strain

$$\varepsilon = \frac{\sigma_0}{k_2} + \frac{\sigma_0}{k_1} \left[1 - \exp(-k_1 t/\eta_1) \right] + \frac{\sigma_0}{\eta_2} t. \tag{2.4}$$

According to Goodman [28] Burger's model is preferable for many practical purposes and Afrouz and Harvey [1] compared a number of spring-dashpot models and found that Burger's model gave the most consistent representation of creep data for sedimentary rocks. Also this model has been used in numerical analyses by Swift and Reddish [62] to successfully simulate the time-dependent deformation of a section of the Winsford salt mine located in Cheshire.

Limitations of viscoelasticity

Due to the simplicity of linear viscoelastic theory, there are many publications where it has been used to simulate the time-dependent behaviour of rock around underground openings (e.g. [11], [18], [27], [28], [39] and [45]). However, linear viscoelastic theory cannot simulate the failure of rock as all time-dependent deformations experienced by a viscoelastic model are recoverable when the applied load is removed. In reality, all time-dependent deformations are not recoverable upon unloading as shown in Figure 2.1 and the relationship between stress and strain is not linear. Under an increment of stress, rock will tend to undergo permanent plastic strains which can involve brittle strains due to microcracking as networks of cracks within the rock grow under loading. Therefore, a linear viscoelastic model should only be applied to competent rocks in which no problems arise [52]. Linear viscoelasticity is able to model the primary stage of creep, as for stresses below a given threshold the associated strains are often assumed to be fully reversible (Figure 2.1). However, when the stress level overcomes this threshold, the strains assume an irreversible nature, increasing first at a constant rate (secondary creep) and eventually leading to an increasing rate (tertiary creep).

Further limitations of viscoelasticity are that large numbers of elements are sometimes required to closely describe the creep data, thus resulting in a complex mathematical equation which can require a great amount of programming effort [49].

Viscoplastic models

Squeezing behaviour in tunnels is mainly related to the progressive yielding and time-dependent deformation and strength properties of the ground [56]. It takes place when a particular combination of induced stresses and material properties pushes some zones around the tunnel beyond the limiting shear stress at which creep starts [3]. Therefore it is important to take this failure of the rock into account.

To include failure processes in rheological models, slider elements (St. Venant elements) are added to the elastic and viscous components of viscoelasticity. Typically a slider element is placed in parallel with a dashpot element, known collectively as a Bingham unit which is immobilised below a specified yield strength. If the yield strength is exceeded, the slider is allowed to move and the dashpot controls the strain rate. Should the applied stress be removed, the slider fails to return to its original position, i.e. the plastic strain is not recoverable upon unloading. This is known as viscoplasticity, proposed by Perzyna [48] and is a modification of

classical plasticity theory by specifying the plastic strain to be time-dependent. In comparison with viscoelasticity, a viscoplastic material only exhibits time-dependent behaviour in the plastic region. This behaviour corresponds to the secondary stage of creep (Figure 2.2). A Bingham unit in series with an elastic spring is shown in 1D form in Figure 2.5, where σ_y is the yield stress of the slider.

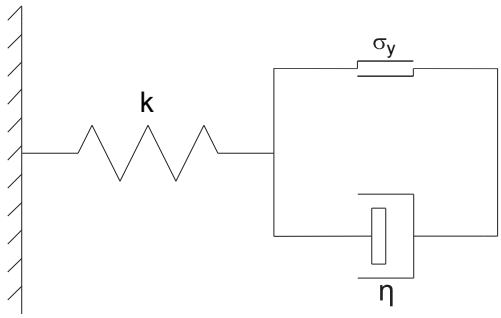

Figure 2.5: Elasto-viscoplastic model

Many different combinations of elastic, viscous and plastic slider elements have been used to describe the creep behaviour of rock. The slider elements are characterised by a range of different yield functions, such as von Mises and Mohr-Coulomb. These models are often viscoelastic-viscoplastic, therefore are able to describe both the primary and secondary stages of creep behaviour shown in Figure 2.1. An example is the VIPLA model [37] which was used by Barla et al. [4] to simulate the Saint Martin La Porte access adit, along the Lyon-Turin Base Tunnel using a von Mises yield function. Gioda [24] and Gioda and Cividini [25] derived a model which features a Kelvin unit in series with a Bingham unit (Figure 2.6). The tertiary stage of creep can be considered by providing suitable laws relating the values of the mechanical parameters to the irreversible part of the time-dependent strain. For example Sterpi and Gioda [59] used the model developed by Gioda [24] and Gioda and Cividini [25], taking into account tertiary creep by way of gradual mechanical damage governed by the cumulative viscoplastic strain. This was achieved by modifying the Mohr-Coulomb parameters of the Bingham unit to have peak and residual values. Other models include those developed by Fakhimi [19] and Fakhimi and Fairhurst [20], who used a viscoelastoplastic constitutive model to simulate the time-dependent behaviour of rock. This consisted of an elasto-plastic Mohr-Coulomb slider in series with Burger's model (Figure 2.7). In this model all time-dependent deformations are elastic.

Viscoplastic constitutive models have been successfully applied to real underground openings as demonstrated by Barla et al. [4] and de Bernardi [15], amongst others.

Despite the viscoplastic models presented here being able to simulate the time-dependent failure processes in the rock, they are unable to take into account discontinuities. Therefore they have limited application to the behaviour of problems where the creep of bedding planes dominates. However, a discontinuum viscoplastic approach can be developed, for example

see Bosman [8].

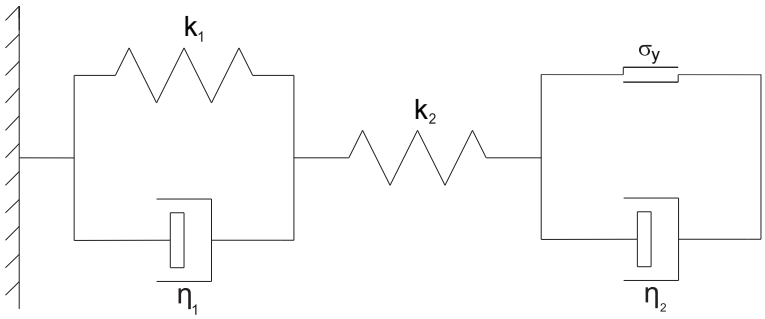

Figure 2.6: Viscoelastic-viscoplastic rheological model (Gioda [24] and Gioda and Cividini [25])

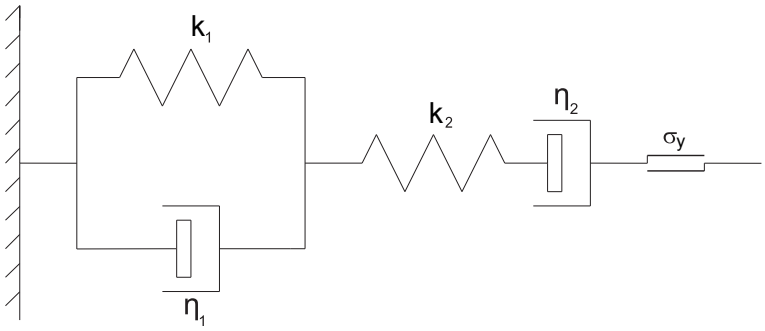

Figure 2.7: Viscoelastoplastic rheological model (Fakhimi [19] and Fakhimi and Fairhurst [20])

2.2.2 Empirical models

Empirical laws are directly derived from the observed relationship of time, stress, and strain rate of creep test results and have been successfully used to describe the observed creep behaviour of soil and rock [49]. They are generally arbitrary functions formulated to fit a set of experimental results. According to Gioda [24] empirical laws usually give a good approximation of the real time-dependent behaviour for stress and strain states, boundary conditions and time spans similar to those of the laboratory tests on which basis they are derived. They are often simple expressions requiring only a few parameters [49]. However, since they are strictly related to a particular type of test it is often difficult to apply them to different conditions. Also, since they are empirical they do not have a firm physical base [17] and cannot be used as a theory which will predict the behaviour of more complicated systems.

The complete spectrum of creep strain shown in Figure 2.1 may be expressed as follows [32]

$$\varepsilon = \varepsilon_e + \varepsilon_1(t) + Vt + \varepsilon_3(t) \tag{2.5}$$

where ε_e is the instantaneous elastic strain, $\varepsilon_1(t)$ is the primary or transient creep strain, Vt is the secondary or steady state creep strain and $\varepsilon_3(t)$ is the tertiary or accelerating creep

strain. Many empirical laws have been proposed to describe the transient creep behaviour of rock. For example, Griggs [29] observed the creep of a range of materials in the laboratory including rocks and represented this behaviour by the following logarithmic law

$$\varepsilon_1(t) = A \log t \tag{2.6}$$

where the constant A refers to the particular conditions of the creep test such as the temperature and confining pressure, and t is time.

Tests carried out by Griggs [29] on Solenhofen limestone subjected to a uniaxial compressive stress of 1400 bars showed that the logarithmic law (equation 2.7) provides a good fit to creep data for times of up to a single year

$$\varepsilon = (6.1 + 5.2 \log t) \times 10^{-5} \tag{2.7}$$

In addition to this expression derived by Griggs [29], other empirical expressions which only represent the primary stage of creep are the power law [7], the exponential law [54, 58] and the hyperbolic law [40]. Creep behaviour of most rocks is found to be adequately described by the power law (e.g. [7], [9], [44] and [57]). For clayey soils, weak shale, mudstone, and faulted rocks, the exponential law and the hyperbolic law are more commonly used (e.g. [21], [38], [40] and [54]). Perhaps the most commonly used is the power law shown below, derived by Boresi and Deere [7] during creep tests on salt rock

$$\varepsilon = K \sigma^n t^m \tag{2.8}$$

where K, n and m are creep parameters derived from strain-time data and σ is the applied stress.

Singh [57] showed that the power law can be used to represent the primary and secondary phases of creep behaviour for Sicilian marble specimens subjected to uniaxial stresses greater than the material yield strength. An investigation carried out by Obert [44] on the creep of model pillars made out of salt rock, trona and potash also showed that a power law successfully describes the observed deformational behaviour. Phienwej et al. [49] states that the power law is especially used for salt rock, potash and evaporites. This is supported by the work of Le Comte [36] on the creep in salt rock, who found excellent agreement between experimental curves and theoretical curves using the power law.

These empirical laws have been used in developing viscoelastic models to predict tunnel closure and the ground pressure on supports. The form of the power law deduced by Boresi and Deere [7] (equation 2.8) was used by Aiyer [2] to develop an analytical solution for the plane strain creep deformation of a circular tunnel. The same power law was used in advanced FE analyses carried out by Shalabi [56] and Yu et al. [68]. The former simulated the time-

dependent squeezing of the Stillwater Tunnel (Utah, USA) which is located in gouge materials (material resulting from grinding and milling when two sides of a fault zone move along each other) of silt and shale, whilst the latter predicted the ground behaviour of a typical room and pillar mining section of a Western Canadian potash mine. Both authors obtained results which provided good correlation with *in situ* measurements. It is important to mention that the power law is commonly used to describe the primary creep following excavation of a cavity, therefore caution should be taken when applying this law to the long term cavity analysis.

Note: many empirical expressions that are derived from creep testing of rocks are only dependent on time (e.g. equation 2.7). Such equations are generally not of use for practical purposes, such as determining the time-dependent closure of an underground opening. This is because the creep behaviour of rock is clearly dependent on the stress level (Figure 2.3), which changes around an underground opening until equilibrium is reached. Therefore, these equations must be modified for stress dependence (e.g. see equation 2.8).

2.2.3 Creep laws based on physical processes

In addition to the common approach of rheological models and empirical laws to describe creep behaviour, creep laws have been developed which are derived from the basic physical processes that govern rock deformation at the atomistic scale. These models start from the analysis of the microscopic structural variation of the material observed under loading, and incorporate a theoretical explanation of the basis of the time-dependent behaviour. Munson and Dawson [42] proposed a multi-mechanism deformation creep model which was used to make creep closure calculations of underground storage and repository rooms in salt rock. This model describes the deformation of salt rock based on the deformation mechanism map for the rock. The mechanism map defines regions of stress and temperature in which a unique deformation mechanism controls or dominates the steady-state creep characteristics of the material. For a repository room, the mechanisms may include (1) dislocation climb at high temperature; (2) an undefined mechanism at low stress and temperature; and (3) dislocation slip at high stress. The mechanisms are parallel processes and are summed up to give a total steady-state strain rate. Details of the changes in the internal structure of the rock govern the macroscopic observations of creep behaviour. One of the most widely used steady state creep laws for salt rock is

$$\dot{\varepsilon}_{ss} = A(\sigma_1 - \sigma_3)^n \exp^{-(\frac{Q}{RT})} \tag{2.9}$$

where A and n are experimental fitting parameters, Q is the activation energy of a given mechanism, $(\sigma_1 - \sigma_3)$ is the maximum deviatoric stress, R is the universal gas constant and T is the absolute temperature. This steady state equation was used by Hansen and Carter [31] to fit creep data obtained from triaxial compression creep testing of samples of Avery Island salt rock and is known as the Weertman relation or Norton-Hoff model. Hansen and Carter [31] found the power law to be inadequate at describing creep data due to the assumption of an infinite primary creep, highlighting the importance of considering secondary

creep. However, the inadequacy of the power law may have been due to the conditions under which creep testing took place, which were appropriate to that of a buried waste repository with temperatures reaching 200^{o} C. Despite this Bérest et al. [5] states that it is important to consider secondary creep as most authors have observed that when a constant mechanical load is applied to a salt sample, a steady state rate is reached after some time; it is a non-linear function of the applied stress, and it is sensitive to temperature.

Even though these physical laws are rigorous due to describing the creep response from fundamental mechanics, they contain many parameters that may not be simple to determine especially for application to creep of clayey soil and fault gouge material [49].

Deformation mechanisms

If an equation is fitted to creep data, an assumption has been made that a certain mechanism dominates creep processes. Creep is caused by different mechanisms related to intrinsic and extrinsic factors. Rates are controlled by the dominate mechanism. Extrapolation of laboratory creep data to other situations requires the appreciation of mechanisms. These mechanisms may include: dislocations, diffusive mass transfer, grain boundary sliding and cataclastic flow, all of which are described below [17].

According to Goodman [28], two types of mechanism are used to explain creep in rocks, namely mass flow (plastic strain) and cracking (brittle strain). This was found by Scott Duncan and Lajtai [53] during uniaxial creep tests on potash rocks. When subjected to a stress greater than the yield stress, plastic creep was dominated by brittle creep caused by microcracking and all three stages of the creep curve were observed for the lateral and volumetric strain of the rock samples. The process of creep in salt rock involves plastic strain through the movement of dislocations [28,33]. Contributions to this plastic strain may also come from the mechanisms of diffusive mass transfer and grain boundary sliding, with the rate of creep being controlled by the dominant mechanism. Brittle strain is caused by cataclastic flow.

Dislocation creep

A dislocation is a crystallographic defect located within a crystal lattice. When subjected to a differential stress, dislocations migrate through the crystal lattice (breaking and forming of bonds) along glide planes causing plastic deformation. Dislocations can be brought to a halt through obstacles such as crystallographic defects and grain boundaries. This causes a hardening and an increase in strength of the material with a decrease in deformability corresponding to the primary stage of creep behaviour. This process known as dislocation glide often occurs under the conditions of high stress and relatively low temperature.

Dislocations that have been blocked can become mobile again by a process known as dislocation climb. This recovery process involves the reduction in dislocation density and is driven by an increase in both temperature and the strain energy stored in the material. In order

for dislocations to climb atomic movement must take place during which atoms jump into neighbouring sites if a vacancy is present. An increase in temperature causes atoms to have increased thermal energy and produces a greater number of vacancies thus allowing climb to occur.

Grain boundary sliding

This process involves deformation by material grains sliding past one another due to shear stresses acting at grain boundaries. With small enough grain sizes this mechanism contributes to the creep deformation of salt rock, particularly at elevated temperatures.

Diffusion creep

At a micro scale some sites of atoms can be occupied by point defects. A point defect is where an atom is missing or is located in an irregular place in the crystal lattice structure. Defects can migrate through the lattice when the activation energy necessary to break inter crystalline bonds is provided. Thus at a higher temperature it becomes easier for migration to take place. Two types of diffusion creep are Nabarro Herring and Coble creep. The former involves vacancies moving through the crystal, whilst the latter involves vacancies moving along grain boundaries.

Cataclastic flow

Cataclastic flow or micro crack generation is brittle deformation, generally at grain contacts, but also passing through crystals. It occurs when loads are applied beyond the frictional limit, beyond the grain strength or beyond pore structure strength. It ceases when stresses are redistributed below these limits.

2.3 Models for predicting the creep deformation of deep cavities

A number of tools have been developed to predict the time-dependent closure of an underground opening. Two main groups are analytical methods and numerical methods, both of which are reviewed below.

2.3.1 Analytical models

Analytical methods tend to be those which produce closed-form solutions or pseudo-closed-form solutions [34]. Their formation often requires simplifications regarding material behaviour, problem geometry and boundary conditions. They are rare in practical rock mechanics and are sometimes difficult to apply to complex practical problems. However, they can often produce a solution in a short period of time with little or no computational effort. The effect of individual parameters on the solution can sometimes be seen easily, thus providing a valuable insight into the problem of cavity design.

2D, plane strain models have been developed for the case of singular, deeply embedded, cylindrical openings. Such models make a number of assumptions such as neglecting gravity stresses, an initial isotropic stress field and instantaneous excavation of the tunnel. These are discussed by Aiyer [2]. Neglecting gravity stresses and assuming an isotropic stress field can be justified when predicting the closure of deep openings. Gravity stresses may play a negligible role in the time-dependent deformation when the size of the opening is small compared to the depth. Also at great depths the materials may not be able to support large stress differences without creeping to equalise the stress. The assumption of instantaneous excavation of the tunnel will lead to overestimation of the creep deformation and therefore can be considered conservative. This may also be reasonably accurate for short excavations which take a short period of time to excavate.

Two of these models have been proposed by Aiyer [2] and Goodman [28], and adopt viscoelastic material behaviour. The closed-form solution proposed by Goodman [28] uses Burger's creep model to describe the time-dependent behaviour of the rock and is illustrated by two examples: (1) an unlined circular tunnel in an anisotropic stress field (horizontal stress σ_h not equal to the vertical stress σ_v) and (2) a lined circular tunnel in an isotropic stress field ($\sigma_h = \sigma_v$). An expression has also been proposed for the installation of rock bolts which can be superimposed onto the example for the unlined opening.

Aiyer [2] also developed a solution for both unlined and lined tunnels. A method was also produced for predicting the time-dependent behaviour of a spherical cavity. These methods use the form of the power creep law deduced by Boresi and Deere [7] (equation 2.8) focusing on openings located in salt rock. A non-linear incremental approach has been adopted. A parametric investigation was carried out in order to determine the influence of various factors on the time-dependent deformation. These factors included both elastic and creep material parameters, the magnitude of the stress field and others. Graphs were produced to show the variation of stress and strain with time and distance from the tunnel centre.

Aiyer's approach assumes the immediate response of the medium is linear elastic and the subsequent response is described using the creep law. A governing differential equation is derived from superimposing this law onto the equilibrium and compatibility equations for an elastic thick walled cylinder. The equation is then solved for a given boundary condition using an incremental approach. Phienwej et al. [49] adopted the method proposed by Aiyer [2] incorporating both a hyperbolic and power creep law. The effect of tunnel support was incorporated into the analysis. The hyperbolic law was able to take into account the elastoplastic behaviour of the ground and was used to predict the closure of a number of different tunnels located in poor rock masses. The predicted values were found to be in good agreement with *in situ* monitoring data.

Elasto-viscoplastic analytical solutions for cavity expansion problems have been developed by

Salamon [52], Nonaka [43] and Fritz [22], amongst others. It is important to note that such solutions are relatively rare. Many of these solutions adopt a von Mises yield criterion for the plastic slider element shown in Figure 2.5, thus only deviatoric viscoplastic strains occur (deviatoric creep only). In contrast Fritz developed a model which uses a Mohr-Coulomb yield criterion, thus dilatancy effects are described. This model takes into account both deviatoric and volumetric viscoplastic strains. Material softening is also incorporated by taking into account both peak and residual strengths of the material. However, a common assumption is that only deviatoric creep occurs in rocks. This is due to rock undergoing limited time-dependent volume changes as stated in Section 1.1. Many viscoplastic constitutive models assume that only deviatoric viscoelastic and viscoplastic strains occur. An example is the model developed by Gioda [24] and Gioda and Cividini [25] (Figure 2.6). This model uses a Mohr-Coulomb yield criterion which is more suitable for representing geomaterials than a von Mises criterion, due to it taking into account frictional behaviour, but assumes viscoelastic-viscoplastic (time-dependent) deviatoric behaviour and only elasto-plastic (time-independent) volumetric behaviour.

A number of models have been developed for cylindrical tunnels, which attempt to take into account the 3D interaction between the tunnels and the surrounding creeping rock. Here the problem is idealised as a 2D plane-strain problem. In this simplified approach, the analysis of stresses and displacements near the tunnel face is performed by regarding the face as providing a fictitious internal support pressure. The magnitude of this internal pressure is related to the face position by using empirical relations based on field measurements or 3D FE analyses. Solutions derived by Sakurai [51]; Sulem et al. [60]; Ladanyi [34]; Panet [46]; and Fahimifar et al. [18] are examples of this approach. The following empirical relation was proposed by Panet [46]

$$\lambda(x) = 0.28 + 0.72 \left[1 - \left(\frac{X}{X + x} \right)^2 \right] \tag{2.10}$$

where x is the distance from the tunnel face, $X = 0.84b$ and b is the tunnel radius. The λ parameter varies between 0 and 1 ($\lambda = 1$ belongs to sections located far away from the tunnel face ($x > 4R$ as shown in Figure 2.8)).

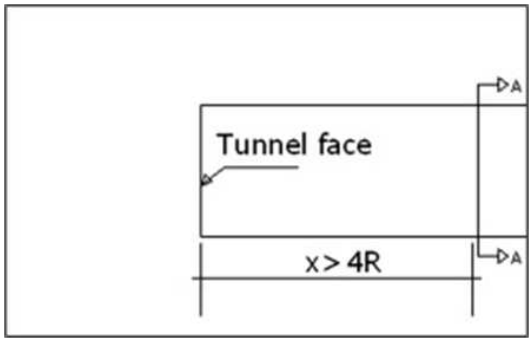

Figure 2.8: Model showing a section located far behind the tunnel face (Fahimifar et al. [18])

These empirical formulas are useful for practical applications because they are often derived directly from the real tunnel performance data. However, the parameters are often difficult to determine and there are significant uncertainties in extrapolating these empirical relations to different design situations and rock behaviour. This is highlighted through the derivation of many different empirical relations (e.g. Corbetta et al. [13], Panet [46]. Carranza-Torres and Fairhurst [10] and Unlu and Gercek [63]).

2.3.2 Numerical models

According to Gioda and Swoboda [26] tunnelling engineering is perhaps one of the areas of applied soil and rock mechanics in which numerical methods are more frequently adopted in practice. This is due to the complex characteristics which are encountered in tunnelling problems. An important characteristic is the strong influence of the excavation and construction procedures on the stress/strain distribution in the rock surrounding the opening. This construction procedure is generally not considered with sufficient accuracy in closed-form solutions. Simulation of construction can be carried out in a numerical analysis with accuracy only being limited by the required computational effort. Secondly, the complex geometrical nature of tunnelling problems can be analysed. This not only includes the shape of excavation, but also the discontinuities located in the rock. Both 2D and 3D analyses can be carried out, only being limited by the computational time.

Numerical methods such as the FE method and finite difference (FD) method are widely used in the analysis of real life tunnelling problems. The FE method is well suited to solving problems involving heterogeneous or non-linear material properties, as each element explicitly models the response of its contained material. However, the FE method is not ideal for modelling infinite boundary problems, such as those involving underground openings. This can be overcome by extending the mesh boundaries beyond the zone of influence of the excavation and by applying appropriate boundary conditions to the mesh edges. An alternative is to use infinite elements of which one edge extends to infinity. There are a wide range of commercial packages into which creep models are incorporated.

Complex numerical analyses have been carried out by a number of authors using complex constitutive models shown in the first part of this chapter, to predict the creep deformation of specific sites (e.g. [4], [6], [12], [23], [24], [30], [47], [56], [59], [62], [67] and [68]). For example Yu et al. [67] carried out a plane strain FE analysis to predict the ground behaviour of a typical room and pillar mining section of a Western Canadian potash mine, thus modelling the interaction between two tunnels and also taking into account the different geological strata. The excavation procedure was simulated through deactivation of model elements inside the openings over a number of steps, with creep deformation being introduced during each step. A similar analysis was conducted by Swift and Reddish [62] for a section of the Winsford Salt Mine located in Cheshire. Other researchers conducted axisymmetric analyses such as Shalabi [56] who developed a model for the Stillwater Tunnel located in Utah.

These numerical models are commonly validated using *in situ* closure measurements and then future predictions of cavity deformation can be made (e.g. Swift and Reddish [62] validated a numerical model through simulation of a 9 year time period and then made predictions of deformation for up to 500 years). The numerical model developed by Yu [67] was validated using model tests constructed in the laboratory due to the *in situ* stress being difficult to measure.

Despite these models being very practical, they are often computationally expensive for routine practice and require a significant time to construct the initial geometry and mesh.

2.4 Summary

From reviewing the creep behaviour of deeply embedded cavities the following observations have been made

- creep behaviour of rock is complex and depends on a wide number of factors, therefore it is very much a site specific process.
- there are a number of difficulties in obtaining rock parameters which are representative of *in situ* conditions. Therefore it is important to conduct a rigorous laboratory creep testing program and *in situ* creep tests and back analysis where possible.
- many different constitutive models are used to describe creep behaviour of rock, which are then used to obtain predictions of the creep behaviour of an underground opening. These models consist of rheological, empirical and those based on physical processes. It is important to select an appropriate model.
- both rheological and empirical models have been used successfully in predicting creep closure of tunnels. The rheological models are particularly attractive as they are not related to a particular creep test and have a firm physical base, and thus can be applied to a wide range of problems with only the material parameters changing. Viscoplastic models are able to describe the constitutive behaviour of geomaterials more accurately than viscoelastic models as they are able to take into account the non-linear relationship between stress and strain and predict non reversible time-dependent deformations.
- analytical models are useful tools for conducting parametric studies into the behaviour of deep cavities. Solutions can often be produced in a short period of time. 2D solutions exist for both lined and unlined cylindrical cavities located in viscoelastic and viscoplastic media. However, few viscoplastic solutions exist. Empirical relations are used to approximate the stresses and displacements occurring at a tunnel face. However, there is significant uncertainty when extrapolating these relations to different design situations and rock behaviour.

- numerical models are able to take into account the complex characteristics encountered in tunelling problems, such as complex material behaviour and the excavation process. As a result they are used frequently for practical applications to accurately predict the time-dependent response. However, they are often computationally expensive for routine practice.

In light of these observations it is evident that there is a need for a new tool which can model a wide range of material behaviour, including complex material behaviour and can be applied to both 2D and 3D problems, whilst being less computationally expensive and more simple to use than FE analysis. This tool could be used in the early cavity design stage. The energy-based method proposed in this thesis will be used to derive a new tool and rheological models will be incorporated due to their ability to describe realistic creep behaviour and their applicability to a wide range of different materials.

2.5 References

1 Afrouz, A. & Harvey, J. (1974). Rheology of rocks within the soft to medium strength range. *International Journal of Rock Mechanics and Mining Sciences & Geomechanics*, 11(7) p. 281-290.

2 Aiyer, A.K. (1969). An analytical study of the time-dependent behaviour of underground openings. Ph.D. thesis, University of Illinois at Urbana Champaign, Urbana, III.

3 Barla, G. (1995). Squeezing rocks in tunnels. *ISRM News Journal*, 2(3-4) p. 44-49.

4 Barla, G., Bonini, M. & Debernardi, D. (2008). Time Dependent Deformations in Squeezing Tunnels. *International Journal of Geoengineering Case Histories*, 2(1) p. 40-65.

5 Bérest, P., Béraud, J.F., Brouard, B., Blum, P.A., Charpentier, J.P., de Greef, V., Gharbi, H. & Valès, F. (2010). Very slow creep tests on salt samples. EPJ Web of Conferences, 6.

6 Bonini, M., Debernardi, D., Barla, M. & Barla G. (2007). The mechanical behaviour of clay shales and implications on the design of tunnels. *Rock Mech Rock Engng* 42(2) p. 361388.

7 Boresi, A.P. & Deere, D.U. (1963). Creep Closure of a Spherical Cavity in an Infinite Medium. *Report*, Holmes and Narver, Las Vegas, NV.

8 Bosman, J.D., Malan, D.F., & Drescher, K. (2000). Time-dependent tunnel deformation at Hartebeestfontein Mine. In:*Proceedings of the AITES-ITA 2000 World Tunnel Congress*, SAIMM, Durban, p.55-62.

9 Campos De Orellana, A.J. (1996). Pressure solution creep and non associated plasticity in the mechanical behaviour of potash mine openings. *International Journal of Rock Mechanics and Mining Science in Geomechanics*, 33(4) p. 347-370.

10 Carranza-Torres, C. & Fairhurst, C. (2000). Application of the convergence-confinement method of tunnel design to rock masses that satisfy the Hoek-Brown failure criterion. *Tunneling and Underground Space Technology*, 15(2) p. 187-213, (Personal communication with Hoek).

11 Chin, H.P. & Rogers, J.D. (1987). Creep Parameters of Rocks on an Engineering Scale. *Rock Mechanics and Rock Engineering*, 20 p. 137-146.

12 Cividini, A., Gioda, G. & Carini, A. (1991). A finite element analysis of time-dependent behaviour of underground openings. In: Beer, Booker, Carter (Eds.), *Computer Methods and Advances in Geomechanics*.

13 Corbetta, F., Bernaud, D. & Nguyen-Minh, D. (1991). Contribution a la methode convergence-confinement par le principe de la similitude. Rev Fr Geotech, 54 p. 5-11.

14 Cristescu, N. (1989). *Rock Rheology.* Kluwer, Dordrecht.

15 Debernardi, D. (2008). Viscoplastic Behaviour and Design of Tunnels. Ph.D. Thesis, Politecnico di Torino, Torino.

16 Dreyer, W. (1973). Flow at a constant stress. In:*The science of rock mechanics*, Part 1, Clausthal: Trans Tech Publications, p. 126-139.

17 Dusseault, M. B. & Fordham, C. J. (1993). Time-dependent behaviour of rocks. In:*Comprehensive rock engineering*, 3 (edited by J.A. Hudson), Pergamon Press, p. 119149.

18 Fahimifar, A., Tehrani, F.M., Hedayat, A. & Vakilzadeh, A. (2010). Analytical solution for the excavation of circular tunnels in a visco-elastic Burger's material under hydrostatic stress field. *Tunnelling and Underground Space Technology*, 25(4) p. 297-304.

19 Fakhimi, A.A. (1992). The influence of time-dependent deformation of rock on the stability of underground excavations. Ph.D. Thesis, University of Minnesota, U.S.A.

20 Fakhimi, A.A. & Fairhurst, C. (1994). A model for the time-dependent behaviour of rock. *International Journal of Rock Mechanics and Mining Sciences*, 31 p. 117-126.

21 Febres-Cordero, E. (1974). Influence on testing conditions on creep behaviour of clay. Ph.D. Thesis, University of Illinois at Urbana Champaign, Urbana, III.

22 Fritz, P. (1984). An analytical solution for axisymmetric tunnel problems in elasto-viscoplastic media. *International Journal for Numerical and Analytical Methods in Geomechanics*, p. 325-342.

23 Ghaboussi, J. & Gioda, G. (1977). On the time dependent effects in advancing tunnels. *International Journal for Numerical and Analytical Methods in Geomechanics*, 1 p. 249-269.

24 Gioda, G. (1982). On the non linear squeezing effects around circular tunnels. *International Journal for Numerical and Analytical Methods in Geomechanics*, 6 p. 21-46.

25 Gioda, G. & Cividini, A. (1996). Numerical methods for the analysis of tunnel performance in squeezing rocks. *Rock Mechanics and Rock Engineering*, 29 p. 171-193.

26 Gioda, G. & Swoboda, G. (1999). Developments and applications of the numerical analysis of tunnels in continuous media. *International Journal for Numerical and Analytical Methods in Geomechanics*, 23 p. 1393-1405.

27 Gnirk, P.F. & Johnson, R.E. (1964). The deformational behaviour of a circular mine shaft situated in a viscoelastic medium under hydrostatic stress. In:*Proceedings of the Sixth U.S. Symposium on Rock Mechanics*, Rolla, p. 231-259.

28 Goodman, R.E. (1989). *Introduction to Rock Mechanics*. Second Edition. John Wiley & Sons, New York.

29 Griggs, D. (1939). Creep of Rocks. *The Journal of Geology*, 47(3) p. 225-251.

30 Hanafy, E.A., & Emery, J.J. (1979). Advancing face simulation of tunnel excavations and lining placements. In:*Proceedings of the 13th Canadian Rock Mechanics Symposium*, Underground Rock Engineering, Toronto, p. 119-125.

31 Hansen, F.D & Carter, N.L. (1984). Creep of Avery Island rocksalt. In:*Proceedings of the 1st Conference on Mechanical Behaviour of Salt*, Clausthal:Trans Tech Publications, p. 53-69.

32 Jaeger, J.C., Cook, N.G.W. & Zimmerman, R.W. (2007). *Fundamentals of rock mechanics*. Fourth Edition. Blackwell, Oxford.

33 Jeremic, M.L. (1994). *Rock Mechanics in Salt Mining*. Balkema, Rotterdam.

34 Ladanyi, B. (1993). Time-dependent response of rock around tunnels. *Comprehensive Rock Engineering*, 2, Elsevier, Amsterdam, p. 77-112.

35 Langer, M. (1982). Geotechnical investigation methods for rock salt. *Bulletin of the International Association of Engineering Geology*, 25 p. 155-164.

36 Le Comte, P. (1965). Creep in Rock Salt. *Journal of Geology*, 73 p. 469-484.

37 Lemaitre, J. & Chaboche, J.L. (1996). Mécanique des matériaux solides. *Dunod*, 253-341.

38 Lin, H.D., & Wang, C.C. (1998). Stress-strain time function of clay. *Liquid Crystal and Ordered Fluids*, 142(4) p. 289-296.

39 Malan, D.F. (1995). A viscoelastic approach to the modelling of transient closure behaviour of tabular excavations after blasting. *Journal of the South African Institute of Mining and Metallurgy*, 95 p. 211220.

40 Mesri, G., Febres-Cordero, E., Shield, D.R. & Castro, A. (1981). Shear-stress-strain behaviour of clays. *Géotechnique*, 31(4) p. 537-552.

41 Mirza, U.A. (1984). Prediction of creep deformations in rock salt pillars. In:*Proceedings of the 1st Conference on the Mechanical Behaviour of Salt*, Clausthal: Trans Tech Publications, p. 311-337.

42 Munson, D.E. & Dawson, P.R. (1984). Salt constitutive modelling using mechanism maps. In:*Proceedings of the 1st Conference on the Mechanical Behaviour of Salt*, Clausthal: Trans Tech Publications, p. 717-737.

43 Nonaka, T. (1981). A time-independent analysis for the final state of an elasto-visco-plastic medium with internal cavities. *International Journal of Solids and Structures*, 17 p. 961-967.

44 Obert, L. (1965). Creep in mine pillars: Report of investigation. Rep. No. 6703, U.S. Bureau of Mines.

45 Pan, Y.W. & Dong, J.J. (1991). Time-dependent tunnel convergence I. Formulation of the model. *International Journal of Rock Mechanics and Mining Sciences*, 28 p. 469-475.

46 Panet, M. (1993). Understanding deformations in tunnels. *Comprehensive rock engineering*, 1, Pergamon Press, Oxford, p. 663-690.

47 Peila, D., Oreste, P., Rabajuli, G. & Trabucco, E. (1995). The pre-tunnel method, a new Italian technology for full-face tunnel excavation: a numerical approach to design. *Tunnelling and Underground Space Technology*, 10(3) p. 367-394.

48 Perzyna, P. (1966). Fundamental problems in viscoplasticity. *Advances in Applied Mechanics*, 9 p. 243-377.

49 Phienwej, N., Thakur, P.K. & Cording, P.E. (2007). Time-Dependent Response of Tunnels Considering Creep Effect. *International Journal of Geomechanics*, 7(4) p. 296-306.

50 Phueakphum, D. & Fuenkajorn, K. (2010). Effects of cycling loading on mechanical properties of Maha Sarakhm salt.*Engineering Geology*, 112(14) p. 4352.

51 Sakurai, S. (1978). Approximate time-dependent analysis of tunnel support structure considering progress of tunnel face. *International Journal for Numerical and Analytical Methods in Geomechanics*, 2 p. 159-175.

52 Salamon, M.D.G. (1974). Rock mechanics of underground excavations. In:*Proceedings of the Third Congress of the International Society of Rock Mechanics* 1 part B p. 994-1000.

53 Scott-Duncan, E.J. & Lajtai, E.Z. (1993). The creep of potash salt rocks from Saskatchewan. *Geotechnical and Geological Engineering*, 11 p. 159-184.

54 Semple, R.M. (1973). Effect of time-dependent properties of altered rocks on tunnel support requirements. Ph.D. Thesis, University of Illinois at Urbana Champaign, Urbana, I11.

55 Senseny, P.E. (1984). Specimen size and history effects on creep of salt. In:*Proceedings of the 1st Conference on the Mechanical Behaviour of Salt*, Clausthal: Trans Tech Publications, p. 369-379.

56 Shalabi, F.I. (2005). FE analysis of time-dependent behaviour of tunnelling in squeezing ground using two different creep models. *Tunnelling and Underground Space Technology*, 20 p. 271-279.

57 Singh, D.P. (1975). A Study of Creep of Rocks. *International Journal of Rock Mechanics and Mining Sciences and Geomechanics*, 12 p. 271-276.

58 Singh, A. & Mitchell, J.K. (1968). General stress-strain time function for soils. *Journal of the Soil Mechanics and Foundations Division*, 94(1) p. 21-46.

59 Sterpi, D. & Gioda, G. (2009). Visco-plastic behaviour around advancing tunnels in squeezing rock. *Rock Mechanics and Rock Engineering*, 42 p. 319-339.

60 Sulem, J., Panet, M. & Guenot, A. (1987). An Analytical Solution for Time-dependent Displacements in a Circular Tunnel. *International Journal of Rock Mechanics and Mining Sciences and Geomechanics*, 24(3) p.155-164.

61 Sulem, J., Panet, M. & Guenot, A. (1987). Closure Analysis in Deep Tunnels. *International Journal of Rock Mechanics and Mining Sciences and Geomechanics*, 24(3) p.145-154.

62 Swift, G.M. & Reddish, D.J. (2005). Underground excavations in rock salt. *Geotechnical and Geological Engineering*, 23 p. 17-42.

63 Unlu, T. & Gercek, H. (2003). Effect of Poisson's ratio on the normalised radial displacements occuring around the face of a circular tunnel. *Tunnelling and Underground Space Technology*, 18 p. 547-553.

64 United States Army Corps of Engineers. (1965). Project Dribble-Petrographic Examination and Physical Tests of Cores, Tatum Salt Dome, Mississippi, Technical Report No. 6-614, Vicksburg, Mississippi.

65 Vouille, G., Tijani, F. & de Grenier, F. (1984). Experimental determination of the rheological behaviour of Tersanne rock salt. In:*Proceedings of the 1st Conference on the Mechanical Behaviour of Salt*, Clausthal: Trans Tech Publications, p. 407-420.

66 Vyalov, S.S. (1972). Creep in rock. *Power Technology and Engineering*, 6 p. 228-234.

67 Yu, C.W. (1998). Creep characteristics of Soft Rock and Modelling of Creep in Tunnel. Ph.D. thesis, University of Bradford, Bradford.

68 Yu, Y.S., Ong, C.G. & Mottahed, P. (1988). Viscoelastic finite element analysis in design of potash mines. *Engineering Computations*, 5 p. 248-253.

69 Zhifa, Y., Zhiyin, W., Luqing, Z., Ruiguang, Z. & Nianxing, X. (2001). Back-analysis of viscoelastic displacements in a soft rock road tunnel. *International Journal of Rock Mechanics and Mining Sciences*, 38 p. 331-341.

Chapter 3

Energy-based approach for the creep analysis of cavities

Synopsis

This chapter begins by introducing the energy-based method in Section 3.1, which is used throughout this thesis to develop new simple tools for cavity design. Here we demonstrate how the method can be used to derive existing cavity solutions. This provides a useful introduction to the energy-based approach and a helpful reference when developing new models in the remaining chapters. Simple linear elastic models are derived in Section 3.2, for cylindrical and spherical cavities located in isotropic stress fields. A linear elastic model is then derived for a cylindrical cavity in an anisotropic stress field shown in Section 3.3. Section 3.4 demonstrates how linear viscoelastic constitutive behaviour can be incorporated in the Laplace domain using Burger's viscoelastic constitutive model in order to predict creep behaviour. Finally elasto-plastic constitutive behaviour is introduced in Section 3.5 and incorporated into the cavity equations in Section 3.6, thus non-reversible deformations are present. This is a step towards incorporating time-dependent viscoplastic constitutive behaviour which is developed in Chapters 5 and 6. All of the models derived in this chapter are validated with existing closed-form solutions or finite element (FE) analysis.

3.1 Energy-based method

The phrase "energy-based method" refers to a method that makes use of the energy of a mechanical system to obtain values of an unknown displacement or force at a specific point in the system. Here we use a variational method which makes use of variational principles, such as the principles of virtual work and minimum total potential energy to determine approximate solutions to the system as continuous functions of position. For example, applying a constant pressure to a cavity located in an elastic medium will cause a displacement field to occur surrounding the cavity. What configuration will this displacement field take? Here we can use the principle of virtual work to minimise the energy in the system and thus derive an equation which governs the displacement field. This displacement field is the optimum

configuration which is in fact the one realised in nature.

Variational calculus was developed by many of the great mathematicians such as the Bernoulli family, Euler and Lagrange. It is a powerful tool which can be used to obtain approximate solutions to a range of practical problems which otherwise may be difficult to solve. Variational principles have been applied to the field of geotechnics, where several studies on piles located in elastic continua have been carried out (e.g. [2], [13], [28]) and Einav [10] solved the problem of a pile located in an elasto-plastic soil by introducing a dissipation function into the energy formulation. Variational principles are independent of any constitutive law and can be applied to elastic (linear and non-linear) and inelastic continuum problems. A summary of variational methods is provided by Reddy [25].

3.1.1 Principle of virtual work

As stated above, the principle of virtual work is a variational principle that can be used to obtain the equations governing the unknown displacements of a system by minimising the energy in the system. This principle is also known as the principle of minimum total potential energy when applied to elastic materials. From a geometric point of view a given mechanical system can take many different configurations which are consistent with the boundary conditions of the system. However, only one of these configurations corresponds to the actual configuration which satisfies Newton's second law (equilibrium of forces and moments). The set of configurations which are consistent with the boundary conditions is known as the set of admissible configurations. These are within the neighbourhood of the actual configuration and are obtained from variations of the actual configuration. During these variations the boundary conditions are not violated and all the forces are fixed at their equilibrium values. When a mechanical system undergoes such variations, it is said to undergo virtual displacements from its equilibrium condition. These displacements are imaginary and the actual loads act at their fixed values. The work done by the actual forces through a virtual displacement of the actual configuration is called virtual work.

The definition of virtual work is as follows: *a continuous body is in equilibrium if the virtual work of all the forces acting on the body is zero in a virtual displacement.* Mathematically the total virtual work for an elastic body at equilibrium can be expressed as

$$\delta\Pi = \delta U - \delta W = 0, \tag{3.1}$$

where δU is the virtual potential energy change when the system is displaced by a virtual displacement δu and δW is the external virtual work due to a virtual displacement δu. The delta operator is known as the variational operator because it is used to denote a variation or change in a given quantity. A visual illustration of the principle of virtual work is shown in Figure 3.1. This figure shows a sketch of the total energy of a system as a function of

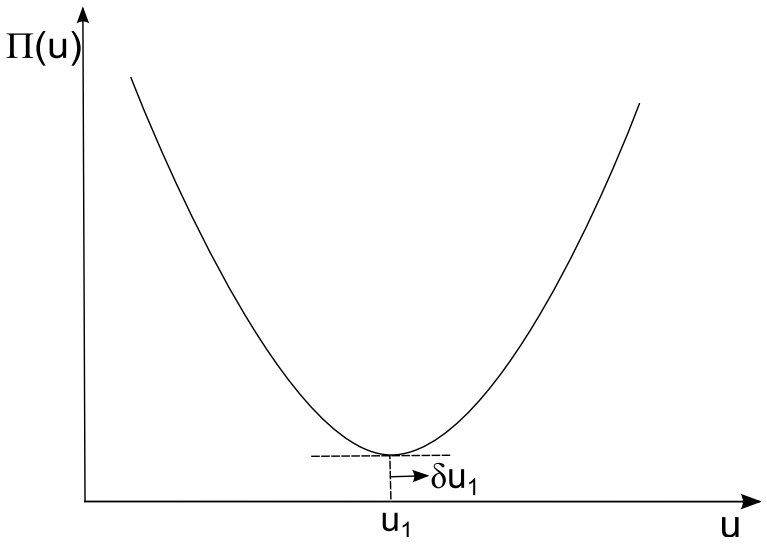

Figure 3.1: Total energy of a system as a function of displacement, where the actual displacement u_1 corresponds to the minimum on the curve at which point the total virtual work is equal to zero

displacement. Equation 3.1 corresponds to the minimum point on the curve at which point the total energy attains a stationary value corresponding to the actual displacement of the system and the point of equilibrium.

3.1.2 Method adopted in this thesis

The method we adopt in this thesis is based on that by Vlasov and Leontiev [32] who developed a method for the analysis of beams on elastic foundations based on an elastic continuum approach. This method has also been used more recently for three-dimensional (3D) pile analysis (e.g. [2], [3]). In this approach each component of the displacement field (e.g. the displacement in the x direction u_x) within the elastic continuum is expressed as a product of independent 1D functions (e.g. $u_x = \phi_x(x)\phi_y(y)$ if u_x varies in the x and y directions). The potential energy U of the elastic continuum can then be expressed in terms of the 1D functions (e.g. ϕ_x and ϕ_y) using standard strain-displacement relations and stress-strain relations. An expression can also be written for the external work W. Applying the principle of virtual work (equation 3.1) results in an equation for $\delta\Pi$ containing terms featuring variations (e.g. $\delta\phi_x$ and $\delta\phi_y$). Collection of the terms associated with each variation (e.g. collection of the terms associated with $\delta\phi_x$) over the problem domain forms a governing differential equation corresponding to the equilibrium of the system. The boundary conditions can be obtained by collecting the terms associated with each variation at the problem boundaries. Once the 1D functions have been solved for (e.g. ϕ_x), the displacements (e.g. u_x) can be evaluated for the system. Examples of how this method has been implemented into cavity problems can be found throughout this chapter.

3.2 Simple cavity problems

The proposed energy-based method is now used to derive solutions for cylindrical and spherical cavities located in both finite and infinite linear elastic bodies. Here the radial displacement is assumed to be positive when directed out of the cavity. Compressive stresses are assumed to be negative.

3.2.1 Cylindrical cavity

Here we develop a solution using the proposed energy-based method for an infinitely long cylindrical cavity subjected to uniform internal and external pressures, p_i and p_o respectively, thus we assume the condition of plane strain.

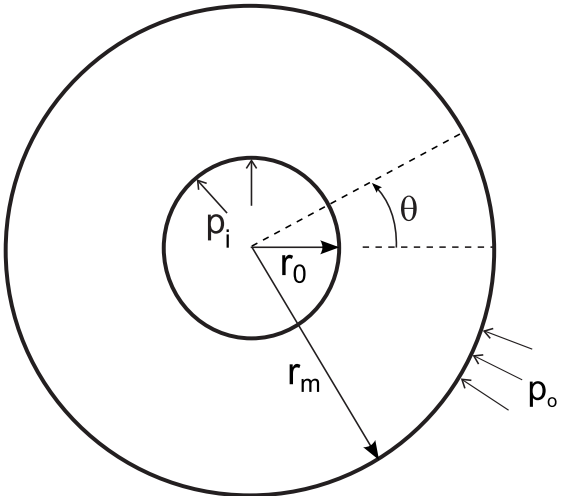

Figure 3.2: Cavity under uniform internal and external pressures

Due to symmetry, this problem is effectively 1D and only radial displacement u_r is present which is a function of the radial distance r. The potential energy U of the system can be written as follows in terms of stress and strain components by integrating over the problem domain

$$U = \frac{1}{2}\int_{r_0}^{r_m}\int_{0}^{2\pi}(\sigma_{rr}\varepsilon_{rr} + \sigma_{\theta\theta}\varepsilon_{\theta\theta})r\,d\theta\,dr, \tag{3.2}$$

where σ_{rr} and $\sigma_{\theta\theta}$ are the radial and circumferential stresses respectively and ε_{rr} and $\varepsilon_{\theta\theta}$ are the radial and circumferential strains respectively. θ is the angular coordinate.

In a linear elastic material, the stress-strain relations in cylindrical coordinates are given by

$$\sigma_{rr} = \lambda(\varepsilon_{rr} + \varepsilon_{\theta\theta}) + 2G\varepsilon_{rr}, \tag{3.3}$$

$$\sigma_{\theta\theta} = \lambda(\varepsilon_{rr} + \varepsilon_{\theta\theta}) + 2G\varepsilon_{\theta\theta}, \tag{3.4}$$

where G and λ are the Lamé constants.

The strains are obtained from the first derivative of displacements as follows

$$\varepsilon_{rr} = \frac{du_r}{dr}, \tag{3.5}$$

$$\varepsilon_{\theta\theta} = \frac{u_r}{r}. \tag{3.6}$$

Using the above stress-strain relations, the strain-displacement relations and the assumed displacement field, equation 3.2 can be evaluated as follows

$$U = \pi \int_{r_0}^{r_m} \left((\lambda + 2G) \left(\left(\frac{du_r}{dr} \right)^2 + \left(\frac{u_r}{r} \right)^2 \right) + 2\lambda \left(\frac{u_r}{r} \frac{du_r}{dr} \right) \right) r dr. \tag{3.7}$$

Variational principles are then used to obtain expressions for δU and δW from which the governing differential equation of the system and appropriate boundary conditions can be written.

The variation in the external work W is given by

$$\delta W = 2\pi p_i r_0 \delta u_r - 2\pi p_o r_m \delta u_r. \tag{3.8}$$

The governing equations for deformation are derived using the principle of virtual work (equation 3.1). Setting the first variation of the total energy $\delta\Pi$ equal to zero produces an equation of the form $\delta\Pi = [C(u_r)\delta u_r] = 0$ as shown below

$$\begin{aligned} \delta\Pi = 2\pi(\lambda + 2G) \left(\left[r \frac{du_r}{dr} \right]_{r_0}^{r_m} \delta u_r - \int_{r_0}^{r_m} \left(r \frac{d^2 u_r}{dr^2} + \frac{du_r}{dr} \right) \delta u_r dr + \int_{r_0}^{r_m} \frac{u_r}{r} \delta u_r dr \right) \\ +2\pi\lambda \left(\int_{r_0}^{r_m} \frac{du_r}{dr} \delta u_r dr + [u_r]_{r_0}^{r_m} \delta u_r - \int_{r_0}^{r_m} \frac{du_r}{dr} \delta u_r dr \right) - 2\pi p_i r_0 \delta u_r + 2\pi p_o r_m \delta u_r = 0. \end{aligned} \tag{3.9}$$

Collection of the terms associated with each variation (δu_r) over the problem domain $r_0 \leq r \leq r_m$ forms the differential equation which governs the displacements of the system. Since the variation of displacement is non-zero over the domain ($\delta u_r \neq 0$), the coefficients of the terms (the integrand) must be equal to zero in order to satisfy equation 3.9. Expressions for the boundary conditions can be formed by collecting the terms associated with each variation at the problem boundaries (collection of the δu_r terms at $r = r_0$ and at $r = r_m$) and setting these expressions equal to zero in order to satisfy equation 3.9. The governing equation and boundary conditions are expressed in the following section.

Governing differential equation and boundary conditions

Collecting the coefficients of δu_r for $r_0 \leq r \leq r_m$ forms the differential equation governing the displacements of the system

$$2\pi(\lambda + 2G)\left(r\frac{d^2u_r}{dr^2} + \frac{du_r}{dr} - \frac{u_r}{r}\right) = 0. \tag{3.10}$$

Collecting the δu_r terms at $r = r_0$ gives

$$\left[2\pi\Big((\lambda + 2G)r\frac{du_r}{dr} + \lambda u_r + p_i r_0\Big)\right]\delta u_r = 0, \tag{3.11}$$

and collecting the δu_r terms at $r = r_m$ gives

$$\left[2\pi\Big((\lambda + 2G)r\frac{du_r}{dr} + \lambda u_r + p_o r_m\Big)\right]\delta u_r = 0. \tag{3.12}$$

To satisfy these boundary conditions we can assume that the bracketed terms are equal to zero. These correspond to the stresses at the cavity boundaries which are known as the natural boundary conditions as they are derived straight from the energy-based method and are not enforced. An alternative boundary condition for a cavity under internal pressure only would be $u_r = 0$ at $r = r_m$, corresponding to zero displacement at the far field boundary, which satisfies the boundary conditions.

The general solution to equation 3.10 is

$$u_r = Ar + \frac{B}{r}, \tag{3.13}$$

where A and B are constants which are found using the boundary conditions.

Implementing the natural boundary conditions we can derive a closed-form solution which is identical to that derived by Jaeger et al. [19]. It is important to note here that there is a change in sign of the displacement between the proposed solution and that derived by Jaeger et al. [19] (radial displacement assumed to be positive when directed into the cavity in Jaeger et al. [19]).

$$2Gu_r = -(1 - 2\nu)\frac{({r_0}^2 p_i - {r_m}^2 p_o)r}{({r_0}^2 - {r_m}^2)} - \frac{{r_0}^2{r_m}^2(p_i - p_o)}{({r_0}^2 - {r_m}^2)r}. \tag{3.14}$$

As $r_m \to \infty$ the following solution can be written

$$2Gu_r = -(1 - 2\nu)p_o r + (p_i - p_o)({r_0}^2/r), \tag{3.15}$$

for a cavity located in an infinite elastic medium.

Assuming that $p_o = 0$, the following equation can be written for a cavity expansion problem

$$2Gu_r = -(1-2\nu)\frac{({r_0}^2 p_i)r}{({r_0}^2 - {r_m}^2)} - \frac{{r_0}^2 {r_m}^2 p_i}{({r_0}^2 - {r_m}^2)r}. \tag{3.16}$$

As $r_m \to \infty$ we can write

$$2Gu_r = p_i({r_0}^2/r). \tag{3.17}$$

Thus the displacements are largest at the cavity wall and decay with radial distance away from the cavity.

Expressions for the stresses can be formed by substituting the strain-displacement relations (equations 3.5 and 3.6) into the stress-strain relations (equations 3.3 and 3.4)

$$\sigma_{rr} = \lambda\left(\frac{\partial u_r}{\partial r} + \frac{u_r}{r}\right) + 2G\frac{du_r}{dr}, \tag{3.18}$$

$$\sigma_{\theta\theta} = \lambda\left(\frac{\partial u_r}{\partial r} + \frac{u_r}{r}\right) + 2G\frac{u_r}{r}. \tag{3.19}$$

Here we can validate the stress components with existing closed-form solutions through substituting the displacement into the stress expressions. For a cavity under internal pressure and located in an infinite medium (substituting equation 3.17 into equations 3.18 and 3.19), we find that the stresses are identical to those derived by Kirsch [20]

$$\sigma_{rr} = -p_i\left(\frac{r_0}{r}\right)^2, \tag{3.20}$$

$$\sigma_{\theta\theta} = p_i\left(\frac{r_0}{r}\right)^2. \tag{3.21}$$

Here we observe that at the cavity wall the radial and circumferential stresses are equal in magnitude to the internal cavity pressure and decay with increasing radial distance.

3.2.2 Spherical cavity

Here we demonstrate how the proposed method can be used to derive solutions for a spherical cavity problem. Analogous to the cylindrical cavity only radial displacement is present which is a function of the radial distance r. The potential energy of the system can be written as follows by integrating over the volume of the sphere (an element of the volume of a sphere is $dV = r^2\sin(\Phi)d\Phi d\theta dr$ where θ is the azimuthal angle, identical to that defined earlier for the cylindrical cavity and Φ is the zenith angle)

$$U = \frac{1}{2}\int_{r_0}^{r_m}\int_{0}^{2\pi}\int_{0}^{\pi}(\sigma_{rr}\varepsilon_{rr} + \sigma_{\Phi\Phi}\varepsilon_{\Phi\Phi} + \sigma_{\theta\theta}\varepsilon_{\theta\theta})r^2\sin(\Phi)d\Phi d\theta dr. \tag{3.22}$$

In a linear elastic material, the stress-strain relations in spherical coordinates are given by

$$\sigma_{rr} = \lambda(\varepsilon_{rr} + \varepsilon_{\theta\theta} + \varepsilon_{\Phi\Phi}) + 2G\varepsilon_{rr}, \tag{3.23}$$

$$\sigma_{\theta\theta} = \lambda(\varepsilon_{rr} + \varepsilon_{\theta\theta} + \varepsilon_{\Phi\Phi}) + 2G\varepsilon_{\theta\theta}, \tag{3.24}$$

$$\sigma_{\Phi\Phi} = \lambda(\varepsilon_{rr} + \varepsilon_{\theta\theta} + \varepsilon_{\Phi\Phi}) + 2G\varepsilon_{\Phi\Phi}. \tag{3.25}$$

The strains are obtained from the first derivative of displacements as follows

$$\varepsilon_{rr} = \frac{du_r}{dr}, \tag{3.26}$$

$$\varepsilon_{\Phi\Phi} = \frac{u_r}{r}, \tag{3.27}$$

$$\varepsilon_{\theta\theta} = \frac{u_r}{r}. \tag{3.28}$$

Using the above stress-strain relations, the strain-displacement relations and the assumed displacement field, equation 3.22 can be evaluated as follows

$$U = 2\pi \int_{r_0}^{r_m} \left((\lambda + 2G) r^2 \left(\frac{du_r}{dr} \right)^2 + 4\lambda \left(r u_r \frac{du_r}{dr} \right) + 2(2\lambda + 2G) {u_r}^2 \right) dr. \tag{3.29}$$

The variation in external work is given by

$$\delta W = 4\pi p_i {r_0}^2 \delta u_r - 4\pi p_o {r_m}^2 \delta u_r. \tag{3.30}$$

Again using the principle of virtual work the following equation can be formed

$$\begin{aligned} \delta\Pi =& 4\pi \Bigg((\lambda + 2G) \Bigg(\left[r^2 \frac{du_r}{dr} \right]_{r_0}^{r_m} \delta u_r - \int_{r_0}^{r_m} \left(r^2 \frac{d^2 u_r}{dr^2} + 2r \frac{du_r}{dr} \right) \delta u_r dr \Bigg) \delta u_r dr \\ &+ 2\lambda \Bigg([r u_r]_{r_0}^{r_m} \delta u_r - \int_{r_0}^{r_m} \left(r \frac{du_r}{dr} + u_r \right) \delta u_r dr + \int_{r_0}^{r_m} r \frac{du_r}{dr} \delta u_r dr \Bigg) + (2\lambda + 2G) \int_{r_0}^{r_m} u_r \delta u_r dr \Bigg) \\ &- 4\pi p_i {r_0}^2 \delta u_r + 4\pi p_o {r_m}^2 \delta u_r = 0. \end{aligned} \tag{3.31}$$

Governing differential equation and boundary conditions

Collecting the coefficients of δu_r for $r_0 \leq r \leq r_m$ forms the differential equation governing the displacements of the system

$$4\pi(\lambda + 2G)\left(r^2\frac{d^2u_r}{dr^2} + 2r\frac{du_r}{dr} - 2u_r\right) = 0. \tag{3.32}$$

Collecting the δu_r terms at $r = r_0$ gives

$$\left[4\pi\Big((\lambda + 2G)r^2\frac{du_r}{dr} + 2\lambda r u_r + p_i {r_0}^2\Big)\right]\delta u_r = 0, \tag{3.33}$$

and collecting the δu_r terms at $r = r_m$ gives

$$\left[4\pi\Big((\lambda + 2G)r^2\frac{du_r}{dr} + 2\lambda r u_r + p_o {r_m}^2\Big)\right]\delta u_r = 0. \tag{3.34}$$

The general solution to equation 3.32 is

$$u_r = Ar + \frac{B}{r^2}. \tag{3.35}$$

As for the cylindrical cavity we can implement the natural boundary conditions and derive a closed-form solution which is identical to that derived by Jaeger et al. [19]

$$4Gu_r = -\frac{(1-2\nu)({r_0}^3 p_i - {r_m}^3 p_o)r}{(1+\nu)({r_0}^3 - {r_m}^3)} - \frac{{r_0}^3 {r_m}^3 (p_i - p_o)}{({r_0}^3 - {r_m}^3)r^2}. \tag{3.36}$$

As $r_m \to \infty$ the following solution can be written

$$4Gu_r = -\frac{(1-2\nu)p_o r}{(1+\nu)} + \frac{{r_0}^3(p_i - p_o)}{r^2}, \tag{3.37}$$

for a cavity located in an infinite elastic medium.

Here we can set $p_o = 0$ and arrive at the following cavity expansion equation

$$4Gu_r = -\frac{(1-2\nu)({r_0}^3 p_i)r}{(1+\nu)({r_0}^3 - {r_m}^3)} - \frac{{r_0}^3 {r_m}^3 p_i}{({r_0}^3 - {r_m}^3)r^2}. \tag{3.38}$$

As $r_m \to \infty$ the following solution can be written

$$4Gu_r = p_i\left(\frac{{r_0}^3}{r^2}\right). \tag{3.39}$$

Expressions for the stresses can be formed by substituting the strain-displacement relations (equations 3.26-3.28) into the stress-strain relations (equations 3.23-3.25)

$$\sigma_{rr} = \lambda \left(\frac{du_r}{dr} + 2\frac{u_r}{r} \right) + 2G\frac{du_r}{dr}, \tag{3.40}$$

$$\sigma_{\theta\theta} = \lambda \left(\frac{du_r}{dr} + 2\frac{u_r}{r} \right) + 2G\frac{u_r}{r}, \tag{3.41}$$

$$\sigma_{\Phi\Phi} = \lambda \left(\frac{du_r}{dr} + 2\frac{u_r}{r} \right) + 2G\frac{u_r}{r}. \tag{3.42}$$

These expressions can then be validated by substituting the displacement and comparing with the existing closed-form solutions derived by Kirsch [20]. For a cavity under internal pressure in an infinite medium we find that the equations are identical

$$\sigma_{rr} = -p_i \left(\frac{r_0}{r} \right)^3, \tag{3.43}$$

$$\sigma_{\theta\theta} = \frac{p_i}{2} \left(\frac{r_0}{r} \right)^3, \tag{3.44}$$

$$\sigma_{\Phi\Phi} = \frac{p_i}{2} \left(\frac{r_0}{r} \right)^3. \tag{3.45}$$

3.3 Cylindrical cavity located in an anisotropic stress field

We now derive a solution for a cylindrical cavity subjected to an anisotropic stress field as shown in Figure 3.3. Here we apply the change in stress due to excavation at the cavity wall, thus modelling a cavity expansion problem. Derivation of such a solution highlights the flexibility of the proposed energy-based method.

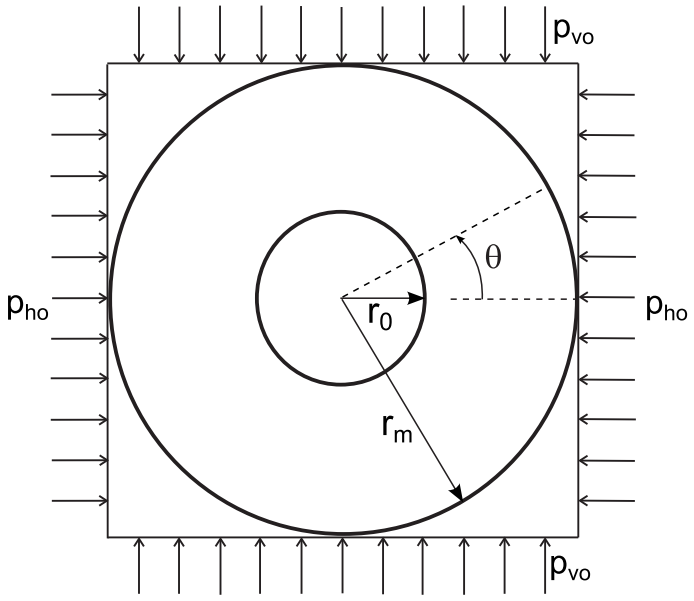

Figure 3.3: A cavity subjected to an anisotropic stress field

Here we assume the radial and tangential displacements to be of the following form

$$u_r = \phi_1 + \phi_2 \cos(2\theta), \tag{3.46}$$

$$u_\theta = \phi_3 \sin(2\theta), \tag{3.47}$$

where ϕ_1, ϕ_2 and ϕ_3 are functions which govern the attenuation of rock displacements away from the cavity wall in the r direction. ϕ_1 corresponds to the isotropic component of stress, whilst ϕ_2 and ϕ_3 correspond to the anisotropic component of stress. Forrest and Hunt [11] used a displacement field of the same form for the anisotropic components when developing a tunnel model for train-induced ground vibration. $\cos(n\theta)$ and $\sin(n\theta)$ were used for the radial and circumferential displacements respectively. $n = 2$ was found to represent the case of a squashed tunnel section, which is the problem that we are modelling here.

The potential energy of the system can be written as follows by integrating over the problem domain

$$U = \frac{1}{2} \int_{r_0}^{\infty} \int_{0}^{2\pi} (\sigma_{rr}\varepsilon_{rr} + \sigma_{\theta\theta}\varepsilon_{\theta\theta} + \tau_{r\theta} 2\varepsilon_{r\theta}) r d\theta dr. \tag{3.48}$$

The stress-strain relations in cylindrical coordinates are given by

$$\sigma_{rr} = \lambda(\varepsilon_{rr} + \varepsilon_{\theta\theta}) + 2G\varepsilon_{rr}, \tag{3.49}$$

$$\sigma_{\theta\theta} = \lambda(\varepsilon_{rr} + \varepsilon_{\theta\theta}) + 2G\varepsilon_{\theta\theta}, \tag{3.50}$$

$$\tau_{r\theta} = 2G\varepsilon_{r\theta}, \tag{3.51}$$

where $\tau_{r\theta}$ is the shear stress and $\varepsilon_{r\theta}$ the shear strain. The strains are obtained from the first derivative of the displacements as follows

$$\varepsilon_{rr} = \frac{\partial u_r}{\partial r}, \tag{3.52}$$

$$\varepsilon_{\theta\theta} = \frac{1}{r}(u_r + \frac{\partial u_\theta}{\partial \theta}), \tag{3.53}$$

$$\varepsilon_{r\theta} = \frac{1}{2}(\frac{1}{r}\frac{\partial u_r}{\partial \theta} + \frac{\partial u_\theta}{\partial r} - \frac{u_\theta}{r}). \tag{3.54}$$

Using the stress-strain relations, the strain displacement relations and the assumed displacement field, equation 3.48 can be evaluated as follows

$$\begin{aligned} U =& \frac{1}{2} \int_{r_0}^{\infty} (\lambda + 2G)\Big(2\pi r\Big(\frac{d\phi_1}{dr}\Big)^2 + \pi r\Big(\frac{d\phi_2}{dr}\Big)^2 + 2\pi\frac{{\phi_1}^2}{r} + \pi\frac{{\phi_2}^2}{r} + 4\pi\frac{{\phi_3}^2}{r} + 4\pi\frac{\phi_2\phi_3}{r}\Big) \\ &+ 2\lambda\Big(2\pi\phi_1\frac{d\phi_1}{dr} + \pi\phi_2\frac{d\phi_2}{dr} + 2\pi\phi_3\frac{d\phi_2}{dr}\Big) \\ &+ G\Big(4\pi\frac{{\phi_2}^2}{r} + \pi r\Big(\frac{d\phi_3}{dr}\Big)^2 + \pi\frac{{\phi_3}^2}{r} - 4\pi\Big(\phi_2\frac{d\phi_3}{dr}\Big) + 4\pi\frac{\phi_2\phi_3}{r} - 2\pi\frac{d\phi_3}{dr}\phi_3\Big) dr. \end{aligned} \tag{3.55}$$

The variation in external work is given by

$$\delta W = \int_0^{2\pi} \sigma_{rr} r_0 \delta u_r d\theta - \int_0^{2\pi} \tau_{r\theta} r_0 \delta u_\theta d\theta. \tag{3.56}$$

The *in situ* stresses, when expressed in cylindrical coordinates give the following stresses acting on a circular boundary [21]

$$\sigma_{rr} = \frac{1}{2}(p_{vo} + p_{ho}) - \frac{1}{2}(p_{vo} - p_{ho})\cos(2\theta), \tag{3.57}$$

$$\sigma_{\theta\theta} = \frac{1}{2}(p_{vo} + p_{ho}) + \frac{1}{2}(p_{vo} - p_{ho})\cos(2\theta), \tag{3.58}$$

$$\tau_{r\theta} = \frac{1}{2}(p_{vo} - p_{ho})\sin(2\theta). \tag{3.59}$$

Thus these equations give the stresses which act at the periphery of the cavity before it is bored and are independent of the cavity radius. When the cavity is bored the radial stress given by equation 3.57 and shear stress given by equation 3.59 is relieved at the cavity periphery. This incremental change in stress fades out with the distance from the cavity wall. It is this incremental change in stress which causes the displacements and which we apply at the cavity wall to expand the cavity.

Thus δW can be expressed as

$$\begin{aligned}
\delta W = &\int_0^{2\pi} \left(\frac{1}{2}(p_{vo} + p_{ho}) - \frac{1}{2}(p_{vo} - p_{ho})\cos(2\theta)\right) r_0(\delta\phi_1 + \delta\phi_2\cos(2\theta))d\theta \\
&+ \int_0^{2\pi} \left(\frac{1}{2}(p_{vo} - p_{ho})\sin(2\theta)\right) r_0(\delta\phi_3\sin(2\theta))d\theta \\
= &\left(\pi(p_{vo} + p_{ho})\delta\phi_1 - \frac{\pi}{2}(p_{vo} - p_{ho})\delta\phi_2\right) r_0 - \left(\frac{\pi}{2}(p_{vo} - p_{ho})\delta\phi_3\right) r_0.
\end{aligned} \tag{3.60}$$

Using the principle of virtual work produces an equation of the following form

$$\delta\Pi = [A(\phi_1)\delta\phi_1] + [B(\phi_2)\delta\phi_2] + [C(\phi_3)\delta\phi_3] = 0, \tag{3.61}$$

as shown below

$$\begin{aligned}
\delta\Pi = (\lambda+2G)\Bigg(&2\pi\Big(\Big[r\frac{d\phi_1}{dr}\Big]_{r_0}^{r_m}\delta\phi_1 - \int_{r_0}^{\infty}\Big(\frac{d\phi_1}{dr} + r\frac{d^2\phi_1}{dr^2}\Big)\delta\phi_1 dr\Big) + \pi\Big(\Big[r\frac{d\phi_2}{dr}\Big]_{r_0}^{r_m}\delta\phi_2 \\
&- \int_{r_0}^{\infty}\Big(\frac{d\phi_2}{dr} + r\frac{d^2\phi_2}{dr^2}\Big)\delta\phi_2 dr\Big) + 2\pi\int_{r_0}^{\infty}\frac{\phi_1}{r}\delta\phi_1 dr + \pi\int_{r_0}^{\infty}\frac{\phi_2}{r}\delta\phi_2 dr + 4\pi\int_{r_0}^{\infty}\frac{\phi_3}{r}\delta\phi_3 dr \\
&+ 2\pi\int_{r_0}^{\infty}\frac{\phi_2}{r}\delta\phi_3 dr + 2\pi\int_{r_0}^{\infty}\frac{\phi_3}{r}\delta\phi_2 dr\Bigg) \\
+\lambda\Bigg(&2\pi\Big([\phi_1]_{r_0}^{r_m}\delta\phi_1 + \int_{r_0}^{\infty}\Big(-\frac{d\phi_1}{dr} + \frac{d\phi_1}{dr}\Big)\delta\phi_1 dr\Big) + \pi\Big([\phi_2]_{r_0}^{r_m}\delta\phi_2 \\
&+ \int_{r_0}^{\infty}\Big(-\frac{d\phi_2}{dr} + \frac{d\phi_2}{dr}\Big)\delta\phi_2 dr\Big) + 2\pi\Big([\phi_3]_{r_0}^{r_m}\delta\phi_2 + \int_{r_0}^{\infty}\Big(-\frac{d\phi_3}{dr}\delta\phi_2 + \frac{d\phi_2}{dr}\delta\phi_3\Big)dr\Big)\Bigg) \\
+G\Bigg(&4\pi\int_{r_0}^{\infty}\frac{\phi_2}{r}\delta\phi_2 + \pi\Big(\Big[r\frac{d\phi_3}{dr}\Big]_{r_0}^{r_m}\delta\phi_3 - \int_{r_0}^{\infty}\Big(\frac{d\phi_3}{dr} + r\frac{d^2\phi_3}{dr^2}\Big)\delta\phi_3 dr + \int_{r_0}^{\infty}\frac{\phi_3}{r}\delta\phi_3 dr\Big) \\
&- 2\pi\Big([\phi_2]_{r_0}^{r_m}\delta\phi_3 + \int_{r_0}^{\infty}\Big(-\frac{d\phi_2}{dr}\delta\phi_3 + \frac{d\phi_3}{dr}\delta\phi_2\Big)dr\Big) + 2\pi\int_{r_0}^{\infty}\frac{\phi_2}{r}\delta\phi_3 dr + 2\pi\int_{r_0}^{\infty}\frac{\phi_3}{r}\delta\phi_2 dr \\
&- \pi\Big([\phi_3]_{r_0}^{r_m}\delta\phi_3 + \int_{r_0}^{\infty}\Big(-\frac{d\phi_3}{dr} + \frac{d\phi_3}{dr}\Big)\delta\phi_3 dr\Big)\Bigg) \\
&- \Big(\pi(p_{vo}+p_{ho})\delta\phi_1 - \frac{\pi}{2}(p_{vo}-p_{ho})\delta\phi_2\Big)r_0 - \Big(\frac{\pi}{2}(p_{vo}-p_{ho})\delta\phi_3\Big)r_0 = 0.
\end{aligned} \tag{3.62}$$

Since the variations $\delta\phi_1$, $\delta\phi_2$ and $\delta\phi_3$ are independent the terms associated with each variation must be equal to zero (e.g. $A(\phi_1)\delta\phi_1 = 0$) in order to satisfy equation 3.62. We now use the same procedure of forming the differential equations and boundary conditions as described for the cylindrical cavity in Section 3.2.1. However, here we have three independent functions, thus we derive three governing equations and three sets of boundary conditions as shown in the following section.

Governing differential equations and boundary conditions

Collecting the coefficients of $\delta\phi_1$ for $r_0 \leq r \leq r_m$ forms the governing differential equation for the displacement of a cavity subjected to a uniform pressure (equation 3.10)

$$2\pi(\lambda+2G)\left(\frac{d\phi_1}{dr}+r\frac{d^2\phi_1}{dr^2}-\frac{\phi_1}{r}\right)=0. \tag{3.63}$$

Collecting the $\delta\phi_1$ terms at $r=r_0$ gives

$$\left[2\pi\left((\lambda+2G)r\frac{d\phi_1}{dr}+\lambda\phi_1+\frac{1}{2}(p_{vo}+p_{ho})r_0\right)\right]\delta\phi_1=0, \tag{3.64}$$

and collecting the $\delta\phi_1$ terms at $r=r_m$ gives

$$\left[2\pi\left((\lambda+2G)r\frac{d\phi_1}{dr}+\lambda\phi_1\right)\right]\delta\phi_1=0. \tag{3.65}$$

Collecting the coefficients of $\delta\phi_2$ for $r_0\leq r\leq r_m$ forms the following governing differential equation

$$\pi\left((\lambda+2G)\left(-\frac{d\phi_2}{dr}-r\frac{d^2\phi_2}{dr^2}\right)+(\lambda+6G)\frac{\phi_2}{r}+2(\lambda+3G)\frac{\phi_3}{r}-2(\lambda+G)\frac{d\phi_3}{dr}\right)=0. \tag{3.66}$$

Collecting the $\delta\phi_2$ terms at $r=r_0$ gives

$$\left[\pi\left((\lambda+2G)r\frac{d\phi_2}{dr}+\lambda(\phi_2+2\phi_3)-\frac{1}{2}(p_{vo}-p_{ho})r_0\right)\right]\delta\phi_2=0, \tag{3.67}$$

and collecting the $\delta\phi_2$ terms at $r=r_m$ gives

$$\left[\pi\left((\lambda+2G)r\frac{d\phi_2}{dr}+\lambda(\phi_2+2\phi_3)\right)\right]\delta\phi_2=0. \tag{3.68}$$

Collecting the coefficients of $\delta\phi_3$ for $r_0\leq r\leq r_m$ forms the following governing differential equation

$$\pi\left(G\left(-\frac{d\phi_3}{dr}-r\frac{d^2\phi_3}{dr^2}\right)+2(\lambda+3G)\frac{\phi_2}{r}+(4\lambda+9G)\frac{\phi_3}{r}+2(\lambda+G)\frac{d\phi_2}{dr}\right)=0. \tag{3.69}$$

Collecting the $\delta\phi_3$ terms at $r=r_0$ gives

$$\left[\pi\left(G\left(r\frac{d\phi_3}{dr}-2\phi_2-\phi_3\right)+\frac{1}{2}(p_{vo}-p_{ho})r_0\right)\right]\delta\phi_3=0, \tag{3.70}$$

and collecting the $\delta\phi_3$ terms at $r = r_m$ gives

$$\left[\pi\left(G\left(r\frac{d\phi_3}{dr} - 2\phi_2 - \phi_3\right)\right)\right]\delta\phi_3 = 0. \tag{3.71}$$

Here we adopt the natural boundary conditions at $r = r_0$ and for simplification we set $\phi_1 = 0$, $\phi_2 = 0$ and $\phi_3 = 0$ at $r = r_m$ (zero displacement).

A closed-form solution can be found for equation 3.63 to obtain ϕ_1, whilst equations 3.66 and 3.69 are simultaneous and require the use of a 1D finite difference (FD) method to solve for ϕ_2 and ϕ_3. Once solved for a selected value of θ, these functions are substituted back into equations 3.46 and 3.47 to obtain the displacement field surrounding the cavity.

The displacements are validated using the closed-form solutions (equations 3.72 and 3.73) derived by Kirsch [20] and shown in Goodman [12] for a cavity embedded in an infinite rock body. Here we use a horizontal pressure p_{ho} of 100 MPa and a vertical pressure p_{vo} of 50 MPa unless otherwise stated. Other parameters are a cavity radius r_0 of 10 m, a shear modulus G of 1000 MPa and a Poisson's ratio ν of 0.2. Figures 3.4 and 3.5 show that there is excellent agreement between the displacements of the proposed solution and that of Goodman [12]. Slight discrepancies are present at large radial distances due to the fact that the numerical results of the proposed method are achieved by truncating all the integrations at $50r_0$ from the cavity centre (i.e. by assuming zero displacements at $r = 50r_0$).

$$u_r = \frac{p_{ho} + p_{vo}}{4G}\frac{{r_0}^2}{r} + \frac{p_{ho} - p_{vo}}{4G}\frac{{r_0}^2}{r}\left[4(1-\nu) - \frac{{r_0}^2}{r^2}\right]\cos(2\theta) \tag{3.72}$$

$$u_\theta = -\frac{p_{ho} - p_{vo}}{4G}\frac{{r_0}^2}{r}\left[2(1-2\nu) + \frac{{r_0}^2}{r^2}\right]\sin(2\theta). \tag{3.73}$$

The stresses are validated through applying the cavity pressure to the external boundary (as shown in Figure 3.3). This will produce the correct stress field for an underground cavity and enable validation with closed-form solutions. The stresses can be expressed as follows by substituting the strain-displacement relations (equations 3.52-3.54) into the stress-strain relations (equations 3.49-3.51)

$$\sigma_{rr} = \lambda\left(\frac{d\phi_1}{dr} + \frac{d\phi_2}{dr}\cos(2\theta) + \frac{1}{r}(\phi_1 + \phi_2\cos(2\theta) + 2\phi_3\cos(2\theta))\right) + 2G\left(\frac{d\phi_1}{dr} + \frac{d\phi_2}{dr}\cos(2\theta)\right), \tag{3.74}$$

$$\begin{aligned}\sigma_{\theta\theta} = {} & \lambda\left(\frac{d\phi_1}{dr} + \frac{d\phi_2}{dr}\cos(2\theta) + \frac{1}{r}(\phi_1 + \phi_2\cos(2\theta) + 2\phi_3\cos(2\theta))\right) \\ & + 2G\left(\frac{1}{r}(\phi_1 + \phi_2\cos(2\theta) + 2\phi_3\cos(2\theta))\right),\end{aligned} \tag{3.75}$$

$$\tau_{r\theta} = G\left(\frac{1}{r}(-2\phi_2\sin(2\theta)) + \frac{d\phi_3}{dr}\sin(2\theta) - \frac{1}{r}(\phi_3\sin(2\theta))\right). \tag{3.76}$$

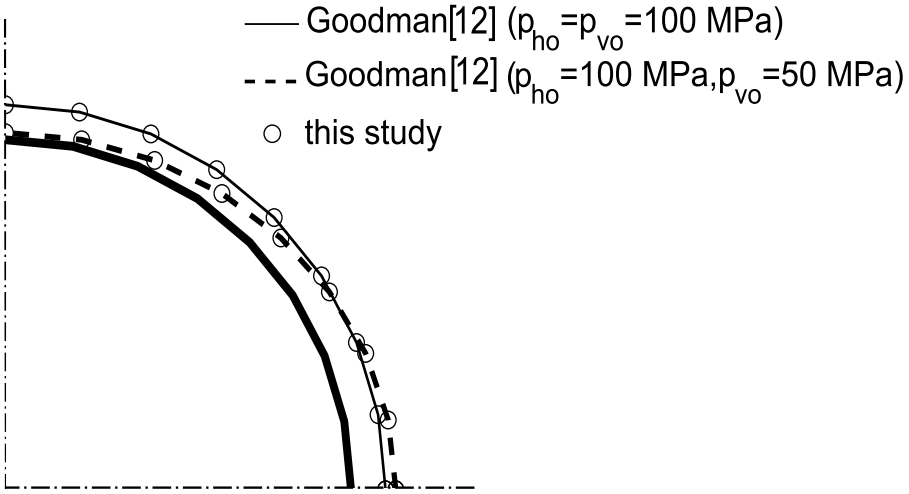

Figure 3.4: Deformed shape of one quarter of the cavity (two lines of symmetry are shown in the figure) under different loading conditions ($G = 500$ MPa used here to emphasise deformation of cavity in the figure)

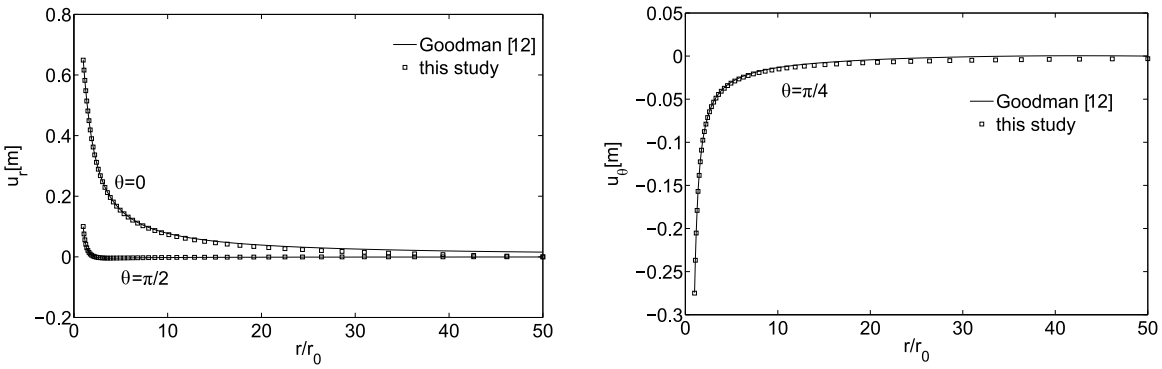

(a) (b)

Figure 3.5: Variation of cavity displacement with radial distance for different angles of θ: (a) radial displacement; (b) circumferential displacement

The closed-form equations for the stresses shown by Goodman [12] are as follows

$$\sigma_{rr} = -\frac{p_{ho}+p_{vo}}{2}\left(1-\frac{{r_0}^2}{r^2}\right)-\frac{p_{ho}-p_{vo}}{2}\left(1-\frac{4{r_0}^2}{r^2}+\frac{3{r_0}^4}{r^4}\right)\cos(2\theta), \tag{3.77}$$

$$\sigma_{\theta\theta} = -\frac{p_{ho}+p_{vo}}{2}\left(1+\frac{{r_0}^2}{r^2}\right)+\frac{p_{ho}-p_{vo}}{2}\left(1+\frac{3{r_0}^4}{r^4}\right)\cos(2\theta), \tag{3.78}$$

$$\tau_{r\theta} = \frac{p_{ho}-p_{vo}}{2}\left(1+\frac{2{r_0}^2}{r^2}-\frac{3{r_0}^4}{r^4}\right)\sin(2\theta). \tag{3.79}$$

Here we use the same parameters as for validating the displacements. The stresses obtained using the proposed method show excellent agreement with the closed-form solutions as demonstrated in Figure 3.6.

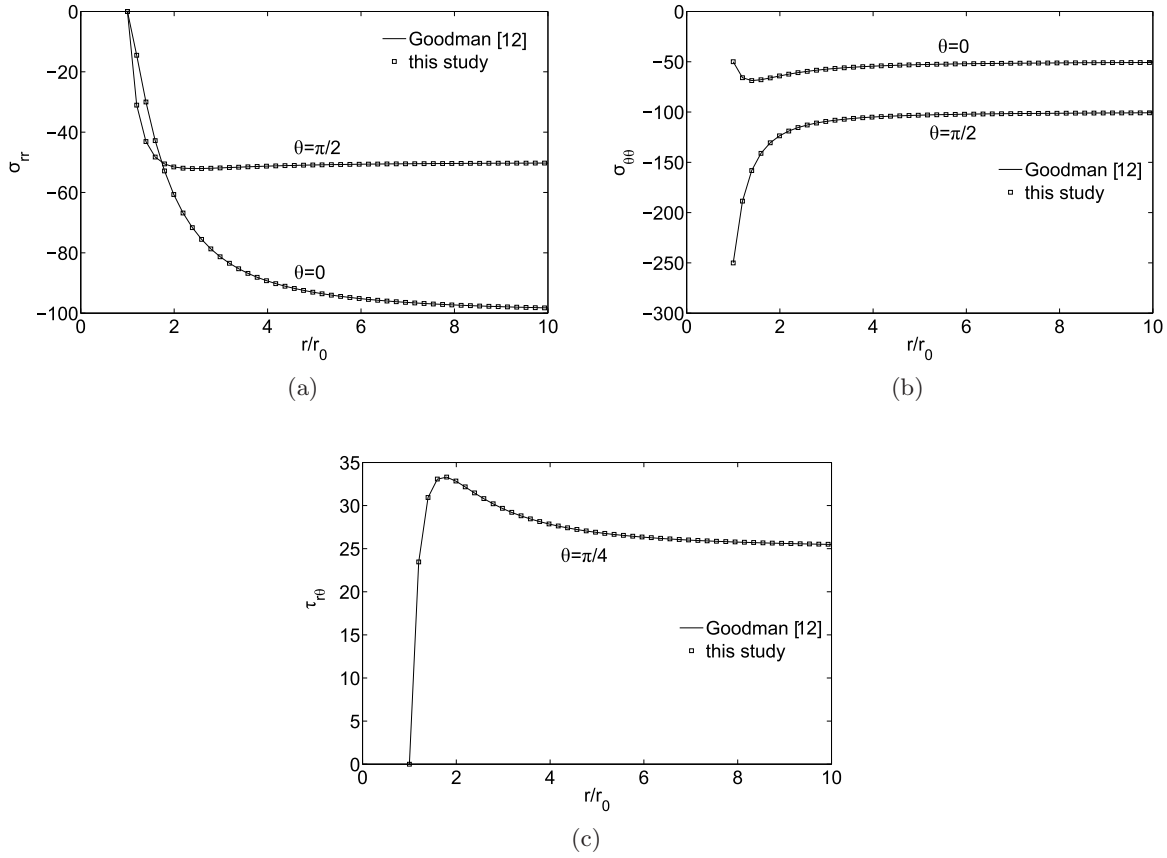

Figure 3.6: Variation of stress with radial distance for different angles of θ: (a) radial stress; (b) circumferential stress; (c) shear stress

3.4 Incorporating viscoelastic constitutive behaviour

Here we demonstrate how viscoelastic constitutive behaviour can be incorporated into the simple cavity expansion solutions derived in the previous section. This is achieved through transforming the viscoelastic cavity problem into the Laplace domain, where it becomes a quasi-elastic problem. A viscoelastic solution can then be found by inverting the Laplace transform. Figure 3.7 provides a summary of this procedure.

Here we use Burger's viscoelastic constitutive model to derive the viscoelastic displacements for the cavity problem shown in Section 3.3; a cylindrical cavity located in an anisotropic stress field. We then provide a validation using Goodman's [12] closed-form solution. For an overview of Burger's model see Section 2.2.1.

Burger's model can be characterized by linear elastic volumetric behaviour and viscoelastic deviatoric behaviour. The deviatoric behavior is schematically illustrated in Figure 3.8, where a Kelvin unit is characterized by its shear modulus G_1 and viscosity η_1, and a Maxwell unit is characterized by its shear modulus G_2 and viscosity η_2. The deviatoric behaviour can be

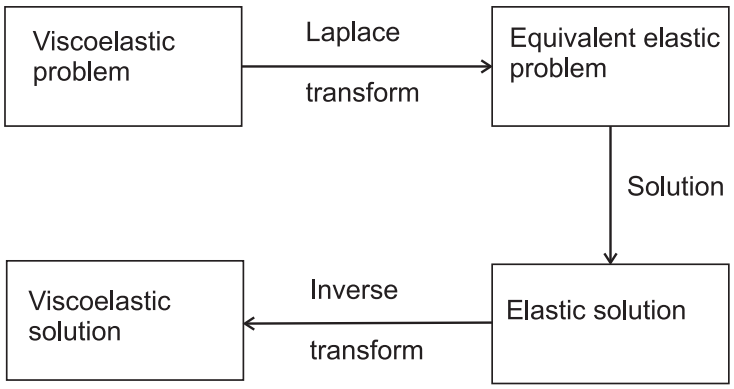

Figure 3.7: Solution procedure for viscoelastic problem based on elastic analogy

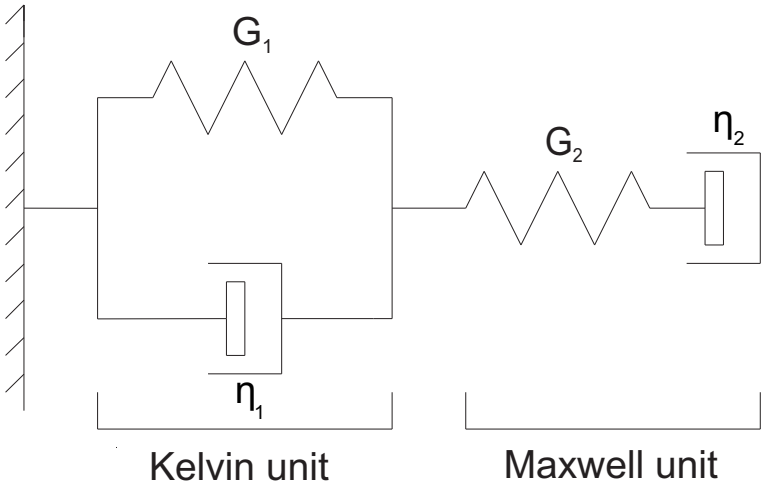

Figure 3.8: A schematic representation of Burger's model

expressed by the following constitutive laws

$$e_{ij} = e_{ij}{}^{(K)} + e_{ij}{}^{(M)}, \tag{3.80}$$

$$s_{ij} = 2\eta_1 \dot{e}_{ij}^{(K)} + 2G_1 e_{ij}{}^{(K)}, \tag{3.81}$$

$$\dot{e}_{ij}^{(M)} = \frac{\dot{s}_{ij}}{2\eta_2} + \frac{s_{ij}}{2G_2}. \tag{3.82}$$

where the superscripts (K) and (M) denote the Kelvin and Maxwell components, $\dot{()}$ denotes the differentiation with respect to time and s_{ij} and e_{ij} are the deviatoric stress and strain components derived from the stress tensor σ_{ij} and the strain tensor ε_{ij}, respectively, given by

$$s_{ij} = \sigma_{ij} - \delta_{ij}\frac{\sigma_{kk}}{3}, \tag{3.83}$$

$$e_{ij} = \varepsilon_{ij} - \delta_{ij}\frac{\varepsilon_{kk}}{3}. \tag{3.84}$$

where δ_{ij} is the Kronecker delta.

The volumetric behaviour is taken to be linear elastic and independent of time. The corresponding constitutive law is given by

$$\sigma_{kk} = 3K\varepsilon_{kk}, \tag{3.85}$$

where K is the bulk modulus which can be expressed as

$$K = \frac{2G_2(1+\upsilon)}{3(1-2\upsilon)}, \tag{3.86}$$

where υ is the Poisson's ratio.

The deviatoric behaviour in the Laplace domain is derived from equation 2.3 which is the 1D differential equation describing Burger's model. By taking the Laplace transform of equation 2.3 we obtain the following

$$\eta_1\hat{\varepsilon}s^2 + k_1\hat{\varepsilon}s = \left(\frac{\eta_1}{k_2}\right)\hat{\sigma}s^2 + \left[1 + \left(\frac{k_1}{k_2}\right) + \left(\frac{\eta_1}{\eta_2}\right)\right]\hat{\sigma}s + \left(\frac{k_1}{\eta_2}\right)\hat{\sigma}, \tag{3.87}$$

where

$$\hat{f}(s) = \int_0^\infty f(t)e^{-st}dt, \tag{3.88}$$

and where t is the time and $\hat{f}(s)$ is the Laplace transform of $f(t)$.

Thus from equation 3.87 we can write the following constitutive relationship between the 1D stress and strain in the Laplace domain

$$\hat{\sigma} = \left(\frac{(\eta_1 s^2 + k_1 s)}{\left(\frac{\eta_1}{k_2}\right)s^2 + \left[1 + \left(\frac{k_1}{k_2}\right) + \left(\frac{\eta_1}{\eta_2}\right)\right]s + \left(\frac{k_1}{\eta_2}\right)}\right)\hat{\varepsilon}. \tag{3.89}$$

As we assume that the deviatoric behaviour is viscoelastic we can use the constitutive relationship in equation 3.89 to write the relationship between the deviatoric stress and deviatoric strain components in the Laplace domain as follows

$$\hat{s}_{ij} = 2\left(\frac{(\eta_1 s^2 + k_1 s)}{\left(\frac{\eta_1}{G_2}\right)s^2 + \left[1 + \left(\frac{G_1}{G_2}\right) + \left(\frac{\eta_1}{\eta_2}\right)\right]s + \left(\frac{G_1}{\eta_2}\right)}\right)\hat{e}_{ij}, \tag{3.90}$$

The solution for the cavity problem is obtained first in the Laplace domain by replacing the Lamé constants G and λ in the governing differential equations and boundary conditions in Section 3.3, with the quantities G^* and λ^*. From the relationship between the deviatoric stress and strain components shown in equation 3.90, G^* is given by

$$G^* = \frac{(\eta_1 s^2 + k_1 s)}{\left(\frac{\eta_1}{G_2}\right)s^2 + \left[1 + \left(\frac{G_1}{G_2}\right) + \left(\frac{\eta_1}{\eta_2}\right)\right]s + \left(\frac{G_1}{\eta_2}\right)}, \tag{3.91}$$

and λ^* is given by

$$\lambda^* = K - \frac{2G^*}{3}, \tag{3.92}$$

The Heaviside function is used to describe the instantaneous application of the cavity pressures at $t = 0$. The horizontal and vertical pressures in the Laplace domain are given by

$$\hat{p}_{ho} = \frac{p_{ho}}{s}, \tag{3.93}$$

$$\hat{p}_{vo} = \frac{p_{vo}}{s} \tag{3.94}$$

3.4.1 Inversion of the Laplace transform

The inversion of the Laplace transform to obtain the cavity displacements is carried out by numerical integration using the efficient scheme devised by de Hoog et al. [16]. This scheme was programmed in MATLAB by Hollenbeck [15] and it is this program that we use here. For further information on how this algorithm is used to solve the viscoelastic cavity problem described here, see Chapter 3 of the MATLAB code located on a CD at the end of this thesis.

For each value of time t, we can obtain a solution for a set of points in the s-coordinates. Like most numerical methods, the de Hoog algorithm employs the Fourier series in the polynomial approximation of the Laplace inverse. This algorithm accelerates the convergence of the series, thus increasing accuracy by reducing errors due to discretisation and rounding. The de Hoog algorithm applies the quotient-difference algorithm of Rutishauser [26] to the series to obtain an approximation in the form of a continued fraction. Compared to the epsilon algorithm derived by Wynn [33], application of the quotient-difference algorithm increases the efficiency for obtaining solutions for many points in time [16]. The de Hoog algorithm accelerates the continued fraction that results from the quotient-difference algorithm, thus minimising the rounding error which is often the major source of error for methods requiring a large number of iterations.

With a suitable numerical inversion algorithm it is not necessary to directly solve the differential equations or to analytically invert the Laplace transform. This is significant as a reliance on the direct analytical inversion can severely limit the adaptability of the proposed method. Thus by incorporating a numerical scheme into this analysis a general tool is produced to determine time-dependent cavity displacements using a wide range of constitutive models.

3.4.2 Validation of viscoelastic response

Goodman [12] derived a closed-form equation for an unlined circular cavity in an infinite viscoelastic Burger's medium subjected to an anisotropic stress field. This equation is for the

radial displacement u_r for a point at coordinates r, θ

$$u_r(t) = \left(A_1 - C_1 + B_1 \frac{d_2}{d_4} \right) \frac{m}{q_1} + \left[\frac{B_1(d_2/G_1 - d_1)}{G_1 d_3 - d_4} - \frac{(A_1 - C_1)}{G_1} \right] e^{-(G_1 t/\eta_1)} + (B_1) \left[\frac{d_2(1 - m/\alpha) + d_1(m - \alpha)}{G_2(G_1 d_3 - d_4)} \right] e^{-(\alpha t/\eta_1)} + \frac{(A_1 - C_1 + B_1/2)}{\eta_2} t, \tag{3.95}$$

where

$$\begin{aligned} A_1 &= \frac{p_{ho} + p_{vo}}{4} \frac{{r_0}^2}{r}, \\ B_1 &= (p_{ho} - p_{vo}) \frac{{r_0}^2}{r} \cos 2\theta, \\ C_1 &= \frac{p_{ho} - p_{vo}}{4} \frac{{r_0}^4}{r^3} \cos 2\theta, \\ m &= G_1 + G_2, \\ q_1 &= G_1 G_2, \\ d_1 &= 3K + 4G_2, \\ d_2 &= 3Km + 4q, \\ d_3 &= 6K + 2G_2, \\ d_4 &= 6Km + 2q, \\ \alpha &= \frac{3Km + q}{3K + G_2}. \end{aligned}$$

Here we use Goodman's [12] solution to validate the response of the proposed method. Analyses were carried out using creep parameters shown in Table 3.1, with a Poisson's ratio of 0.2. We assume that the horizontal stress is twice the vertical stress, 13.794 MPa and 6.897 MPa respectively, and we use a cavity radius of 4.57 m. Figure 3.9 shows that there is excellent agreement between the two solutions for the time-dependent displacement of the cavity wall.

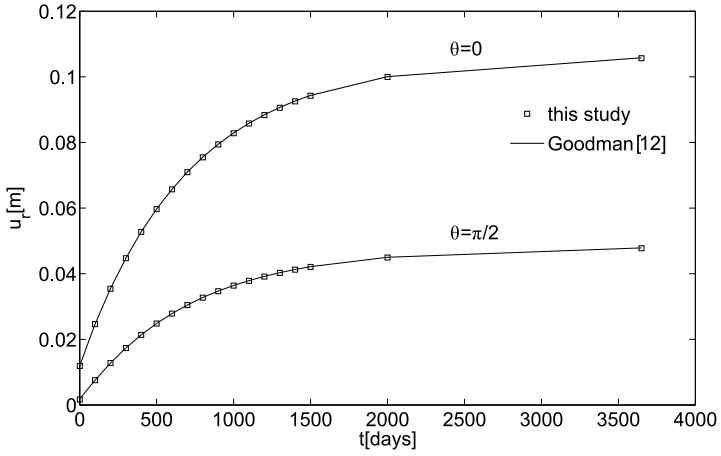

Figure 3.9: Variation of displacement with time for different points on the cavity wall

η_1[MPa Day]	η_2[MPa Day]	G_1[MPa]	G_2[MPa]
239486.1	47897222.2	344.86	3448.6

Table 3.1: Creep parameters used in the analysis (Goodman [12])

3.5 Incorporation of elasto-plastic constitutive behaviour

Thus far we have only considered linear elastic and linear viscoelastic constitutive behaviour when developing models for cavity design. In these material models there exists a linear relationship between stress and strain and all deformations are reversible upon unloading. In order to more accurately represent the constitutive behaviour of geomaterials, such as soil and rock, non-linear constitutive models need to be used.

The theory of plasticity is concerned with solid materials that undergo permanent plastic deformations when stressed. The early applications of plasticity theory were to metals [14], but now an equally important area of application is to soils, rocks and concrete, termed geomaterials. In contrast to metals, these materials commonly show frictional behaviour and undergo volumetric plastic strains. The application of plasticity concepts to soil mechanics is traced back to Coulomb [8] who published a theory of evaluating the earth pressure on retaining structures in 1773.

There are several approaches to the theory of plasticity. Here we use a hyperplastic approach which ensures that we are consistent with the laws of thermodynamics. This approach is outlined in Section 3.5.2.

Stresses and strains are generally referred to in vector notation throughout this section on elasto-plasticity. These vectors take the same form, each with six independent values. The stress vector can be expressed as follows

$$\{\sigma\} = \{\sigma_{xx} \quad \sigma_{yy} \quad \sigma_{zz} \quad \sigma_{xy} \quad \sigma_{yz} \quad \sigma_{zx}\}^T, \tag{3.96}$$

or alternatively in matrix form

$$[\sigma] = \begin{bmatrix} \sigma_{xx} & \sigma_{xy} & \sigma_{xz} \\ \sigma_{yx} & \sigma_{yy} & \sigma_{yz} \\ \sigma_{zx} & \sigma_{zy} & \sigma_{zz} \end{bmatrix} = \sum_{i=1}^{3} \sigma_i \{v_i\}\{v_i\}^T, \tag{3.97}$$

where σ_i are the principal stress components and the eigenvalues of $[\sigma]$ and $\{v_i\}$ are the eigenvectors of $[\sigma]$. In principal stress space all the shear components of stress are equal to zero and only the normal components σ_i may be non-zero. The principal stresses allow any state of stress to be visualized in 3D space and are used to formulate isotropic constitutive relations, as the principal directions of stress and strain are coincident.

3.5.1 A general elasto-plastic constitutive model

A general elasto-plastic constitutive model requires an elastic law, the specification of a scalar yield function f, a plastic flow rule defining the evolution of plastic strain and a hardening law characterising the evolution of the yield function [30].

The yield function defines a boundary or surface in stress space and at this boundary $f = 0$. Stress states cannot lie outside this boundary when considering time-independent plasticity. Note that this is not true for viscoplasticity, but this will be covered in Chapter 5. Thus a state of stress must either lie inside the yield surface ($f < 0$) or on the yield surface ($f = 0$). Being inside the yield surface corresponds to an elastic state of stress, whilst being on the yield surface corresponds to an elasto-plastic state of stress, therefore $f \leq 0$.

A fundamental assumption in the small strain theory of plasticity is the decomposition of the total strain $\{\varepsilon\}$ into the sum of an elastic (or reversible) component $\{\varepsilon^e\}$ and a plastic (or permanent) component $\{\varepsilon^p\}$

$$\{\varepsilon\} = \{\varepsilon^e\} + \{\varepsilon^p\}. \tag{3.98}$$

The elastic constitutive law can be written as follows

$$\{\dot{\sigma}\} = [D^e]\{\dot{\varepsilon^e}\}. \tag{3.99}$$

where $\{\sigma\}$ is the stress and $[D^e]$ is the elastic stiffness matrix defined below

$$[D^e] = \frac{E}{(1+\nu)(1-2\nu)}\left[(1-2\nu)[I] + \nu\{1\}\{1\}^T\right], \qquad \text{where} \qquad \{1\} = \{1 \;\; 1 \;\; 1 \;\; 0 \;\; 0 \;\; 0\}^T, \tag{3.100}$$

E is the Young's modulus, ν is the Poisson's ratio and $[I]$ is the six by six identity matrix.

The plastic strains are calculated using a plastic flow rule which can be expressed as follows

$$\{\dot{\varepsilon^p}\} = \dot{\gamma}\{g_{,\sigma}\}, \tag{3.101}$$

where $\{g_{,\sigma}\}$ is the direction of plastic flow (the derivative of a plastic potential g with respect to stress) and $\dot{\gamma}$ is the plastic consistency parameter which controls the magnitude of the plastic strains. The plastic flow is called associated if the plastic potential function is equal to the yield function ($g = f$), otherwise the plastic flow is non-associated ($g \neq f$). For the associated case, the direction of plastic flow is the outward normal of the yield surface, whereas for non-associated flow it is the gradient of the plastic potential surface.

Similarly to the evolution of plastic strains, the hardening law is given by

$$\{\dot{\beta}\} = \dot{\gamma}\{H\}, \tag{3.102}$$

where $\{H\}$ is the hardening modulus which defines the evolution of the hardening variables.

The Kuhn-Tucker-Karush (KTK) consistency conditions are enforced which establish when plastic flow may occur

$$\dot{\gamma} \geq 0, \qquad f(\{\sigma\}, \{\beta\}) \leq 0, \qquad \dot{\gamma} f(\{\sigma\}, \{\beta\}) = 0 \tag{3.103}$$

where f is a function of stress $\{\sigma\}$, and the hardening variables $\{\beta\}$ which characterise the evolution of the yield surface.

3.5.2 Hyperplasticity

This is an approach to plasticity theory based on thermodynamic principles. The first and second laws of thermodynamics are enforced in this approach, so that any model defined within the framework of hyperplasticity will automatically obey these laws. In this approach the entire constitutive behaviour can be derived from two scalar potentials; a free energy potential which provides the elasticity law, and a dissipation potential which provides the yield function and the direction of plastic flow. No additional assumptions are required. This approach has its roots in the work of Ziegler [35], who applied this technique to modelling a wide range of dissipative materials. The theory of hyperplasticity has since been developed by Houlsby [17], Collins and Houlsby [6], Houlsby and Puzrin [18] and Einav [9].

We now present the mathematical formulation of the theory of hyperplasticity. In this formulation and throughout the remainder of the thesis we assume that no kinematic hardening takes place, therefore no translation of the yield surface. Any isotropic hardening (uniform expansion of the yield surface) is controlled by the dissipation potential, $\dot{D}$.

For isothermal deformation of a material the first and second laws of thermodynamics can be written as

$$\{\sigma\}^T \{\dot{\varepsilon}\} = \dot{\psi} + \dot{D}, \qquad \text{where} \qquad \dot{D} \geq 0. \tag{3.104}$$

where the transpose of the stress vector $\{\sigma\}$ multiplied by the total strain rate vector $\{\dot{\varepsilon}\}$ is the mechanical work input, ψ is the free energy potential or the elastic energy stored in the material and $\dot{D}$ is the dissipation potential describing the rate at which energy is dissipated from the material. When plastic deformation occurs the dissipation potential must be positive, which is the statement of the second law of thermodynamics for isothermal deformations.

The state of a material is assumed to be completely defined by knowledge of the total strains $\{\varepsilon\}$ and a set of internal variables. For elasto-plasticity a single internal variable can be defined as the plastic strain vector $\{\varepsilon^p\}$. The free energy potential is a function of the total strains and the plastic strains, $\psi(\{\varepsilon\}, \{\varepsilon^p\}) = \psi(\{\varepsilon^e\})$ and thus the rate of the free energy potential can be defined as follows

$$\dot{\psi} = \{\psi_{,\varepsilon^e}\}^T \{\dot{\varepsilon^e}\}, \tag{3.105}$$

where $\{\psi_{,\varepsilon^e}\}$ is the partial derivative of the free energy potential with respect to the elastic strain vector.

The dissipation potential is taken to be $\dot{D}(\{\varepsilon\}, \{\varepsilon^p\}, \{\dot{\varepsilon^p}\})$. For rate-independent elasto-plasticity models, the dissipation potential is a homogeneous first-order function of the internal variable rate (the plastic strain rate vector $\{\dot{\varepsilon^p}\}$). Mathematically this can be expressed through Euler's equation as

$$\dot{D} = \{\dot{D}_{,\dot{\varepsilon^p}}\}^T \{\dot{\varepsilon^p}\}. \tag{3.106}$$

Substitution of equations 3.105 and 3.106 into equation 3.104 produces the following

$$\{\sigma\}^T \{\dot{\varepsilon}\} = \{\psi_{,\varepsilon^e}\}^T \{\dot{\varepsilon^e}\} + \{\dot{D}_{,\dot{\varepsilon^p}}\}^T \{\dot{\varepsilon^p}\}. \tag{3.107}$$

It follows from this equation that

$$\{\sigma\} = \{\psi_{,\varepsilon^e}\}, \tag{3.108}$$

which defines the elasticity law derived from the free energy potential and

$$\{\chi\} = \{\dot{D}_{,\dot{\varepsilon^p}}\}, \tag{3.109}$$

which is the dissipative stress vector derived from the dissipation potential.

Thus by substituting equations 3.108 and 3.109 into 3.107 and noting that $\{\dot{\varepsilon^e}\} = \{\dot{\varepsilon}\} - \{\dot{\varepsilon^p}\}$ we find that

$$\{\sigma\}^T \{\dot{\varepsilon}\} = \{\sigma\}^T \{\dot{\varepsilon}\} - \{\sigma\}^T \{\dot{\varepsilon^p}\} + \{\chi\}^T \{\dot{\varepsilon^p}\}. \tag{3.110}$$

Thus from equation 3.110 we can write

$$(\{\sigma\} - \{\chi\})^T \{\dot{\varepsilon^p}\} = 0. \tag{3.111}$$

The theory of hyperplasticity adopts Ziegler's orthogonality condition [35] and according to this condition we can write $(\{\sigma\} - \{\chi\}) = 0$ from equation 3.111. This implies that $(\{\sigma\} - \{\chi\})$ is always orthogonal to $\{\dot{\varepsilon^p}\}$ and allows us to derive a range of constitutive models. According to Houlsby and Puzrin [18] there is debate over whether Ziegler's hypothesis is proven or not, but this will not be regarded as important here. Thus following Ziegler's condition we can state that the true stress is equal to the dissipative stress when there is no kinematic hardening of the yield surface

$$\{\sigma\} = \{\chi\}. \tag{3.112}$$

When developing an elasto-plastic constitutive model using the theory of hyperplasticity, the elasticity law can be derived from the free energy potential using equation 3.108 and the yield function and direction of plastic flow can be derived from the dissipation potential using equations 3.109 and 3.112. All that is required to begin with is a free energy potential and a dissipation potential.

3.5.3 Hyperplastic derivation of simple elasto-plastic models

We now use the hyperplastic approach to derive the constitutive behaviour for elasto-plastic von Mises and Drucker-Prager models. These classical models are widely used during elasto-plastic analyses and can be found in a large number of text books (e.g. [1], [23], [29] and [30]). Although the hyperplastic derivation of these models is found in the literature (e.g. [6]) we have chosen to show the derivation here as these particular models are developed further in Chapters 5 and 6 to incorporate viscoplastic-damage behaviour, thus describing the full range of creep behaviour shown in Figure 2.1.

The von Mises model is pressure insensitive and thus is used to model materials that do not yield under hydrostatic pressure (when the principal stresses are equal, $\sigma_1 = \sigma_2 = \sigma_3$) as shown in Figure 3.10. This model assumes that there is no volumetric component of plastic strain and also behaviour in tension and compression is identical. Common applications are the modelling of undrained soils, metals and crystalline rocks. It has been found experimentally that hydrostatic pressure does not cause yield in metals and crystalline rocks [19] suggesting that only stress deviation should enter into a criterion for yield. Crystalline rocks are of particular interest in this research, as these include salt rock and potash which exhibit ductile behaviour when highly stressed.

In contrast the Drucker-Prager model is pressure sensitive, meaning that hydrostatic pressure can cause yield as shown in Figure 3.12, and volumetric plastic strains do occur. Different behaviour is observed in tension and compression. This model is widely applied to geomaterials, which exhibit a property called friction.

A free energy potential can be written for an elastic material as follows

$$\psi = \frac{1}{2}\{\varepsilon^e\}^T[D^e]\{\varepsilon^e\}. \tag{3.113}$$

Differentiating the free energy potential with respect to the elastic strain vector produces the elasticity law (equation 3.108)

$$\{\sigma\} = \{\psi_{,\varepsilon^e}\} = [D^e]\{\varepsilon^e\}. \tag{3.114}$$

We now derive the yield criteria and expressions for the plastic strain vectors for each of the constitutive models. Here we make use of the following invariants, the mean stress p and the equivalent deviatoric or von Mises stress q, which are expressed as

$$p = \frac{I_1}{3}, \tag{3.115}$$

$$q = \sqrt{3J_2}, \tag{3.116}$$

where

$$I_1 = \mathrm{tr}([\sigma]), \tag{3.117}$$

$$J_2 = \frac{1}{2}\mathrm{tr}([s][s]), \tag{3.118}$$

where the deviatoric stress is $[s] = [\sigma] - I_1[1]/3$ and $[1]$ is the three by three identity matrix.

von Mises elasto-plasticity

The von Mises yield criterion plots as a cylinder in principal stress space (Figure 3.10) and as a circle in deviatoric stress space (Figure 3.11). This yield function can be used to approximate that of Tresca and different approximations can be made. Figure 3.11 shows the von Mises yield criterion circumscribing and inscribing the Tresca yield surface. The circumscribed yield surface matches Tresca in a state of triaxial compression, whilst the inscribed yield surface matches Tresca in pure shear. The cavity problems modelled in this thesis are neither triaxial compression or pure shear. Therefore here and for the Drucker-Prager constitutive model derived later in this section, we decide to use the circumscribed yield surface. This is justified as the cavity problems into which we implement these elasto-plastic constitutive models and the viscoplastic-damage constitutive models shown in Chapters 5 and 6 do not feature shear stresses.

The dissipation potential $\dot{D}$ can be defined as follows after [6]

$$\dot{D} = \sigma_y \dot{\alpha}_s \tag{3.119}$$

where σ_y is the uniaxial yield strength and $\dot{\alpha}_s$ is an internal variable representing the equivalent plastic strain rate

$$\dot{\alpha}_s = \sqrt{\frac{2}{3}\mathrm{tr}([\dot{e}^p][\dot{e}^p])}, \tag{3.120}$$

where $[\dot{e}^p]$ is the deviatoric plastic strain rate. The deviatoric plastic strain rate can be defined as $[\dot{e}^p] = [\dot{\varepsilon}^p] - \dot{\alpha}_v[1]/3$, where the volumetric plastic strain rate is $\dot{\alpha}_v = \mathrm{tr}([\dot{\varepsilon}^p])$. As we are deriving a von Mises model $\alpha_v = 0$.

Differentiation of the dissipation potential with respect to the equivalent plastic strain rate

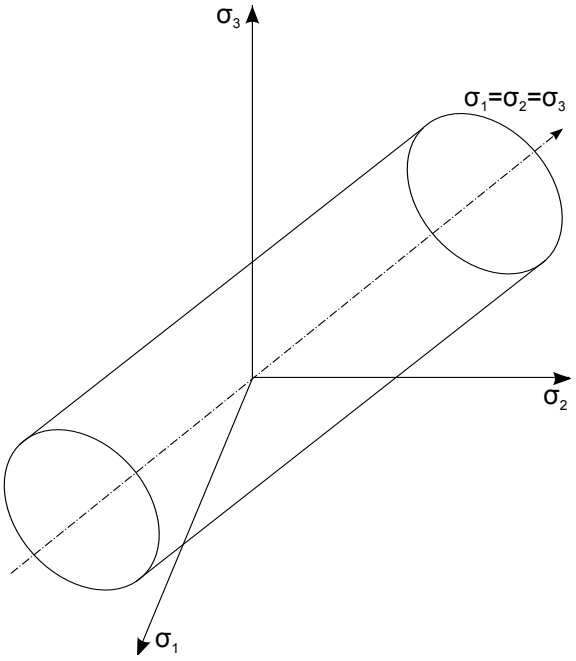

Figure 3.10: The von Mises yield criterion in principal stress space

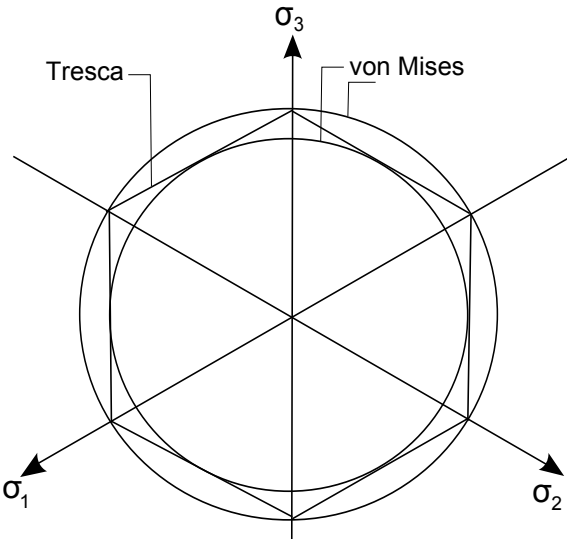

Figure 3.11: Comparison of Tresca and von Mises failure criteria in the deviatoric plane

gives the dissipative stress (equation 3.109)

$$\chi_q = \frac{\partial \dot{D}}{\partial \dot{\alpha}_s} = \sigma_y, \tag{3.121}$$

Since we assume that there is no kinematic hardening, the true stress and the dissipative stress are identical (equation 3.112)

$$\chi_q = q. \tag{3.122}$$

Thus substituting equation 3.122 into 3.121 produces the equation for the yield criterion f

$$f = q - \sigma_y. \tag{3.123}$$

The general expression for the yield surface in the deviatoric plane can be written as follows [30]

$$f = \sqrt{3J_2} - \sigma_y, \tag{3.124}$$

which is the same as equation 3.123, when considering equation 3.116.

The plastic strain components can be expressed from equation 3.101 using an associated flow rule ($g = f$)

$$\{\dot{\varepsilon}^p\} = \dot{\gamma}\{f_{,\sigma}\}, \tag{3.125}$$

where $\dot{\gamma}$ is equal to the equivalent plastic strain $\dot{\alpha}_s$ for the von Mises model and the direction of plastic flow $\{f_{,\sigma}\}$ is expressed as follows using equation 3.123

$$\{f_{,\sigma}\} = \frac{3}{2}\frac{\{s\}}{q}. \tag{3.126}$$

Drucker-Prager elasto-plasticity

The Drucker-Prager yield criterion plots as a cone in principal stress space (Figure 3.12) and as a circle in the deviatoric plane (Figure 3.13). This yield function can be used to approximate that of Mohr-Coulomb and different approximations can be made. Figure 3.13 shows the Drucker-Prager yield criterion circumscribing and inscribing the Mohr-Coulomb yield surface. The yield surface in $q - p$ space plots as a line with gradient greater than zero (Figure 3.14).

The dissipation potential $\dot{D}$ can be defined as follows after [6]. Note that here we also include cohesion in the model, rather than just friction as shown in [6].

$$\dot{D} = \mu p \dot{\alpha}_s + d\dot{\alpha}_s \tag{3.127}$$

where μ is a constant related to the friction angle, p is the mean stress and d is a constant related to the cohesion.

As a side condition we will impose a linear relationship between the volumetric and shear strain rates, $\dot{\alpha_v}$ and $\dot{\alpha_s}$ respectively. This constraint is a device used to introduce dilation into the model (e.g [17]).

$$\dot{\alpha_v} + \beta\dot{\alpha}_s = 0, \tag{3.128}$$

where β is a constant related to the dilation angle. A modified dissipation potential can now

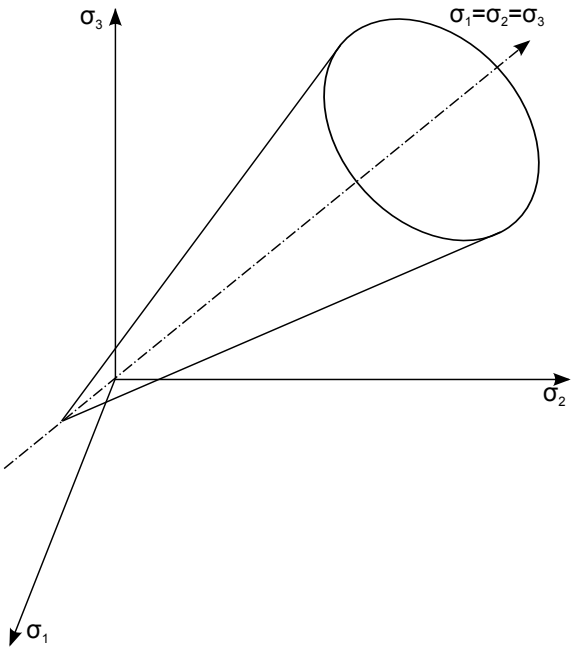

Figure 3.12: The Drucker-Prager yield surface in principal stress space

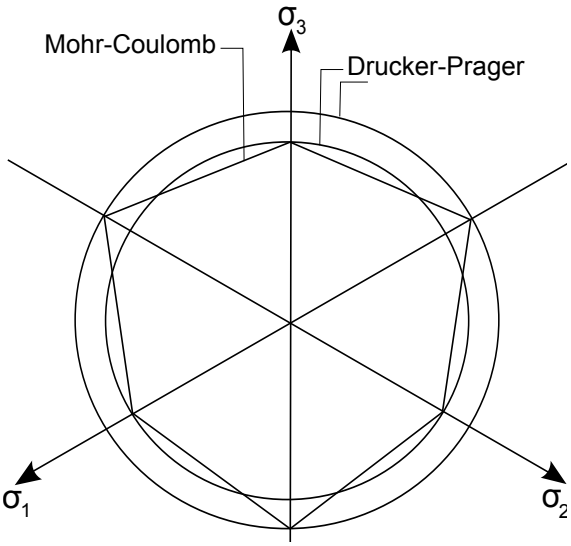

Figure 3.13: Comparison of Mohr-Coulomb and Drucker-Prager failure criteria in the deviatoric plane

be formed

$$\dot{D}^* = (\mu p + d + \Lambda\beta)\dot{\alpha}_s + \Lambda\dot{\alpha}_v \tag{3.129}$$

with Λ as a Lagrange multiplier. Differentiation of the modified dissipation potential with respect to the plastic strain rates gives the dissipative stresses (equation 3.109), due to the volumetric plastic strain rate and due to the deviatoric plastic strain rate respectively

$$\chi_p = \frac{\partial \dot{D}^*}{\partial \dot{\alpha}_v} = \Lambda \tag{3.130}$$

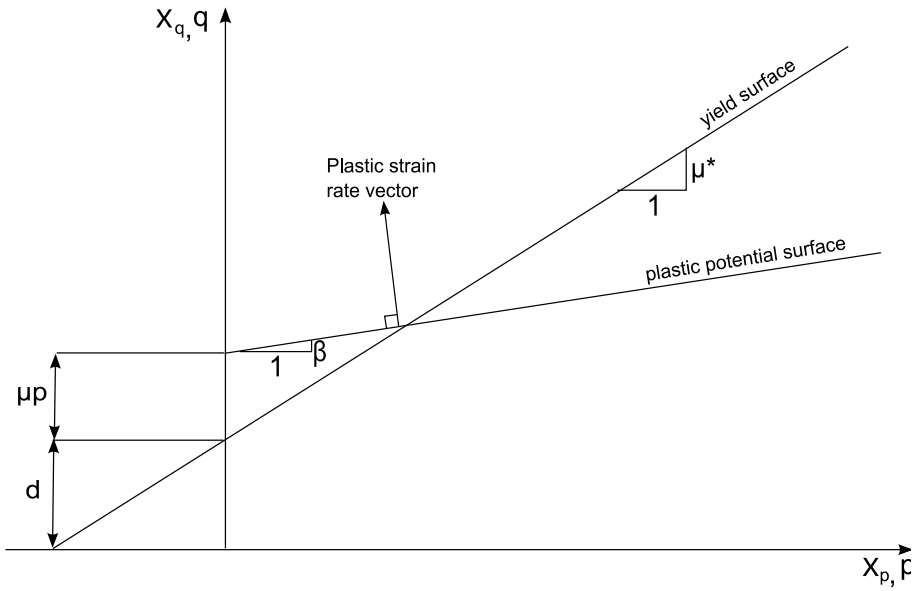

Figure 3.14: Yield surface and plastic potential for the Drucker-Prager model

and

$$\chi_q = \frac{\partial \dot{D}^*}{\partial \dot{\alpha}_s} = \mu p + d + \beta\Lambda. \tag{3.131}$$

Substituting equation 3.130 into equation 3.131 gives an equation for the yield function in dissipative stress space

$$\chi_q = (\mu p + d) + \beta\chi_p. \tag{3.132}$$

The plastic strain-rate vector is orthogonal to this yield surface from equations 3.128 and 3.132, shown in Figure 3.14. Thus equation 3.132 represents the plastic potential function g.

Since we assume that there is no kinematic hardening, the true stresses and the dissipative stresses are identical (equation 3.112)

$$\chi_q = q \qquad \chi_p = p. \tag{3.133}$$

Thus by substituting equation 3.133 into equation 3.132 we can write the following expression for the yield criterion f

$$f = q - \mu^* p - d, \tag{3.134}$$

where $\mu^* = \mu + \beta$. This yield function is shown in Figure 3.14. We now only have associated flow if $\mu = 0$ and $\mu^* = \beta$. The material is incompressible when $\beta = 0$.

The general expression for the yield surface in the deviatoric plane is defined as follows [30]

$$f = \eta I_1 + \sqrt{J_2} - k \tag{3.135}$$

and the plastic potential function [30]

$$g = \bar{\eta} I_1 + \sqrt{J_2}, \tag{3.136}$$

where η and k are constants and are chosen according to the required approximation to the Mohr-Coulomb criterion, and $\bar{\eta}$ depends on the dilatancy angle. Comparing equations 3.134 and 3.135, and 3.132 and 3.136 we can write the following expressions for μ^*, d and β

$$\mu^* = -3\sqrt{3}\eta, \tag{3.137}$$

$$d = \sqrt{3}k, \tag{3.138}$$

$$\beta = -3\sqrt{3}\bar{\eta}. \tag{3.139}$$

The plastic strain components can be expressed from equation 3.101 using a non-associated flow rule. The plastic strain can be divided into deviatoric and volumetric components as follows $\{\dot{\varepsilon}^p\} = \{\dot{e}^p\} + \dot{\alpha}_v\{1\}/3$. By applying the constraint of equation 3.128 and noting that $\dot{\gamma} = \dot{\alpha}_s$, it can be shown that

$$\{g_{,\sigma}\} = \frac{3}{2}\frac{\{s\}}{q} - \frac{\beta}{3}\{1\}. \tag{3.140}$$

If we assume that the Drucker-Prager yield surface circumscribes the Mohr-Coulomb yield surface as shown in Figure 3.13 in deviatoric stress space, then the Drucker-Prager parameters η, k and $\bar{\eta}$ are expressed as follows

$$\eta = \frac{2\sin\phi}{\sqrt{3}(3-\sin\phi)}, \tag{3.141}$$

$$k = \frac{6c\cos\phi}{\sqrt{3}(3-\sin\phi)}, \tag{3.142}$$

$$\bar{\eta} = \frac{2\sin\psi}{\sqrt{3}(3-\sin\psi)} \tag{3.143}$$

where ϕ is the friction angle and ψ the dilation angle. Note that when $\phi = \psi = 0$ the Drucker-Prager model reduces to the von Mises model.

3.5.4 Stress integration

As seen in Section 3.5.1 elasto-plastic constitutive models are developed in rate form, as one can relate the current stress to the current increment in strain. In order for a model to be used practically for boundary value problems or for a single material point, it is necessary to integrate the constitutive equations 3.99, 3.101 and 3.102 subject to the KTK contraints (equation 3.103). Starting from an initial state with a known elastic strain $\{\varepsilon^e_n\}$ and hardening variables $\{\beta_n\}$, when subjected to a strain increment $\{\Delta\varepsilon\}$, what is the updated stress $\{\sigma_{n+1}\}$, the corresponding elastic strain $\{\varepsilon^e_{n+1}\}$ and the hardening variables $\{\beta_{n+1}\}$?

When the trial stress σ_t which corresponds to the trial elastic strain ($\{\varepsilon_t^e\} = \{\varepsilon_n^e\} + \{\Delta\varepsilon\}$) lies inside the yield surface ($f < 0$) there is no need to integrate the constitutive equations as the material remains elastic. However, if the trial stress lies outside the yield surface ($f > 0$), an integration algorithm is required to update the stress (return the stress to the yield surface) and hardening variables. A large amount of research has focused on these algorithms and as a result many different types of algorithms currently exist. A useful overview of these different integration procedures is provided by Coombs [7]. These consist of explicit methods, implicit methods and exact methods, as well as several alternative methods. In this thesis we use a fully implicit backward Euler (bE) stress integration scheme as this can be applied to many different constitutive models and it is now used as the benchmark when assessing other integration methods [4]. In this method the stress integration problem is split into two parts as follows

(1) an elastic predictor where we assume that the material is purely linear elastic after a strain increment $\{\Delta\varepsilon\}$ has been applied as shown below

$$\{\sigma_t\} = [D^e]\{\{\varepsilon_n^e\} + \{\Delta\varepsilon\}\}, \tag{3.144}$$

(2) and a plastic corrector which accounts for the occurrence of plastic strains.

$$\{\sigma_{n+1}\} = [D^e]\{\{\varepsilon_t^e\} - \{\Delta\varepsilon^p\}\}, \tag{3.145}$$

where $\{\Delta\varepsilon^p\}$ are the incremental plastic strains and $\{\varepsilon_{n+1}^e\} = \{\{\varepsilon_t^e\} - \{\Delta\varepsilon^p\}\}$ are the updated elastic strains.

The elastic predictor (part (1)) shown in equation 3.144 is used to calculate the trial stress. This trial stress is then used to calculate a value for f. If $f > 0$ the material shows plastic behaviour and the plastic corrector (part (2)) needs to be used. This is used to obtain the updated stress $\{\sigma_{n+1}\}$ in equation 3.145. In order to do this we must solve for two unknowns (three unknowns if hardening is considered). These unknowns are commonly solved for using an iterative procedure until the residuals associated with the unknowns fall within a specified tolerance. An overview of this stress integration scheme is explained in the following subsection.

It is important to note that some simple elasto-plastic models allow for analytical integration based on the implicit bE method. These include the von Mises, Tresca, Mohr-Coulomb and Drucker-Prager models, amongst others. The main advantages of analytical integration over iterative methods are robustness and speed. In this thesis we use the general iterative implicit bE method, and use the Newton-Raphson method during the plastic corrector stage. This is due to complex constitutive models being developed in Chapters 5 and 6. The development of

analytical integration algorithms for these complex models is beyond the scope of this thesis. We use the Newton-Raphson scheme here due to the quadratic rates of convergence achieved by this method which generally results in very computationally efficient return mapping procedures [30].

Implicit backward Euler stress integration

This section describes the iterative implicit bE method for a general elasto-plastic constitutive model. Note that here we use the stresses $\{\sigma\}$ as unknowns, shown below, as used by de Borst et al. [5]. An alternative approach is to use the elastic strains $\{\varepsilon^e\}$ as unknowns (e.g. [30]). Since there is a linear relationship between the stress and strain, either of these approaches could be used. Substitution of the elastic constitutive law ($\{\sigma\} = [D^e]\{\varepsilon^e\}$) into the expression for the residual $\{b_1\}$ in equation 3.149, produces

$$[D^e]\{\varepsilon^e\} - [D^e]\{\varepsilon_t^e\} + [D^e]\Delta\gamma\{g_{,\sigma}\}, \tag{3.146}$$

and since $[D^e]$ is a constant $\{b_1\}$ could be written as

$$\{\varepsilon^e\} - \{\varepsilon_t^e\} + \Delta\gamma\{g_{,\sigma}\}, \tag{3.147}$$

if the elastic strains are used as the unknowns.

Starting with the following unknowns

$$\{x\} = \{\{\sigma\} \;\; \{\beta\} \;\; \Delta\gamma\}^T, \tag{3.148}$$

where $\Delta\gamma$ is the increment in the plastic consistency parameter. The residuals associated with the unknowns are written as follows

$$\Big\{b\Big\} = \begin{Bmatrix} \{\sigma\} - [D^e]\{\varepsilon_t^e\} + [D^e]\Delta\gamma\{g_{,\sigma}\} \\ \{\beta\} - \{\beta_t\} - \{\Delta\beta\} \\ f \end{Bmatrix} = \begin{Bmatrix} \{b_1\} \\ \{b_2\} \\ b_3 \end{Bmatrix}, \tag{3.149}$$

where $\{\Delta\beta\}$ and $\{\beta_t\}$ are the incremental and trial values respectively, for the hardening variables. The Hessian matrix is defined as follows from the derivatives of the residuals with respect to the unknowns

$$\Big[A\Big] = \begin{bmatrix} [b_{1,\sigma}] & [b_{1,\beta}] & \{b_{1,\Delta\gamma}\} \\ [b_{2,\sigma}] & [b_{2,\beta}] & \{b_{2,\Delta\gamma}\} \\ \{b_{3,\sigma}\}^T & \{b_{3,\beta}\}^T & b_{3,\Delta\gamma} \end{bmatrix}. \tag{3.150}$$

Using equations 3.149 and 3.150, this matrix can then be written as follows

$$\Big[A\Big] = \begin{bmatrix} [I] + \Delta\gamma[g_{,\sigma\sigma}][D^e] & [D^e]\Delta\gamma[g_{,\sigma\beta}] & [D^e]\{g_{,\sigma}\} \\ -[\Delta\beta_{,\sigma}] & [I] - [\Delta\beta_{,\beta}] & -\{\Delta\beta_{,\Delta\gamma}\} \\ \{f_{,\sigma}\}^T & \{f_{,\beta}\}^T & 0 \end{bmatrix} \tag{3.151}$$

The increment in the unknowns is given by

$$\{\delta x\} = -[A]^{-1}\{b\}, \tag{3.152}$$

with the starting conditions for the algorithm

$$\{\sigma\} = \{\sigma_t\}, \quad \{\beta\} = \{\beta_t\} \quad \Delta\gamma = 0, \quad \{b\} = \{\{0\} \;\; \{0\} \;\; f\}^T \tag{3.153}$$

After calculation of the Hessian matrix from equation 3.151, the unknowns are updated using equation 3.152 and the residuals determined from equation 3.149. If these residuals are greater than a specified tolerance, we recalculate the Hessian matrix using equation 3.151 and solve equation 3.152 again to update the unknowns. We continue to iterate until the residuals fall within a specified tolerance.

von Mises model with linear isotropic hardening

We now apply the implicit bE stress integration algorithm to an isotropically hardening von Mises constitutive model (for the von Mises yield function and plastic flow rule see the earlier part of this chapter). This provides a clearer idea of how we integrate the constitutive equations. Here we assume the hardening to be linear for simplification, with $\{\beta\}$ equal to the yield stress σ_y, where σ_y is a function of the equivalent plastic strain γ.

The residuals are written as follows using equation 3.149

$$\Big\{b\Big\} = \begin{Bmatrix} \{\sigma\} - [D^e]\{\varepsilon^e_t\} + [D^e]\Delta\gamma\{f_{,\sigma}\} \\ \sigma_y - \sigma_{yt} - \Delta\gamma H \\ f \end{Bmatrix} = \begin{Bmatrix} \{b_1\} \\ b_2 \\ b_3 \end{Bmatrix}, \tag{3.154}$$

where H is a constant hardening modulus. $H = 0$ corresponds to perfect plasticity.

Using equation 3.150 we can express the Hessian matrix as follows

$$\Big[A\Big] = \begin{bmatrix} [I] + \Delta\gamma[f_{,\sigma\sigma}][D^e] & \{0\} & [D^e]\{f_{,\sigma}\} \\ \{0\}^T & 1 & -H \\ \{f_{,\sigma}\}^T & -1 & 0 \end{bmatrix} \tag{3.155}$$

We can then follow the same iterative solution procedure as described for the general elasto-

plastic model.

von Mises analytical solution

Here we show how an analytical solution based on the implicit bE method can be derived for the von Mises model with linear isotropic hardening. Here we can obtain closed-form solutions for the unknowns. Analytical solutions are not investigated in this research, but can play an extremely important role due to their computational efficiency.

Here we seek to simplify the system of equations (the residuals) shown in equation 3.154. Firstly it should be noted that the von Mises flow vector $\{f_{,\sigma}\}$ is purely deviatoric, therefore we can write the following equation for the unknown deviatoric stress from residual $\{b_1\}$

$$\{s_{n+1}\} = \{s_t\} - \Delta\gamma 2G \left(\sqrt{\frac{3}{2}} \frac{\{s_{n+1}\}}{||\{s_{n+1}\}||} \right), \tag{3.156}$$

meaning that only the deviatoric stress component is updated in the plastic corrector stage, while the hydrostatic stress has the value computed in the elastic predictor stage. Equation 3.156 can be rearranged to form

$$\{s_t\} = \left(1 + \sqrt{\frac{3}{2}} \frac{\Delta\gamma 2G}{||\{s_{n+1}\}||} \right) \{s_{n+1}\}, \tag{3.157}$$

implying that

$$\frac{\{s_{n+1}\}}{||\{s_{n+1}\}||} = \frac{\{s_t\}}{||\{s_t\}||}. \tag{3.158}$$

Substitution of equation 3.158 into equation 3.156 leads to the following equation for the updated deviatoric stress

$$\{s_{n+1}\} = \left(1 - \frac{\Delta\gamma 3G}{q_t} \right) \{s_t\}. \tag{3.159}$$

Finally, substitution of equation 3.159 and the expression for the residual b_2 (from equation 3.154) into the expression for the residual b_3 (from equation 3.154), reduces the system of equations shown in equation 3.154 to a single equation

$$f = q_t - 3G\Delta\gamma - (\sigma_{yt} + \Delta\gamma H) = 0. \tag{3.160}$$

The change of the plastic consistency parameter $\Delta\gamma$ can be expressed as follows

$$\Delta\gamma = \frac{f_t}{3G + H}, \tag{3.161}$$

where the trial yield function $f_t = q_t - \sigma_{yt}$.

3.6 Modelling cavity in an elasto-plastic medium

Here we develop a solution using the proposed energy-based method for a infinitely long cylindrical cavity subjected to a uniform internal pressure p_i (same cavity expansion problem as shown in Figure 3.2, but with $p_o = 0$). The purpose here is to demonstrate how elasto-plastic constitutive behaviour can be incorporated into the energy-based method for cavity analysis.

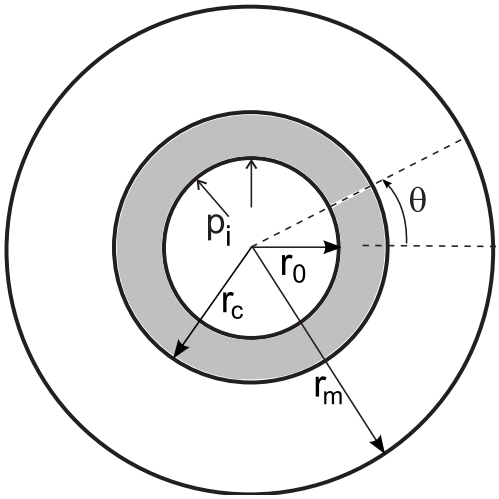

Figure 3.15: Cavity under uniform internal pressure with a plastic radius r_c

The potential energy U of the system can be written similar to the simple elastic cylindrical cavity problem shown in Section 3.2.1 in terms of stress and strain components by integrating over the problem domain. Note that here we take into account energy dissipation using the dissipative stresses χ_{rr}, $\chi_{\theta\theta}$ and χ_{zz} with the corresponding plastic strain components.

$$U = \frac{1}{2}\int_{r_0}^{r_m}\int_{0}^{2\pi}(\sigma_{rr}\varepsilon^e_{rr} + \sigma_{\theta\theta}\varepsilon^e_{\theta\theta} + \sigma_{zz}\varepsilon^e_{zz})rd\theta dr + \int_{r_0}^{r_m}\int_{0}^{2\pi}(\chi_{rr}\varepsilon^p_{rr} + \chi_{\theta\theta}\varepsilon^p_{\theta\theta} + \chi_{zz}\varepsilon^p_{zz})rd\theta dr. \quad (3.162)$$

According to Ziegler's condition (see Section 3.5.2) the dissipative stresses are equal to the true stresses (equation 3.112 obtained from equation 3.110). Therefore from observing equation 3.110 the variation of the potential energy can be expressed in terms of the stress components multiplied by the variation of the total strains. For the cavity problem, this can be expressed as follows

$$\delta U = \int_{r_0}^{r_m}\int_{0}^{2\pi}(\sigma_{rr}\delta\varepsilon_{rr} + \sigma_{\theta\theta}\delta\varepsilon_{\theta\theta} + \sigma_{zz}\delta\varepsilon_{zz})rd\theta dr. \quad (3.163)$$

The stress components are a function of the elastic strain components shown below

$$\sigma_{rr} = \lambda(\varepsilon^e_{rr} + \varepsilon^e_{\theta\theta} + \varepsilon^e_{zz}) + 2G\varepsilon^e_{rr}, \tag{3.164}$$
$$\sigma_{\theta\theta} = \lambda(\varepsilon^e_{rr} + \varepsilon^e_{\theta\theta} + \varepsilon^e_{zz}) + 2G\varepsilon^e_{\theta\theta}, \tag{3.165}$$
$$\sigma_{zz} = \lambda(\varepsilon^e_{rr} + \varepsilon^e_{\theta\theta} + \varepsilon^e_{zz}) + 2G\varepsilon^e_{zz}. \tag{3.166}$$

The total strains can be divided into elastic and plastic components as follows

$$\varepsilon_{rr} = \varepsilon^e_{rr} + \varepsilon^p_{rr}, \tag{3.167}$$
$$\varepsilon_{\theta\theta} = \varepsilon^e_{\theta\theta} + \varepsilon^p_{\theta\theta}, \tag{3.168}$$
$$\varepsilon_{zz} = \varepsilon^e_{zz} + \varepsilon^p_{zz}. \tag{3.169}$$

Thus the elastic strains are expressed as follows using the expressions for the total strains shown in equations 3.5 and 3.6

$$\varepsilon^e_{rr} = \left(\frac{du_r}{dr} - \varepsilon^p_{rr}\right), \tag{3.170}$$
$$\varepsilon^e_{\theta\theta} = \left(\frac{u_r}{r} - \varepsilon^p_{\theta\theta}\right), \tag{3.171}$$
$$\varepsilon^e_{zz} = -\varepsilon^p_{zz}. \tag{3.172}$$

Substituting these elastic strain expressions into equations 3.164-3.166 and using the expressions for the total strains in terms of the displacements we can write an expression for δU using equation 3.163. The principal of virtual work (equation 3.1) can then be used to write an equation for the variation of the total energy Π. The variation in the external work W is given by

$$\delta W = 2\pi p_i r_0 \delta u_r. \tag{3.173}$$

Thus the variation of the total energy can be expressed as follows

$$\begin{aligned}
\delta\Pi = \pi\Bigg(& (\lambda+2G)\Bigg(2\Big(\Big[r\frac{du_r}{dr}\Big]^{r_m}_{r_0}\delta u_r - \int_{r_0}^{r_m}\Big(r\frac{d^2u_r}{dr^2} + \frac{du_r}{dr}\Big)\delta u_r dr\Big) \\
& - 2\Big([\varepsilon^p_{rr} r]^{r_m}_{r_0}\delta u_r - \int_{r_0}^{r_m}\Big(\frac{d\varepsilon^p_{rr}}{dr}r + \varepsilon^p_{rr}\Big)\delta u_r dr\Big) + \int_{r_0}^{r_m}\frac{2u_r}{r}\delta u_r dr - \int_{r_0}^{r_m} 2\varepsilon^p_{\theta\theta}\delta u_r dr\Bigg) \\
& + 2\lambda\Bigg(\Big(\int_{r_0}^{r_m}\frac{du_r}{dr}\delta u_r dr + \Big([u_r]^{r_m}_{r_0}\delta u_r - \int_{r_0}^{r_m}\frac{du_r}{dr}\delta u_r dr\Big)\Big) - \int_{r_0}^{r_m}\varepsilon^p_{rr}\delta u_r dr \\
& - \Big([r\varepsilon^p_{\theta\theta}]^{r_m}_{r_0}\delta u_r - \int_{r_0}^{r_m}\Big(r\frac{d\varepsilon^p_{\theta\theta}}{dr} + \varepsilon^p_{\theta\theta}\Big)\delta u_r dr\Big) \\
& - \Big([r\varepsilon^p_{zz}]^{r_m}_{r_0}\delta u_r - \int_{r_0}^{r_m}\Big(r\frac{d\varepsilon^p_{zz}}{dr} + \varepsilon^p_{zz}\Big)\delta u_r dr\Big) - \int_{r_0}^{r_m}\varepsilon^p_{zz}\delta u_r dr\Bigg)\Bigg) - 2\pi p_i r_0 \delta u_r
\end{aligned} \tag{3.174}$$

We now use the same method described in Section 3.2.1 to form the governing differential equation and boundary conditions, shown in the following section.

3.6.1 Governing differential equation and boundary conditions

Collecting the coefficients of δu_r for $r_0 \leq r \leq r_m$ forms the differential equation governing the displacements of the system. It is important to note that this equation is the same as that derived for the elastic case in Section 3.2.1, but here the righthand side of this equation is a function of the plastic strain components

$$r\frac{d^2u_r}{dr^2} + \frac{du_r}{dr} - \frac{u_r}{r} = F\left(\varepsilon^p_{rr}; \varepsilon^p_{\theta\theta}; \varepsilon^p_{zz}\right) \tag{3.175}$$

$$F\left(\varepsilon^p_{rr}; \varepsilon^p_{\theta\theta}; \varepsilon^p_{zz}\right) = r\frac{d\varepsilon^p_{rr}}{dr} + \frac{\lambda}{(\lambda+2G)}\left(r\frac{d\varepsilon^p_{\theta\theta}}{dr} + r\frac{d\varepsilon^p_{zz}}{dr}\right) + \frac{2G}{(\lambda+2G)}(\varepsilon^p_{rr} - \varepsilon^p_{\theta\theta}) \tag{3.176}$$

Collecting the δu_r terms at $r = r_0$ gives

$$\left[2\pi\left(\lambda\left(\frac{du_r}{dr} - \varepsilon^p_{rr} + \frac{u_r}{r} - \varepsilon^p_{\theta\theta} - \varepsilon^p_{zz}\right) + 2G\left(\frac{du_r}{dr} - \varepsilon^p_{rr}\right) + p_i\right)\right]\delta u_r = 0 \tag{3.177}$$

and collecting the δu_r terms at $r = r_m$ gives

$$\left[2\pi\left(\lambda\left(\frac{du_r}{dr} - \varepsilon^p_{rr} + \frac{u_r}{r} - \varepsilon^p_{\theta\theta} - \varepsilon^p_{zz}\right) + 2G\left(\frac{du_r}{dr} - \varepsilon^p_{rr}\right)\right)\right]\delta u_r = 0 \tag{3.178}$$

It is important to note that when no plastic strain is present these boundary conditions are the same as for the elastic case in Section 3.2.1. Here we use the stresses as the boundary conditions (terms in square brackets are equal to zero).

3.6.2 Solution procedure

We now implement the two constitutive models derived in Section 3.5.3 into the energy-based method for cavity analysis. A summary of the solution procedure is shown in Figure 3.16. Initially the design pressure p_i is applied to the cavity wall and assuming that the plastic strain components are equal to zero we solve the governing equation (equation 3.175) using a 1D FD technique, analogous to Perry and Aboudi [22]. We can then obtain the stress components in the medium from the calculated displacements and calculate a yield criterion f, whose expression depends on the chosen elasto-plastic constitutive model. If the medium surrounding the cavity remains elastic, the solution is found. If plasticity occurs, we use the implicit bE stress integration scheme to calculate the unknowns for each plastic point. Thus, the plastic strain components in equations 3.175, 3.177 and 3.178 can be updated. We repeat this procedure until the relative error between the cavity wall displacements in successive

iterations (iterations denoted by $_i$) is less than a specified tolerance. This iterative procedure was solved using a program written in MATLAB 7.9.0.

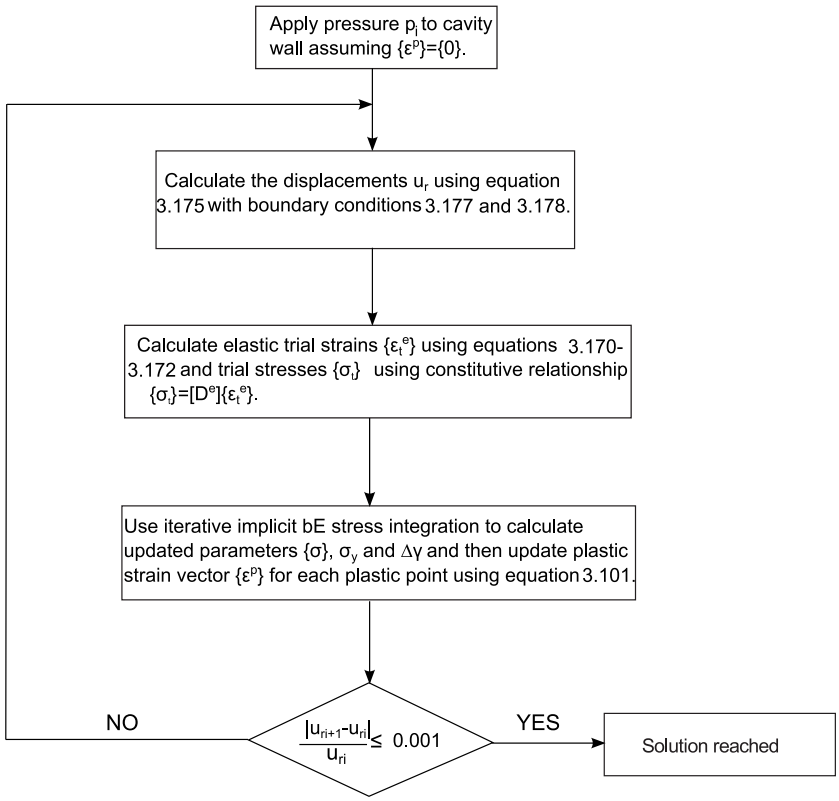

Figure 3.16: Flowchart of solution procedure when yield criterion $f > 0$

3.6.3 Validating the elasto-plastic response of the cavity

In this section we validate the elasto-plastic response of the cavity for the von Mises and Drucker-Prager constitutive models. Here we validate both the displacements and stresses. In the proposed method, the stresses can be calculated from the strains by either using the stress-strain relations in cylindrical coordinates presented earlier (equations 3.164-3.166), or by using the elastic law (equation 3.114). Expressions for the stresses using equations 3.164-3.166 are presented below

$$\sigma_{rr} = \lambda\left(\left(\frac{du_r}{dr} - \varepsilon_{rr}^p\right) + \left(\frac{u_r}{r} - \varepsilon_{\theta\theta}^p\right) - \varepsilon_{zz}^p\right) + 2G\left(\frac{du_r}{dr} - \varepsilon_{rr}^p\right) \tag{3.179}$$

$$\sigma_{\theta\theta} = \lambda\left(\left(\frac{du_r}{dr} - \varepsilon_{rr}^p\right) + \left(\frac{u_r}{r} - \varepsilon_{\theta\theta}^p\right) - \varepsilon_{zz}^p\right) + 2G\left(\frac{u_r}{r} - \varepsilon_{\theta\theta}^p\right) \tag{3.180}$$

$$\sigma_{zz} = \lambda\left(\left(\frac{du_r}{dr} - \varepsilon_{rr}^p\right) + \left(\frac{u_r}{r} - \varepsilon_{\theta\theta}^p\right) - \varepsilon_{zz}^p\right) + 2G\left(-\varepsilon_{zz}^p\right) \tag{3.181}$$

The response of the cavity in von Mises and Drucker-Prager materials is validated using ABAQUS 6.8-1 FE software. Here we assume perfect plasticity for simplification (hardening

modulus $\{H\} = 0$). Three different cavity pressures were used ($p_i = 20$, 25 and 40 MPa) and a cavity radius r_0 of 10 m, along with the following elastic material parameters, $\nu = 0.2$ and $G = 1000$MPa. A cohesion c of 15 MPa was used, which equates to a yield stress σ_y of 30 MPa in the von Mises model. For the Drucker-Prager model we assume non-associated flow. The following parameters were used in the analyses, $\phi = 15^0$ and $\psi = 7.5^o$ unless otherwise stated.

Figures 3.17 and 3.18 show that there is good agreement between the proposed solution and FE analysis. It is important to note that the accuracy of the proposed solution could be improved through a greater number of integration points (1000 integration points used here), however the run time of the program increases. Note that for the von Mises model it was found that both the iterative stress integration algorithm and the analytical stress integration produced identical results when analysing the cavity.

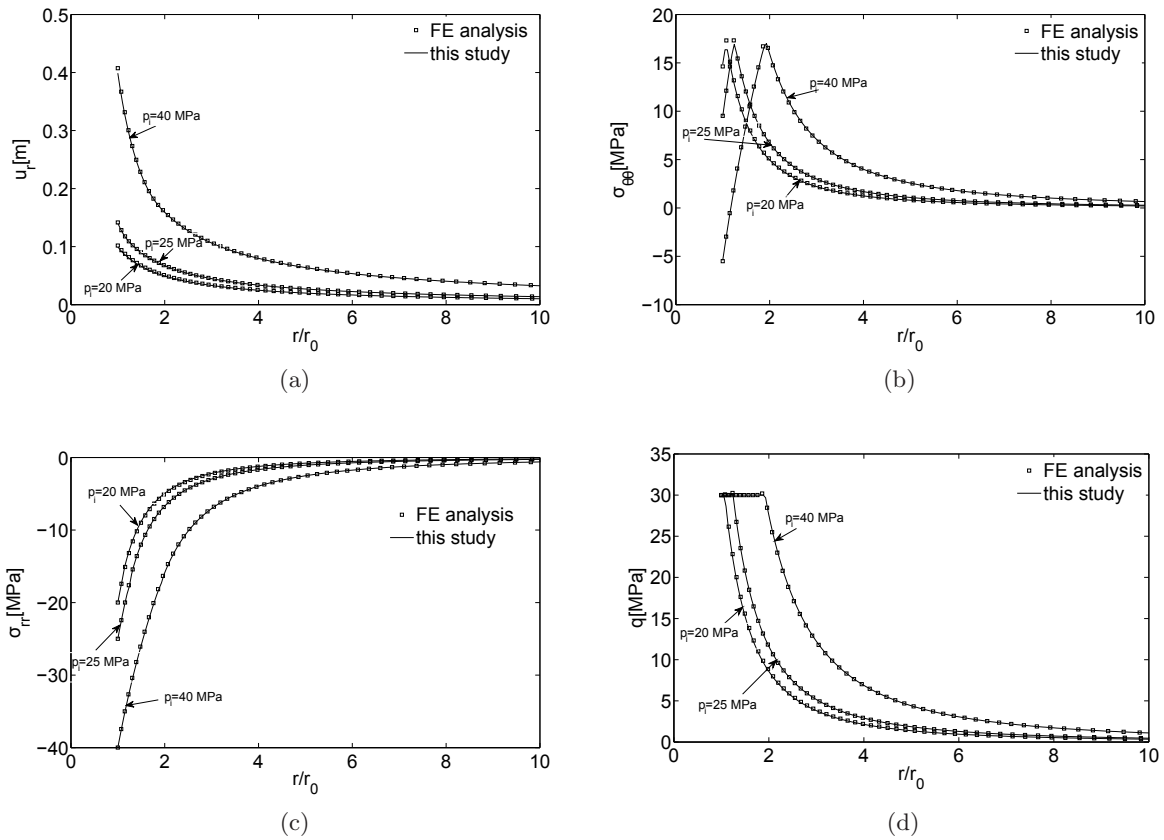

Figure 3.17: Cavity response under different pressures for a von Mises constitutive model: (a) radial displacement; (b) circumferential stress; (c) radial stress; (d) von Mises equivalent stress

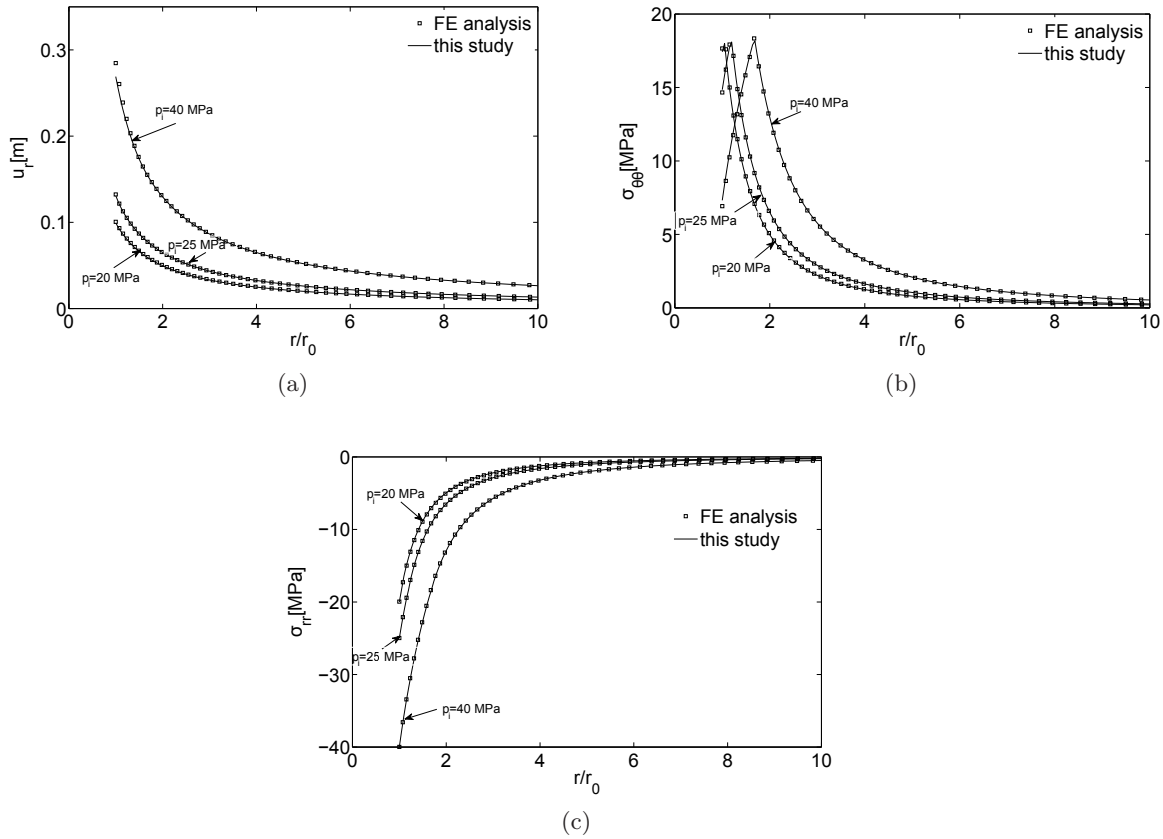

Figure 3.18: Cavity response under different pressures for a Drucker-Prager non-associated flow constitutive model: (a) radial displacement; (b) circumferential stress; (c) radial stress

3.7 Summary

- the proposed energy-based method uses the variational method of virtual work to derive governing equations and boundary conditions for a system. Variational methods are powerful tools that can be used to obtain approximate solutions to a range of practical problems. A number of authors have used the variational method of virtual work to analyse the 3D behaviour of piles.
- variational methods can be used to solve problems in both elastic and inelastic media.
- this chapter demonstrates that the principle of virtual work can be used to derive closed form energy-based solutions for the displacements and stresses of simple elastic cavity problems, e.g. a cylindrical cavity and a spherical cavity shown in this chapter. Cavity expansion solutions can be applied to the area of geomechanics.
- more complex solutions for cavities can be derived through knowledge of the form of the displacement field, e.g. a cylindrical cavity located in an anisotropic stress field shown in this chapter. Both closed-form solutions and the 1D FD method can be used to solve for the cavity displacements and stresses. The displacements and stresses show excellent agreement with existing closed-form solutions.
- viscoelastic material behaviour can be incorporated in the Laplace domain. Results were obtained for the viscoelastic Burger's response of a cylindrical cavity located in an anisotropic stress field. Displacements were successfully validated using an existing closed-form solution.
- hyperplasticity is an approach to plasticity theory that is consistent with the laws of thermodynamics. The entire constitutive behaviour can be derived from two scalar potentials; a free energy potential which provides the elasticity law, and a dissipation potential which provides the yield function and the direction of plastic flow. No additional assumptions are required. Simple elasto-plastic constitutive models have been derived using the theory of hyperplasticity in this chapter.
- the energy-based approach can be used to derive elasto-plastic cavity models. Both the von Mises and Drucker-Prager constitutive models were incorporated into a cylindrical cavity model and the results match well with FE analysis.
- the results of the models derived in this chapter are a reliable building block for the development of more advanced models in the following chapters.

3.8 References

1 Anandarajah, A. (2010). *Computational Methods in Elasticity and Plasticity, Solids and Porous Media*. Springer.

2 Basu, D. & Salgado, R. (2007). Elastic analysis of laterally loaded pile in multi-layered soil. *Geomechanics and Geoengineering*, 2(3) p. 183-196.

3 Basu, D. & Salgado, R. & Prezzi, M. (2009). A continuum-based model for analysis of laterally loaded piles in layered soils. *Géotechnique*, 59(2) p. 127-140.

4 Becker, R. (2011). An alternative approach to integrating plasticity relations. *International Journal of Plasticity*, 27 p.1224-1238.

5 de Borst, R, Crisfield, M.A., Remmers, J.J.C. & Verhoosel, C.V. (2012). *Non-linear Finite Element Analysis of Solids and Structures*. 2nd Edition. John Wiley & Sons, Chichester, UK.

6 Collins, I.F. & Houlsby, G.T. (1997). Application of thermomechanical principles to the modelling of geotechnical materials. In: *Proceedings of the Royal Society*, London, England, p. 1975-2001.

7 Coombs, W.M. (2011). Finite deformation of particulate geomaterials: frictional and anisotropic Critical State elasto-plasticity. Ph.D. Thesis, Durham University.

8 Coulomb, C.A.(1773). Sur une application des régles de Maximis et Minimis a quelques problémes de statique relatifs á l'Architecture. *Acad. Roy. des Sciences Memoires de math. et de physique par divers savans*, 7 p. 343-382.

9 Einav, I. (2002). Applications of thermodynamical approaches to mechanics of soils. Ph.D. Thesis, Technion- Israel Institute of Technology, Haifa.

10 Einav, I. (2005). Energy and variational principles for piles in dissipative soil. *Géotechnique*, 55(7) p. 515-525.

11 Forrest, J.A. & Hunt, H.E.M. (2006). A three-dimensional tunnel model for calculation of train-induced ground vibration. *Journal of Sound and Vibration*, 294 p. 678-705.

12 Goodman, R.E. (1989). *Introduction to Rock Mechanics.* 2nd Edition, John Wiley & Sons, New York.

13 Guo, W.D., & Lee, F.H. (2001). Load transfer approach for laterally loaded piles. *International Journal for Numerical and Analytical Methods in Geomechanics*, 25(11) p. 1101-1129.

14 Hill, R. (1950). *The Mathematical Theory of Plasticity.* Oxford University Press, London.

15 Hollenbeck, K.J. (1998). INVLAP.m: A MATLAB function for numerical inversion of Laplace transforms by the de Hoog algorithm, http://www.isva.dtu.dk/staff/karl/invlap.html.

16 de Hoog, F.R., Knight, J.H. & Stokes, A.N. (1982). An improved method for numerical inversion of Laplace transforms. SIAM (Society for Industrial and Applied Mathematics). *Journal on Scientific and Statistical Computing*, 3(3) p. 357-366.

17 Houlsby, G.T. (1981). A study of plasticity theories and their applicability to soils. Ph.D. Thesis, University of Cambridge.

18 Houlsby, G.T. & Puzrin, A.M. (2006). *Principles of hyperplasticity: an approach to plasticity theory based on thermodynamic principles*. Springer-Verlag, London.

19 Jaeger, J.C., Cook, N.G.W. & Zimmerman, R.W. (2007). *Fundamentals of rock mechanics.* John Wiley & Sons.

20 Kirsch, G. (1898). Die Theorie der Elastizität und die Bedürfnisse der Festigkeitslehre. *Zeitschrift des Vereines deutscher Ingenieure*, 42 p. 797-807.

21 Pender, M.J. (1980). Elastic solutions for a deep circular tunnel. *Géotechnique*, 30(2) p. 216-222.

22 Perry, J. & Aboudi, J. (2003). Elasto-Plastic Stresses in Thick Walled Cylinders. *Journal of Pressure Vessel Technology*, 125 p. 248-252.

23 Potts, D.M. & Zdravkovic, L. (1999). *Finite element analysis in geotechnical engineering, theory.* Thomas Telford.

24 Puzrin, A.M. (2012). *Constitutive Modelling in Geomechanics: Introduction*. Springer.

25 Reddy, J.N. (2002). *Energy and Variational Methods in Applied Mechanics*. 2nd Edition, John Wiley & Sons.

26 Rutishauser H. (1957). Der Quotienten-Differenzen-Algorithmus. *Mitt. Inst. Agnew. Math. ETH*, 7. Birkhauser Verlag, Basel.

27 Sadd, M.H. (2005). *Elasticity, Theory, Applications, and Numerics*. Elsevier.

28 Shen, W.Y., Chow, Y.K. & Yong, K.Y. (1997). Variational approach for vertical deformation analysis of pile group. *International Journal for Numerical and Analytical Methods in Geomechanics*, 21(11) p. 741-752.

29 Simo, J.C. & Hughes, T.J.R. (1998). *Computational Inelasticity*. Volume 7. Springer.

30 de Souza Neto, E.A., Peric, D. & Owen, D.R.J. (2008). *Computational Methods for Plasticity: Theory and Applications*. John Wiley & Sons.

31 Timoshenko, S.P. & Goodier, J.N. (1987). *Theory of Elasticity.* 3rd Edition, McGraw-Hill.

32 Vlasov, V.Z. & Leontiev, U.N. (1966). Beams, plates and shells on elastic foundations. In: *Israel Program for Scientific Translations*, Jerusalem, translated from Russian.

33 Wynn, P. (1967). Transformations to accelerate the convergence of fourier series. Blanch Anniversary Volume. In: Mond, B. (Ed.), US Air Force, Washington DC, p. 339-379.

34 Yu, H.S. (2000). *Cavity Expansion Methods in Geomechanics*. Kluwer, Dordrecht.

35 Ziegler, H. (1983). *An introduction to thermomechanics*. 2nd Edition, North Holland Pub. Co, Amsterdam.

Chapter 4

Response of a tunnel in a viscoelastic medium

Synopsis

This chapter uses the proposed energy-based method presented in Chapter 3 to derive a three-dimensional (3D) approximate solution for the time-dependent response of a deeply embedded and unsupported tunnel, of circular cross-section. The solution takes into account the effect of a tunnel face. The tunnel is excavated quasi-instantaneously from an infinite viscoelastic rock body which is modelled by means of Burger's model in the Laplace domain and exhibits an initial isotropic stress state. Validation is carried out using closed-form solutions and finite element (FE) analysis.

Unlike previous analytical solutions that are based on a 2D idealisation [4,11,13,15,19] and use empirical relations to take into account the affect of the tunnel face (see Section 2.3.1), our new 3D solution can predict the full interaction between a tunnel and the surrounding creeping rock. In this respect, the new solution can be incorporated together with field monitoring data in an expert system for tunnel design similar to that illustrated by Schubert et al. [17].

This new solution has been developed into a stand alone design tool, which is presented in Section 4.4. The development of such a tool enables practical use of the model. The work presented in this chapter has been published in the *International Journal of Numerical and Analytical Methods in Geomechanics* [2].

4.1 Analysis

We consider a tunnel of circular cross-section and radius r_0 (Figure 4.1). A cylindrical coordinate system is adopted $(r - \theta - z)$ with its origin coinciding with the centre of the tunnel face. We focus here on the prediction of creep behaviour after the creation of the cylindrical cavity, thus the excavation of the tunnel is assumed to take place instantaneously.

The rock surrounding the tunnel is divided into three zones as shown in Figure 4.1. The displacement field around the cylindrical cavity is expressed as the product of two separate variables r and z as shown in Table 4.1, where u_r and u_z are the radial and the longitudinal displacements, respectively. $\psi_{r1}(z)$, $\psi_{r2}(z)$ and $\psi_{z1}(z)$, $\psi_{z2}(z)$ are functions describing the variation of the radial and the longitudinal displacement, respectively, in the z-direction. $\phi_1(r)$, $\phi_2(r)$ and $\phi_3(r)$ are functions describing the attenuation of rock displacement away from the tunnel axis. It is assumed that the tunnel face remains plane at all times in order to simplify the assumed displacement field.

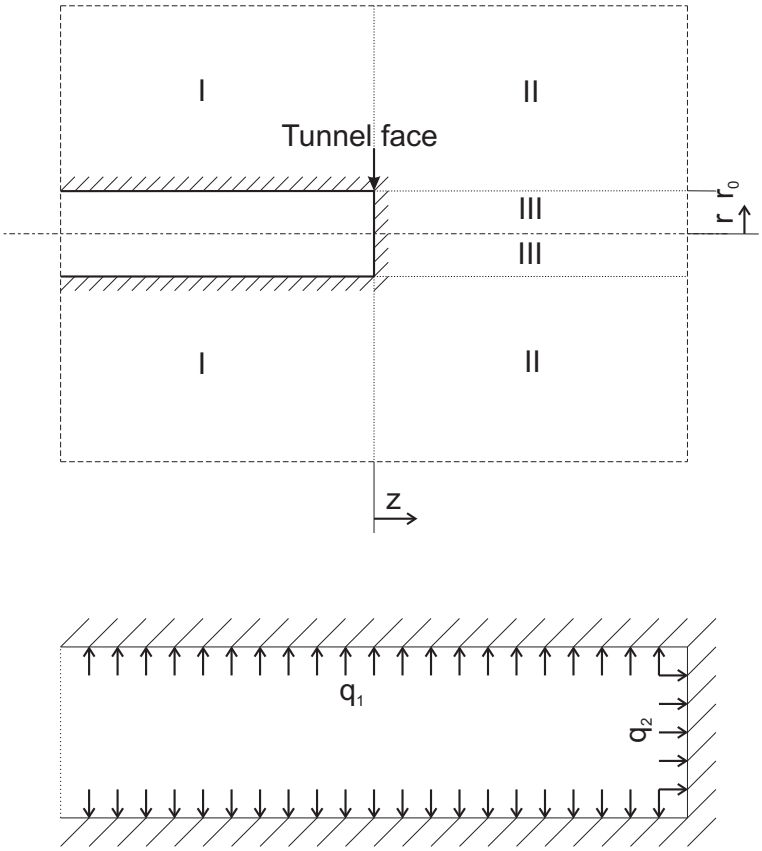

Figure 4.1: Model geometry, location of zones in which energy is dissipated and applied pressure

zone	bounds	$u_r(r,z)$	$u_z(r,z)$
I	$r_0 \leq r \leq \infty$	$\phi_1(r)\psi_{r1}(z)$	$\phi_2(r)\psi_{z1}(z)$
	$-\infty \leq z \leq 0$		
II	$r_0 \leq r \leq \infty$	$\phi_1(r)\psi_{r2}(z)$	$\phi_2(r)\psi_{z2}(z)$
	$0 \leq z \leq \infty$		
III	$0 \leq r \leq r_0$	$\phi_3(r)\psi_{r2}(z)$	$\psi_{z2}(z)$
	$0 \leq z \leq \infty$		

Table 4.1: Displacements u_r and u_z for each of the rock zones

As $z \to -\infty$ the plane-strain condition can be assumed, therefore $\frac{d\psi_{r1}}{dz} = 0$ and $\psi_{z1}(z) = 0$.

At a far distance ahead of the face the displacement reduces to zero, therefore $\psi_{r2}(z) = 0$ and $\psi_{z2}(z) = 0$ as $z \to \infty$. It is assumed that $\phi_1(r) = 1$ and $\phi_2(r) = 1$ at $r = r_0$ and $\phi_1(r) = 0$ and $\phi_2(r) = 0$ as $r \to \infty$ (this ensures that rock displacements decrease with increasing radial distance from the tunnel wall). Thus ϕ_1 and ϕ_2 vary between 1 at the tunnel wall and 0 at an infinite radial distance from the wall. Finally, it is assumed that $\phi_3(r) = 0$ at $r = 0$ and $\phi_3(r) = 1$ at $r = r_0$ (this ensures compatibility in the region ahead of the tunnel face). Thus ϕ_3 varies between 0 at the tunnel axis and 1 at the tunnel wall.

4.1.1 Linear elastic formulation

In order to derive a solution for the time-dependent response of the tunnel, first we need to derive the governing differential equations, boundary conditions and a solution algorithm for the linear elastic, time-independent case.

The potential energy U of the tunnel-rock system for a linear elastic rock is given by

$$\begin{aligned} U =& \frac{1}{2}\int_{r_0}^{\infty}\int_{0}^{2\pi}\int_{-\infty}^{\infty}(\sigma_{rr}\varepsilon_{rr} + \sigma_{\theta\theta}\varepsilon_{\theta\theta} + \sigma_{zz}\varepsilon_{zz} + 2\tau_{zr}\varepsilon_{zr})rdzd\theta dr \\ &+ \frac{1}{2}\int_{0}^{r_0}\int_{0}^{2\pi}\int_{0}^{\infty}(\sigma_{rr}\varepsilon_{rr} + \sigma_{\theta\theta}\varepsilon_{\theta\theta} + \sigma_{zz}\varepsilon_{zz} + 2\tau_{zr}\varepsilon_{zr})rdzd\theta dr, \end{aligned} \tag{4.1}$$

where the first integral term represents the internal potential energy of the rock in zones I and II and the second term represents the energy in zone III.

In a linear elastic material, the stress-strain relations in cylindrical coordinates are given by

$$\sigma_{rr} = \lambda(\varepsilon_{rr} + \varepsilon_{\theta\theta} + \varepsilon_{zz}) + 2G\varepsilon_{rr}, \tag{4.2}$$

$$\sigma_{\theta\theta} = \lambda(\varepsilon_{rr} + \varepsilon_{\theta\theta} + \varepsilon_{zz}) + 2G\varepsilon_{\theta\theta}, \tag{4.3}$$

$$\sigma_{zz} = \lambda(\varepsilon_{rr} + \varepsilon_{\theta\theta} + \varepsilon_{zz}) + 2G\varepsilon_{zz}, \tag{4.4}$$

$$\tau_{zr} = 2G\varepsilon_{zr}. \tag{4.5}$$

The strains are obtained from the first derivative of displacements as follows

$$\varepsilon_{rr} = \frac{\partial u_r}{\partial r}, \tag{4.6}$$

$$\varepsilon_{\theta\theta} = \frac{1}{r}\left(u_r + \frac{\partial u_\theta}{\partial \theta}\right), \tag{4.7}$$

$$\varepsilon_{zz} = \frac{\partial u_z}{\partial z}, \tag{4.8}$$

$$\varepsilon_{zr} = \frac{1}{2}\left(\frac{\partial u_r}{\partial z} + \frac{\partial u_z}{\partial r}\right). \tag{4.9}$$

Using the above stress-strain relations, the strain-displacement relations and the assumed displacement field, equation 4.1 can be evaluated as detailed in Appendix A.

Variational principles are then used to obtain expressions for δU and δW from which the governing differential equations of the system and appropriate boundary conditions can be written.

The variation in the external work W is given by

$$\delta W = \int_0^{2\pi} \int_{-\infty}^{0} q_1 r_0 \delta\psi_{r1} dz d\theta + q_2 \pi {r_0}^2 \delta\psi_{z2}. \tag{4.10}$$

The governing equations for deformation can be derived using the principle of virtual work by minimising the energy in the tunnel-rock system

$$\delta\Pi = \delta U - \delta W = 0. \tag{4.11}$$

Setting the first variable of the total energy $\delta\Pi$ equal to zero produces an equation of the form (see details in Appendix A)

$$\begin{aligned}\delta\Pi =& [A(\phi_1)\delta\phi_1] + [B(\phi_2)\delta\phi_2] + [C(\phi_3)\delta\phi_3] + [D(\psi_{r1})\delta\psi_{r1}] + [E(\psi_{z1})\delta\psi_{z1}] \\ &+ [F(\psi_{r2})\delta\psi_{r2}] + [G(\psi_{z2})\delta\psi_{z2}] = 0.\end{aligned} \tag{4.12}$$

We use the same method described in Chapter 3 to form the governing equations and boundary conditions. Here we describe the method again for the purpose of clarity.

Since the variations $\delta\phi_1$, $\delta\phi_2$, $\delta\phi_3$, $\delta\psi_{r1}$, $\delta\psi_{z1}$, $\delta\psi_{r2}$, $\delta\psi_{z2}$ are independent, the terms associated with each variation must be equal to zero (e.g.$A(\phi_1)\delta\phi_1 = 0$) in order to satisfy $\delta\Pi = 0$. Collection of these terms over the corresponding rock domain (e.g. collecting the $\delta\phi_1$ terms for $r_0 \leq r < \infty$) forms the differential equations which govern the displacements of the tunnel-rock system. Since the variations are non-zero over the rock domains (e.g. $\delta\phi_1 \neq 0$), the coefficients of the terms (e.g. integrand associated with $\delta\phi_1$) must be equal to zero in order to satisfy $\delta\Pi = 0$. Expressions for the boundary conditions can be formed by collecting the terms associated with each variation at the appropriate boundaries (e.g. collection of the $\delta\phi_1$ terms at $r = r_0$ and as $r \to \infty$) and setting these equal to zero in order to satisfy $\delta\Pi = 0$. The governing equations and boundary conditions are expressed in the following section.

Governing differential equations and boundary conditions

Firstly we consider the variation of $\phi_1(r)$. Collecting the coefficients of $\delta\phi_1$ for $r_0 \leq r < \infty$

produces

$$r\frac{d^2\phi_1}{dr^2}+\frac{d\phi_1}{dr}-\frac{\phi_1}{r}-\gamma_1 r\phi_1+\gamma_2 r\frac{d\phi_2}{dr}=0, \tag{4.13}$$

where

$$\gamma_1=\frac{G\int_{-\infty}^{0}\left(\frac{d\psi_{r1}}{dz}\right)^2dz+G\int_{0}^{\infty}\left(\frac{d\psi_{r2}}{dz}\right)^2dz}{(\lambda+2G)\int_{-\infty}^{0}{\psi_{r1}}^2dz+(\lambda+2G)\int_{0}^{\infty}{\psi_{r2}}^2dz}, \tag{4.14}$$

$$\gamma_2=\frac{\lambda\int_{-\infty}^{0}\psi_{r1}\frac{d\psi_{z1}}{dz}dz-G\int_{-\infty}^{0}\psi_{z1}\frac{d\psi_{r1}}{dz}dz+\lambda\int_{0}^{\infty}\psi_{r2}\frac{d\psi_{z2}}{dz}dz-G\int_{0}^{\infty}\psi_{z2}\frac{d\psi_{r2}}{dz}dz}{(\lambda+2G)\int_{-\infty}^{0}{\psi_{r1}}^2dz+(\lambda+2G)\int_{0}^{\infty}{\psi_{r2}}^2dz}. \tag{4.15}$$

and collecting the coefficients of $\delta\phi_2$ for $r_0\leq r<\infty$ produces

$$r\frac{d^2\phi_2}{dr^2}+\frac{d\phi_2}{dr}-\gamma_3 r\phi_2+\gamma_4\left(r\frac{d\phi_1}{dr}+\phi_1\right)=0, \tag{4.16}$$

where

$$\gamma_3=\frac{(\lambda+2G)\int_{-\infty}^{0}\left(\frac{d\psi_{z1}}{dz}\right)^2dz+(\lambda+2G)\int_{0}^{\infty}\left(\frac{d\psi_{z2}}{dz}\right)^2dz}{G\int_{-\infty}^{0}{\psi_{z1}}^2dz+G\int_{0}^{\infty}{\psi_{z2}}^2dz}, \tag{4.17}$$

$$\gamma_4=\frac{G\int_{-\infty}^{0}\psi_{z1}\frac{d\psi_{r1}}{dz}dz-\lambda\int_{-\infty}^{0}\psi_{r1}\frac{d\psi_{z1}}{dz}dz+G\int_{0}^{\infty}\psi_{z2}\frac{d\psi_{r2}}{dz}dz-\lambda\int_{0}^{\infty}\psi_{r2}\frac{d\psi_{z2}}{dz}dz}{G\int_{-\infty}^{0}{\psi_{z1}}^2dz+G\int_{0}^{\infty}{\psi_{z2}}^2dz}. \tag{4.18}$$

Collecting the $\delta\phi_1$ terms at $r=r_0$ or as $r\to\infty$ for $-\infty<z\leq 0$ gives

$$\left[-2\pi\int_{-\infty}^{0}\psi_{r1}\left(\lambda\phi_1\psi_{r1}+r\left((\lambda+2G)\psi_{r1}\frac{d\phi_1}{dr}+\lambda\phi_2\frac{d\psi_{z1}}{dz}\right)\right)dz\right]\delta\phi_1=0. \tag{4.19}$$

Collecting the $\delta\phi_2$ terms at $r=r_0$ or as $r\to\infty$ for $-\infty<z\leq 0$ gives

$$\left[-2\pi rG\int_{-\infty}^{0}\psi_{z1}\left(\psi_{z1}\frac{d\phi_2}{dr}+\phi_1\frac{d\psi_{r1}}{dz}\right)dz\right]\delta\phi_2=0. \tag{4.20}$$

Collecting the $\delta\phi_1$ terms at $r = r_0$ or as $r \to \infty$ for $0 \leq z < \infty$ gives

$$\left[-2\pi \int_0^\infty \psi_{r2} \left(\lambda\phi_1\psi_{r2} + r\left((\lambda + 2G)\psi_{r2}\frac{d\phi_1}{dr} + \lambda\phi_2\frac{d\psi_{z2}}{dz}\right)\right) dz\right] \delta\phi_1 = 0. \tag{4.21}$$

Collecting the $\delta\phi_2$ terms at $r = r_0$ or as $r \to \infty$ for $0 \leq z < \infty$ gives

$$\left[-2\pi r G \int_0^\infty \psi_{z2} \left(\psi_{z2}\frac{d\phi_2}{dr} + \phi_1\frac{d\psi_{r2}}{dz}\right) dz\right] \delta\phi_2 = 0. \tag{4.22}$$

As the displacements decay to zero as $r \to \infty$, equations 4.19-4.22 can be satisfied by

$$\phi_1(\infty) = 0, \tag{4.23}$$
$$\phi_2(\infty) = 0. \tag{4.24}$$

At the tunnel wall the displacements reach a maximum, therefore the attenuation functions can be taken to be fixed at $r = r_0$ and have a value of 1

$$\phi_1(r_0) = 1, \tag{4.25}$$
$$\phi_2(r_0) = 1. \tag{4.26}$$

Therefore, ϕ_1 and ϕ_2 are governed by equations 4.13 and 4.16 together with the boundary conditions given by equations 4.23-4.26.

Collecting the coefficients of $\delta\phi_3$ for $0 \leq r \leq r_0$ produces the following governing equation

$$r\frac{d^2\phi_3}{dr^2} - \gamma_5 r\phi_3 + \frac{d\phi_3}{dr} - \frac{\phi_3}{r} = 0, \tag{4.27}$$

where

$$\gamma_5 = \frac{G\int_0^\infty \left(\frac{d\psi_{r2}}{dz}\right)^2 dz}{(\lambda + 2G)\int_0^\infty {\psi_{r2}}^2 dz}. \tag{4.28}$$

The solution for ϕ_3 requires that $\phi_3 = 0$ at $r = 0$. It also requires that $\phi_3 = 1$ at $r = r_0$ so that a compatible displacement field can be obtained. Therefore, the solution of equation 4.27 takes the form of

$$\phi_3(r) = \frac{I_1(\sqrt{\gamma_5}r)}{I_1(\sqrt{\gamma_5}r_0)}, \tag{4.29}$$

where $I_1(x)$ is a modified Bessel function of the first kind of order one.

Collecting the coefficients of $\delta\psi_{r1}$ for $-\infty < z \leq 0$ produces

$$m_1\frac{d^2\psi_{r1}}{dz^2} + m_2\psi_{r1} + m_3\frac{d\psi_{z1}}{dz} + 2\pi q_1 r_0 = 0, \tag{4.30}$$

where

$$m_1 = 2\pi G\int_{r_0}^{\infty} r{\phi_1}^2 dr, \tag{4.31}$$

$$m_2 = -2\pi\left((\lambda+2G)\int_{r_0}^{\infty}\frac{{\phi_1}^2}{r}dr + 2\lambda\int_{r_0}^{\infty}\phi_1\frac{d\phi_1}{dr}dr + (\lambda+2G)\int_{r_0}^{\infty} r\left(\frac{d\phi_1}{dr}\right)^2 dr\right), \tag{4.32}$$

$$m_3 = 2\pi\left(G\int_{r_0}^{\infty} r\phi_1\frac{d\phi_2}{dr}dr - \lambda\int_{r_0}^{\infty}\phi_1\phi_2 dr - \lambda\int_{r_0}^{\infty} r\phi_2\frac{d\phi_1}{dr}dr\right). \tag{4.33}$$

and collecting the coefficients of $\delta\psi_{z1}$ for $-\infty < z \leq 0$ produces

$$m_4\frac{d^2\psi_{z1}}{dz^2} + m_5\psi_{z1} - m_3\frac{d\psi_{r1}}{dz} = 0, \tag{4.34}$$

where

$$m_4 = 2\pi(\lambda+2G)\int_{r_0}^{\infty} r{\phi_2}^2 dr, \tag{4.35}$$

$$m_5 = -2\pi G\int_{r_0}^{\infty} r\left(\frac{d\phi_2}{dr}\right)^2 dr. \tag{4.36}$$

Collecting the $\delta\psi_{r1}$ terms as $z \to -\infty$ for $r_0 \leq r < \infty$ gives

$$\left[-2\pi G\int_{r_0}^{\infty} r\phi_1\left(\psi_{z1}\frac{d\phi_2}{dr} + \phi_1\frac{d\psi_{r1}}{dz}\right)dr\right]\delta\psi_{r1} = 0. \tag{4.37}$$

Collecting the $\delta\psi_{z1}$ terms as $z \to -\infty$ for $r_0 \leq r < \infty$ gives

$$\left[-2\pi \int_{r_0}^{\infty} \phi_2 \left(\lambda\phi_1\psi_{r1} + r\left(\lambda\psi_{r1}\frac{d\phi_1}{dr} + (\lambda+2G)\phi_2\frac{d\psi_{z1}}{dz}\right)\right) dr\right] \delta\psi_{z1} = 0. \tag{4.38}$$

It should be noted that away from the tunnel face (as $z \to -\infty$), the displacement in the longitudinal direction reduces to zero and there will be no variation in the radial displacement along the tunnel axis and the plane strain condition can be assumed. Therefore equations 4.37 and 4.38 can be satisfied if

$$\psi_{z1}(-\infty) = 0, \tag{4.39}$$

$$\frac{d\psi_{r1}}{dz} \mid_{z\to-\infty} = 0. \tag{4.40}$$

Collecting the coefficients of $\delta\psi_{r2}$ for $0 \leq z < \infty$ produces

$$a_1\frac{d^2\psi_{r2}}{dz^2} + a_2\psi_{r2} + a_3\frac{d\psi_{z2}}{dz} = 0, \tag{4.41}$$

where

$$a_1 = 2\pi\left(G\int_{r_0}^{\infty} r{\phi_1}^2 dr + G\int_{0}^{r_0} r{\phi_3}^2 dr\right), \tag{4.42}$$

$$\begin{aligned} a_2 = -2\pi\Bigg((\lambda+2G)\int_{r_0}^{\infty}\frac{{\phi_1}^2}{r}dr + 2\lambda\int_{r_0}^{\infty}\phi_1\frac{d\phi_1}{dr}dr + (\lambda+2G)\int_{r_0}^{\infty} r\left(\frac{d\phi_1}{dr}\right)^2 dr + (\lambda+2G)\int_{0}^{r_0}\frac{{\phi_3}^2}{r}dr \\ + 2\lambda\int_{0}^{r_0}\phi_3\frac{d\phi_3}{dr}dr + (\lambda+2G)\int_{0}^{r_0} r\left(\frac{d\phi_3}{dr}\right)^2 dr\Bigg), \end{aligned} \tag{4.43}$$

$$a_3 = -2\pi\left(-G\int_{r_0}^{\infty} r\phi_1\frac{d\phi_2}{dr}dr + \lambda\int_{r_0}^{\infty}\phi_1\phi_2 dr + \lambda\int_{r_0}^{\infty} r\phi_2\frac{d\phi_1}{dr}dr + \lambda\int_{0}^{r_0}\phi_3 dr + \lambda\int_{0}^{r_0} r\frac{d\phi_3}{dr}dr\right). \tag{4.44}$$

and collecting the coefficients of $\delta\psi_{z2}$ for $0 \leq z < \infty$ produces

$$a_4\frac{d^2\psi_{z2}}{dz^2} + a_5\psi_{z2} - a_3\frac{d\psi_{r2}}{dz} = 0, \tag{4.45}$$

where

$$a_4 = \pi(\lambda + 2G)\left(2\int_{r_0}^{\infty} r{\phi_2}^2 dr + {r_0}^2\right), \tag{4.46}$$

$$a_5 = -2\pi G\int_{r_0}^{\infty} r\left(\frac{d\phi_2}{dr}\right)^2 dr. \tag{4.47}$$

Collecting the $\delta\psi_{r2}$ terms as $z \to \infty$ for $r_0 \leq r < \infty$ gives

$$\left[-2\pi G\int_{r_0}^{\infty} r\phi_1\left(\psi_{z2}\frac{d\phi_2}{dr} + \phi_1\frac{d\psi_{r2}}{dz}\right)dr\right]\delta\psi_{r2} = 0. \tag{4.48}$$

Collecting the $\delta\psi_{z2}$ terms as $z \to \infty$ for $r_0 \leq r < \infty$ gives

$$\left[-2\pi\int_{r_0}^{\infty}\phi_2\left(\lambda\phi_1\psi_{r2} + r\left(\lambda\psi_{r2}\frac{d\phi_1}{dr} + (\lambda+2G)\phi_2\frac{d\psi_{z2}}{dz}\right)\right)dr\right]\delta\psi_{z2} = 0. \tag{4.49}$$

Collecting the $\delta\psi_{r2}$ terms as $z \to \infty$ for $0 \leq r \leq r_0$ gives

$$\left[-2\pi G\int_{0}^{r_0} r{\phi_3}^2\frac{d\psi_{r2}}{dz}dr\right]\delta\psi_{r2} = 0. \tag{4.50}$$

Collecting the $\delta\psi_{z2}$ terms as $z \to \infty$ for $0 \leq r \leq r_0$ gives

$$\left[-2\pi\int_{0}^{r_0}\left(\lambda\phi_3\psi_{r2} + r\left(\lambda\psi_{r2}\frac{d\phi_3}{dr} + (\lambda+2G)\frac{{r_0}^2}{2}\frac{d\psi_{z2}}{dz}\right)\right)dr\right]\delta\psi_{z2} = 0. \tag{4.51}$$

At a large distance ahead of the tunnel face, the displacements in both the radial and longitudinal directions vanish, therefore

$$\psi_{r2}(\infty) = 0, \tag{4.52}$$

$$\psi_{z2}(\infty) = 0. \tag{4.53}$$

By collecting the coefficients of $\delta\psi_{r1}$ and $\delta\psi_{r2}$ at $z = 0$ and noting that $\delta\psi_{r1}$ and $\delta\psi_{r2}$ are not equal to zero at the tunnel face, the deformation of the tunnel can be shown to be governed

by the following boundary condition at $z = 0$

$$c_1\psi_{z1} + c_2\frac{d\psi_{r1}}{dz} + c_3\frac{d\psi_{r2}}{dz} + c_4\psi_{z2} \mid_{z=0}= 0, \tag{4.54}$$

where

$$c_1 = -2\pi G\int_{r_0}^{\infty} r\phi_1\frac{d\phi_2}{dr}dr, \tag{4.55}$$

$$c_2 = -2\pi G\int_{r_0}^{\infty} r{\phi_1}^2 dr, \tag{4.56}$$

$$c_3 = 2\pi G\left(\int_{r_0}^{\infty} r{\phi_1}^2 dr + \int_{0}^{r_0} r{\phi_3}^2 dr\right), \tag{4.57}$$

$$c_4 = 2\pi G\int_{r_0}^{\infty} r\phi_1\frac{d\phi_2}{dr}dr. \tag{4.58}$$

Similarly by collecting the coefficients of $\delta\psi_{z1}$ and $\delta\psi_{z2}$ at z=0, it can be shown that

$$c_5\psi_{r1} + c_6\frac{d\psi_{z2}}{dz} + c_7\frac{d\psi_{z1}}{dz} + c_8\psi_{r2} + q_2\pi {r_0}^2 \mid_{z=0}= 0, \tag{4.59}$$

where

$$c_5 = -2\pi\lambda\left(\int_{r_0}^{\infty}\phi_1\phi_2 dr + \int_{r_0}^{\infty} r\phi_2\frac{d\phi_1}{dr}dr\right), \tag{4.60}$$

$$c_6 = 2\pi(\lambda + 2G)\int_{r_0}^{\infty} r{\phi_2}^2 dr + \pi {r_0}^2(\lambda + 2G), \tag{4.61}$$

$$c_7 = -2\pi(\lambda + 2G)\int_{r_0}^{\infty} r{\phi_2}^2 dr, \tag{4.62}$$

$$c_8 = 2\pi\lambda\left(\int_{r_0}^{\infty}\phi_1\phi_2 dr + \int_{r_0}^{\infty} r\phi_2\frac{d\phi_1}{dr} + \int_{0}^{r_0}\phi_3 dr + \int_{0}^{r_0} r\frac{d\phi_3}{dr}dr\right). \tag{4.63}$$

Combining equations 4.41 and 4.45 and eliminating ψ_{z2} leads to

$$\frac{d^4\psi_{r2}}{dz^4} + d_1\frac{d^2\psi_{r2}}{dz^2} + d_2\psi_{r2} = 0, \tag{4.64}$$

where

$$d_1 = \frac{{a_3}^2 + a_2 a_4 + a_1 a_5}{a_1 a_4}, \tag{4.65}$$

$$d_2 = \frac{a_2 a_5}{a_1 a_4}. \tag{4.66}$$

A closed-form solution can then be obtained for ψ_{r2}. This solution requires that ψ_{r2} should remain finite and reduces to zero as $z \to \infty$ (equation 4.52). Therefore

$$\psi_{r2} = b_1 e^{-x_1 z} + b_2 e^{-x_2 z}, \tag{4.67}$$

where b_1 and b_2 are constants and

$$x_1 = \sqrt{-\frac{d_1}{2} + \frac{1}{2}\sqrt{{d_1}^2 - 4d_2}}, \tag{4.68}$$

$$x_2 = \sqrt{-\frac{d_1}{2} - \frac{1}{2}\sqrt{{d_1}^2 - 4d_2}}. \tag{4.69}$$

By substituting equation 4.67 into equation 4.41, an expression of the following form can then be derived for ψ_{z2}

$$\psi_{z2} = \frac{1}{a_3 x_1 x_2} e^{-z(x_1+x_2)}(a_1 x_1 x_2(b_1 e^{z x_2} x_1 + b_2 e^{z x_1} x_2) + a_2(b_2 e^{z x_1} x_1 + b_1 e^{z x_2} x_2)). \tag{4.70}$$

Since there is no displacement discontinunity at the boundary between zones I and II (at $z = 0$), the following conditions must hold at the tunnel face

$$\psi_{r1}(0) = \psi_{r2}(0), \tag{4.71}$$

$$\psi_{z1}(0) = \psi_{z2}(0). \tag{4.72}$$

Therefore, using equations 4.67 and 4.70 with equations 4.71 and 4.72, the constants b_1 and b_2 can be written as follows

$$b_1 = \frac{x_1(a_2\psi_{r1}(0) + x_2(a_1 x_2 \psi_{r1}(0) - a_3\psi_{z1}(0)))}{(x_1 - x_2)(a_2 - a_1 x_1 x_2)}, \tag{4.73}$$

$$b_2 = \frac{x_2(a_2\psi_{r1}(0) + x_1(a_1 x_1 \psi_{r1}(0) - a_3\psi_{z1}(0)))}{(x_1 - x_2)(-a_2 + a_1 x_1 x_2)}. \tag{4.74}$$

Solutions for ψ_{r1} and ψ_{z1} can then be obtained by solving equations 4.30 and 4.34 simultaneously together with the boundary conditions given by equations 4.39, 4.40, 4.54 and 4.59. The boundary conditions given by equations 4.54 and 4.59 can be rewritten in terms of ψ_{r1} and ψ_{z1} only, using the expressions given by equations 4.67, 4.70, 4.73 and 4.74.

4.2 Solution Procedure

It should be noted that from the above derivations, the solutions for ψ_{r1}, ψ_{z1}, ψ_{r2} and ψ_{z2} depend on ϕ_1, ϕ_2 and ϕ_3. However, in order to evaluate ϕ_1, ϕ_2 and ϕ_2, the values of γ_1 to γ_5 are needed. It can be seen from equations 4.14, 4.15, 4.17, 4.18 and 4.28 that these values depend on ψ_{r1}, ψ_{z1}, ψ_{r2} and ψ_{z2}, therefore an iterative technique is required.

The iterative procedure employed here is illustrated in Figure 4.2. Initial values of the parameters γ_1 to γ_5 are guessed first, then ϕ_1 and ϕ_2 are evaluated by solving equations 4.13 and 4.16 together with the boundary conditions given by equations 4.23-4.26. The solution is obtained numerically using the finite difference (FD) method [3]. ϕ_3 is calculated from equation 4.29.

Once ϕ_1, ϕ_2 and ϕ_3 are evaluated, the FD method is used to obtain solutions for ψ_{r1} and ψ_{z1} by solving equations 4.30 and 4.34 simultaneously together with the boundary conditions given by equations 4.39, 4.40, 4.54 and 4.59. The values of ψ_{r1} and ψ_{z1} at $z = 0$ are then used to evaluate ψ_{r2} and ψ_{z2} using equations 4.67 and 4.70. New values of γ_1 to γ_5 can then be evaluated from equations 4.14, 4.15, 4.17, 4.18 and 4.28. These new values are then used to repeat the calculations until the difference between the ith and $(i + 1)$th values of γ_1 to γ_5 is less than a specific tolerance. A computer program was written using MATLAB 7.9.0 to carry out these calculations.

Here we use the γ terms for the convergence criterion as this produces quick convergence. Very similar algorithms have been used by a number of authors when developing 3D models for pile analysis using the energy-based method, producing accurate results in a short period of time (e.g. [20]). An alternative approach to ensure correct solutions are obtained would be to use the ϕ and ψ terms which are the solutions which are sought. However, using these terms for the criterion would involve checking against a greater number of parameters. Care must be taken when using the type of approach adopted here as convergence of the γ terms does not necessarily indicate convergence of the ϕ and ψ terms. However, the results obtained using the model developed in this chapter match well with closed form solutions and FE analysis, therefore using the γ terms provides an efficient and accurate algorithm for this model.

4.2.1 Time-dependent response

For the time-dependent response, the solution is obtained first in the Laplace domain and the Lamé constants G and λ are replaced with the quantities G^* and λ^* as described in Chapter 3. The only difference here is that the two pressures applied are a wall pressure and a face pressure, q_1 and q_2 respectively. Thus the applied pressures in the Laplace domain are given

by

$$\hat{q}_1 = \frac{q_1}{s}, \tag{4.75}$$

$$\hat{q}_2 = \frac{q_2}{s}. \tag{4.76}$$

See Section 3.4.1 for inversion of the Laplace transform.

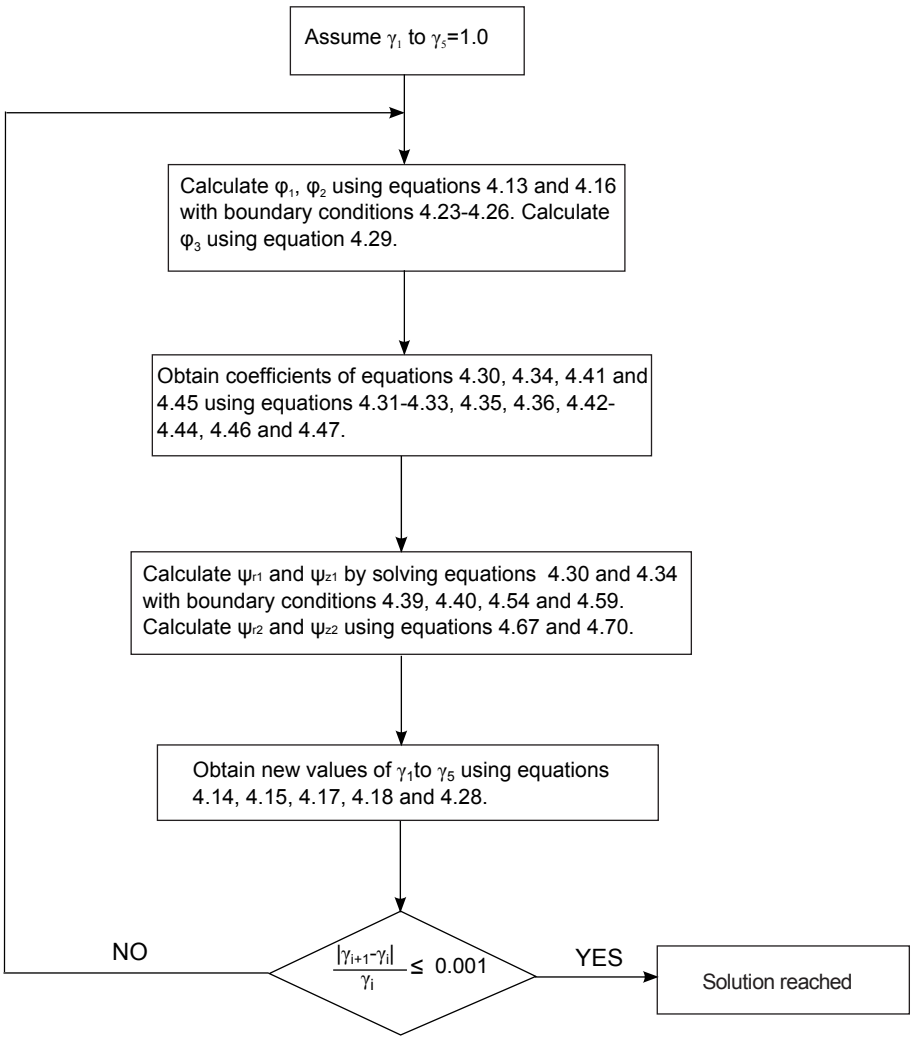

Figure 4.2: Flowchart of solution procedure for each value of time t

4.3 Results and Discussion

4.3.1 Comparison with cavity expansion theory

The proposed solution is validated by considering a tunnel cross-section located at a large distance behind the face so that comparisons can be made with plane strain cavity expansion solutions derived for the cylindrical cavity in Section 3.2.1. The closed-form cavity expansion equation (equation 3.17) is used to validate the linear elastic instantaneous displacement, whilst the stress distribution around the tunnel is validated using the Kirsch solution [10]

(equations 3.20 and 3.21). These equations are written below in terms of the pressure applied to the tunnel wall q_1

$$u_r = \frac{q_1 {r_0}^2}{2Gr}, \tag{4.77}$$

$$\sigma_{rr} = -q_1 \left(\frac{r_0}{r}\right)^2, \tag{4.78}$$

$$\sigma_{\theta\theta} = q_1 \left(\frac{r_0}{r}\right)^2. \tag{4.79}$$

Figure 4.3a shows the variation of displacements in the radial direction for a cross-section located at a distance of $25r_0$ behind the tunnel face. This figure shows that the results of the proposed solution are consistent with cavity expansion theory. The slight discrepancies at large radial distances are due to the fact that the numerical results of the proposed method are achieved by truncating all the integrations at $50r_0$ from the tunnel centre (i.e. by assuming zero displacements at $r = 50r_0$). Figure 4.3b shows the variation of the radial and circumferential stresses in the radial direction. This figure shows that there is excellent agreement between the proposed energy-based solution and cavity expansion theory.

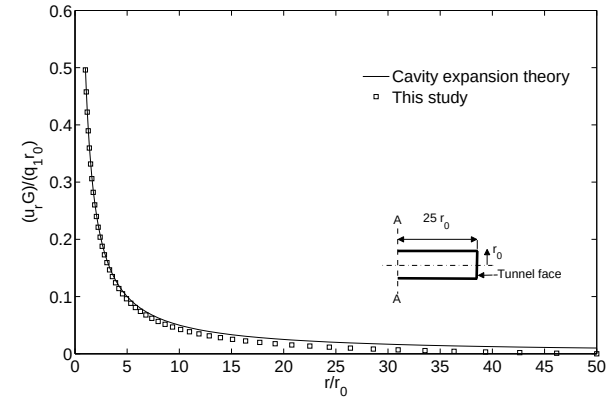

(a)

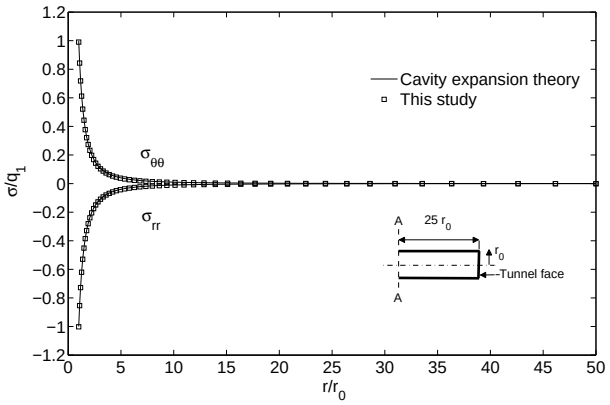

(b)

Figure 4.3: Comparison between the proposed solution and cavity expansion theory at section A-A: (a) radial displacement; (b) radial and circumferential stress

4.3.2 Comparison with plane-strain closed-form viscoelastic solution

At a large distance behind the tunnel face, the time-dependent response of the proposed solution can be compared with the plane strain solution of Fahimifar et al. [4]. Both solutions use Burger's model to describe the creep response. The radial displacement in Fahimifar et al. [4] is given by

$$u_r(t) = \frac{q_1 {r_0}^2}{2r}\left(\frac{1}{G_2} + \frac{t}{\eta_2} + \frac{1}{G_1}\left[1 - \exp\left(-\frac{G_1 t}{\eta_1}\right)\right]\right) \tag{4.80}$$

Analyses were carried out with the creep parameters shown in Table 3.1, together with a Poisson's ratio of 0.2. The tunnel radius is taken to be 4.57 m and the initial stress in the rock considered to be equal to 6.897 MPa. Figure 4.4a shows the radial creep deformation of the tunnel wall at a distance of $25r_0$ behind the tunnel face and Figure 4.4b shows the variation of this deformation in the radial direction at different time periods. These figures clearly demonstrate that there is consistent agreement between the proposed solution and the plane strain solution of Fahimifar et al. [4].

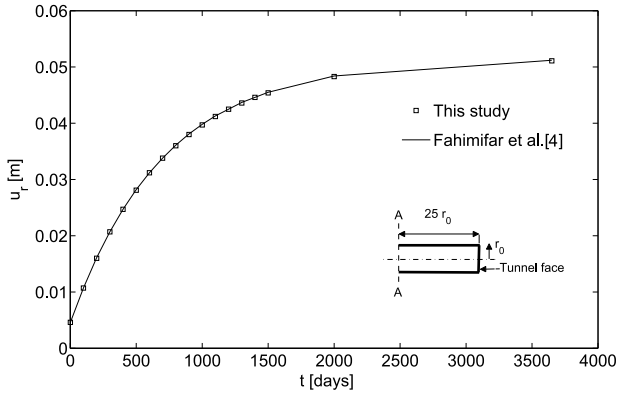

(a)

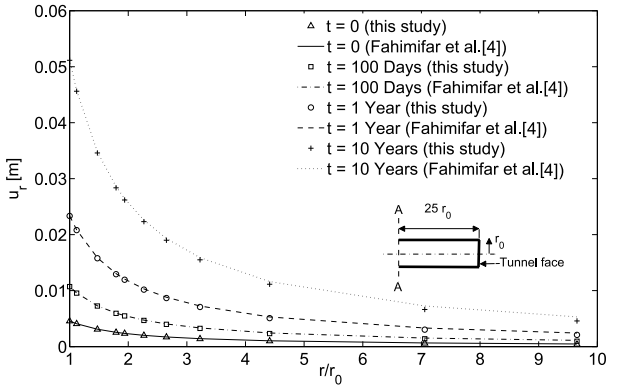

(b)

Figure 4.4: Comparison between the proposed energy-based solution and the plane strain solution of Fahimifar et al. [4] at section A-A: (a) radial displacement with time; (b) radial displacement with radial distance for different time periods

4.3.3 Displacement profile along the tunnel axis

An axisymmetric FE analysis using ABAQUS 6.8-1 software was carried out in order to plot the radial displacement u_r and the longitudinal displacement u_z along the tunnel axis. The FE mesh consists of 2285 axisymmetric eight-node elements with a total of 7024 nodes. The mesh domain is sufficiently large so that changes in stresses and displacements at the boundary are negligible. Smaller elements are located near the tunnel where the changes of stresses and strains are significant. The vertical and horizontal boundaries are constrained in the normal direction. Details of the FE mesh are shown in Figure 4.5.

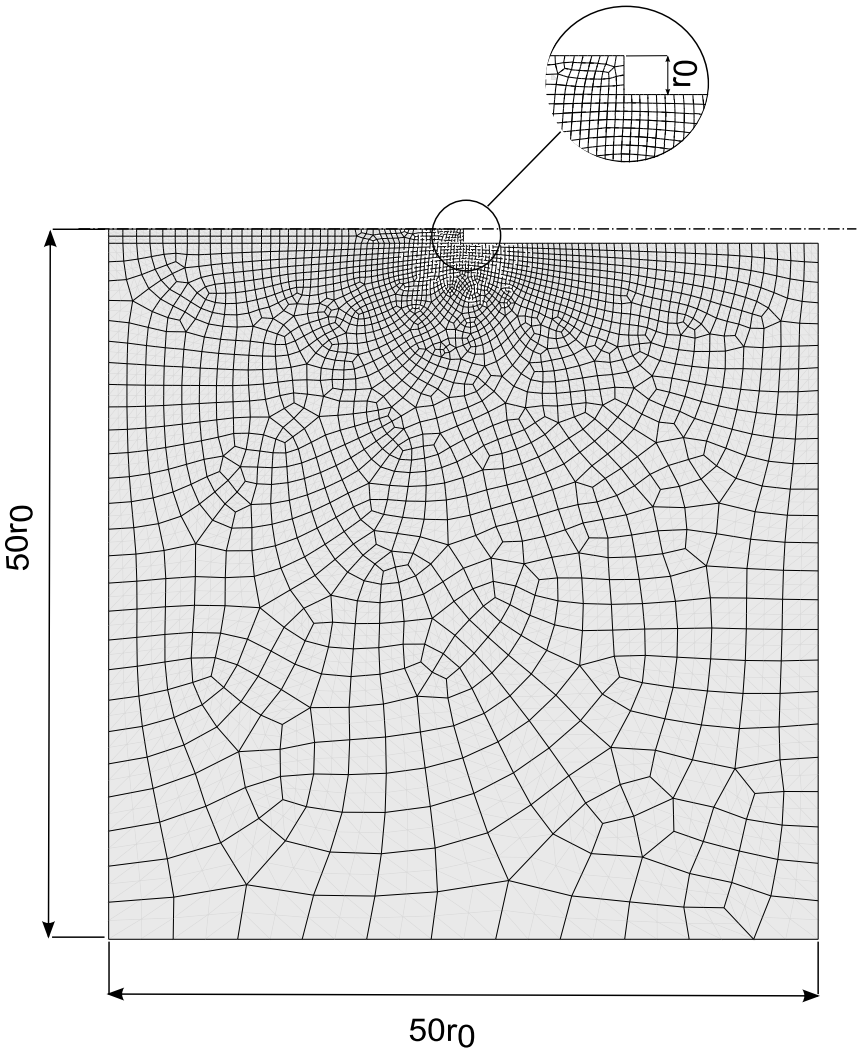

Figure 4.5: FE mesh

Figure 4.6 shows the instantaneous radial displacement u_r at $r = r_0$ (i.e. at the tunnel wall and in front of the tunnel face). This figure shows that the current FE analysis is consistent with the previous FE analysis of Panet [12]. Figure 4.6 shows that the radial displacement profile ($t = 0$) predicted by the energy-based solution is in good agreement with the FE results. The slight inconsistency could be attributed to the simplified displacement field

(particularly in zone III) in the proposed solution.

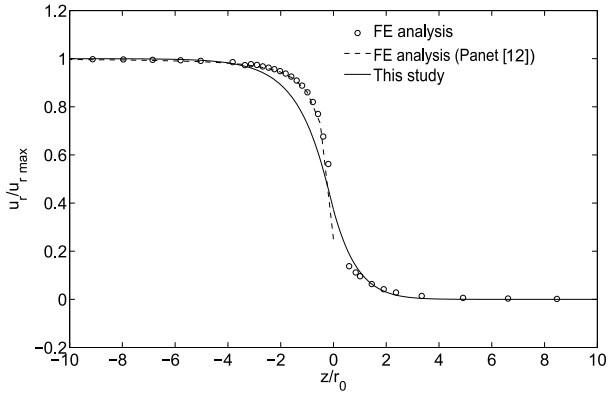

Figure 4.6: Comparison of energy-based solution with FE analyses for the instantaneous radial displacement of the tunnel wall along the tunnel axis

Figure 4.7 compares the longitudinal displacement u_z predicted by the energy-based solution with that calculated using the FE analysis at $t = 0$. Figure 4.7 shows that the energy-based solution gives a reasonable approximation of the longitudinal displacements. It should be noted that in this solution it is assumed there is no variation of the longitudinal displacement u_z in the radial direction in zone III (in front of the tunnel face). However, the displacements in front of deeply embedded tunnels are localised as illustrated from the FE results shown in Figures 4.6 and 4.7. The magnitude of the longitudinal displacement is small relative to the radial displacement, so the contribution to the potential energy (equation 4.1) is negligible. Therefore, the assumed simplified displacement field shown in Table 4.1 can be justified.

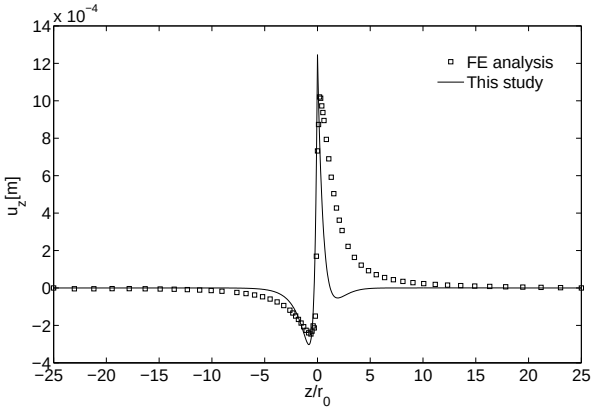

Figure 4.7: Comparison of energy-based solution and FE analysis for the instantaneous longitudinal displacement of the tunnel wall along the tunnel axis

The effect of the tunnel face on the time-dependent deformation is shown in Figure 4.8. As time increases the tunnel face has a greater effect on the deformational shape. It is noticeable that the radial displacement appears to level off at a greater distance behind the

face for $t = 10$ years than $t = 0$. For example, for $t = 10$ years the displacement only starts to level off at approximately $6r_0$ behind the face as opposed to $4r_0$ when $t = 0$. This remark is also drawn by Shalabi [16] from FE analysis.

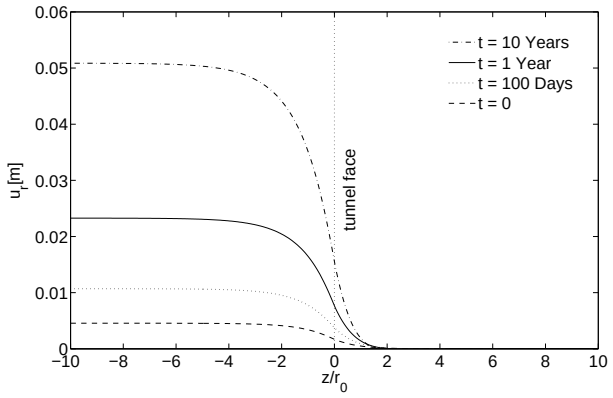

Figure 4.8: The effect of time on the radial displacement of the tunnel wall along the tunnel axis

4.4 Stand alone program

The model presented in this chapter has been developed into a stand alone application using MATLAB 7.9.0. This application is able to run on any machine and does not require MATLAB software to operate, thus is convenient for a company to use. The user can adhere to any model and material parameter units that they wish. The screen displays shown in Figure 4.9 demonstrate the ease of use of the program. The user simply enters the model parameters (Figure 4.9a), clicks Next to move to the following screen (Figure 4.9b), and clicks Calculate, after which a short period of time the radial displacement of the tunnel wall is plotted along the tunnel axis. The user can then select a distance behind the tunnel face at which they wish to observe the tunnel displacement with radial distance and the displacement of the tunnel wall with time, without carrying out any further calculations. Note that the program could be modified to show the stresses surrounding the tunnel.

4.5 Limitations and possible extension of the proposed solution

It is well known that a complete solution for any deformable body needs satisfaction of three requirements: equilibrium, compatibility and constitutive relationship. The proposed solution is derived by considering compatibility and constitutive laws; therefore it is not an exact solution. However, it gives good approximation of the time-dependent creep behaviour due to tunnelling as demonstrated through comparison with FE analyses and closed-form solutions. As shown in Appendix B, equilibrium is found to be satisfied everywhere apart from at the tunnel face, where stress singularity is expected, i.e. the stress tends towards infinity. In

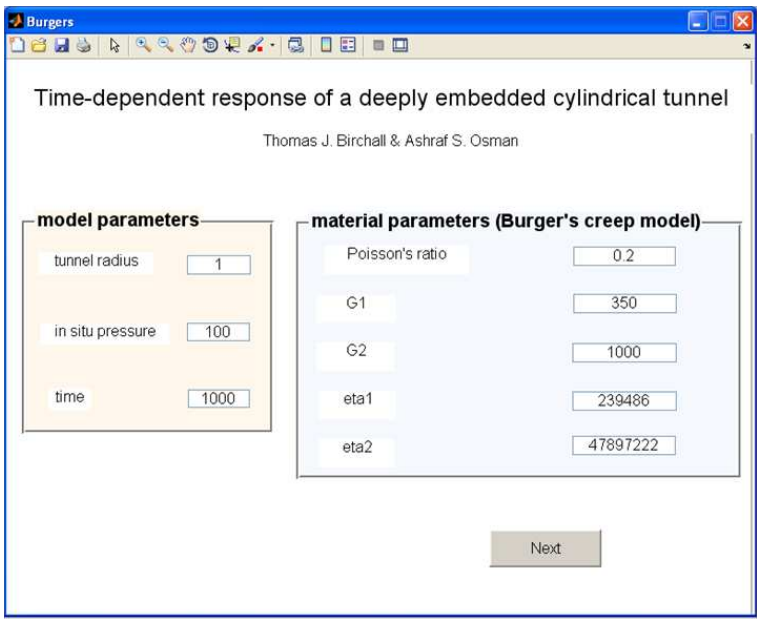

(a)

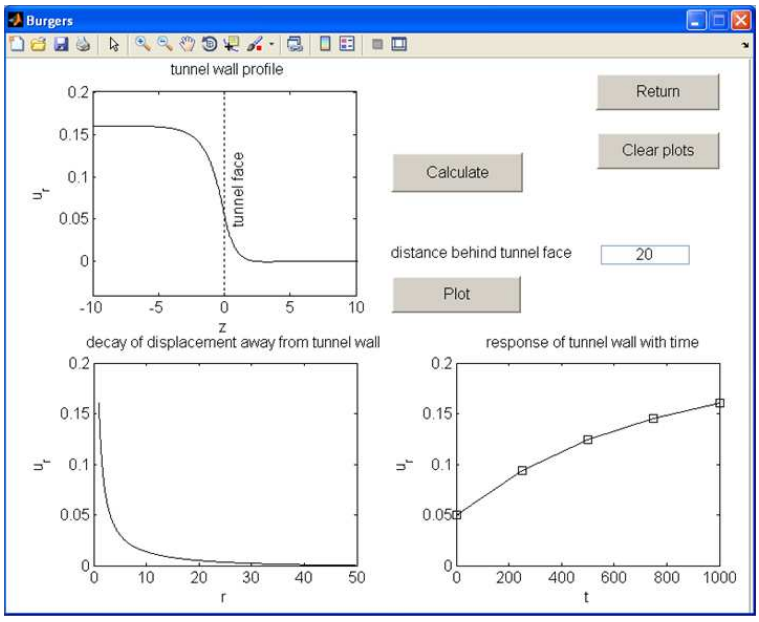

(b)

Figure 4.9: Screen displays of design tool: (a) entering model parameters; (b) calculating and plotting results

this respect, the new approach is analogous to the upper bound limit theorems of plasticity which are widely used to estimate collapse loads in engineering practice. Our new approach is much more efficient, from a practical point of view, than FE analysis. In addition to being faster, the input to our analysis (the dimensions, loading and material properties) is accomplished through a simple text file, while the geometry (domain) and optimal meshing for an FE analysis requires considerable time.

In this chapter, an energy-based solution for creep behaviour is developed by assuming that the rock is a viscoelastic material which is modelled by the classical Burger's model. The energy-based solution is not restricted to viscoelastic materials. Different constitutive models can be implemented. Plastic response can be incorporated as shown in Chapter 3 by considering a function describing the mechanical dissipation (which is strictly non-negative). Discussion on mechanical dissipation functions can be found in [8].

4.6 Summary

- the energy-based method presented in Chapter 3 has been used successfully to develop a 3D approximate solution for the time-dependent convergence of a deeply embedded, unsupported, circular tunnel, subjected to an isotropic stress field and embedded in a linear viscoelastic medium. This viscoelastic problem was transformed into the Laplace domain where it represents a quasi-elastic problem. The approximations in this analysis concern the assumption of a rock displacement field composed of separable variables. The differential equations governing the displacements of the tunnel-rock system and appropriate boundary conditions were obtained using the principle of virtual work. Both closed-form solutions and the 1D FD method were used to solve for the rock displacements in the Laplace domain. Transformation to the time domain was evaluated numerically.

- the predicted response of the tunnel away from the face is consistent with closed-form solutions and the predicted tunnel displacement profile was found to be consistent with FE analysis.

- the proposed energy-based method represents an efficient tool to predict the time-dependent response around tunnels. This approximate solution is more efficient, from a practical point of view, than FE analysis. In addition to being faster, the input to the proposed analysis is accomplished through a simple text file. In this chapter, we modelled the creep response using Burger's model. However, a wide range of constitutive models can easily be incorporated into this analysis.

4.7 References

1 Afrouz, A. & Harvey, J.M. (1974). Rheology of rocks within the soft to medium strength range. *International Journal of Rock Mechanics and Mining Science and Geomechanics*, 11(7) p. 281-290.

2 Birchall, T.J. & Osman, A.S. (2011). Response of a tunnel deeply embedded in a viscoelastic medium. *International Journal for Numerical and Analytical Methods in Geomechanics*, Doi: 10.1002/nag.1069.

3 Desai, C.S. & Christian, J.T. (eds.). (1977). *Numerical Methods in Geotechnical Engineering*. McGraw-Hill, New York.

4 Fahimifar, A., Tehrani, F.M., Hedayat, A. & Vakilzadeh, A. (2010). Analytical solution for the excavation of circular tunnels in a visco-elastic Burger's material under hydrostatic stress field. *Tunnelling and Underground Space Technology*, 25(4) p. 297-304.

5 Ghaboussi, J. & Gioda, G. (1977). On the time dependent effects in advancing tunnels. *International Journal for Numerical and Analytical Methods in Geomechanics*, 1 p. 249-269.

6 Goodman, R.E. (1989). *Introduction to Rock Mechanics*. 2nd Edition. John Wiley & Sons, New York.

7 de Hoog, F.R., Knight, J.H. & Stokes, A.N. (1982). An improved method for numerical inversion of Laplace transforms, SIAM (Society for Industrial and Applied Mathematics). *Journal on Scientific and Statistical Computing*, 3(3) p. 357-366.

8 Houlsby, G.T. & Puzrin, A.M. (2006). *Principles of hyperplasticity: an approach to plasticity theory based on thermodynamic principles*. Springer-Verlag, London.

9 Jaeger, J., Cook, N.G. & Zimmerman, R. (2007). *Fundamentals of Rock Mechanics*. 4th edition. Blackwell.

10 Kirsch, G. (1898). Die Theorie der Elastizität und die Bedürfnisse der Festigkeitslehre. *Zeitschrift des Vereines deutscher Ingenieure*, 42 p. 797-807.

11 Ladanyi, B. (1993). Time-dependent response of rock around tunnels. *Comprehensive Rock Engineering*, 2, Elsevier, Amsterdam, p. 77-112.

12 Panet, M. (1995). Le calcul des tunnels par la method convergence-confinement. *Presses de l'Ecole Nationale des Ponts et Chaussees*, Paris, France.

13 Panet, M. (1993). Understanding deformations in tunnels. *Comprehensive rock engineering*, 1, Pergamon Press, Oxford, p. 663-690.

14 Rutishauser, H. (1957). Der Quotienten-Differenzen-Algorithmus. *Mitt. Inst. Agnew. Math. ETH*, 7, Birkhauser Verlag, Basel.

15 Sakurai, S. (1978). Approximate time-dependent analysis of tunnel support structure considering progress of tunnel face. *International Journal for Numerical and Analytical Methods in Geomechanics*, 2 p. 159-175.

16 Shalabi, F.I. (2005). FE analysis of time-dependent behaviour of tunnelling in squeezing ground using two different creep models. *Tunnelling and Underground Space Technology*, 20 p. 271-279.

17 Schubert, W., Moritz, B. & Sellner, P. (2009). Tunnelling methods for squeezing ground. *9th International congress on rock mechanics*, 1-2 p. 233-236.

18 Sterpi, D. & Gioda, G. (2009). Visco-plastic behaviour around advancing tunnels in squeezing rock. *Rock Mechanics and Rock Engineering* 42, p. 319-339.

19 Sulem, J., Panet, M. & Guenot, A. (1987). An Analytical Solution for Time-dependent Displacements in a Circular Tunnel. *International Journal of Rock Mechanics and Mining Sciences and Geomechanics*, 24(3) p. 155-164.

20 Sun, K. (1994). Laterally Loaded Piles in Elastic Media. *Journal of Geotechnical Engineering*, 120(8) p.1324-1344.

21 Wynn, P. (1967). Transformations to accelerate the convergence of fourier series. Blanch Anniversary Volume. In:*Mond, B. (Ed.)*, US Air Force, Washington DC, p. 339-379.

22 Yu, C.W. (1998). Creep characteristics of soft rock and modelling of creep in tunnel. Ph.D. Thesis, University of Bradford, United Kingdom.

4.8 Appendix A

Expanded expressions for the potential energy U and the first variation of the total energy Π

$$
\begin{aligned}
U = \pi \int_{r_0}^{\infty}\int_{-\infty}^{0} \Bigg[& (\lambda+2G)\Bigg(\left(\psi_{r1}\frac{d\phi_1}{dr}\right)^2 + \left(\psi_{r1}\frac{\phi_1}{r}\right)^2 + \left(\phi_2\frac{d\psi_{z1}}{dz}\right)^2\Bigg) \\
& + 2\lambda\Bigg({\psi_{r1}}^2\frac{d\phi_1}{dr}\frac{\phi_1}{r} + \frac{\phi_2\phi_1}{r}\psi_{r1}\frac{d\psi_{z1}}{dz} + \phi_2\psi_{r1}\frac{d\psi_{z1}}{dz}\frac{d\phi_1}{dr}\Bigg) \\
& + G\Bigg(\left(\phi_1\frac{d\psi_{r1}}{dz}\right)^2 + 2\Bigg(\frac{d\psi_{r1}}{dz}\phi_1\psi_{z1}\frac{d\phi_2}{dr}\Bigg) + \left(\psi_{z1}\frac{d\phi_2}{dr}\right)^2\Bigg)\Bigg] r\,dz\,dr \\
+\pi \int_{r_0}^{\infty}\int_{0}^{\infty} \Bigg[& (\lambda+2G)\Bigg(\left(\psi_{r2}\frac{d\phi_1}{dr}\right)^2 + \left(\psi_{r2}\frac{\phi_1}{r}\right)^2 + \left(\phi_2\frac{d\psi_{z2}}{dz}\right)^2\Bigg) \\
& + 2\lambda\Bigg({\psi_{r2}}^2\frac{d\phi_1}{dr}\frac{\phi_1}{r} + \frac{\phi_2\phi_1}{r}\psi_{r2}\frac{d\psi_{z2}}{dz} + \phi_2\psi_{r2}\frac{d\psi_{z2}}{dz}\frac{d\phi_1}{dr}\Bigg) \\
& + G\Bigg(\left(\phi_1\frac{d\psi_{r2}}{dz}\right)^2 + 2\Bigg(\frac{d\psi_{r2}}{dz}\phi_1\psi_{z2}\frac{d\phi_2}{dr}\Bigg) + \left(\psi_{z2}\frac{d\phi_2}{dr}\right)^2\Bigg)\Bigg] r\,dz\,dr \\
+\pi \int_{0}^{r_0}\int_{0}^{\infty} \Bigg[& (\lambda+2G)\Bigg(\left(\psi_{r2}\frac{d\phi_3}{dr}\right)^2 + \left(\psi_{r2}\frac{\phi_3}{r}\right)^2 + \left(\frac{d\psi_{z2}}{dz}\right)^2\Bigg) \\
& + 2\lambda\Bigg({\psi_{r2}}^2\frac{d\phi_3}{dr}\frac{\phi_3}{r} + \psi_{r2}\frac{d\psi_{z2}}{dz}\frac{d\phi_3}{dr} + \frac{\phi_3}{r}\psi_{r2}\frac{d\psi_{z2}}{dz}\Bigg) + G\Bigg(\phi_3\frac{d\psi_{r2}}{dz}\Bigg)^2\Bigg] r\,dz\,dr
\end{aligned}
\tag{4.81}
$$

$$
\begin{aligned}
\delta\Pi = & 2\pi(\lambda+2G)\Bigg(\int_{r_0}^{\infty} r\left(\frac{d\phi_1}{dr}\right)^2 dr \int_{-\infty}^{0} \psi_{r1}\delta\psi_{r1}\,dz + \int_{-\infty}^{0} {\psi_{r1}}^2 dz\left[r\frac{d\phi_1}{dr}\delta\phi_1\right]_{r_0}^{\infty} \\
& - \int_{-\infty}^{0} {\psi_{r1}}^2 dz \int_{r_0}^{\infty}\left(r\frac{d^2\phi_1}{dr^2} + \frac{d\phi_1}{dr}\right)\delta\phi_1\,dr + \int_{r_0}^{\infty}\frac{{\phi_1}^2}{r}dr \int_{-\infty}^{0} \psi_{r1}\delta\psi_{r1}\,dz + \int_{-\infty}^{0} {\psi_{r1}}^2 dz \int_{r_0}^{\infty}\frac{\phi_1}{r}\delta\phi_1\,dr \\
& + \int_{-\infty}^{0}\left(\frac{d\psi_{z1}}{dz}\right)^2 dz \int_{r_0}^{\infty} r\phi_2\delta\phi_2\,dr + \int_{r_0}^{\infty} r{\phi_2}^2 dr\left[\frac{d\psi_{z1}}{dz}\delta\psi_{z1}\right]_{-\infty}^{0} - \int_{r_0}^{\infty} r{\phi_2}^2 dr \int_{-\infty}^{0}\frac{d^2\psi_{z1}}{dz^2}\delta\psi_{z1}\,dz\Bigg) \\
& + 2\pi\lambda\Bigg(2\int_{r_0}^{\infty}\phi_1\frac{d\phi_1}{dr}dr \int_{-\infty}^{0} \psi_{r1}\delta\psi_{r1}\,dz + \int_{-\infty}^{0} {\psi_{r1}}^2 dz[\phi_1\delta\phi_1]_{r_0}^{\infty} - \int_{-\infty}^{0} {\psi_{r1}}^2 dz \int_{r_0}^{\infty}\frac{d\phi_1}{dr}\delta\phi_1\,dr \\
& + \int_{-\infty}^{0} {\psi_{r1}}^2 dz \int_{r_0}^{\infty}\frac{d\phi_1}{dr}\delta\phi_1\,dr + \int_{-\infty}^{0}\psi_{r1}\frac{d\psi_{z1}}{dz}dz \int_{r_0}^{\infty}\phi_1\delta\phi_2\,dr + \int_{-\infty}^{0}\psi_{r1}\frac{d\psi_{z1}}{dz}dz \int_{r_0}^{\infty}\phi_2\delta\phi_1\,dr \\
& + \int_{r_0}^{\infty}\phi_1\phi_2 dr \int_{-\infty}^{0}\frac{d\psi_{z1}}{dz}\delta\psi_{r1}\,dz + \int_{r_0}^{\infty}\phi_2\phi_1 dr[\psi_{r1}\delta\psi_{z1}]_{-\infty}^{0} - \int_{r_0}^{\infty}\phi_1\phi_2 dr \int_{-\infty}^{0}\frac{d\psi_{r1}}{dz}\delta\psi_{z1}\,dz
\end{aligned}
$$

$$+\int_{-\infty}^{0}\psi_{r1}\frac{d\psi_{z1}}{dz}dz\int_{r_0}^{\infty}r\frac{d\phi_1}{dr}\delta\phi_2 dr+\int_{-\infty}^{0}\psi_{r1}\frac{d\psi_{z1}}{dz}dz[r\phi_2\delta\phi_1]_{r_0}^{\infty}-\int_{-\infty}^{0}\psi_{r1}\frac{d\psi_{z1}}{dz}dz\int_{r_0}^{\infty}\left(r\frac{d\phi_2}{dr}+\phi_2\right)\delta\phi_1 dr$$

$$+\int_{r_0}^{\infty}r\phi_2\frac{d\phi_1}{dr}dr\int_{-\infty}^{0}\frac{d\psi_{z1}}{dz}\delta\psi_{r1}dz+\int_{r_0}^{\infty}r\phi_2\frac{d\phi_1}{dr}dr[\psi_{r1}\delta\psi_{z1}]_{-\infty}^{0}-\int_{r_0}^{\infty}r\phi_2\frac{d\phi_1}{dr}dr\int_{-\infty}^{0}\frac{d\psi_{r1}}{dz}\delta\psi_{z1}dz\Bigg)$$

$$+2\pi G\Bigg(\int_{-\infty}^{0}\left(\frac{d\psi_{r1}}{dz}\right)^2dz\int_{r_0}^{\infty}r\phi_1\delta\phi_1 dr+\int_{r_0}^{\infty}r{\phi_1}^2dr\left[\frac{d\psi_{r1}}{dz}\delta\psi_{r1}\right]_{-\infty}^{0}-\int_{r_0}^{\infty}r{\phi_1}^2dr\int_{-\infty}^{0}\frac{d^2\psi_{r1}}{dz^2}\delta\psi_{r1}dz$$

$$+\int_{r_0}^{\infty}r\phi_1\frac{d\phi_2}{dr}dr[\psi_{z1}\delta\psi_{r1}]_{-\infty}^{0}-\int_{r_0}^{\infty}r\phi_1\frac{d\phi_2}{dr}dr\int_{-\infty}^{0}\frac{d\psi_{z1}}{dz}\delta\psi_{r1}dz+\int_{r_0}^{\infty}r\phi_1\frac{d\phi_2}{dr}dr\int_{-\infty}^{0}\frac{d\psi_{r1}}{dz}\delta\psi_{z1}dz$$

$$+\int_{-\infty}^{0}\psi_{z1}\frac{d\psi_{r1}}{dz}dz\int_{r_0}^{\infty}r\frac{d\phi_2}{dr}\delta\phi_1 dr+\int_{-\infty}^{0}\psi_{z1}\frac{d\psi_{r1}}{dz}dz[r\phi_1\delta\phi_2]_{r_0}^{\infty}-\int_{-\infty}^{0}\psi_{z1}\frac{d\psi_{r1}}{dz}dz\int_{r_0}^{\infty}\left(r\frac{d\phi_1}{dr}+\phi_1\right)\delta\phi_2 dr$$

$$+\int_{r_0}^{\infty}r\left(\frac{d\phi_2}{dr}\right)^2dr\int_{-\infty}^{0}\psi_{z1}\delta\psi_{z1}dz+\int_{-\infty}^{0}{\psi_{z1}}^2dz\left[r\frac{d\phi_2}{dr}\delta\phi_2\right]_{r_0}^{\infty}-\int_{0}^{\infty}{\psi_{z1}}^2dz\int_{r_0}^{\infty}\left(r\frac{d^2\phi_2}{dr^2}+\frac{d\phi_2}{dr}\right)\delta\phi_2 dr\Bigg)$$

$$+2\pi(\lambda+2G)\Bigg(\int_{r_0}^{\infty}r\left(\frac{d\phi_1}{dr}\right)^2dr\int_{0}^{\infty}\psi_{r2}\delta\psi_{r2}dz+\int_{0}^{\infty}{\psi_{r2}}^2dz\left[r\frac{d\phi_1}{dr}\delta\phi_1\right]_{r_0}^{\infty}$$

$$-\int_{0}^{\infty}{\psi_{r2}}^2dz\int_{r_0}^{\infty}\left(r\frac{d^2\phi_1}{dr^2}+\frac{d\phi_1}{dr}\right)\delta\phi_1 dr+\int_{r_0}^{\infty}\frac{{\phi_1}^2}{r}dr\int_{0}^{\infty}\psi_{r2}\delta\psi_{r2}dz+\int_{0}^{\infty}{\psi_{r2}}^2dz\int_{r_0}^{\infty}\frac{\phi_1}{r}\delta\phi_1 dr$$

$$+\int_{0}^{\infty}\left(\frac{d\psi_{z2}}{dz}\right)^2dz\int_{r_0}^{\infty}r\phi_2\delta\phi_2 dr+\int_{r_0}^{\infty}r{\phi_2}^2dr\left[\frac{d\psi_{z2}}{dz}\delta\psi_{z2}\right]_{0}^{\infty}-\int_{r_0}^{\infty}r{\phi_2}^2dr\int_{0}^{\infty}\frac{d^2\psi_{z2}}{dz^2}\delta\psi_{z2}dz\Bigg)$$

$$+2\pi\lambda\Bigg(2\int_{r_0}^{\infty}\phi_1\frac{d\phi_1}{dr}dr\int_{0}^{\infty}\psi_{r2}\delta\psi_{r2}dz+\int_{0}^{\infty}{\psi_{r2}}^2dz[\phi_1\delta\phi_1]_{r_0}^{\infty}-\int_{0}^{\infty}{\psi_{r2}}^2dz\int_{r_0}^{\infty}\frac{d\phi_1}{dr}\delta\phi_1 dr$$

$$+\int_{0}^{\infty}{\psi_{r2}}^2dz\int_{r_0}^{\infty}\frac{d\phi_1}{dr}\delta\phi_1 dr+\int_{0}^{\infty}\psi_{r2}\frac{d\psi_{z2}}{dz}dz\int_{r_0}^{\infty}\phi_1\delta\phi_2 dr+\int_{0}^{\infty}\psi_{r2}\frac{d\psi_{z2}}{dz}dz\int_{r_0}^{\infty}\phi_2\delta\phi_1 dr$$

$$+\int_{r_0}^{\infty}\phi_1\phi_2 dr\int_{0}^{\infty}\frac{d\psi_{z2}}{dz}\delta\psi_{r2}dz+\int_{r_0}^{\infty}\phi_2\phi_1 dr[\psi_{r2}\delta\psi_{z2}]_{0}^{\infty}-\int_{r_0}^{\infty}\phi_1\phi_2 dr\int_{0}^{\infty}\frac{d\psi_{r2}}{dz}\delta\psi_{z2}dz$$

$$+\int_{0}^{\infty}\psi_{r2}\frac{d\psi_{z2}}{dz}dz\int_{r_0}^{\infty}r\frac{d\phi_1}{dr}\delta\phi_2 dr+\int_{0}^{\infty}\psi_{r2}\frac{d\psi_{z2}}{dz}dz[r\phi_2\delta\phi_1]_{r_0}^{\infty}-\int_{0}^{\infty}\psi_{r2}\frac{d\psi_{z2}}{dz}dz\int_{r_0}^{\infty}\left(r\frac{d\phi_2}{dr}+\phi_2\right)\delta\phi_1 dr$$

$$+\int_{r_0}^{\infty}r\phi_2\frac{d\phi_1}{dr}dr\int_{0}^{\infty}\frac{d\psi_{z2}}{dz}\delta\psi_{r2}dz+\int_{r_0}^{\infty}r\phi_2\frac{d\phi_1}{dr}dr[\psi_{r2}\delta\psi_{z2}]_{0}^{\infty}-\int_{r_0}^{\infty}r\phi_2\frac{d\phi_1}{dr}dr\int_{0}^{\infty}\frac{d\psi_{r2}}{dz}\delta\psi_{z2}dz\Bigg)$$

$$+2\pi G\Bigg(\int_{0}^{\infty}\left(\frac{d\psi_{r2}}{dz}\right)^2dz\int_{r_0}^{\infty}r\phi_1\delta\phi_1 dr+\int_{r_0}^{\infty}r{\phi_1}^2dr\left[\frac{d\psi_{r2}}{dz}\delta\psi_{r2}\right]_{0}^{\infty}-\int_{r_0}^{\infty}r{\phi_1}^2dr\int_{0}^{\infty}\frac{d^2\psi_{r2}}{dz^2}\delta\psi_{r2}dz$$

$$+\int_{r_0}^{\infty} r\phi_1\frac{d\phi_2}{dr}dr[\psi_{z2}\delta\psi_{r2}]_0^{\infty} - \int_{r_0}^{\infty} r\phi_1\frac{d\phi_2}{dr}dr\int_0^{\infty}\frac{d\psi_{z2}}{dz}\delta\psi_{r2}dz + \int_{r_0}^{\infty} r\phi_1\frac{d\phi_2}{dr}dr\int_0^{\infty}\frac{d\psi_{r2}}{dz}\delta\psi_{z2}dz$$

$$+\int_0^{\infty}\psi_{z2}\frac{d\psi_{r2}}{dz}dz\int_{r_0}^{\infty} r\frac{d\phi_2}{dr}\delta\phi_1 dr + \int_0^{\infty}\psi_{z2}\frac{d\psi_{r2}}{dz}dz[r\phi_1\delta\phi_1]_{r_0}^{\infty} - \int_0^{\infty}\psi_{z2}\frac{d\psi_{r2}}{dz}dz\int_{r_0}^{\infty}\left(r\frac{d\phi_1}{dr}+\phi_1\right)\delta\phi_2 dr$$

$$+\int_{r_0}^{\infty} r\left(\frac{d\phi_2}{dr}\right)^2 dr\int_0^{\infty}\psi_{z2}\delta\psi_{z2}dz + \int_0^{\infty}{\psi_{z2}}^2 dz\left[r\frac{d\phi_2}{dr}\delta\phi_2\right]_{r_0}^{\infty} - \int_0^{\infty}{\psi_{z2}}^2 dz\int_{r_0}^{\infty}\left(r\frac{d^2\phi_2}{dr^2}+\frac{d\phi_2}{dr}\right)\delta\phi_2 dr\Bigg)$$

$$+2\pi(\lambda+2G)\Bigg(\int_0^{r_0} r\left(\frac{d\phi_3}{dr}\right)^2 dr\int_0^{\infty}\psi_{r2}\delta\psi_{r2}dz + \int_0^{\infty}{\psi_{r2}}^2 dz\left[r\frac{d\phi_3}{dr}\delta\phi_3\right]_0^{r_0}$$

$$-\int_0^{\infty}{\psi_{r2}}^2 dz\int_0^{r_0}\left(r\frac{d^2\phi_3}{dr^2}+\frac{d\phi_3}{dr}\right)\delta\phi_3 dr + \int_0^{r_0}\frac{{\phi_3}^2}{r}dr\int_0^{\infty}\psi_{r2}\delta\psi_{r2}dz + \int_0^{\infty}{\psi_{r2}}^2 dz\int_0^{r_0}\frac{\phi_3}{r}\delta\phi_3 dr$$

$$+\frac{{r_0}^2}{2}\left[\frac{d\psi_{z2}}{dz}\delta\psi_{z2}\right]_0^{\infty} - \frac{{r_0}^2}{2}\int_0^{\infty}\frac{d^2\psi_{z2}}{dz^2}\delta\psi_{z2}dz\Bigg)$$

$$+2\pi\lambda\Bigg(2\int_0^{r_0}\frac{d\phi_3}{dr}\phi_3 dr\int_0^{\infty}\psi_{r2}\delta\psi_{r2}dz + \int_0^{\infty}{\psi_{r2}}^2 dz[\phi_3\delta\phi_3]_0^{r_0} - \int_0^{\infty}{\psi_{r2}}^2 dz\int_0^{r_0}\frac{d\phi_3}{dr}\delta\phi_3 dr$$

$$+\int_0^{\infty}{\psi_{r2}}^2 dz\int_0^{r_0}\frac{d\phi_3}{dr}\delta\phi_3 dr + \int_0^{r_0} r\frac{d\phi_3}{dr}dr\int_0^{\infty}\frac{d\psi_{z2}}{dz}\delta\psi_{r2}dz + \int_0^{r_0} r\frac{d\phi_3}{dr}dr[\psi_{r2}\delta\psi_{z2}]_0^{\infty}$$

$$-\int_0^{r_0} r\frac{d\phi_3}{dr}dr\int_0^{\infty}\frac{d\psi_{r2}}{dz}\delta\psi_{z2}dz + \int_0^{\infty}\psi_{r2}\frac{d\psi_{z2}}{dz}dz[r\delta\phi_3]_0^{r_0} - \int_0^{\infty}\psi_{r2}\frac{d\psi_{z2}}{dz}dz\int_0^{r_0}\delta\phi_3 dr$$

$$+\int_0^{\infty}\psi_{r2}\frac{d\psi_{z2}}{dz}dz\int_0^{r_0}\delta\phi_3 dr + \int_0^{r_0}\phi_3 dr\int_0^{\infty}\frac{d\psi_{z2}}{dz}\delta\psi_{r2}dz + \int_0^{r_0}\phi_3 dr[\psi_{r2}\delta\psi_{z2}]_0^{\infty} - \int_0^{r_0}\phi_3 dr\int_0^{\infty}\frac{d\psi_{r2}}{dz}\delta\psi_{z2}dz\Bigg)$$

$$+2\pi G\Bigg(\int_0^{\infty}\left(\frac{d\psi_{r2}}{dz}\right)^2 dz\int_0^{r_0} r\phi_3\delta\phi_3 dr + \int_0^{r_0} r{\phi_3}^2 dr\left[\frac{d\psi_{r2}}{dz}\delta\psi_{r2}\right]_0^{\infty} - \int_0^{r_0} r{\phi_3}^2 dr\int_0^{\infty}\frac{d^2\psi_{r2}}{dz^2}\delta\psi_{r2}dz\Bigg)$$

$$-2\pi\int_{-\infty}^{0} q_1 r_0\delta\psi_{r1}dz - q_2\pi{r_0}^2\delta\psi_{z2} = 0 \tag{4.82}$$

4.9 Appendix B

The equilibrium conditions in the analysis are assessed in order to obtain an indicator of the reliability of the solution. Both the equilibrium in the radial direction and in the longitudinal direction are calculated using the following

$$\frac{\partial\sigma_{rr}}{\partial r} + \frac{\partial\tau_{zr}}{\partial r} + \frac{1}{r}(\sigma_{rr}-\sigma_{\theta\theta}) = 0 \tag{4.83}$$

$$\frac{\partial\tau_{zr}}{\partial r} + \frac{\partial\sigma_{zz}}{\partial z} + \frac{1}{r}\tau_{zr} = 0 \tag{4.84}$$

Figures 4.10a and 4.10b are normalised plots of the equilibrium in the radial and longitudinal directions respectively. Figure 4.10a shows the equilibrium in the radial direction along the longitudinal axis of the tunnel at $r = r_0$ (at the tunnel wall) and $r = 2r_0$. The unbalanced stresses appear to attain maxima in close proximity to the tunnel face as the error for $r = 2r_0$ is less significant than that at $r = r_0$. Figure 4.10b shows the equilibrium in the longitudinal direction at the tunnel face. Equilibrium is found to be satisfied everywhere apart from near the tunnel face, where stress singularity is expected.

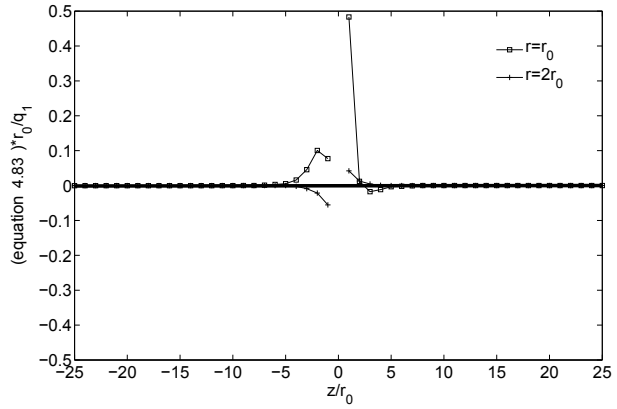

(a)

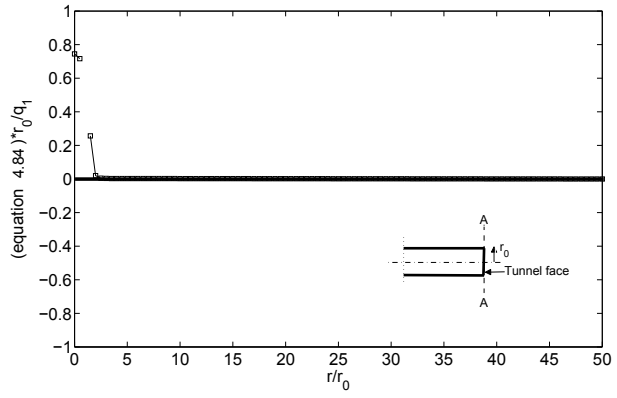

(b)

Figure 4.10: Equilibrium: (a) radial direction; (b) longitudinal direction

Chapter 5

Incorporation of viscoplastic constitutive behaviour

Synopsis

This chapter builds on the tools developed in Chapter 3, through the incorporation of time-dependent viscoplastic constitutive behaviour into the cavity equations, thus developing new models that can be used to analyse cavities located in creeping rock. The cavity pressure is applied incrementally to enable different rates of loading to be modelled, thus being able to approximate the rate of excavation of a cavity. Here we develop viscoplastic constitutive models within the framework of hyperplasticity, therefore ensuring that thermodynamic principles are adhered to. A novel contribution in this chapter is the development of a frictionless viscoplastic-damage constitutive model which is able to describe both the secondary and tertiary stages of creep behaviour (see Figure 2.1).

The first section of this chapter (5.1) focuses on the theory of viscoplasticity. Within this section the theory of rate-dependent hyperplasticity is described. Section 5.2 shows the derivation of the constitutive equations for a von Mises viscoplastic model using this thermodynamically consistent approach. The stress integration procedure for this model is described, followed by incorporation of the model into the cavity equations and validation using the von Mises rate-independent finite element (FE) results shown in Chapter 3. Section 5.3 focuses on a von Mises viscoplastic-damage model, stress integration of the model and incorporation into the cavity equations.

5.1 Viscoplasticity

The theory of viscoplasticity is similar to rate-independent plasticity in that we define an identical elastic law, yield function, hardening law and form of the flow rule (see Section 3.5.1). However, the crucial difference lies in the definition of the plastic consistency parameter $\dot{\gamma}$. When considering rate-independent plasticity in Chapter 3, $\dot{\gamma}$ was an unknown and therefore had to be solved for when determining the plastic strains. However when consider-

ing viscoplasticity an explicit function for $\dot{\gamma}$ can be derived. This function controls how the magnitude of plastic strain varies with the level of stress. Many forms have been proposed for $\dot{\gamma}$, with each form defining a different model of viscoplasticity [16].

An overview of viscoplasticity is provided in Section 2.2.1. Schematically viscoplastic behaviour can be represented by a plastic slider element placed in parallel with a viscous dashpot element (Figure 2.5). This is known collectively as a Bingham unit which is immobilised below a specified failure strength. If the slider is loaded above the failure strength plastic strain occurs and the rate of strain is controlled by the viscous element. Stresses outside the yield envelope are permissable, as the stress is shared by both the slider and the viscous element.

5.1.1 Rate-dependent hyperplasticity

In Chapter 3 Section 3.5.2 we introduced the theory of hyperplasticity for rate-independent materials. Here we present the theory for rate-dependent materials as shown in Houlsby and Puzrin [5]. The theory builds on that presented for rate-independent materials where the material response is the same irrespective of the strain rate and the dissipation potential $\dot{D}$ can be written as a homogeneous first-order function of the internal variable rate $\{\dot{\varepsilon}^p\}$, expressed through Euler's equation as

$$\dot{D} = \{\dot{D}_{,\dot{\varepsilon}^p}\}^T\{\dot{\varepsilon}^p\}. \tag{5.1}$$

Now when considering a rate-dependent material, the following can be defined

$$\nu = \frac{\dot{D}}{\{\dot{D}_{,\dot{\varepsilon}^p}\}^T\{\dot{\varepsilon}^p\}}. \tag{5.2}$$

By comparing equations 5.1 and 5.2 we can see that for a rate-independent material $\nu = 1$. For any dissipation potential $\dot{D}$ which is a homogeneous function of degree n in $\{\dot{\varepsilon}^p\}$, it follows from Euler's theorem that ν is a constant equal to $\frac{1}{n}$. Therefore equation 5.1 can be rewritten as

$$\dot{D} = \frac{1}{n}\{\dot{D}_{,\dot{\varepsilon}^p}\}^T\{\dot{\varepsilon}^p\}. \tag{5.3}$$

A dissipative stress vector can then be defined from the dissipation potential as follows

$$\{\chi\} = \frac{1}{n}\{\dot{D}_{,\dot{\varepsilon}^p}\}. \tag{5.4}$$

5.2 von Mises viscoplastic model

Here we derive the equations for a viscoplastic constitutive model within the hyperplastic framework, thus developing a model which is thermodynamically consistent. We assume that the plastic behaviour is governed by the von Mises yield criterion (deviatoric creep only), which is applicable to ductile rocks as stated in Chapter 3 [6] and has been used by Barla et al. [1] in the VIPLA viscoplastic model [9] to simulate the Saint Martin La Porte access adit, along the Lyon-Turin Base Tunnel. However, later in the chapter and in Chapter 6 more complex constitutive models will be developed using the hyperplastic framework.

For this derivation we will use the same free energy potential and elastic law as used for the rate-independent models in Chapter 3 (equations 3.113 and 3.114). The dissipation potential $\dot{D}$ can be defined as follows

$$\dot{D} = \sigma_y(\dot{\alpha}_s + \eta^{n-1}\dot{\alpha}_s^n), \tag{5.5}$$

where σ_y is the yield stress, η is the viscous coefficient which controls the extent of plastic strain, n is a material constant and $\dot{\alpha}_s$ is an internal variable representing the equivalent plastic strain rate defined by equation 3.120. This dissipation potential can be schematically represented by the Bingham unit (Figure 2.5) and is composed of two terms, the first term in the bracket representing the plastic slider element and the second term the viscous dashpot element. Note here that as $\eta \to 0$ the dissipation potential reduces to the rate-independent von Mises dissipation potential shown in equation 3.119.

We can write equation 5.5 in the following form

$$\dot{D} = \sigma_y(\dot{\alpha}_{s1} + \eta^{n-1}\dot{\alpha}_{s2}^n). \tag{5.6}$$

where $\dot{\alpha}_{s1}$ is the plastic strain rate in the plastic slider element and $\dot{\alpha}_{s2}$ is the plastic strain rate in the viscous dashpot element.

Differentiation of the dissipation potential with respect to the plastic strain rates gives the dissipative stress

$$\chi_q = \frac{\partial \dot{D}}{\partial \dot{\alpha}_{s1}} + \frac{1}{n}\frac{\partial \dot{D}}{\partial \dot{\alpha}_{s2}}, \tag{5.7}$$

where the first term is the stress dissipated in the plastic slider element as seen previously for the rate-independent von Mises model in Chapter 3 (equation 3.121) and the second term is the stress dissipated in the viscous dashpot element which introduces rate-dependency into this new model as derived in equation 5.4. Since the plastic slider element and the viscous dashpot element are in parallel the plastic strain rates in each must be equal and therefore $\dot{\alpha}_{s1} = \dot{\alpha}_{s2} = \dot{\alpha}_s$, therefore

$$\chi_q = \sigma_y(1 + (\eta\dot{\alpha}_s)^{n-1}). \tag{5.8}$$

Since there is no kinematic hardening, the true stress and the dissipative stress are identical as shown for the rate-independent model (equation 3.122)

$$\chi_q = q. \tag{5.9}$$

Manipulating the above stress expressions (equations 5.8 and 5.9) leads to the following equation

$$\left(\frac{q}{\sigma_y(1+(\eta\dot{\alpha}_s)^{n-1})}\right)^2 = 1. \tag{5.10}$$

Rearranging equation 5.10 we obtain

$$\dot{\alpha}_s = \frac{1}{\eta}\left(\frac{q}{\sigma_y} - 1\right)^{\frac{1}{n-1}}, \tag{5.11}$$

which is the explicit expression for the plastic consistency parameter and is the same as that derived by Perzyna [12] and [13], which is widely used in computational mechanics [16].

From equation 5.11 we can derive an equation which governs plastic behaviour. The plastic strain rate $\dot{\alpha}_s$ is a non negative quantity, therefore the expression inside the bracket in equation 5.11 must be greater than or equal to zero. Therefore the yield criterion is given by

$$f = \frac{q}{\sigma_y} - 1. \tag{5.12}$$

As for the rate-independent von Mises model the plastic strain components can be expressed as follows using an associated flow rule

$$\{\dot{\varepsilon}^p\} = \dot{\gamma}\{f_{,\sigma}\}, \tag{5.13}$$

where $\dot{\gamma}$ is equal to the equivalent plastic strain rate $\dot{\alpha}_s$ defined by equation 5.11 and where

$$\{f_{,\sigma}\} = \frac{3}{2}\frac{\{s\}}{q}. \tag{5.14}$$

5.2.1 Stress integration and response of the constitutive model

Here we adopt an implicit backward Euler (bE) stress integration scheme as outlined in Section 3.5.4. As for the von Mises constitutive model shown in Chapter 3, here we assume linear isotropic hardening of the yield surface. For a strain and time increment, $\{\Delta\varepsilon\}$ and Δt, over $[t_n, t_{n+1}]$ and the state variables at t_n ($\{\varepsilon^e_n\}$ and σ_{yn}), we can obtain the updated stress vector $\{\sigma_{n+1}\}$ and yield stress σ_{yn+1} when the yield criterion f is greater than zero by solving the following system of non linear equations (equation 5.15). Note that these equations are the same as those for the rate-independent case (equation 3.154), but here $\Delta\gamma$ is no longer

an unknown, as we have an explicit expression for this parameter, therefore this system only contains two equations. Note that $\Delta\gamma = \Delta t\dot{\gamma}$.

$$\Big\{b\Big\} = \begin{Bmatrix} \{\sigma\} - [D^e]\{\varepsilon_t^e\} + [D^e]\Delta\gamma\{f_{,\sigma}\} \\ \sigma_y - \sigma_{yt} - \Delta\gamma H \end{Bmatrix} = \begin{Bmatrix} \{b_1\} \\ b_2 \end{Bmatrix}. \tag{5.15}$$

We can express the Hessian matrix (equation 3.150) as follows from the derivative of the residuals with respect to the unknowns

$$\Big[A\Big] = \begin{bmatrix} [I] + \Delta\gamma[f_{,\sigma\sigma}][D^e] + \{f_{,\sigma}\}\{\Delta\gamma_{,\sigma}\}^T[D^e] & [D^e]\{f_{,\sigma}\}\Delta\gamma_{,\sigma_y} \\ -H\{\Delta\gamma_{,\sigma}\}^T & 1 - H\Delta\gamma_{,\sigma_y} \end{bmatrix}. \tag{5.16}$$

We can then follow the same iterative solution procedure as described in Section 3.5.4 for the general elasto-plastic model. The starting conditions for the algorithm are

$$\{\sigma\} = \{\sigma_t\}, \quad \{\sigma_y\} = \{\sigma_{yt}\} \quad \Delta\gamma = \Delta\gamma_t. \tag{5.17}$$

where $\Delta\gamma_t$ is a trial value of the plastic consistency parameter.

This constitutive model was programmed using MATLAB 7.9.0 for a single material point. Three types of simulation were carried out; a creep test (stress held constant with time), a relaxation test (strain held constant with time) and a test in which different rates of loading are applied (constant increase of strain with time). Here we assume for simplification that no hardening of the yield surface takes place ($H = 0$). An investigation was carried out into the effect of the material parameters n and η and the results are shown in Figures 5.1-5.3. The material parameters used in these analyses are $G = 1000$MPa, $\nu = 0.2$, $\sigma_y = 15$MPa, $n = 1.5$ and $\eta = 1000$MPa, unless otherwise stated. A time step Δt of 0.05 was also used.

Note that the results of these simulations are shown in terms of equivalent stress q and equivalent strain ε_q. The equivalent strain can be defined as

$$\varepsilon_q = \sqrt{\frac{2}{3}\mathrm{tr}([e][e])}, \tag{5.18}$$

where $[e] = [\varepsilon] - \varepsilon_v[1]/3$ is the deviatoric strain, where the volumetric strain is $\varepsilon_v = \mathrm{tr}([\varepsilon])$.

The results of the creep test are shown in Figure 5.1. Here we applied increments of strain (total strain $\varepsilon = \{-0.1, 0.1, 0\}$ applied over 100 load steps) until the yield function f was greater than zero. We then held the stress constant with time, shown in Figure 5.1a. It is important to note here that the shape of the strain-time response shown in Figures 5.1b and 5.1c is the same as the secondary stage of the typical three stage creep curve commonly observed in laboratory creep testing (Figure 2.1). Figure 5.1b shows that when n is increased, the strain rate increases, while Figure 5.1c shows that an increase in η causes a decrease in

strain rate.

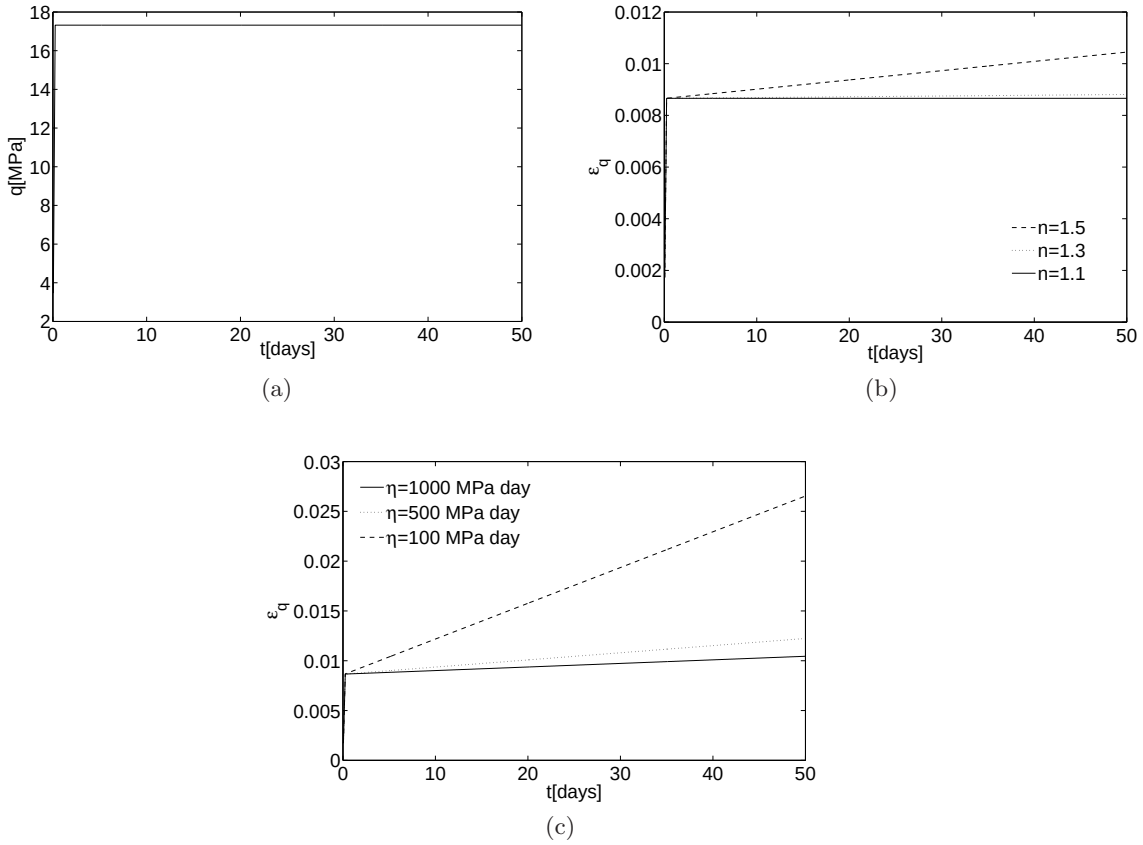

Figure 5.1: Creep simulation: (a) stress held constant with time; (b) effect of n on strain-time response; (c) effect of η on strain-time response

The results of the relaxation test are shown in Figure 5.2. Here we applied a total strain $\varepsilon = \{-0.01, 0.01, 0\}$ over 200 load steps. We then held the strain constant with time, shown in Figure 5.2a. Figures 5.2b and 5.2c show that as time passes, the stress relaxes and tends towards the yield stress σ_y of 15 MPa. Figure 5.2b shows that the larger the value of n, the more quickly the stresses relax, whilst Figure 5.2c shows that an increase in η causes the stresses to relax more slowly.

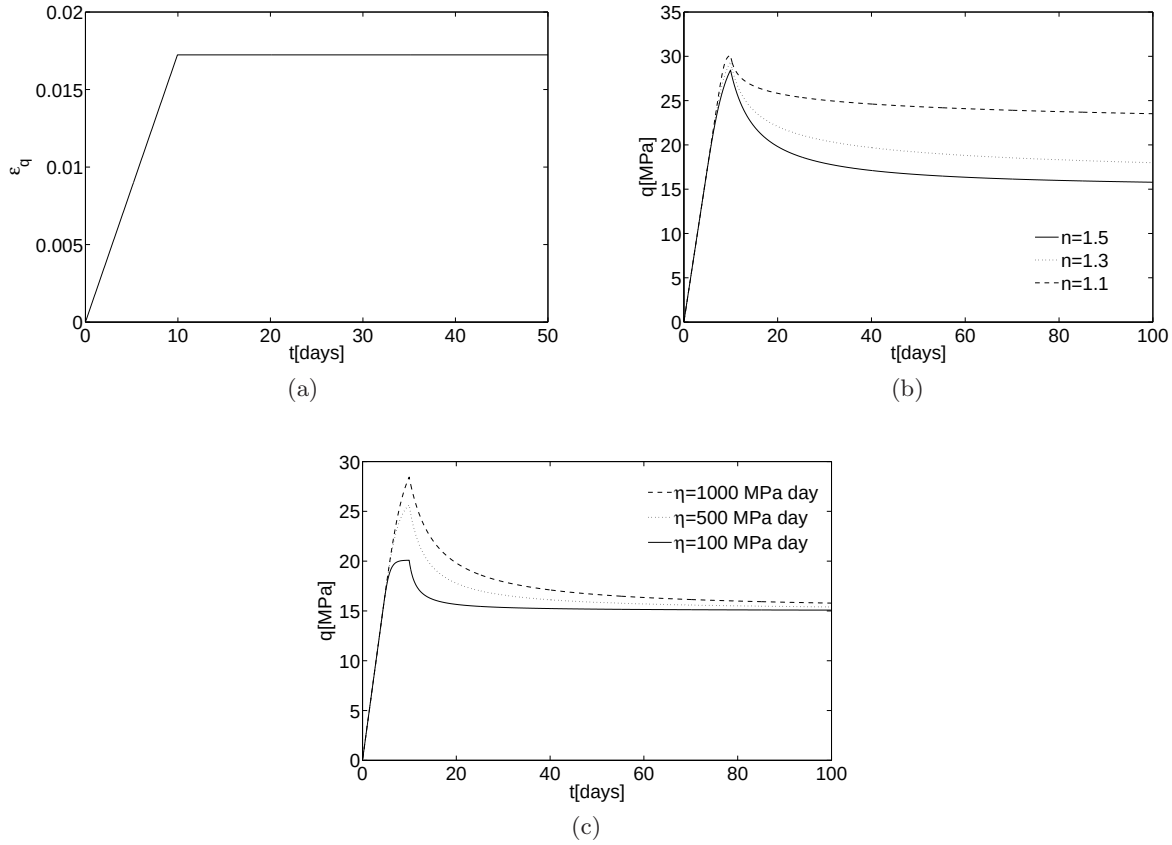

Figure 5.2: Relaxation simulation: (a) strain held constant with time; (b) effect of n on stress-time response; (c) effect of η on stress-time response

The results for a constant rate of loading are shown in Figure 5.3. As for the relaxation simulation we applied a total strain $\varepsilon = \{-0.01, 0.01, 0\}$ over different periods of time, thus simulating different rates of loading. The rate of loading used in the analyses shown here is $\dot{\varepsilon}$ =1.7x10^{-4}days^{-1}, unless otherwise stated. Figure 5.3a shows that an increase in the rate of loading results in a larger stress. Figure 5.3b shows that an increase in n causes an increase in stress, whilst Figure 5.3c shows that an increase in η causes an increase in stress.

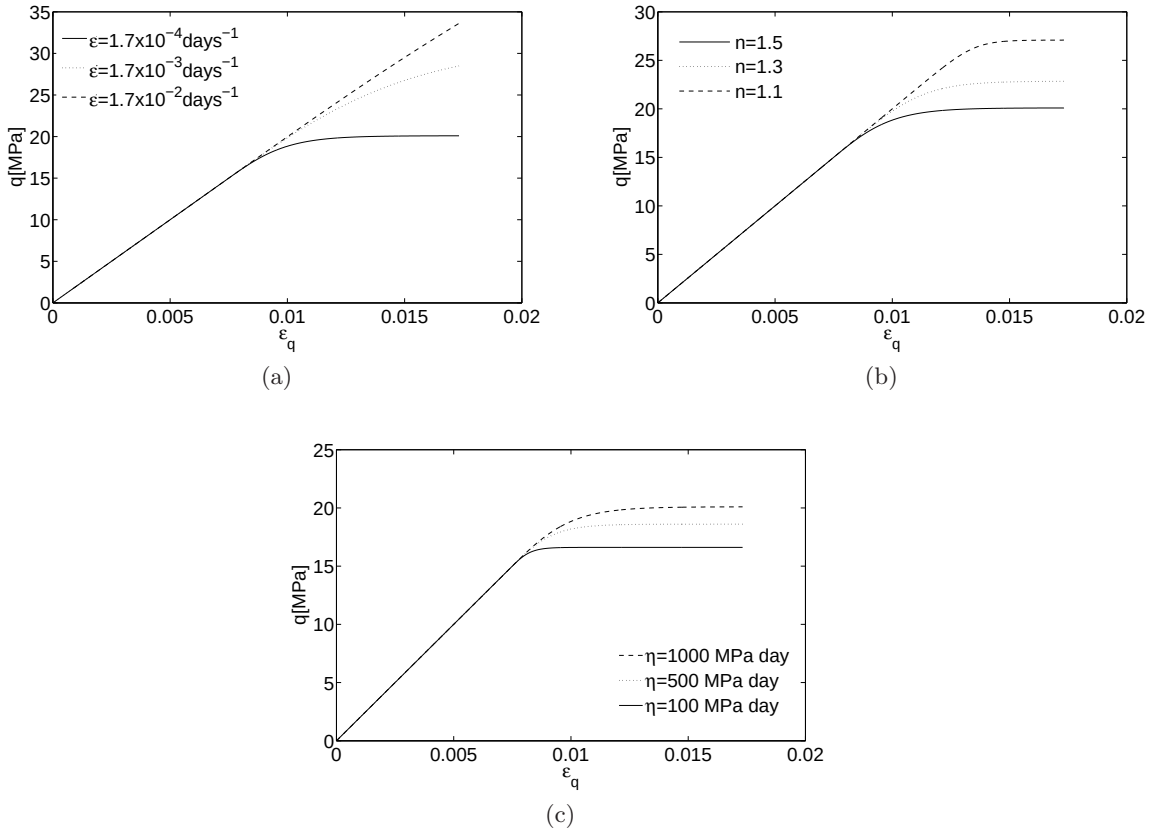

Figure 5.3: Constant rate of loading: (a) effect of rate of loading on stress-strain response; (b) effect of n on stress-strain response; (c) effect of η on stress-strain response

5.2.2 Modelling cavity in a viscoplastic medium

We now demonstrate how this viscoplastic model can be incorporated into the energy-based method for an internally pressurised two-dimensional (2D) cylindrical cavity. The same cavity problem is used here as in Chapter 3 (Figure 3.15). In fact the same governing equation and boundary conditions derived in Chapter 3 are used here. The only difference is the method of loading the cavity. Whilst in Chapter 3 we applied the full load to the cavity wall instantaneously, here we produce a model where the total load is applied in increments over time, to the cavity wall. This allows us to simulate different rates of loading, thus providing an approximation to the excavation of an underground cavity. The governing equation (equation 5.19) is expressed in terms of increments of displacement Δu_r and the boundary conditions (equations 5.21 and 5.22) expressed in terms of the cumulative stress increments as follows

$$r\frac{d^2\Delta u_r}{dr^2}+\frac{d\Delta u_r}{dr}-\frac{\Delta u_r}{r}=F\left(\Delta\varepsilon^p_{rr};\Delta\varepsilon^p_{\theta\theta};\Delta\varepsilon^p_{zz}\right) \tag{5.19}$$

$$F\left(\Delta\varepsilon^p_{rr};\Delta\varepsilon^p_{\theta\theta};\Delta\varepsilon^p_{zz}\right)=r\frac{d\Delta\varepsilon^p_{rr}}{dr}+\frac{\lambda}{(\lambda+2G)}\left(r\frac{d\Delta\varepsilon^p_{\theta\theta}}{dr}+r\frac{d\Delta\varepsilon^p_{zz}}{dr}\right)+\frac{2G}{(\lambda+2G)}(\Delta\varepsilon^p_{rr}-\Delta\varepsilon^p_{\theta\theta}) \tag{5.20}$$

Boundary condition at $r=r_0$

$$\lambda\left(\varepsilon^e_{rrj}+\frac{d\Delta u_r}{dr}-\Delta\varepsilon^p_{rr}+\varepsilon^e_{\theta\theta j}+\frac{\Delta u_r}{r}-\Delta\varepsilon^p_{\theta\theta}+\varepsilon^e_{zzj}-\Delta\varepsilon^p_{zz}\right)+2G\left(\varepsilon^e_{rrj}+\frac{d\Delta u_r}{dr}-\Delta\varepsilon^p_{rr}\right) \tag{5.21}$$
$$+\frac{p_i(j+1)}{totj}=0$$

and at $r=r_m$

$$\lambda\left(\varepsilon^e_{rrj}+\frac{d\Delta u_r}{dr}-\Delta\varepsilon^p_{rr}+\varepsilon^e_{\theta\theta j}+\frac{\Delta u_r}{r}-\Delta\varepsilon^p_{\theta\theta}+\varepsilon^e_{zzj}-\Delta\varepsilon^p_{zz}\right)+2G\left(\varepsilon^e_{rrj}+\frac{d\Delta u_r}{dr}-\Delta\varepsilon^p_{rr}\right)=0 \tag{5.22}$$

where j refers to the previous load step, the elastic strain terms (e.g. ε^e_{rrj}) refer to the elastic strains at the end of the previous load step and the Δ terms (e.g. Δu_r, $\Delta\varepsilon^p_{rr}$) refer to the increment of displacement and increment of plastic strain respectively during the current load step. $totj$ is the total number of load steps.

The following flowchart (Figure 5.4) provides an overview of the solution procedure. In box 1 of Figure 5.4 we apply an increment of pressure Δp_i over an increment of time Δt to the cavity wall. We then calculate the incremental cavity displacements Δu_r by solving the governing equation (equation 5.19) with the boundary conditions (equations 5.21 and 5.22) using a 1D finite difference (FD) technique (box 2). The change in displacements is then converted to a change in elastic strains, and the elastic trial strains $\{\varepsilon^e_t\}$ are calculated by adding the change in elastic strains to the total elastic strains found at the end of the previous load increment (box 3). The trial strains are then converted to trial stresses $\{\sigma_t\}$ using the elastic law (box 3). Here we assume the material is yielding ($f>0$), therefore we must use the bE stress integration procedure outlined earlier in this chapter to update the stresses, plastic strains and yield stress for each plastic material point (box 4). The parameters in equations 5.19-5.22 are then updated and we return to box 2. We must iterate within each load step (boxes 2-5) until the relative error in displacements at the cavity wall between two consecutive iterations is within a specified tolerance (0.001) (box 5). Once this tolerance is met the elastic strains in equations 5.21 and 5.22 are updated and the next load step is applied in box 1. When

the full load has been applied to the cavity wall, we continue looping through boxes 2 to 5, but the load at the cavity wall remains constant as time increases. This procedure continues until the total desired time is reached.

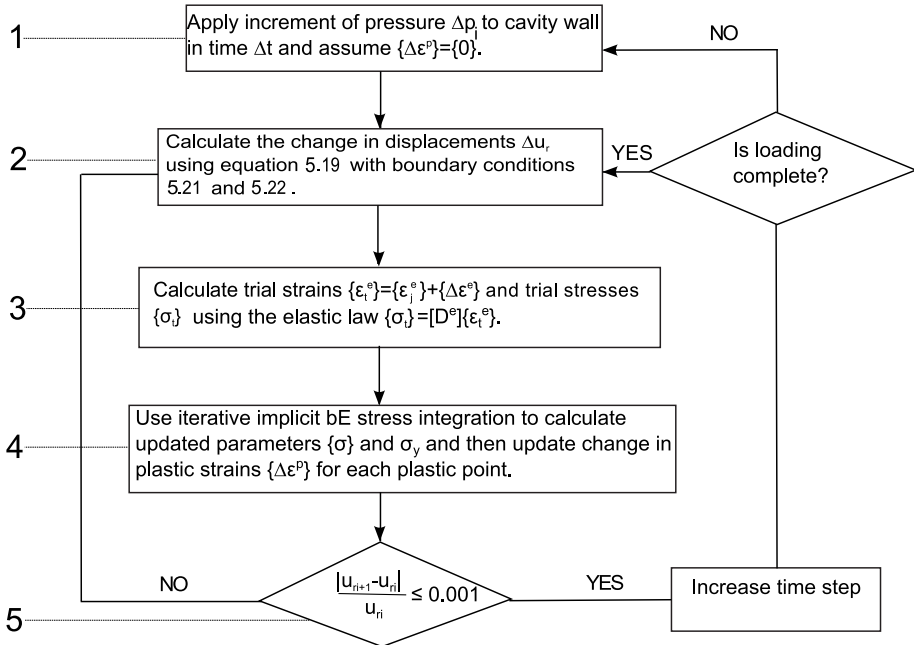

Figure 5.4: Flowchart of solution procedure when yield criterion $f > 0$

5.2.3 Validating the viscoplastic response of the cavity

The model parameters used in the analyses presented here are the same as those used for the von Mises model in Section 3.6.3, with additional parameters $n = 1.5$ and $\Delta t = 0.05$. A pressure p_i of 25 MPa is used here. The proposed solution is validated by comparing the displacements and stresses of the cavity with the FE time-independent perfectly plastic solution as seen in Section 3.6.3. This solution is a limit for the viscoplastic model as $t \to \infty$ or as $\eta \to 0$. This same limit was used in Fritz's viscoplastic analytical solution [3] for a cylindrical cavity, shown in Yu [20]. Figures 5.5 and 5.6 show that the time-independent displacement and stresses of the FE solution are approached as t increases and as η decreases. It has been found that the relative error between the time-dependent and time-independent displacement as $t \to \infty$ or as $\eta \to 0$ is no greater than a few percent. Figure 5.5 also shows two different rates of cavity loading. We see that the higher the rate of the loading, the smaller the cavity response once the full load has been applied.

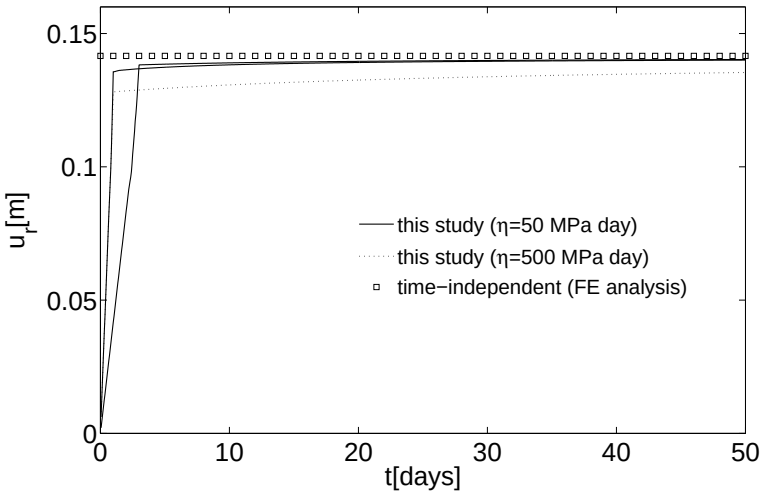

Figure 5.5: Variation of cavity wall displacement with time

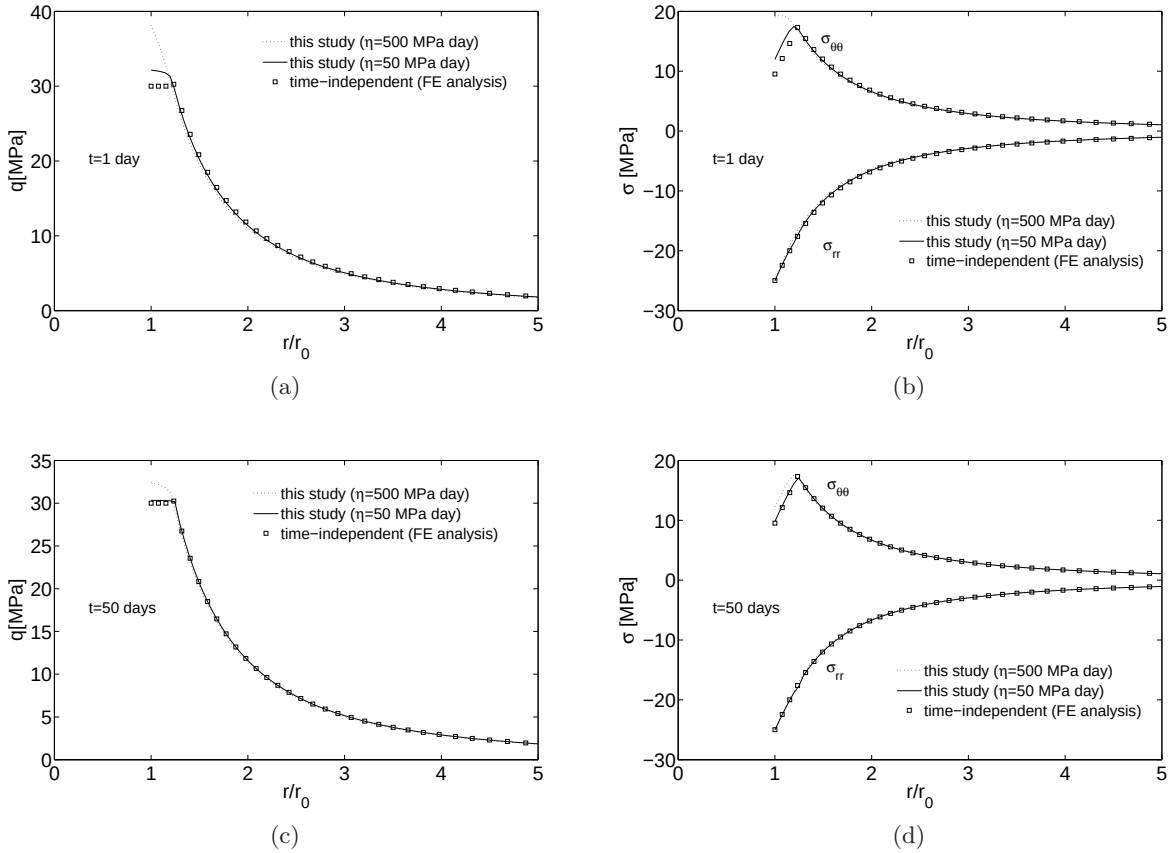

Figure 5.6: Variation of stresses with radial distance at different values of time: (a) q at end of loading stage ($t = 1$); (b) σ_{rr} and $\sigma_{\theta\theta}$ at end of loading stage ($t = 1$); (c) q at $t = 50$; (d) σ_{rr} and $\sigma_{\theta\theta}$ at $t = 50$

5.3 von Mises viscoplastic-damage model

Here we extend the viscoplastic constitutive model derived in the previous section to take into account material damage. This allows us to model the tertiary stage of creep behaviour

(Figure 2.1) which appears due to progressive micro cracking of the material. This results in a loss of strength and stiffness, which may eventually lead to failure corresponding to a complete loss of load carrying capability of the material. Here we use the theory of continuum damage mechanics (CDM) which was pioneered by Kachanov [7], who introduced a scalar internal variable to model the creep failure of metals under uniaxial loads. Other significant contributions to this theory were made by Lemaitre and Chaboche [8], amongst others. Here we express CDM within the framework of hyperplasticity, thus encompassing viscoplasticity and damage within a single theory. The evolution of the damage variable is derived from a dissipation potential, thus no separate evolution law is required. For simplification we assume that the damage is isotropic, and thus is defined using a scalar damage parameter. We also assume that the viscoplasticity and damage are coupled, thus they always occur simultaneously.

5.3.1 Material damage using the theory of hyperplasticity

In this section we demonstrate how material damage can be modelled using the hyperplastic framework. In Section 3.5.2 the free energy potential for an elasto-plastic model is a function of the total strains and plastic strains. Now when considering damage the free energy potential is also a function of α_d, the internal variable representing the damage parameter such that $\psi(\{\varepsilon\}, \{\varepsilon^p\}, \alpha_d) = \psi(\{\varepsilon^e\}, \alpha_d)$. This damage parameter was given physical significance by Rabotnov [14] who proposed the reduction of the undamaged cross-sectional area of the material as a suitable measure of the state of internal damage. This can be expressed as follows [2]

$$\alpha_d = \frac{A - A_s}{A} \tag{5.23}$$

where A is the total cross-sectional area of a surface within a unit cell in one of the three perpendicular directions and A_s is the solid matrix area within A. $\alpha_d = 0$ corresponds to the undamaged virgin material and $\alpha_d = 1$ represents a total loss of load bearing capacity. A schematic illustration of material damage is shown in Figure 5.7. This figure shows a sample of material in which cracks have developed due to material damage.

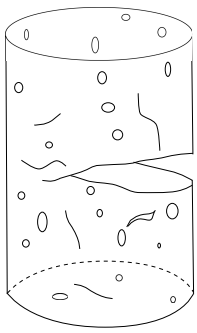

Figure 5.7: Schematic illustration of damage

Given the free energy potential stated above the rate of the free energy potential can now be

defined as follows

$$\dot{\psi} = \{\psi_{,\varepsilon^e}\}^T\{\dot{\varepsilon}^e\} + \psi_{,\alpha_d}\dot{\alpha}_d. \tag{5.24}$$

The dissipation potential is taken to be $\dot{D}(\{\varepsilon\}, \{\varepsilon^p\}, \{\dot{\varepsilon}^p\}, \alpha_d, \dot{\alpha}_d)$ which is now a function of the damage parameter and the rate of the damage parameter. For a rate-independent elasto-plastic-damage model we can write the dissipation potential as follows

$$\dot{D} = \{\dot{D}_{,\dot{\varepsilon}^p}\}^T\{\dot{\varepsilon}^p\} + \dot{D}_{,\dot{\alpha}_d}\dot{\alpha}_d. \tag{5.25}$$

Substitution of equations 5.24 and 5.25 into the expression for the first and second laws of thermodynamics (equation 3.104) produces the following

$$\{\sigma\}^T\{\dot{\varepsilon}\} = \{\psi_{,\varepsilon^e}\}^T\{\dot{\varepsilon}^e\} + \psi_{,\alpha_d}\dot{\alpha}_d + \{\dot{D}_{,\dot{\varepsilon}^p}\}^T\{\dot{\varepsilon}^p\} + \dot{D}_{,\dot{\alpha}_d}\dot{\alpha}_d. \tag{5.26}$$

From this equation we can define the elasticity law, which is identical to equation 3.108 and a dissipative stress vector identical to equation 3.109. Therefore

$$\{\sigma\}^T\{\dot{\varepsilon}\} = \{\sigma\}^T\{\dot{\varepsilon}^e\} + \psi_{,\alpha_d}\dot{\alpha}_d + \{\chi\}^T\{\dot{\varepsilon}^p\} + \dot{D}_{,\dot{\alpha}_d}\dot{\alpha}_d. \tag{5.27}$$

Substituting $\{\dot{\varepsilon}^e\} = \{\dot{\varepsilon}\} - \{\dot{\varepsilon}^p\}$ into equation 5.27 produces the following

$$\{\sigma\}^T\{\dot{\varepsilon}\} = \{\sigma\}^T\{\dot{\varepsilon}\} - \{\sigma\}^T\{\dot{\varepsilon}^p\} + \psi_{,\alpha_d}\dot{\alpha}_d + \{\chi\}^T\{\dot{\varepsilon}^p\} + \dot{D}_{,\dot{\alpha}_d}\dot{\alpha}_d. \tag{5.28}$$

Thus from equation 5.28 we can write

$$(\{\sigma\} - \{\chi\})^T\{\dot{\varepsilon}^p\} = 0, \tag{5.29}$$

$$(\bar{\chi}_d - \chi_d)\dot{\alpha}_d = 0, \tag{5.30}$$

where

$$\bar{\chi}_d = -\psi_{,\alpha_d} \quad \text{and} \quad \chi_d = \dot{D}_{,\dot{\alpha}_d}, \tag{5.31}$$

where $\bar{\chi}_d$ is a generalised damage stress and χ_d is the dissipative stress due to damage. Following Ziegler's orthogonality condition [21]

$$\bar{\chi}_d = \chi_d, \tag{5.32}$$

and the true stress is equal to the dissipative stress when there is no kinematic hardening of the yield surface (equation 3.112)

$$\{\sigma\} = \{\chi\}. \tag{5.33}$$

As shown in Section 3.5.2 the elasticity law and the dissipative stress can be used as the building blocks for the development of a constitutive model using the theory of hyperplasticity. In a similar way we will now use the elasticity law (equation 3.108), the dissipative stress due to plasticity (equation 3.109), the dissipative stress due to damage and the generalised damage stress (equation 5.31) as the building blocks for a new constitutive model which incorporates damage. We will now show the development of this constitutive model in the following section.

5.3.2 Viscoplastic-damage constitutive equations

A free energy potential can be written for a damaged material as follows

$$\psi = \frac{1}{2}\{\varepsilon^e\}^T(1-\alpha_d)[D^e]\{\varepsilon^e\}. \tag{5.34}$$

Differentiating the free energy potential with respect to the elastic strain vector produces the elasticity law (equation 3.108)

$$\{\sigma\} = \{\psi_{,\varepsilon^e}\} = (1-\alpha_d)[D^e]\{\varepsilon^e\}. \tag{5.35}$$

The free energy potential (equation 5.34) can be expressed as follows in terms of deviatoric and mean stresses

$$\psi = \frac{q^2}{6G(1-\alpha_d)} + \frac{p^2}{2K(1-\alpha_d)}. \tag{5.36}$$

The generalised damage stress can be derived from the free energy potential as follows using equation 5.31

$$\bar{\chi}_d = -\frac{\partial\psi}{\partial\alpha_d} = \frac{q^2}{6G(1-\alpha_d)^2} + \frac{p^2}{2K(1-\alpha_d)^2}. \tag{5.37}$$

The dissipation potential we use here is based on a coupled elasto-plastic-damage model proposed by Einav et al. [2]. His work included the development of rate-independent elasto-plastic-damage models. Einav et al. [2] stated that a decoupled form of the dissipation potential could be used as shown in equation 5.25. As noted by Einav et al. [2] adopting decoupled dissipation for elasto-plastic-damage models may result in damage prior to plastic straining, or plastic straining prior to damage. Coupling plasticity and damage ensures that they occur simultaneously. Einav et al. [2] proposed the following equation for a general coupled dissipation potential

$$\dot{D} = \sqrt[\bar{n}]{\sum_{i=1}^{N}[c_i(\{\varepsilon\},\bar{A})\Phi_i(\dot{\alpha}_i)]^{\bar{n}}}, \tag{5.38}$$

where $c_i(\{\varepsilon\},\bar{A})$ is a positive definite function, $\Phi_i(\alpha_i)$ is a homogeneous first order function

operator returning a positive scalar, $\bar{A}$ is a function of a set of internal variables, $\bar{A}(\alpha_1, ..., \alpha_N)$ and $\bar{n}$ is a parameter which controls the coupling intensity.

For a viscoplastic-damage constitutive model we have two internal variables, the damage parameter α_d and the equivalent plastic strain α_s. Thus $N = 2$ in equation 5.38 and the coupled dissipation potential is the sum of two components, one describing the viscoplastic behaviour and the other describing the damage behaviour. Einav et al. [2] developed coupled elasto-plastic-damage models within the framework of hyperplasticity and the form of the dissipation potential we propose below reduces to the form given by Einav et al. [2] when modelling a rate-independent von Mises material.

For a coupled viscoplastic-damage material the dissipation potential $\dot{D}$ is similar to equation 5.5 but now includes an additional damage term.

$$\dot{D} = \sigma_y \sqrt{(r_p \dot{\alpha}_s + r_p \eta^{n-1} \dot{\alpha}_s^n)^2 + (r_d \rho \dot{\alpha}_d)^2} \tag{5.39}$$

where r_p and r_d are constants governing the ratio of viscoplasticity and damage, $\sigma_y = \sigma_{y0}\Pi(\alpha_d)$, where σ_{y0} is the initial yield stress and $\Pi(\alpha_d) = (1 - \alpha\alpha_d)$, where α is the softening/hardening parameter. $\rho = \frac{\bar{X}_d}{q}$ and thus using equation 5.37 can be written as

$$\rho = \frac{q}{6G(1-\alpha_d)^2} + \frac{p^2}{2qK(1-\alpha_d)^2}. \tag{5.40}$$

α produces a more flexible model and allows hardening to be incorporated when a negative value of α is used. This parameter was also used by Shao et al. [15] to describe material damage when modelling creeping rocks. The effect of α on the stress-strain curve is shown below in Figure 5.8.

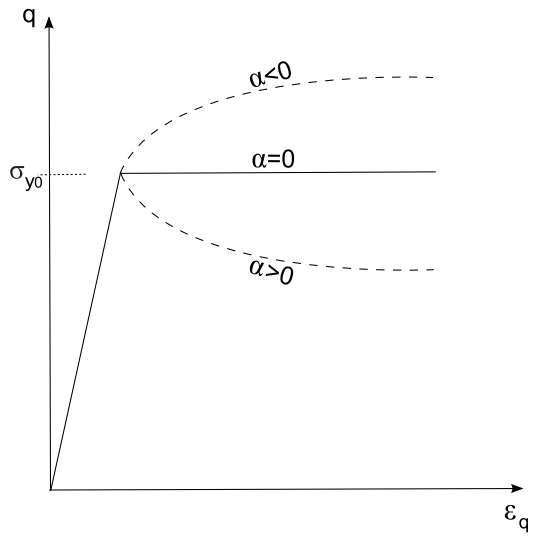

Figure 5.8: Effect of the softening/hardening parameter α on the stress-strain response

Having now defined the dissipation potential for a viscoplastic-damage material we can now follow a similar method to that used to develop the viscoplastic constitutive model in Section 5.2.

We can write equation 5.39 in the following form

$$\dot{D} = \sigma_y \sqrt{(r_p \dot{\alpha}_{s1} + r_p \eta^{n-1} \dot{\alpha}_{s2}^n)^2 + (r_d \rho \dot{\alpha}_d)^2} \tag{5.41}$$

Differentiation of the dissipation potential with respect to the plastic strain rates gives the dissipative stress, due to plasticity

$$\chi_q = \frac{\partial \dot{D}}{\partial \dot{\alpha}_{s1}} + \frac{1}{n} \frac{\partial \dot{D}}{\partial \dot{\alpha}_{s2}}. \tag{5.42}$$

However, $\dot{\alpha}_{s1} = \dot{\alpha}_{s2} = \dot{\alpha}_s$, therefore

$$\chi_q = \frac{\sigma_y (r_p \dot{\alpha}_s + r_p \eta^{n-1} \dot{\alpha}_s^n) r_p (1 + (\eta \dot{\alpha}_s)^{n-1})}{\sqrt{(r_p \dot{\alpha}_s + r_p \eta^{n-1} \dot{\alpha}_s^n)^2 + (r_d \rho \dot{\alpha}_d)^2}}. \tag{5.43}$$

Differentiating with respect to $\dot{\alpha}_d$ gives the dissipative stress due to damage (equation 5.31)

$$\chi_d = \frac{\partial \dot{D}}{\partial \dot{\alpha}_d} = \frac{\sigma_y \dot{\alpha}_d (r_d \rho)^2}{\sqrt{(r_p \dot{\alpha}_s + r_p \eta^{n-1} \dot{\alpha}_s^n)^2 + (r_d \rho \dot{\alpha}_d)^2}}. \tag{5.44}$$

Since there is no kinematic hardening, the true stress and the dissipative stress are identical as shown in equation 5.9.

Manipulating the above stress expressions (equations 5.43 and 5.44), leads to the following equation

$$\left(\frac{\chi_q}{\sigma_y r_p (1 + (\eta \dot{\alpha}_s)^{n-1})} \right)^2 + \left(\frac{\chi_d}{r_d \sigma_y \rho} \right)^2 = 1. \tag{5.45}$$

Substitution of $\rho = \frac{\bar{\chi}_d}{q}$ into this equation and using equations 5.9 and 5.32 produces the following

$$\left(\frac{q}{\sigma_y r_p (1 + (\eta \dot{\alpha}_s)^{n-1})} \right)^2 + \left(\frac{q}{r_d \sigma_y} \right)^2 = 1. \tag{5.46}$$

Rearranging equation 5.46 we obtain

$$\dot{\alpha}_s = \frac{1}{\eta} \left(\frac{1}{\sqrt{\left(\frac{\sigma_y r_p}{q} \right)^2 - \left(\frac{r_p}{r_d} \right)^2}} - 1 \right)^{\frac{1}{n-1}}, \tag{5.47}$$

which is equal to the plastic consistency parameter $\dot{\gamma}$.

From equation 5.47 we can derive an equation which governs plastic behaviour. The plastic strain rate $\dot{\alpha}_s$ is a non negative quantity, therefore the expression inside the bracket in equation 5.47 must be greater than or equal to zero. Therefore the yield criterion is given by

$$f = \left(\frac{q}{\sigma_y}\right)^2 \left(\frac{1}{r_p^2} + \frac{1}{r_d^2}\right) - 1. \tag{5.48}$$

From this equation we can find that the constants r_p and r_d are related by the following expression

$$\frac{1}{r_p^2} + \frac{1}{r_d^2} = 1, \tag{5.49}$$

from which it follows that $r_p \geq 1$ and $r_d \geq 1$. In the limiting case when $r_p = 1$, $r_d \to \infty$ and the constitutive model simplifies to the viscoplastic model derived in Section 5.2.

An expression for the rate of the damage internal variable can be found from equations 5.43 and 5.44 using $\rho = \frac{\bar{X}_d}{q}$, along with equations 5.9 and 5.32

$$\dot{\alpha}_d = \frac{\dot{\alpha}_s(1 + (\eta\dot{\alpha}_s)^{n-1})^2}{\rho} \left(\frac{r_p}{r_d}\right)^2. \tag{5.50}$$

The plastic strain components can then be expressed as follows using an associated flow rule

$$\{\dot{\varepsilon}^p\} = \dot{\gamma}\{f_{,\sigma}\}, \tag{5.51}$$

where $\{f_{,\sigma}\}$ is defined in equation 5.14.

5.3.3 Stress integration and response of the constitutive model

For a strain and time increment, $\{\Delta\varepsilon\}$ and Δt, over $[t_n, t_{n+1}]$ and the state variables at t_n ($\{\varepsilon_n^e\}$ and α_{dn}), we can obtain the updated stress vector $\{\sigma_{n+1}\}$ and damage parameter α_{dn+1} when the yield criterion f is greater than zero by solving the following system of non linear equations (equation 5.52).

$$\left\{b\right\} = \begin{Bmatrix} \{\sigma\} - (1-\alpha_d)[D^e]\{\varepsilon_t^e\} + (1-\alpha_d)[D^e]\Delta\gamma\{f_{,\sigma}\} \\ \alpha_d - \alpha_{dt} - \Delta\alpha_d \end{Bmatrix} = \begin{Bmatrix} \{b_1\} \\ b_2 \end{Bmatrix}. \tag{5.52}$$

We can express the Hessian matrix as follows

$$\Big[A\Big] =$$

$$\begin{bmatrix} [I] + (1-\alpha_d)\Delta\gamma[f_{,\sigma\sigma}][D^e] + (1-\alpha_d)\{f_{,\sigma}\}\{\Delta\gamma_{,\sigma}\}^T[D^e] & (1-\alpha_d)[D^e]\Delta\gamma\{f_{,\sigma\alpha_d}\} \\ & +(1-\alpha_d)[D^e]\{f_{,\sigma}\}\Delta\gamma_{,\alpha_d} \\ & +[D^e]\{\varepsilon_t^e\} - \Delta\gamma[D^e]\{f_{,\sigma}\} \\ -\{\Delta\alpha_{d,\sigma}\}^T & 1 - \Delta\alpha_{d,\alpha_d} \end{bmatrix}. \tag{5.53}$$

The starting conditions for the algorithm are

$$\{\sigma\} = \{\sigma_t\}, \quad \{\alpha_d\} = \{\alpha_{dt}\} \quad \Delta\gamma = \Delta\gamma_t. \tag{5.54}$$

where α_{dt} is a trial value of the damage parameter.

This constitutive model was programmed in MATLAB 7.9.0 for a single material point and the same simulations carried out as for the viscoplastic constitutive model shown in Section 5.2. An investigation was carried out into the effect of the material parameters r_p, n and η and the results are shown in Figures 5.9-5.11. The same material parameters, total strain, number of load steps and time step are used here as for the viscoplastic constitutive model. The only difference here is the presence of damage which requires two additional material parameters, r_p and α. We take $r_p = 1.1$ and $\alpha = 0.2$ unless otherwise stated.

The results of the creep test are shown in Figure 5.9. It is important to note here that the shape of the strain-time response shown in Figures 5.9b-5.9d is the same as the tertiary stage of the typical three stage creep curve commonly observed in laboratory creep testing, shown in Figure 2.1. Figure 5.9b shows that an increase in damage (increase in r_p) causes an increase in strain, particularly when $r_p = 1.2$. When $r_p = 1.0$ we see that the response is identical to that of the viscoplastic constitutive model shown in Figure 5.1. Comparing Figures 5.9c and 5.9d to Figures 5.1b and 5.1c we can see the effect of material damage on the strain-time response. A significant difference is observed when $\eta = 100$MPa day.

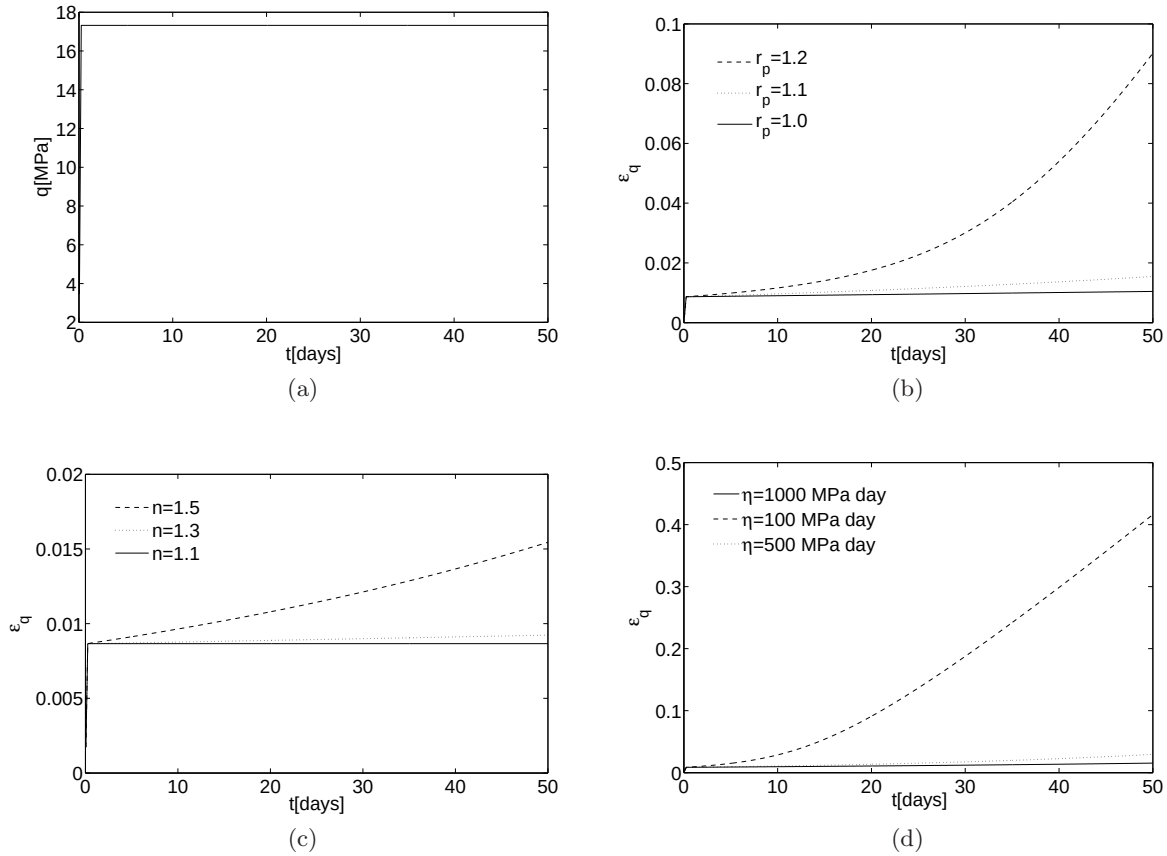

Figure 5.9: Creep simulation: (a) stress held constant with time; (b) effect of r_p on strain-time response; (c) effect of n on strain-time response; (d) effect of η on strain-time response

The results of the relaxation test are shown in Figure 5.10. Figure 5.10b shows that as damage increases the smaller the magnitude of peak stress. When $r_p = 1.0$ we see that the response is identical to that of the viscoplastic constitutive model shown in Figure 5.2. Comparing Figures 5.10c and 5.10d to Figures 5.2b and 5.2c we can see the effect of material damage on the stress-time response. We observe that an increase in damage causes a reduction in the value of peak stress.

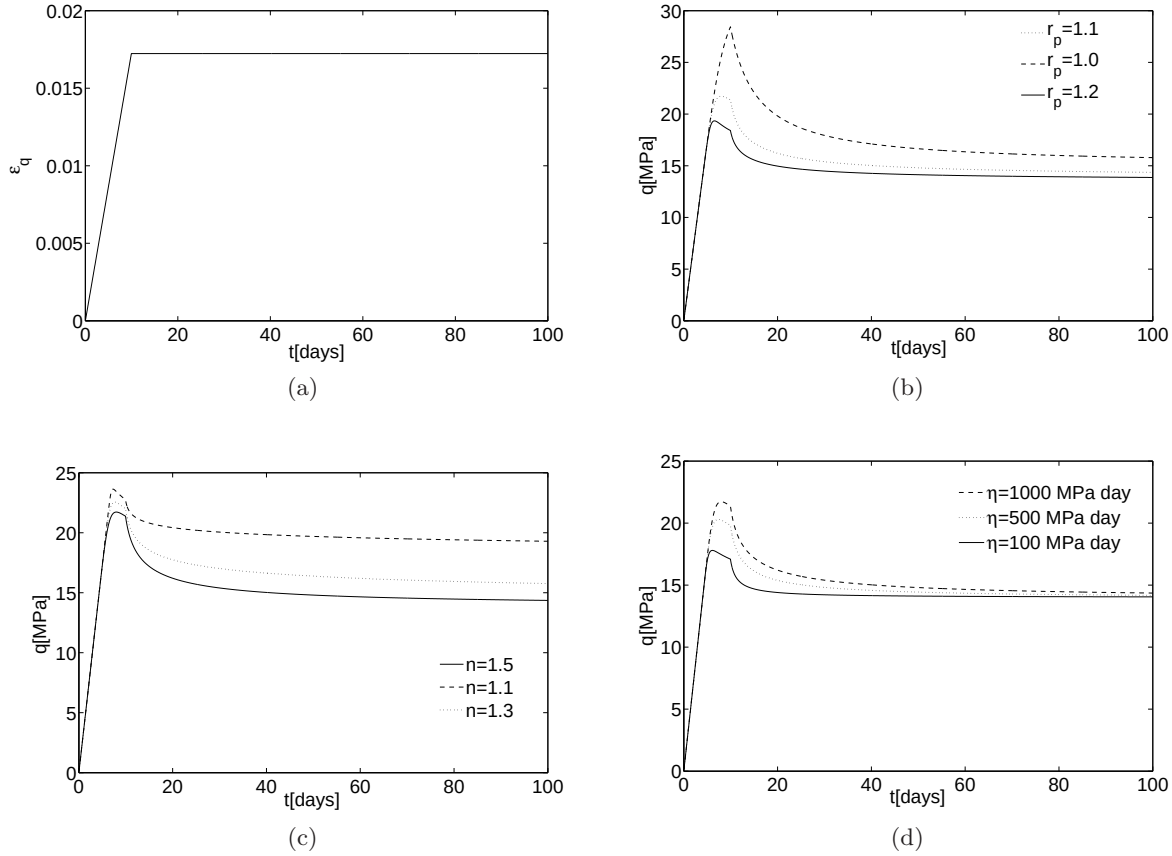

Figure 5.10: Relaxation simulation: (a) strain held constant with time; (b) effect of r_p on stress-time response; (c) effect of n on stress-time response; (d) effect of η on stress-time response

The results for a constant rate of loading are shown in Figure 5.11. Figure 5.11b shows that as damage increases, the peak stress reduces and we observe softening behaviour. When $r_p = 1.0$ we see that the response is identical to that of the viscoplastic constitutive model shown in Figure 5.3. Comparing Figures 5.11a, 5.11c and 5.11d to Figures 5.3a, 5.3b and 5.3c we can see the effect of material damage on the stress-time response. We observe that an increase in damage causes a reduction in the value of peak stress and material softening is present.

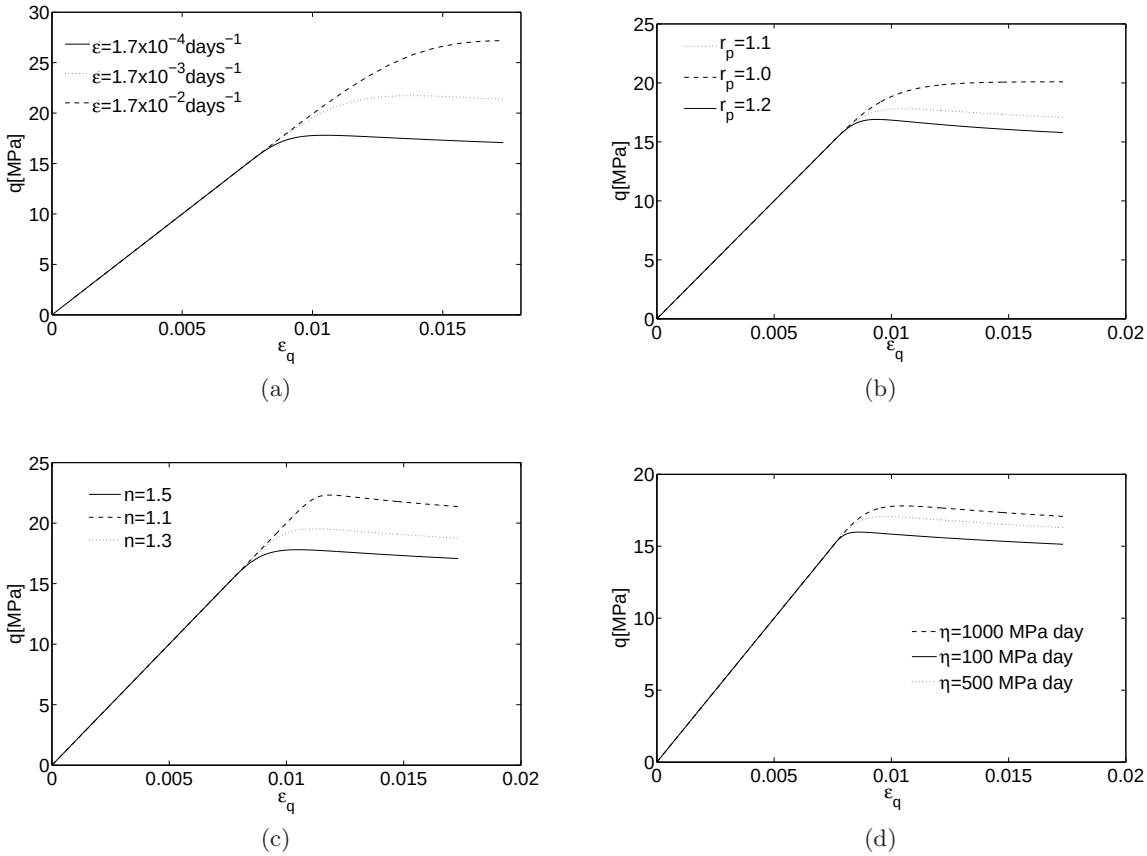

Figure 5.11: Constant rate of loading: (a) effect of rate of loading on stress-strain response; (b) effect of r_p on stress-strain response; (c) effect of n on stress-strain response; (d) effect of η on stress-strain response

5.3.4 Modelling cavity in a viscoplastic-damage medium

Here we follow the same procedure as for the viscoplastic constitutive model (Section 5.2.2). Since we are modelling a damage material, the stresses are dependent on the damage parameter α_d. Therefore the boundary conditions for the cavity are dependent on material damage.

The boundary conditions can be written as follows, at $r = r_0$

$$(1-\alpha_{dj}-\Delta\alpha_d)\Bigg(\lambda\Bigg(\varepsilon^e_{rrj}+\frac{d\Delta u_r}{dr}-\Delta\varepsilon^p_{rr}+\varepsilon^e_{\theta\theta j}+\frac{\Delta u_r}{r}-\Delta\varepsilon^p_{\theta\theta}+\varepsilon^e_{zzj}-\Delta\varepsilon^p_{zz}\Bigg)$$
$$+2G\Bigg(\varepsilon^e_{rrj}+\frac{d\Delta u_r}{dr}-\Delta\varepsilon^p_{rr}\Bigg)\Bigg)+\frac{p_i(j+1)}{totj}=0 \tag{5.55}$$

and at $r = r_m$

$$(1-\alpha_{dj}-\Delta\alpha_d)\Bigg(\lambda\Bigg(\varepsilon^e_{rrj}+\frac{d\Delta u_r}{dr}-\Delta\varepsilon^p_{rr}+\varepsilon^e_{\theta\theta j}+\frac{\Delta u_r}{r}-\Delta\varepsilon^p_{\theta\theta}+\varepsilon^e_{zzj}-\Delta\varepsilon^p_{zz}\Bigg)$$
$$+2G\Bigg(\varepsilon^e_{rrj}+\frac{d\Delta u_r}{dr}-\Delta\varepsilon^p_{rr}\Bigg)\Bigg)=0 \tag{5.56}$$

The flowchart shown in Figure 5.12 is used here. The solution procedure is very similar to that explained earlier for the viscoplastic model (Figure 5.4). The only difference here is that the increment in the damage parameter $\Delta\alpha_d$ must also be updated in addition to the increment in plastic strain (box 4). Note also that the elastic law depends on the damage parameter α_d (box 3). Once the tolerance is met in box 5, the damage parameter and the elastic strains in equations 5.55 and 5.56 are updated and the next load step is applied in box 1.

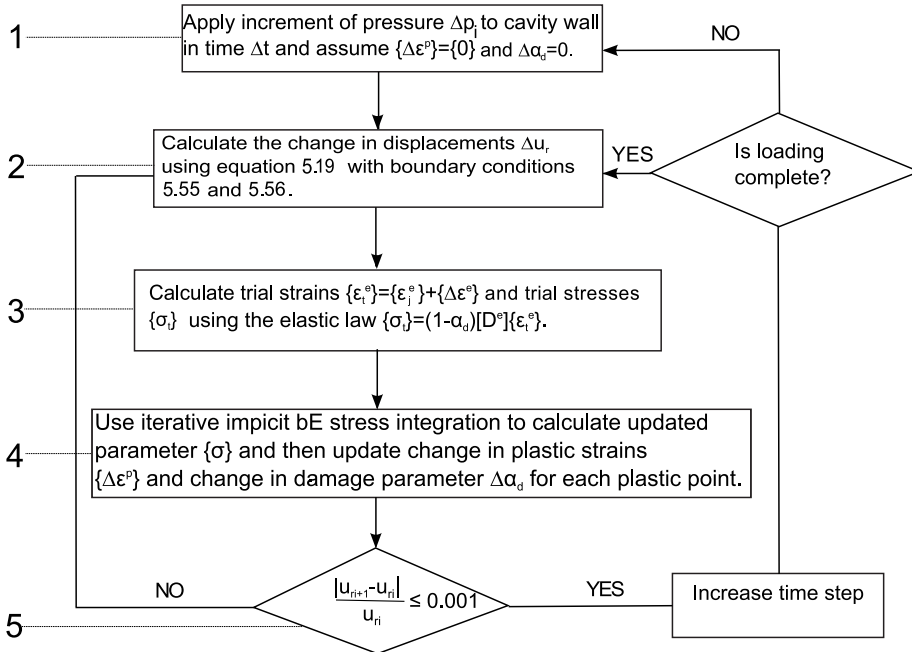

Figure 5.12: Flowchart of solution procedure when yield criterion $f > 0$

5.3.5 Viscoplastic-damage response of the cavity

The model parameters used in the analyses presented here are the same as those used for the viscoplastic model (Section 5.2.3), with the additional softening/hardening parameter $\alpha = 0.2$. Here we investigate the effect of r_p and η on the response of the cavity. Figures 5.13 and 5.14 show the effect of r_p when $\eta = 50$ MPa day and Figures 5.15 and 5.16 show the effect of r_p when $\eta = 500$ MPa day. In Figures 5.14 and 5.16 we observe that the radial stress σ_{rr} is equal to 25 MPa at the cavity wall which is equal to the applied pressure. We observe that when $r_p = 1.0$ we obtain the same response as the viscoplastic model (Figures 5.5 and 5.6).

An increase in r_p (increase in damage) causes the displacement of the cavity wall to increase (Figures 5.13 and 5.15) and the plastic radius of the cavity to increase (Figures 5.14 and 5.16). We observe softening behaviour resulting in a reduction in the equivalent stress q in close

proximity to the cavity wall. The displacement reaches a stable condition at a much higher value of convergence than for the viscoplastic model. This is expected due to a reduction in material stiffness due to cracking and was observed by Sterpi and Gioda [17] when carrying out an FE analysis of a tunnel. We also observe tertiary creep in Figure 5.13 when $r_p = 1.07$, where the rate of displacement of the cavity wall increases with time. The stresses associated with the tertiary creep (Figure 5.14) are only shown up to 10 days as at shortly after this time the material lost all load bearing capacity and the damage parameter $\alpha_d = 1$.

As t increases the cavity wall displacement increases and the plastic radius increases. This is due to the plastic strains developing with time. For a lower value of η (Figures 5.13 and 5.14) the material is more viscous and larger plastic strains are present, and thus the material is more sensitive to an increase in r_p. This results in both a larger displacement and plastic radius. These results highlight the importance of considering damage when estimating the convergence of an underground cavity.

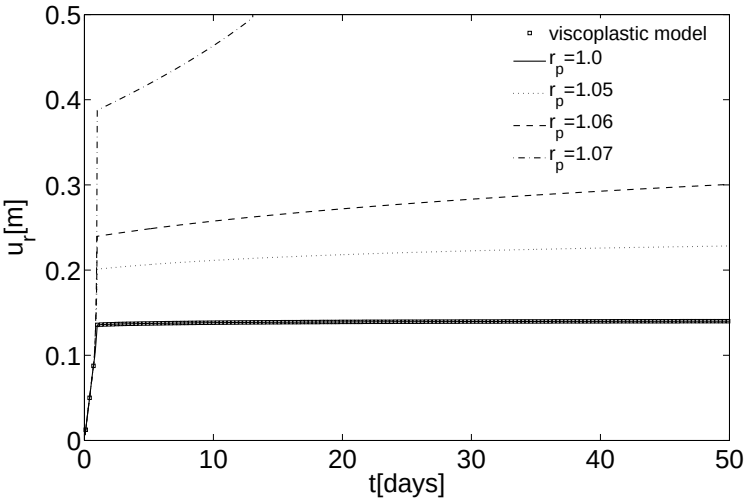

Figure 5.13: Variation of cavity wall displacement with time for $\eta = 50$MPa

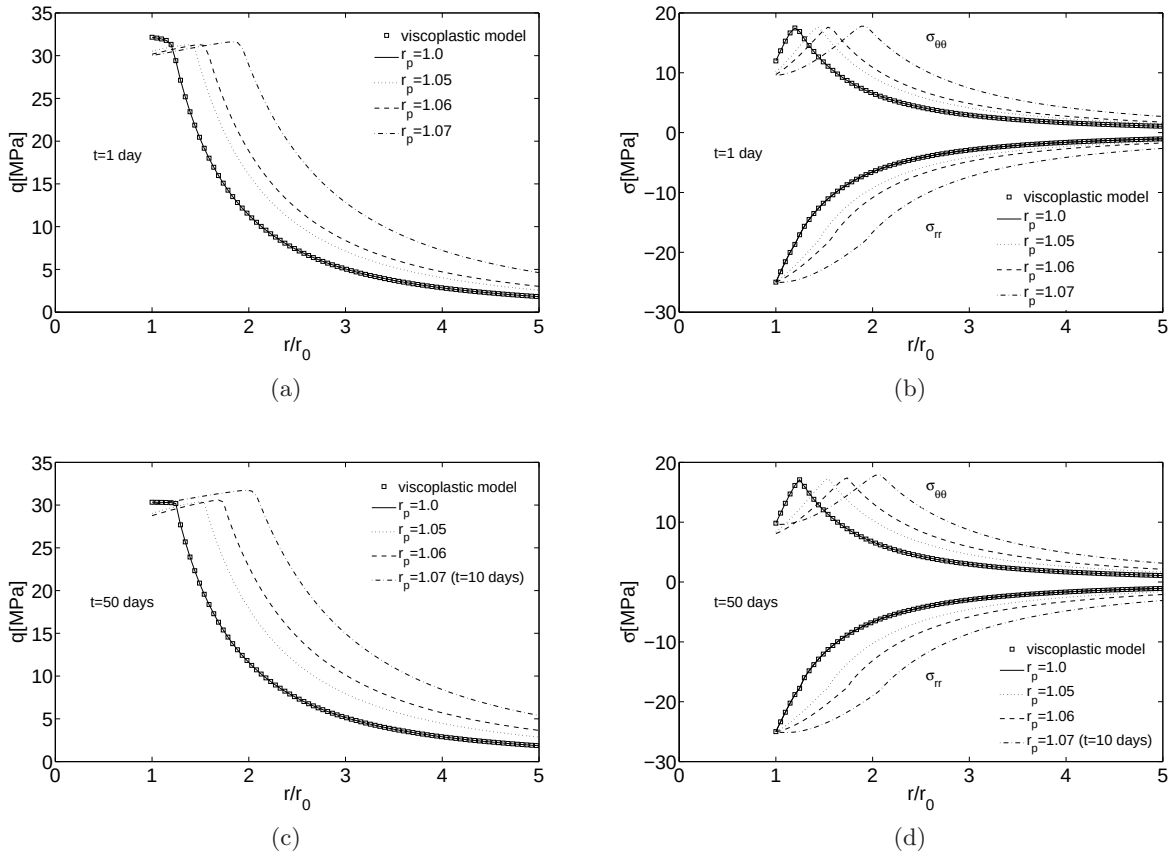

Figure 5.14: Variation of stresses with radial distance at different values of time for $\eta = 50$MPa: (a) q at end of loading stage ($t = 1$); (b) σ_{rr} and $\sigma_{\theta\theta}$ at end of loading stage ($t = 1$); (c) q at $t = 50$; (d) σ_{rr} and $\sigma_{\theta\theta}$ at $t = 50$

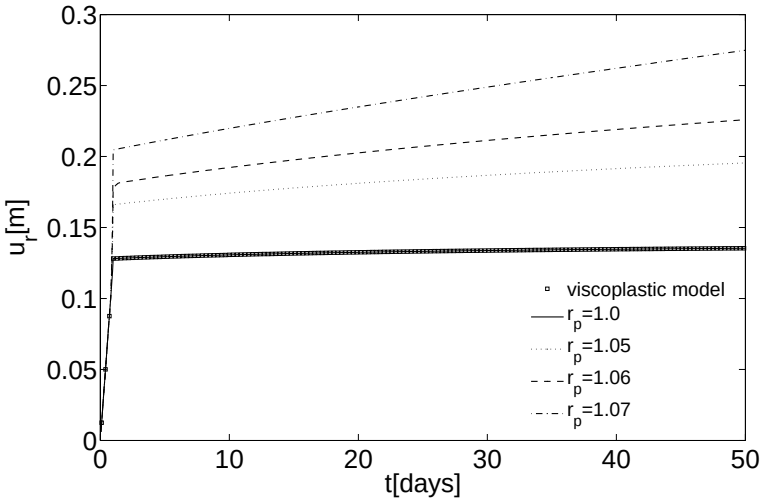

Figure 5.15: Variation of cavity wall displacement with time for $\eta = 500$MPa

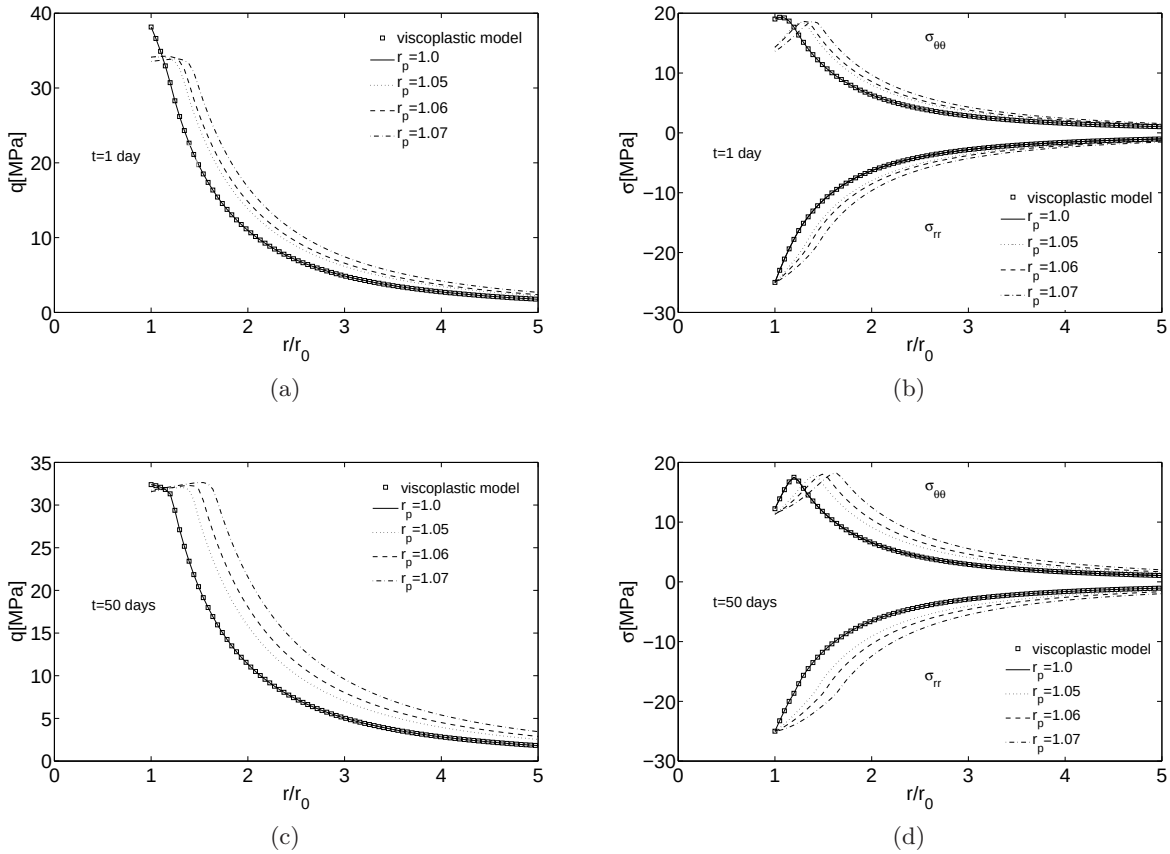

Figure 5.16: Variation of stresses with radial distance at different values of time for $\eta = 500$MPa: (a) q at end of loading stage ($t = 1$); (b) σ_{rr} and $\sigma_{\theta\theta}$ at end of loading stage ($t = 1$); (c) q at $t = 50$; (d) σ_{rr} and $\sigma_{\theta\theta}$ at $t = 50$

5.4 Summary

- both thermodynamically consistent viscoplastic and viscoplastic-damage constitutive models have been developed within the framework of hyperplasticity in this chapter. The former describes secondary creep behaviour, whilst the latter describes both secondary and tertiary creep behaviour (see Figure 2.1). Both of these models use a von Mises yield criterion. The theory of CDM has been used to develop the viscoplastic-damage constitutive model. Both of the models have been used to conduct creep, relaxation and constant rate of loading tests for a single material point.

- the viscoplastic constitutive models have been incorporated into the energy-based method for cavity problems. Here we adopt an incremental loading approach in order to simulate different rates of loading of the cavity and thus approximate cavity excavation.

- the cavity displacements and stresses obtained for the perfectly viscoplastic von Mises model have been successfully validated when $t \to \infty$ or when $\eta \to 0$ using the FE time-independent cavity solutions obtained in Chapter 3. The response of the cavity in a viscoplastic-damage material is identical to the perfectly viscoplastic response when the parameter $r_p = 1.0$ (no damage).

- the results from the cavity highlight the importance of taking into account material damage due to its notable affect on the displacements.

5.5 References

1 Barla, G., Bonini, M. & Debernardi, D. (2008). Time Dependent Deformations in Squeezing Tunnels. *International Journal of Geoengineering Case Histories*, 2(1) p. 40-65.

2 Einav, I., Houlsby, G.T. & Nguyen, G.D. (2007). Coupled damage and plasticity models derived from energy and dissipation potentials. *International Journal of Solids and Structures*, 44 p. 2487-2508.

3 Fritz, P. (1984). An analytical solution for axisymmetric tunnel problems in elasto-viscoplastic media. *International Journal for Numerical and Analytical Methods in Geomechanics*, 8 p. 325-342.

4 Goodman, R.E. (1989). *Introduction to Rock Mechanics*. 2nd Edition. John Wiley & Sons, New York.

5 Houlsby, G.T. & Puzrin, A.M. (2006). *Principles of hyperplasticity: an approach to plasticity theory based on thermodynamic principles*. Springer-Verlag, London.

6 Jaeger, J.C., Cook, N.G.W. & Zimmerman, R.W. (2007). *Fundamentals of rock mechanics.* John Wiley & Sons.

7 Kachanov, L.M. (1958). Time of the Rupture Process under Creep Condition. *Izv. Akad. Nauk. SSSR, Otd. Tekhn. Nauk.*, 8 p. 26-31.

8 Lemaitre, J. & Chaboche, J.L. (1990). *Mechanics of Solid Materials*. Cambridge University Press.

9 Lemaitre, J. & Chaboche, J.L. (1996). Mécanique des matériaux solides. *Dunod*, 253-341.

10 Nguyen, G.D. (2005). A thermodynamic approach to constitutive modelling of concrete using damage mechanics and plasticity theory. D.Phil Thesis, Department of Engineering Science, Oxford University.

11 Perry, J. & Aboudi, J. (2003). Elasto-Plastic Stresses in Thick Walled Cylinders. *Journal of Pressure Vessel Technology*, 125 p. 248-252.

12 Perzyna, P. (1966). Fundamental Problems in Viscoplasticity. *Advances in Applied Mechanics*, vol. 9. New York: Academic Press. p. 243-377.

13 Perzyna, P. (1971). Thermodynamic Theory of Viscoplasticity. *Advances in Applied Mechanics*, vol. 11. New York: Academic Press. p. 313-354.

14 Rabotnov, Y.N. (1963). On the equations of state for creep. *Page 307 of: Progress in Applied Mechanics, Prager Anniversary Volume.* New York: Macmillan.

15 Shao, J.F., Zhu, Q.Z. & Su, K. (2003). Modeling of creep in rock materials in terms of material degradation. *Computers and Geotechnics*, 30(7) p. 549-555.

16 de Souza Neto, E.A., Peric, D. & Owen, D.R.J. (2008). *Computational Methods for Plasticity: Theory and Applications*. John Wiley & Sons.

17 Sterpi, D. & Gioda, G. (2009). Visco-plastic behaviour around advancing tunnels in squeezing rock. *Rock Mechanics and Rock Engineering* 42, p. 319-339.

18 Vlasov, V.Z. & Leontiev, N.N. (1966). Beams, plates and shells on elastic foundations. *NTIS Accession No. N67-14238*, Israel Program for Scientific Translations, Washington, D.C.

19 Yu, C.W. (1998). Creep characteristics of soft rock and modelling of creep in tunnel. Ph.D. Thesis, University of Bradford, United Kingdom.

20 Yu, H.S. (2000). *Cavity Expansion Methods in Geomechanics*. Kluwer, Dordrecht.

21 Ziegler, H. (1983). *An introduction to thermomechanics*. 2nd Edition, North Holland Pub. Co, Amsterdam.

Chapter 6

Frictional viscoplastic constitutive behaviour

Synopsis

In this chapter we derive a novel viscoplastic-damage constitutive model within the framework of hyperplasticity. This model is applicable to geomaterials due to it taking into account frictional behaviour. The model is compared with experimental data obtained by Yang and Jiang [16] during the triaxial compression testing of sandstone.

Section 6.1 introduces the constitutive model and the key constitutive equations are derived. Comparison with experimental data is carried out in Section 6.2, and finally the model is incorporated into the energy-based method for cavity analysis in Section 6.3.

6.1 Drucker-Prager viscoplastic-damage model

Here we derive a viscoplastic-damage constitutive model for a frictional material. We derive a Drucker-Prager model, whose constitutive behaviour was derived in Section 3.5.3 for the simple elasto-plastic case. This model builds on the von Mises viscoplastic-damage model shown in Section 5.3.2 and is derived in a similar way. As for the von Mises viscoplastic-damage model, here we assume that the damage is isotropic and that viscoplasticity and damage are coupled and therefore occur simultaneously.

For this derivation we will use the same free energy potential and elastic law as used for the von Mises viscoplastic-damage model in Chapter 5 (equations 5.34 and 5.35). We also use the same expression for the generalised damage stress (equation 5.37).

The dissipation potential $\dot{D}$ can be defined below. It takes the same general form as that used to derive the von Mises viscoplastic-damage model (equation 5.39). Note that this dissipation potential reduces to the elasto-plastic Drucker-Prager dissipation potential in

Chapter 3 (equation 3.127) when there is no viscoplasticity ($\eta \to 0$) and no damage ($\alpha_d = 0$).

$$\dot{D} = \sqrt{(r_p(c_2 p + c_1)\dot{\alpha}_s + r_p \eta^{n-1} \dot{\alpha}_s^n)^2 + (r_d \rho (c_2 p + c_1)\dot{\alpha}_d)^2}, \tag{6.1}$$

where r_p and r_d are constants governing the ratio of viscoplasticity and damage, p is the mean stress, η is the viscous coefficient which controls the extent of plastic strain, n is a material constant, $\dot{\alpha}_s$ is an internal variable representing the equivalent deviatoric plastic strain rate, α_d is the damage parameter, $c_1 = d\Pi(\alpha_d)$ and $c_2 = \mu\Pi(\alpha_d)$, where d is a constant related to the cohesion, μ is a constant related to the frictional angle and $\Pi(\alpha_d)$ is the softening/hardening function defined for the von Mises viscoplastic-damage model in Section 5.3.2. $\rho = \frac{\bar{\chi}_d}{(q - c_3 p)}$ and thus using equation 5.37 can be written as

$$\rho = \frac{q^2}{6G(1-\alpha_d)^2(q - c_3 p)} + \frac{p^2}{2K(1-\alpha_d)^2(q - c_3 p)}, \tag{6.2}$$

where $c_3 = \beta\Pi(\alpha_d)$ and where β is a constant, related to the dilation angle. d, μ and β can be calculated from material parameters (c, ϕ and ψ) using equations 3.141-3.143. As for the elasto-plastic model we assume that the Drucker-Prager yield surface circumscribes the Mohr-Coulomb yield surface, which matches the Mohr-Coulomb yield criterion for triaxial compression.

As a side condition we will impose a linear relationship between the volumetric and shear strain rates as shown for the elasto-plastic Drucker-Prager model (equation 3.128)

$$\dot{\alpha_v} + c_3 \dot{\alpha}_s = 0 \tag{6.3}$$

A modified dissipation potential can now be formed

$$\dot{D}^* = \sqrt{(r_p(c_2 p + c_1)\dot{\alpha}_s + r_p \eta^{n-1} \dot{\alpha}_s^n)^2 + (r_d \rho (c_2 p + c_1)\dot{\alpha}_d)^2} + \Lambda \dot{\alpha}_v + c_3 \Lambda \dot{\alpha}_s, \tag{6.4}$$

with Λ as a Lagrange multiplier.

Having now defined the dissipation potential together with the constraint given by equation 6.3, we can follow the same method used to derive the constitutive equations for the von Mises viscoplastic-damage model in Section 5.3.2.

We can write equation 6.4 in the following form

$$\dot{D}^* = \sqrt{(r_p(c_2 p + c_1)\dot{\alpha}_{s1} + r_p \eta^{n-1} \dot{\alpha}_{s2}^n)^2 + (r_d \rho (c_2 p + c_1)\dot{\alpha}_d)^2} + \Lambda \dot{\alpha}_v + c_3 \Lambda \dot{\alpha}_{s1}. \tag{6.5}$$

Differentiation of the dissipation potential with respect to the plastic strain rates gives the dissipative stresses, due to the volumetric plastic strain

$$\chi_p = \frac{\partial \dot{D}^*}{\partial \dot{\alpha}_v} = \Lambda, \tag{6.6}$$

and due to the deviatoric plastic strain

$$\chi_q = \frac{\partial \dot{D}^*}{\partial \dot{\alpha}_{s1}} + \frac{1}{n}\frac{\partial \dot{D}^*}{\partial \dot{\alpha}_{s2}}. \tag{6.7}$$

Noting that $\dot{\alpha}_{s1} = \dot{\alpha}_{s2} = \dot{\alpha}_s$, we can show that

$$\chi_q = \frac{(r_p(c_2 p + c_1)\dot{\alpha}_s + r_p \eta^{n-1}\dot{\alpha}_s^n) r_p((c_2 p + c_1) + (\eta\dot{\alpha}_s)^{n-1})}{\sqrt{(r_p(c_2 p + c_1)\dot{\alpha}_s + r_p\eta^{n-1}\dot{\alpha}_s^n)^2 + (r_d\rho(c_2 p + c_1)\dot{\alpha}_d)^2}} + c_3\Lambda. \tag{6.8}$$

Differentiating with respect to $\dot{\alpha}_d$ gives the dissipative stress due to damage

$$\chi_d = \frac{\partial \dot{D}^*}{\partial \dot{\alpha}_d} = \frac{\dot{\alpha}_d (r_d\rho(c_2 p + c_1))^2}{\sqrt{(r_p(c_2 p + c_1)\dot{\alpha}_s + r_p\eta^{n-1}\dot{\alpha}_s^n)^2 + (r_d\rho(c_2 p + c_1)\dot{\alpha}_d)^2}}. \tag{6.9}$$

Since there is no kinematic hardening, the true stresses and the dissipative stresses are identical

$$\chi_q = q \qquad \chi_p = p, \tag{6.10}$$

as shown for the elasto-plastic model (equation 3.133).

Manipulating the above stress expressions (equations 6.8 and 6.9), leads to the following equation

$$\left(\frac{\chi_q - c_3\Lambda}{r_p((c_2 p + c_1) + (\eta\dot{\alpha}_s)^{n-1})}\right)^2 + \left(\frac{\chi_d}{r_d(c_2 p + c_1)\rho}\right)^2 = 1. \tag{6.11}$$

Substitution of $\rho = \frac{\bar{\chi}_d}{(q - c_3 p)}$ into this equation and using equations 6.6, 6.10 and 5.32 produces the following

$$\left(\frac{q - c_3 p}{r_p((c_2 p + c_1) + (\eta\dot{\alpha}_s)^{n-1})}\right)^2 + \left(\frac{q - c_3 p}{r_d(c_2 p + c_1)}\right)^2 = 1. \tag{6.12}$$

Rearranging equation 6.12 we obtain

$$\dot{\alpha}_s = \frac{1}{\eta}\left((c_2 p + c_1)\left(\frac{1}{\sqrt{\left(\frac{r_p}{c_k}\right)^2 - \left(\frac{r_p}{r_d}\right)^2}} - 1\right)\right)^{\frac{1}{n-1}} \tag{6.13}$$

which is equal to the plastic consistency parameter $\dot{\gamma}$, where

$$c_k = \frac{(q - c_3 p)}{(c_2 p + c_1)}. \tag{6.14}$$

From equation 6.13 we can derive the yield criterion given $\dot{\alpha}_s \geq 0$

$$f = {c_k}^2 \left(\frac{1}{{r_p}^2} + \frac{1}{{r_d}^2} \right) - 1. \tag{6.15}$$

An expression for the rate of the damage internal variable can be found from equations 6.8 and 6.9 using $\rho = \frac{\bar{\chi}_d}{(q - c_3 p)}$, along with equations 6.6, 6.10 and 5.32

$$\dot{\alpha}_d = \frac{\dot{\alpha}_s \left(1 + \frac{(\dot{\alpha}_s \eta)^{n-1}}{(c_2 p + c_1)} \right)^2}{\rho} \left(\frac{r_p}{r_d} \right)^2. \tag{6.16}$$

As for the elasto-plastic Drucker-Prager model the plastic strain components can be expressed as follows using a non-associated flow rule

$$\{\dot{\varepsilon}^p\} = \dot{\gamma} \{g_{,\sigma}\}, \tag{6.17}$$

where

$$\{g_{,\sigma}\} = \frac{3}{2} \frac{\{s\}}{q} - \frac{c_3}{3} \{1\}. \tag{6.18}$$

6.1.1 Stress integration and response of the constitutive model

In order to use this constitutive model for practical application we must use a stress integration procedure. Here we use the iterative implicit backward Euler (bE) stress integration scheme as used in Chapters 3 and 5. The stress integration procedure for this constitutive model is the same as that described for the von Mises viscoplastic-damage model in Section 5.3.3. The form of the Hessian matrix $[A]$ is identical to that shown in equation 5.53.

This constitutive model was programmed in MATLAB 7.9.0 for a single material point and identical simulations to those shown in Chapter 5 were carried out; creep, relaxation and constant rate of loading. An investigation was carried out into the effect of the different material parameters ϕ, ψ, r_p, n and η and the results are shown in Figures 6.1-6.3. We use the same material parameters as used for the von Mises model, but with the viscous parameter $\eta = 100000$ MPa day and the additional strength parameters; a friction angle $\phi = 30^{\text{o}}$, a dilation angle $\psi = 7.5^{\text{o}}$ and a cohesion c=7.5 MPa, unless otherwise stated. Note that here we apply different strains than those used in Chapter 5, which are stated in the following discussions. This is to ensure that the mean stress p is greater than zero and therefore ϕ and ψ have a noticeable effect on the response of the model.

The results of the creep test are shown in Figure 6.1. The total strain used in this test was $\varepsilon = \{-0.1, 0.1, -0.05\}$. Figure 6.1b shows that an increase in damage (increase in r_p) causes an increase in strain rate and tertiary creep behaviour is more pronounced. We also observe that an increase in n or η causes a decrease in strain rate (Figures 6.1c and 6.1d respectively).

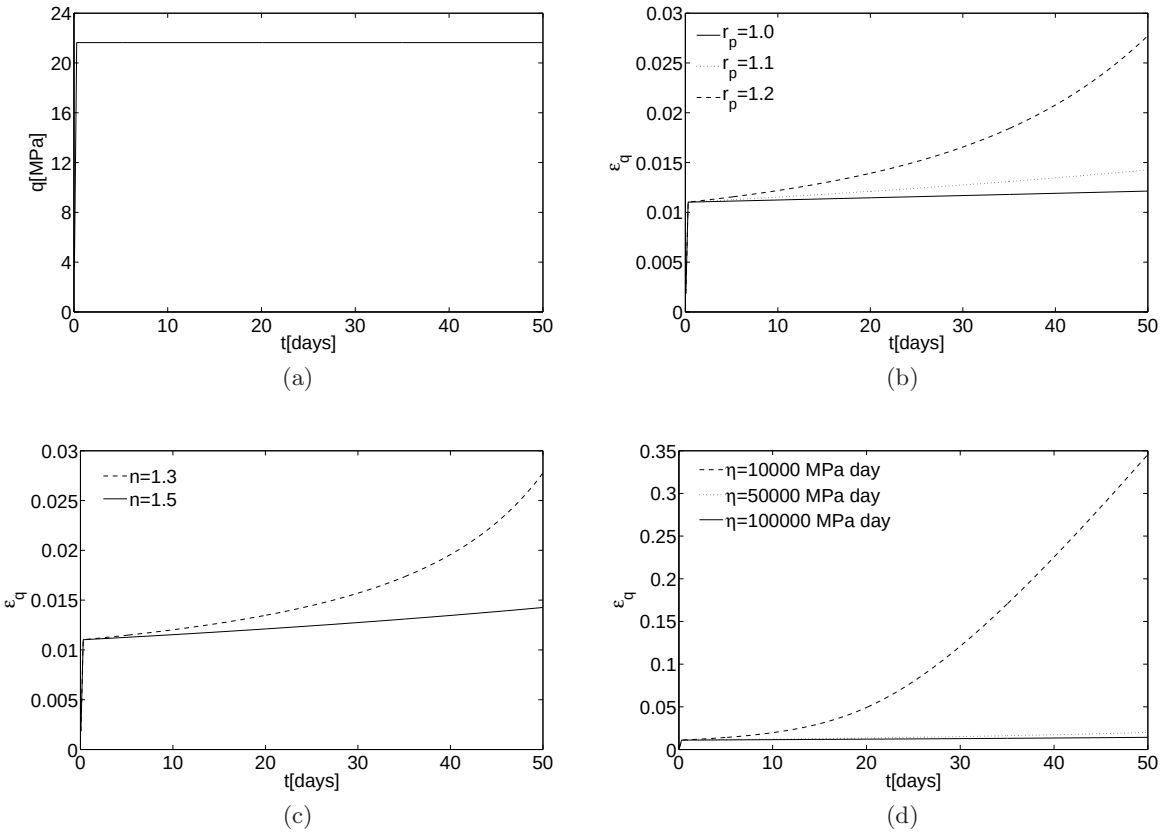

Figure 6.1: Creep simulation: (a) stress held constant with time; (b) effect of r_p; (c) effect of n; (d) effect of η

The results of the relaxation test are shown in Figure 6.2. In this test we applied a total strain $\varepsilon = \{-0.01, 0.01, -0.005\}$. An increase in ϕ or ψ causes the strength to increase and thus the peak stress increases (Figures 6.2b and 6.2c respectively). An increase in r_p causes the peak stress to reduce due to material softening (Figure 6.2d). Increasing n or η causes the peak stress to increase and the stresses to relax more slowly (Figures 6.2e and 6.2f respectively).

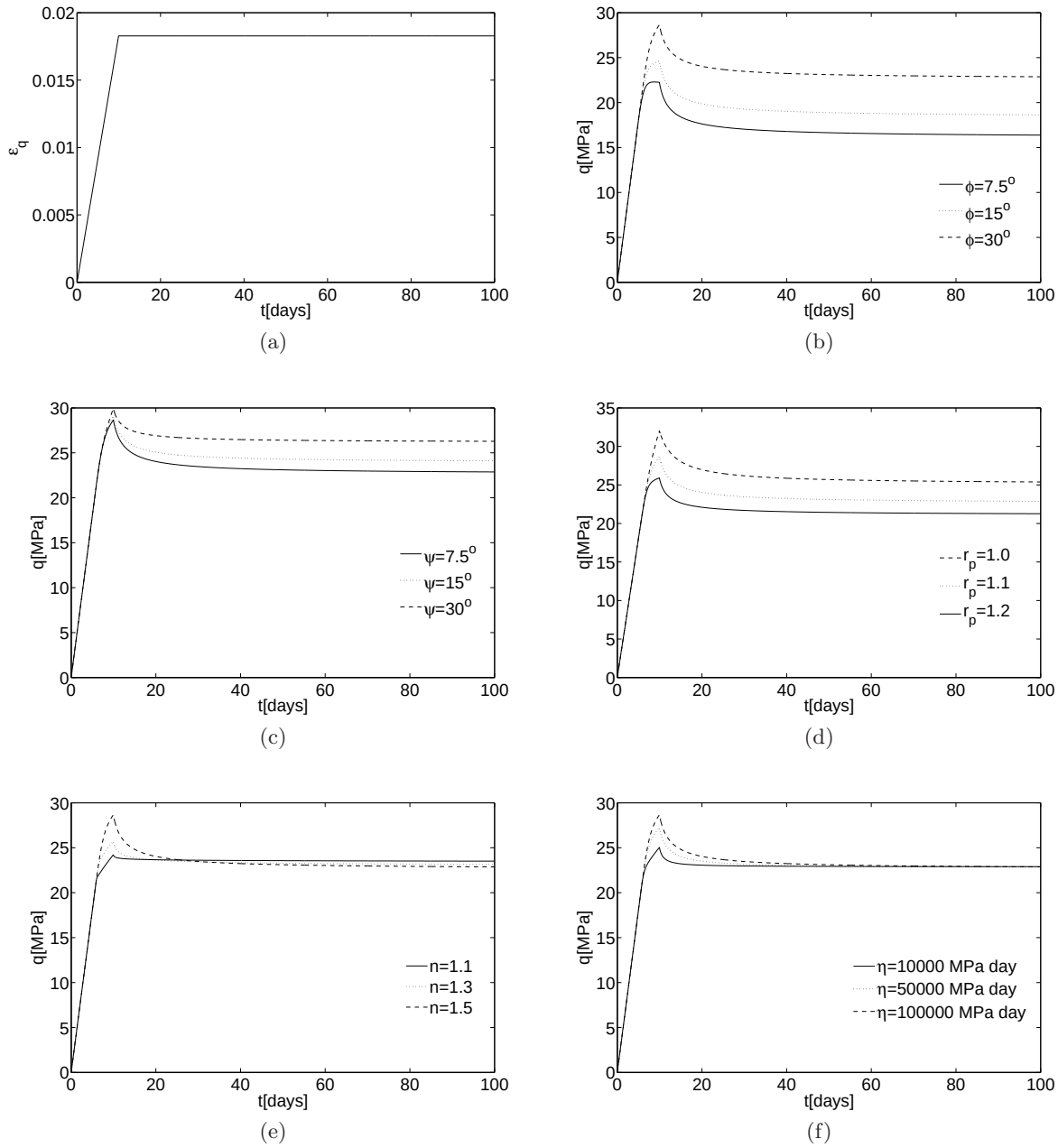

Figure 6.2: Relaxation simulation: (a) strain held constant with time; (b) effect of ϕ; (c) effect of ψ; (d) effect of r_p; (e) effect of n; (f) effect of η

The results for a constant rate of loading are shown in Figure 6.3. A total strain $\varepsilon = \{-0.01, 0.01, -0.005\}$ was applied. The rate of loading applied in this test was $\dot{\varepsilon} = 1.8\text{x}10^{-4}\text{days}^{-1}$ unless otherwise stated. From Figure 6.3a we observe that an increase in the rate of loading causes an increase in the peak stress. As in the relaxation simulations we observe that an increase in either ϕ or ψ causes the peak stress to increase (Figures 6.3b and 6.3c respectively), an increase in r_p causes the peak stress to reduce (Figure 6.3d) and an increase in either n or η causes the peak stress to increase (Figures 6.3e and 6.3f respectively).

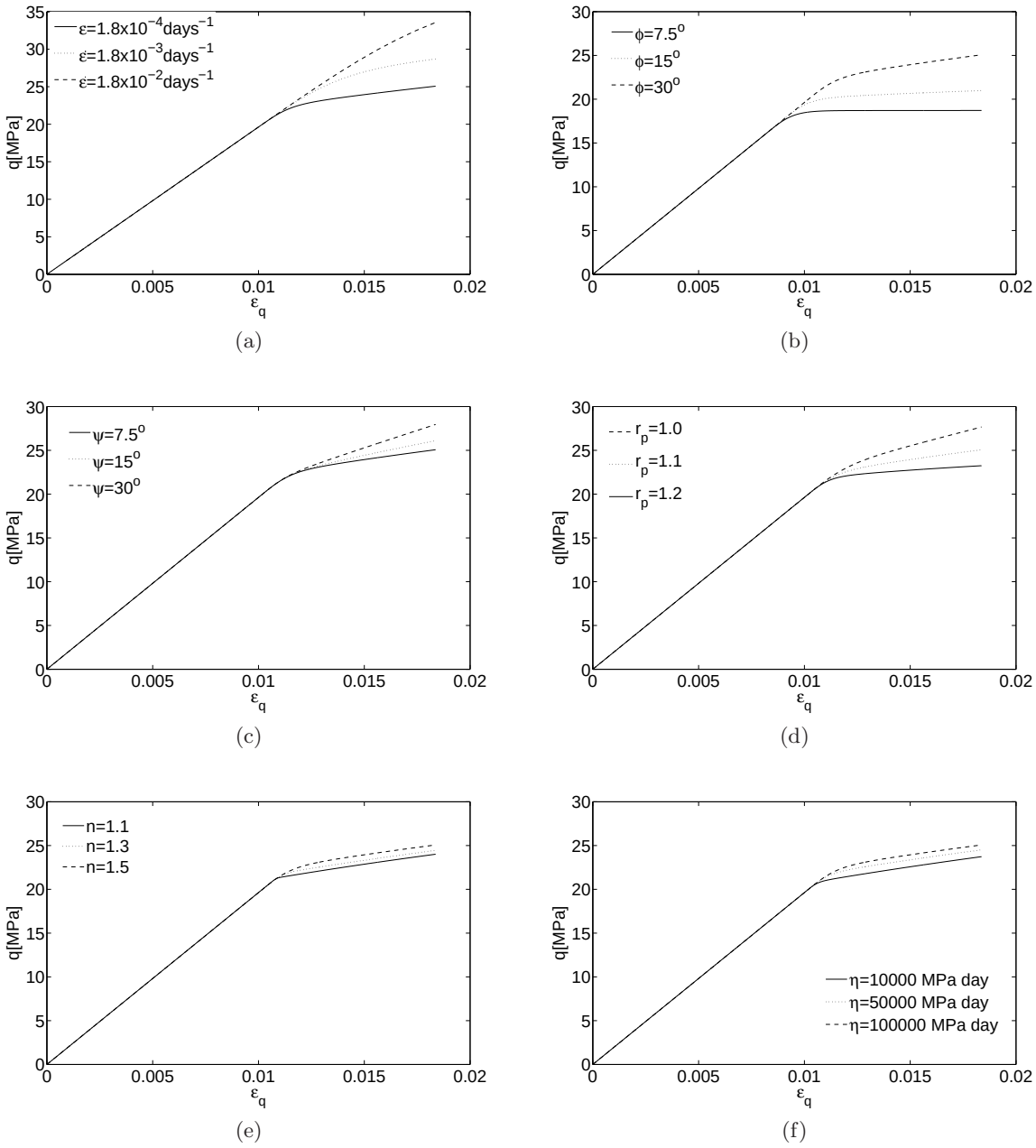

Figure 6.3: Constant rate of loading: (a) effect of rate of loading on stress-strain response; (b) effect of ϕ; (c) effect of ψ; (d) effect of r_p; (e) effect of n; (f) effect of η

6.2 Comparison of constitutive model with experimental data

Here we compare the Drucker-Prager viscoplastic-damage model with data from triaxial compression testing of sandstone by Yang and Jiang [16]. The experimental data was obtained from short-term loading tests and long-term creep tests. Note that here we use a softening/hardening function $\Pi(\alpha_d)$ equal to $(1 - \alpha\alpha_d)^2$, which fits well with the experimental data.

6.2.1 Short-term loading tests

The short-term loading tests were conducted by Yang and Jiang [16] under three different confining pressures ($\sigma_3 = 3, 5$ and 7 MPa). We simulated these triaxial tests by using a single material point in MATLAB 7.9.0. We apply the initial confining pressure in the first time step and then apply an increment of strain over each subsequent time step, ensuring that the rate of applied strain corresponds to a rate of applied stress of 0.127 MPa/s, which is the value used in the triaxial experiments. Within each time step we must ensure that the confining pressure remains equal to the initial confinement, e.g. if the initial confinement is equal to 3 MPa, then σ_2 and σ_3 must remain equal to 3 MPa throughout the analysis. This is achieved in the elastic stage through applying increments of strain which do not affect the values of σ_2 and σ_3. The increments of strain $\{d\varepsilon\}$ are calculated using an approach by Bardet and Choucair [1] as follows

$$\{d\varepsilon\} = ([Smat][D^e] + [Emat])^{-1}\{dY\}, \tag{6.19}$$

where

$$[Smat] = \begin{bmatrix} 0 & 1 & 0 \\ 0 & 0 & 1 \\ 0 & 0 & 0 \end{bmatrix}, \qquad [Emat] = \begin{bmatrix} 0 & 0 & 0 \\ 0 & 0 & 0 \\ 1 & 0 & 0 \end{bmatrix} \quad \text{and} \quad \{dY\} = \begin{bmatrix} 0 \\ 0 \\ dX \end{bmatrix}, \tag{6.20}$$

where dX controls the evolution of the loading process.

The elastic parameters used in the simulation are the same as those calculated by Yang and Jiang [16]. We use the average Young's modulus $(E_s + E_{50})/2$, where E_{50} is the slope of the line connecting the origin and half the peak strength of the stress-strain curve, and where E_s is the slope of the approximately linear part of the stress-strain curve, whose values are shown in Table 6.1. We also use a Poisson's ratio ν of 0.22.

σ_3[MPa]	E_s[MPa]	E_{50}[MPa]	$(E_s + E_{50})/2$[MPa]
3	25770	21410	23590
5	27730	22680	25205
7	32630	30910	31770

Table 6.1: Values of Young's moduli of the sandstone under different confining pressures (Yang and Jiang [16])

6.2.2 Long-term creep tests

Yang and Jiang [16] conducted a creep test under multi levels of stress. The applied rate of stress was the same as that used in the short-term tests ($\sigma_1 - \sigma_3 = 0.127$ MPa/s), with a confinement σ_3 of 5 MPa. When a required level of stress was obtained it was held constant

and the sandstone was allowed to creep for 48 hours. The final and highest level of stress used was $\sigma_1 - \sigma_3 = 160$ MPa. Under this constant level of stress, the three typical stages of creep were observed (see Figure 2.1). This stress was below the peak strength of the material, but corresponded to the point where yield was initiated. In order to simulate a creep test, we modified the program used for the short-term tests by keeping $\sigma_1 - \sigma_3$ constant when yield begins. Here we do not simulate a multi-stage creep test, but rather use a single level of stress similar to the final level of stress used by Yang and Jiang [16]. This is justified from the results of triaxial tests carried out by Yang and Jiang [16]. Their findings showed that very little creep occurred below the yield stress of the sandstone.

6.2.3 Selection of model parameters

In this section we explain how the model parameters were selected to fit the experimental data. Here we use the short-term loading test data to obtain the model parameters. The purpose here is to simply show that the constitutive model is able to describe the experimental data. A complete validation is not provided here and in order to carry this out an experimental program would need to be conducted.

Selection of strength parameters

First we must determine the model strength parameters; the cohesion c, the friction angle ϕ and the dilation angle ψ, which correspond to the initiation of yield of the sandstone. These parameters have not been calculated by Yang and Jiang [16] and only the peak strength parameters were calculated by fitting a Mohr-Coulomb failure criterion to the peak stresses of the sandstone obtained from the short-term loading tests. This produced a value of c equal to 17.97 MPa and a value of ϕ equal to 58.4^o. Yang and Jiang [16] did state values for the yield stresses under the three different confining pressures, however these yield stresses are approximate as they were obtained by applying steps in stress $\sigma_1 - \sigma_3$ of 5 MPa to the material for a confining pressure of 3 MPa and steps of 10 MPa under confining pressures of 5 and 7 MPa until yield occurred. This produced the yield stresses shown in column two of Table 6.2. We substituted these yield stresses and the corresponding values of confining pressure into the Mohr-Coulomb failure criterion, resulting in three equations with the unknowns c and ϕ, and thus three possible sets of simultaneous equations. Solving these equations for c and ϕ resulted in a wide variation, with c ranging from 16.6 to 27.6 MPa and ϕ ranging from 45.6^o to 56.4^o.

Therefore it was decided to simply adjust the peak strength parameters calculated by Yang and Jiang [16] to obtain the strength parameters corresponding to the yield stresses. c was adjusted from 17.97 MPa to 15 MPa and ϕ was kept constant at 58.4^o. The yield stresses corresponding to these new strength parameters for the three confining pressures are shown in Table 6.2 alongside the approximate yield stresses stated by Yang and Jiang [16]. We can see that the new yield stresses are reasonably close to those stated by Yang and Jiang [16], with a maximum difference of 8 MPa when the confining pressure is equal to 3 MPa.

Note that more experimental data is required to determine the strength parameters more accurately. Triaxial tests under different rates of loading are required, as the magnitude of the peaks of the short-term stress strain curves obtained by Yang and Jiang [16] is dependent on the rate of loading. A higher rate of loading could produce higher peaks, whilst a slower rate of loading could produce lower peaks (e.g. see Figure 6.3a). In order to obtain the strength parameters c and ϕ more accurately it is necessary to conduct triaxial tests under low rates of loading.

σ_3[MPa]	yield stresses (Yang and Jiang [16]) [MPa]	yield stresses predicted by model [MPa]
3	150	142
5	160	165
7	180	187

Table 6.2: Yield stresses for the sandstone under different confining pressures

Selection of parameters describing the viscoplastic-damage response

Here we use the short-term loading test data for a confining pressure of 5 MPa to obtain the remaining model parameters. For simplification we assume an associated flow rule ($\phi = \psi$ and thus $\mu = 0$). The effect of using a non-associated flow rule is shown in Section 6.2.5. For simplification we assume that $n = 1.5$ and $r_p = 1.05$ and thus in this section we report on how η and α were selected to best fit the experimental data. Note that an increase in n causes the peak stress to increase (Figure 6.3e) and an increase in r_p causes the peak stress to decrease (Figure 6.3d).

Figure 6.4 shows the response of the model for different values of η and α. Three values of η were used; 1500, 1000 and 500 MPa, shown in Figures 6.4a, 6.4b and 6.4c respectively, whilst α was varied between 0.3 and 0.4. Figure 6.4 shows that the peak of the stress-strain curve increases as η increases. This is because the material is less viscous and this behaviour was also seen in Figure 6.3f. We also see that an increase in α causes greater material softening. The red lines in Figure 6.4 represent the value of α which best fits the experimental data for each value of η. Here we observe that the experimental data is best represented by $\eta = 1000$ MPa h and $\alpha = 0.375$ (Figure 6.4b) or $\eta = 500$ MPa h and $\alpha = 0.4$ (Figure 6.4c). However when using these parameters in the long-term creep test we find that tertiary creep occurs after a much shorter period of time than shown by the experimental data. We therefore use $\eta = 1500$MPa h and $\alpha = 0.375$ (Figure 6.4a), which provides a better fit to the creep data and also provides a good fit to the short-term data.

All of the selected model parameters are shown in Table 6.3 and provide a good fit to the experimental data obtained by Yang and Jiang [16] during triaxial compression testing of

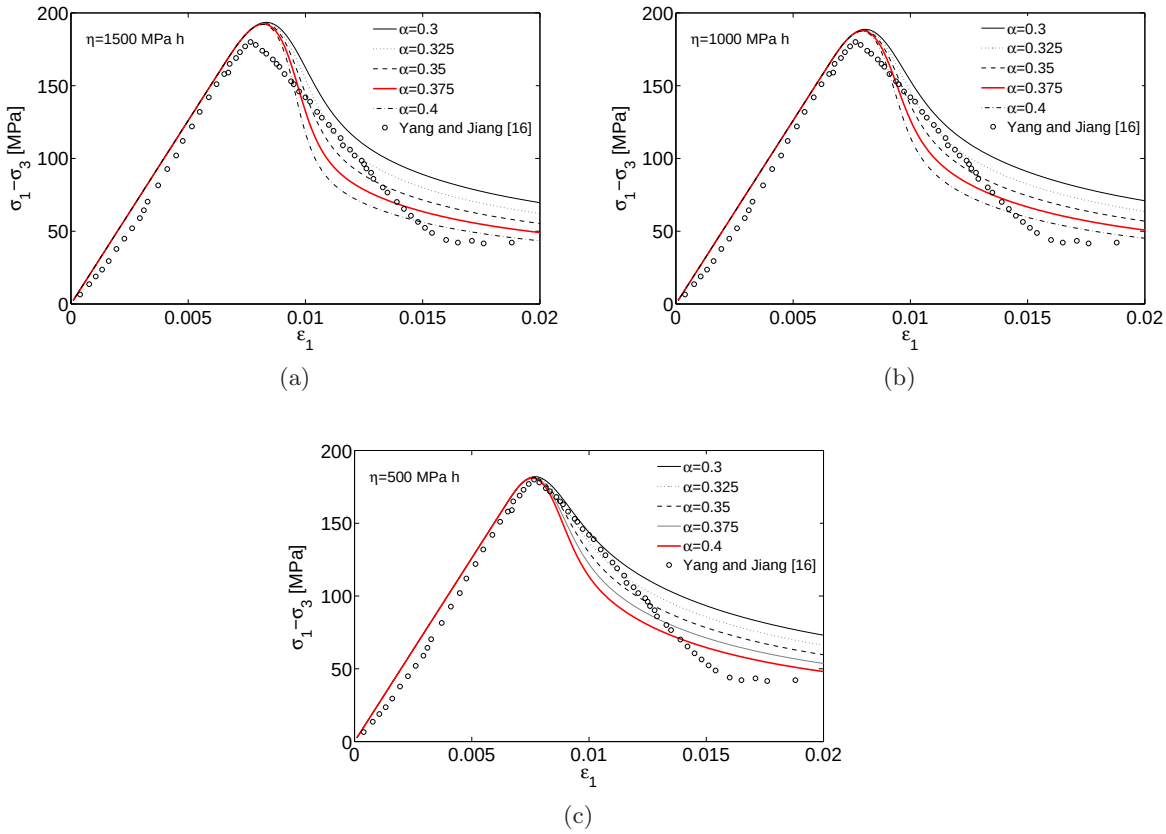

Figure 6.4: Selecting model parameters to fit experimental data (confining pressure=5 MPa): (a) $\eta = 1500$MPa h; (b) $\eta = 1000$MPa h; (c) $\eta = 500$MPa h

sandstone. Note that the strength parameters d, μ and β are calculated from c, ϕ and ψ as explained in the derivation of the model in Section 6.1.

d[MPa]	μ	β	η[MPa h]	n	α	r_p
21.95	0	−2.38	1500	1.5	0.375	1.05

Table 6.3: Values of constitutive model parameters used to fit both the short and long-term triaxial data

6.2.4 Model results using the newly selected parameters

Figure 6.5 compares the short-term stress-strain curves obtained by Yang and Jiang [16] and those obtained using the new constitutive model. Results for the three different confining pressures are shown. We observe that the constitutive model provides a good prediction of the experimental data for all three confining pressures, at both peak stress and in the region of material softening. The experimental data obtained from the long-term tests is shown in Figure 6.6, along with the response of the new constitutive model. Here we observe that the constitutive model generally underestimates the strain shown in the experimental data. However the overall shape of the curves is very similar, therefore the constitutive model

provides a useful approximation.

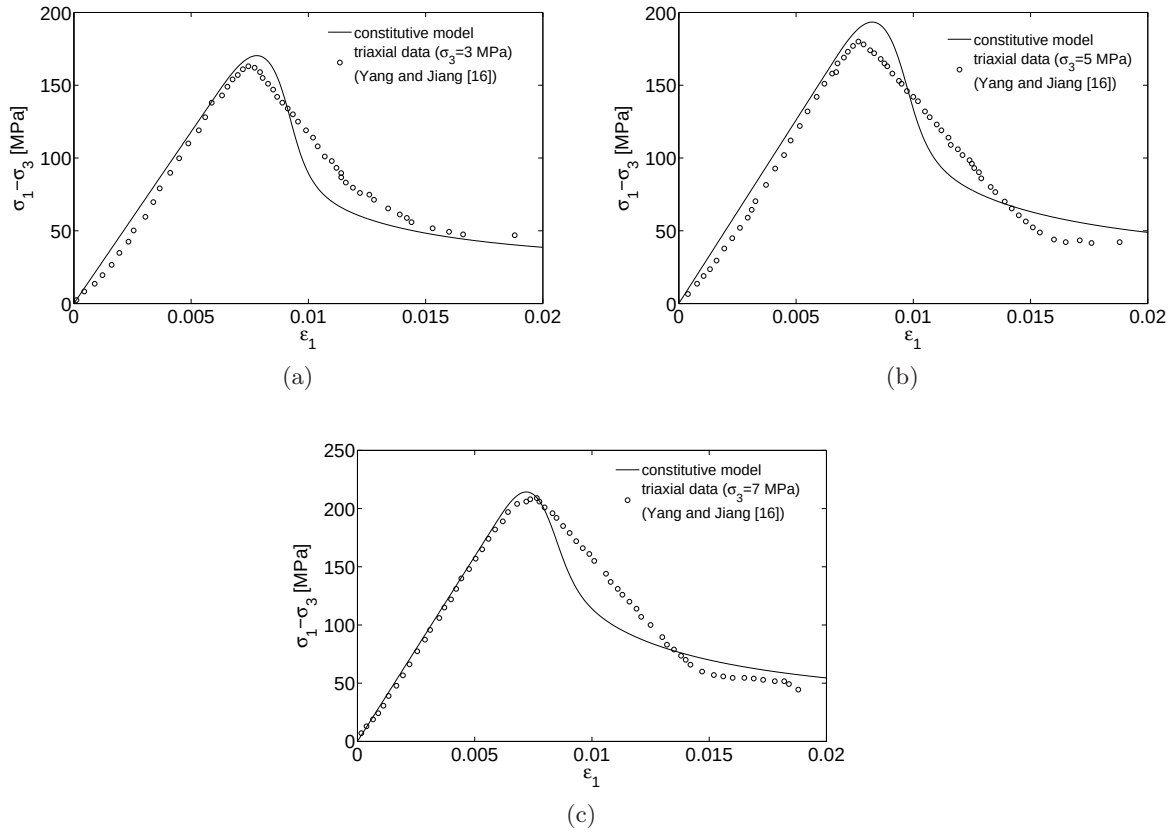

Figure 6.5: Validating constitutive model using short-term stress-strain triaxial data: (a) $\sigma_3 = 3$MPa; (b) $\sigma_3 = 5$MPa; (c) $\sigma_3 = 7$MPa

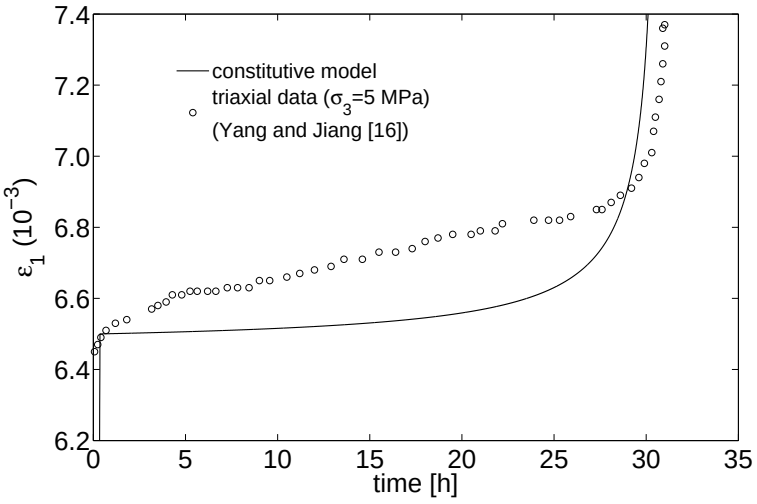

Figure 6.6: Creep response of model under yield stress

Figure 6.7 shows the Mohr's circles corresponding to the peak stresses of the constitutive

model for the three different confining pressures (peak stresses obtained from Figure 6.5). From Figure 6.7 we calculated c and ϕ corresponding to these peak stresses. These values were then compared to those calculated by Yang and Jiang [16]. From Table 6.4 we observe that the peak strength parameters obtained for the new constitutive model are close to those calculated from the experimental data.

	c[MPa]	$\phi[^o]$
Yang and Jiang [16]	17.97	58.4
Constitutive model	20.1	58.1

Table 6.4: Peak strength parameters obtained from experimental data and the new constitutive model (see Figure 6.5)

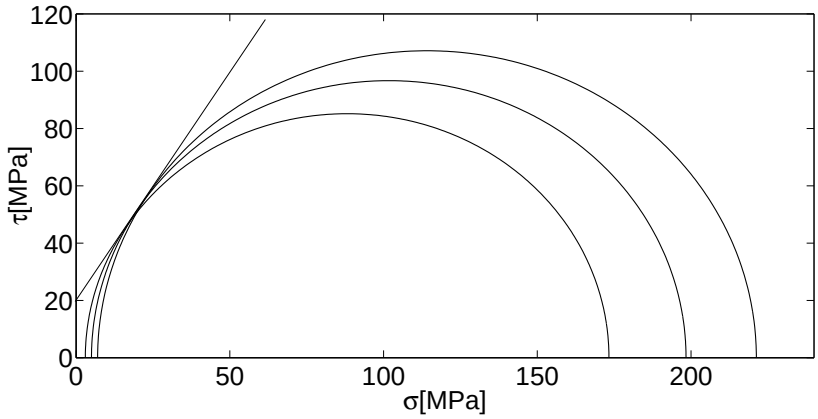

Figure 6.7: Calculating peak strength parameters

6.2.5 Non-associated flow

Figure 6.8 shows the effect of ψ on the short-term stress-strain response of the model for all three confining pressures using the model parameters selected earlier in the chapter (see Table 6.3, however note that both μ and β require recalculation due to the effect of ψ). Three values of ψ are shown; $20^o, 40^o$ and 58.4^o (associated flow). Here we observe that a smaller value of ψ causes the strength of the material to be reduced, as expected, and the peaks of the stress-strain curves are lower than when using associated flow. Therefore a new set of model parameters would need to be determined when using non-associated flow.

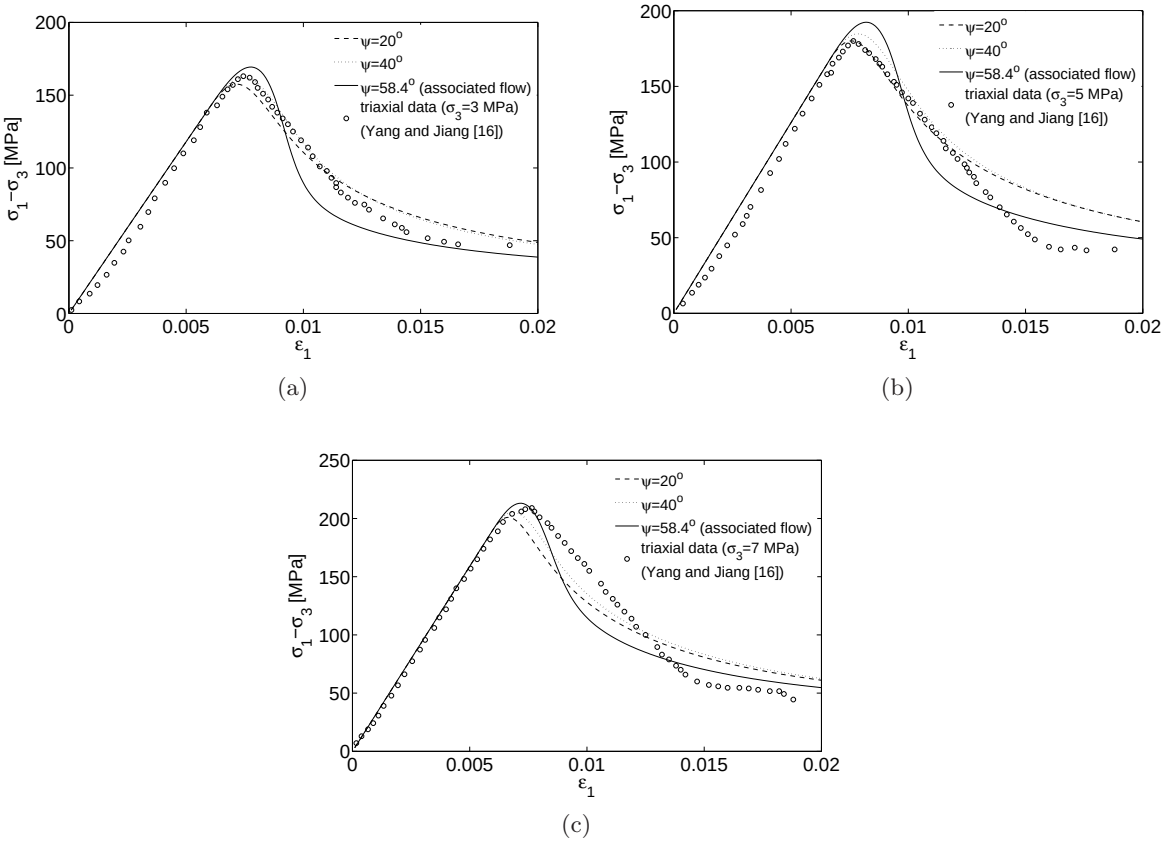

Figure 6.8: Effect of dilation angle on the model response: (a) $\sigma_3 = 3$MPa; (b) $\sigma_3 = 5$MPa; (c) $\sigma_3 = 7$MPa

6.3 Modelling cavity in a frictional viscoplastic-damage medium

We now implement the constitutive model into the energy-based method for cavity analysis analogous to the von Mises viscoplastic-damage model shown in Chapter 5. Figure 5.12 provides an overview of the incremental loading procedure. The model parameters used here are the same as for the elastoplastic Drucker-Prager model in Section 3.6.3, with additional parameters $\Delta t = 0.05$, $n = 1.5$, $\eta = 50000$ MPa day, $r_p = 1.05$ and $\alpha = 0.2$. The cavity pressure p_i is 25 MPa. As for the von Mises viscoplastic-damage model we find that for the selected parameters the cavity reaches a stable condition. This is shown in Figure 6.9 through the displacement of the cavity wall reaching a constant value. From Figure 6.11 we can see the effect of damage on the cavity stresses. Figure 6.10 shows the variation of the cavity wall displacement with time for a greater level of damage ($r_p = 1.15$). Here we clearly observe both secondary and tertiary creep behaviour (see Figure 2.1). When $r_p = 1.0$ the model reduces to a perfectly viscoplastic model with no damage. As $t \to \infty$ we can see from Figure 6.9 and 6.11 that the displacements and stresses match well with the rate-independent finite element (FE) results obtained in Chapter 3 for the Drucker-Prager model.

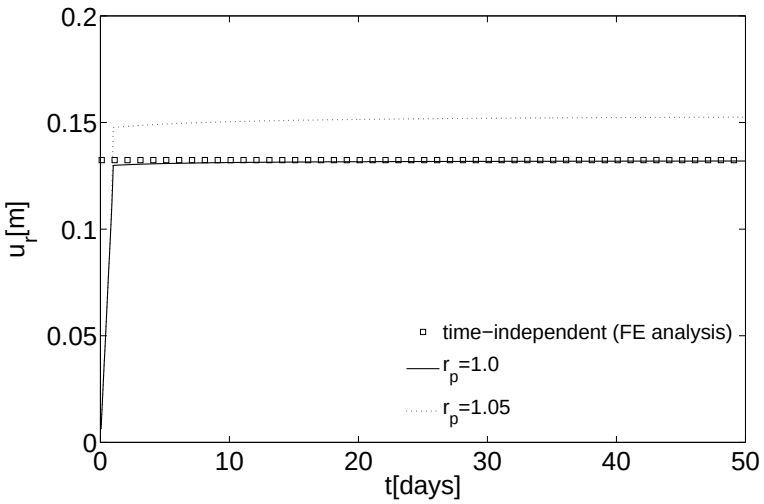

Figure 6.9: Variation of cavity wall displacement with time

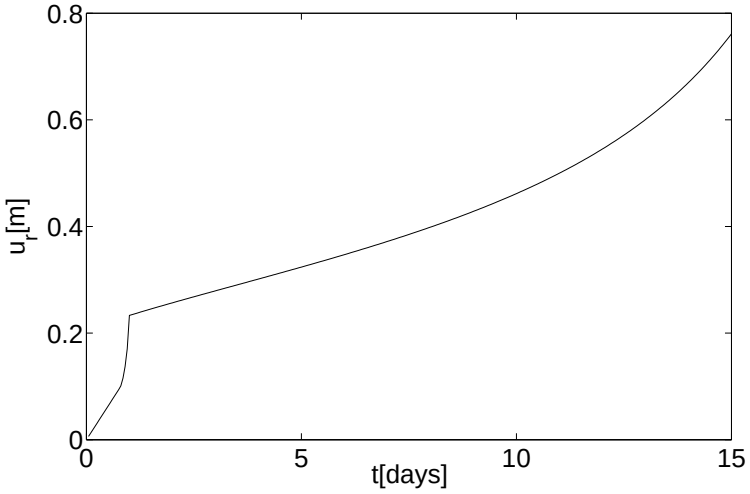

Figure 6.10: Variation of cavity wall displacement with time ($r_p = 1.15$)

6.4 Summary

- a novel frictional viscoplastic-damage constitutive model has been derived within the framework of hyperplasticity. This model is able to describe both secondary and tertiary creep behaviour (see Figure 2.1).

- both short-term and long-term triaxial tests have been simulated using MATLAB 7.9.0 in order to compare the model with experimental data obtained by Yang and Jiang [16]. The model provides a good fit to short-term stress-strain curves obtained for different confining pressures, and a reasonable fit to the long-term creep data.

- this new constitutive model has been successfully implemented into the energy-based method for cavity analysis.

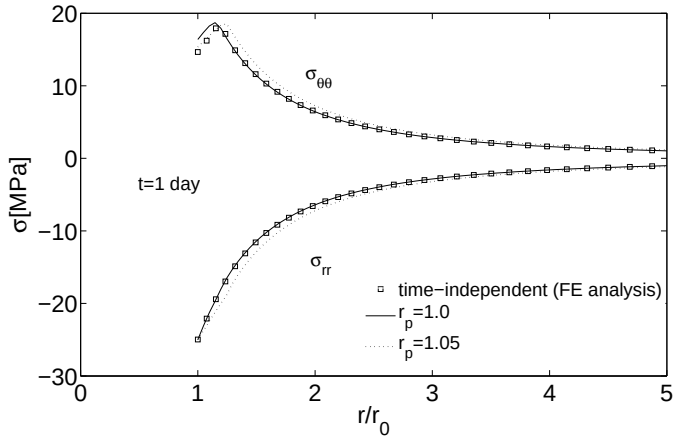

(a)

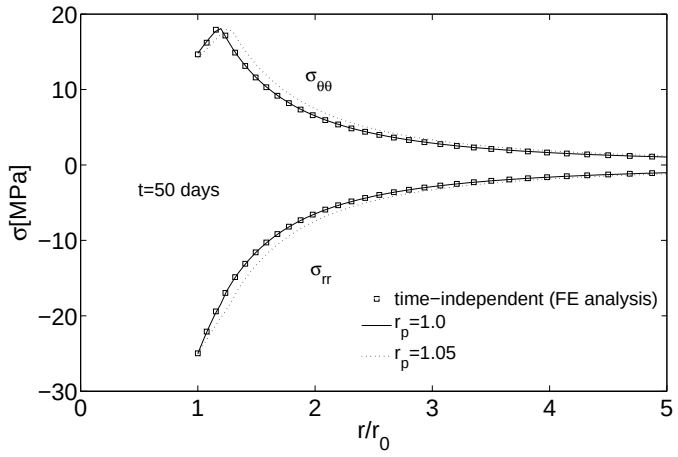

(b)

Figure 6.11: Variation of stresses with radial distance at different values of time: (a) σ_{rr} and $\sigma_{\theta\theta}$ at end of loading stage ($t = 1$); (b) σ_{rr} and $\sigma_{\theta\theta}$ at $t = 50$

6.5 References

1 Bardet, J.P. & Choucair, W. (1991). Triaxial mechanical creep behaviour of sandstone. *International Journal for Numerical and Analytical Methods in Geomechanics*, 15 p. 1-19.

2 Einav, I., Houlsby, G.T. & Nguyen, G.D. (2007). Coupled damage and plasticity models derived from energy and dissipation potentials. *International Journal of Solids and Structures*, 44 p. 2487-2508.

3 Goodman, R.E. (1989). *Introduction to Rock Mechanics*. 2nd Edition. John Wiley & Sons, New York.

4 Houlsby, G.T. & Puzrin, A.M. (2006). *Principles of hyperplasticity: an approach to plasticity theory based on thermodynamic principles*. Springer-Verlag, London.

5 Jaeger, J.C., Cook, N.G.W. & Zimmerman, R.W. (2007). *Fundamentals of rock mechanics.* John Wiley & Sons.

6 Kachanov, L.M. (1958). Time of the Rupture Process under Creep Condition. *Izv. Akad. Nauk. SSSR, Otd. Tekhn. Nauk.*, 8 p. 26-31.

7 Lemaitre, J. (1971). Evaluation of dissipation and damage in metals. *In Proc. I.C.M., 1*, Kyoto, Japan.

8 Lemaitre, J. (1985). Coupled elasto-plasticity and damage constitutive equations. *Comput. Meth. Appl. Mech.Eng.*, 51 p. 31-49.

9 Nguyen, G.D. (2005). A thermodynamic approach to constitutive modelling of concrete using damage mechanics and plasticity theory. D.Phil Thesis, Department of Engineering Science, Oxford University.

10 Perry, J. & Aboudi, J. (2003). Elasto-Plastic Stresses in Thick Walled Cylinders. *Journal of Pressure Vessel Technology*, 125 p. 248-252.

11 Perzyna, P. (1966). Fundamental Problems in Viscoplasticity. Advances in Applied Mechanics, vol. 9. New York: Academic Press. p. 243-377.

12 Perzyna, P. (1971). Thermodynamic Theory of Viscoplasticity. Advances in Applied Mechanics, vol. 11. New York: Academic Press. p. 313-354.

13 de Souza Neto, E.A., Peric, D. & Owen, D.R.J. (2008). *Computational Methods for Plasticity: Theory and Applications*. John Wiley & Sons.

14 Sterpi, D. & Gioda, G. (2009). Visco-plastic behaviour around advancing tunnels in squeezing rock. *Rock Mechanics and Rock Engineering* 42, p. 319-339.

15 Vlasov, V.Z. & Leontiev, N.N. (1966). Beams, plates and shells on elastic foundations. *NTIS Accession No. N67-14238*, Israel Program for Scientific Translations, Washington, D.C.

16 Yang, S. & Jiang, Y. (2010). Triaxial mechanical creep behaviour of sandstone. *Mining Science and Technology*, 20 p. 0339-0349.

17 Yu, C.W. (1998). Creep characteristics of soft rock and modelling of creep in tunnel. Ph.D. Thesis, University of Bradford, United Kingdom.

18 Yu, H.S. (2000). *Cavity Expansion Methods in Geomechanics*. Kluwer, Dordrecht.

19 Ziegler, H. (1983). *An introduction to thermomechanics*. 2nd Edition, North Holland Pub. Co, Amsterdam.

Chapter 7

Conclusions and suggestions for further work

In this thesis it has been shown that an energy-based method can be used to develop new analytical solutions for the time-dependent creep closure of deeply embedded cavities, where the method of cavity analysis and the constitutive behaviour are consistent with the laws of thermodynamics. An objective for this work was to produce models which could be used in the early stages of the cavity design process. This has been achieved as both two-dimensional (2D) and 3D cavity models have been developed using the energy-based method, and a wide range of different constitutive behaviour has been incorporated.

The novel work in this thesis can be found in Chapters 4, 5 and 6. We will now summarise the key conclusions drawn from this thesis by looking at how each of the three specific objectives stated in Section 1.3 has been achieved. As we do this the novel work will be highlighted.

7.1 Achievement of specific objectives

7.1.1 Development of cavity models which can incorporate different material behaviour

This thesis has shown that both linear and non-linear material behaviour can be incorporated into models for cavity analysis developed using the energy-based method, showing that the first aim of Section 1.3 has been achieved. Chapter 3 provides background information describing how the energy-based method can be used to derive existing cavity solutions for elastic, viscoelastic and elasto-plastic constitutive behaviour. Chapters 5 and 6 build on this work and present novel viscoplastic-damage constitutive models.

Initially, simple plane strain elastic solutions are presented in Chapter 3 for 2D cylindrical and spherical cavities located in an isotropic stress field. Closed-form solutions for the displacements and stresses were derived, which were shown to be identical to those found by other authors using an alternative approach of system equilibrium. A more complex solution

was then derived for the cylindrical cavity located in an anisotropic stress field. This solution required use of a 1D finite difference (FD) technique to solve the governing equations for the displacements. The displacements and stresses showed excellent agreement with existing closed-form solutions.

Creep behaviour was first introduced into the energy-based method in Chapter 3 in the form of linear viscoelasticity in the Laplace domain. The inversion of the Laplace transform was carried out numerically in order to obtain the time-dependent displacements. Both the cavity displacements and stresses showed excellent agreement with existing closed-form solutions. The use of a numerical inversion of the transform produces a general solution into which different viscoelastic constitutive models can be incorporated with ease and we do not have to rely on an analytical inversion scheme.

Plastic material behaviour was introduced in Chapter 3 using the theory of hyperplasticity and two simple elasto-plastic constitutive models were derived using this approach; von Mises and Drucker-Prager. These models were successfully incorporated into the energy-based approach for cavity analysis. The displacements and stresses surrounding the cavity showed good agreement with finite element (FE) analysis.

Viscoplastic material behaviour was introduced in Chapter 5 and a thermodynamically consistent von Mises viscoplastic constitutive model was derived using the theory of hyperplasticity. This model was incorporated into the energy-based method for cavity analysis, using an incremental loading procedure in order to provide an approximation to the excavation of an underground cavity. The time-independent displacements and stresses obtained in Chapter 3 for the elasto-plastic model were used as a limit for the time-dependent solution. As time tended towards infinity or as the viscous material parameter tended towards zero, the displacements and stresses corresponded well. This close match gives us confidence that the viscoplastic model provides sensible results.

New viscoplastic-damage constitutive models developed in Chapters 5 and 6 (for which conclusions are drawn in Section 7.1.3) describe both the secondary and tertiary stages of creep and were successfully incorporated into the energy-based method for cavity analysis. Findings showed that damage increases the displacement of the cavity significantly, highlighting the importance of designing for such behaviour and the usefulness of these new models for the design of deeply embedded cavities. When no damage was present we found that the displacements and stresses surrounding the cavity were identical to the time-independent values obtained for the elasto-plastic models, as time tended towards infinity or as the viscous material parameter tended towards zero. This finding and the results from the parametric study carried out in Section 5.3.5 suggests that the models successfully describe both the secondary and tertiary stages of creep behaviour.

The adopted approach of using the energy-based method has shown itself to be flexible through allowing a wide range of material behaviour to be incorporated, including the new viscoplastic-damage constitutive models to analyse deeply embedded cavities.

7.1.2 Development of a 3D model

In Chapter 4 a 3D solution for a cavity deeply embedded in a viscoelastic medium has been developed for the first time. This model was developed using the concepts introduced in Chapter 3; the energy-based method for cavity analysis and the incorporation of viscoelasticity in the Laplace domain. The problem is 3D due to the effect of a tunnel face. The development of this model satisfies the second specific objective of this research stated in Section 1.3. The displacements and stresses showed excellent agreement with closed-form solutions away from the tunnel face in the plane strain condition, and the displacements showed good agreement with finite element (FE) analysis at the tunnel face. Previous analytical solutions are based on a 2D idealisation (e.g. [5], [8], [9], [10], [12]) and the analysis of stresses and displacements near the tunnel face is performed by regarding the face as providing a fictitious support pressure. The magnitude of the internal pressure is related to the face position using empirical relations based on field measurements or 3D FE analyses. However, there are significant uncertainties in extrapolating these empirical relations to different design situations and rock behaviour. Our new 3D solution can predict the full interaction between the tunnel and the surrounding creeping rock. In this respect, the new solution can be incorporated together with field monitoring data in an expert system for tunnel design similar to that illustrated by Schubert [11].

7.1.3 Development of new energy-based constitutive models

To fulfil the requirement of the last objective proposed in Section 1.3 a new class of thermodynamically consistent constitutive models was developed in Chapters 5 and 6. These models couple viscoplasticity and damage and they successfully describe both the secondary and tertiary stages of creep behaviour, proving it is possible to model the full range of creep behaviour using the framework of hyperplasticity. Models were derived for both frictionless and frictional materials. The frictionless model presented in Chapter 5 uses a von Mises yield function, whilst the frictional model shown in Chapter 6 uses a Drucker-Prager yield function. Material damage was incorporated using the theory of continuum damage mechanics (CDM). In Chapter 6 it was shown that the model can provide a good fit to the experimental data obtained by Yang and Jiang [14] during short-term and long-term triaxial testing of sandstone, suggesting that these models could be used to realistically describe the creep behaviour of rock.

7.2 Practical application

It is common place to conduct complex FE (e.g. [6]) or FD (e.g. [1]) analyses to accurately predict the time-dependent response during the excavation process of a cavity. However, such

analyses are computationally expensive for routine practice. The design tools developed in this thesis could be used in addition to FE analysis, but in the early cavity design process to carry out a parametric study on the long term behaviour to determine whether additional support or a change in the excavation procedure is required. It is important to note that the tools developed here only require a simple text file as an input (e.g. material parameters, geometry, pressure) and do not require the construction of an initial geometry or FE mesh. These tools are user friendly and require minimal skill to operate. This has been shown through the development of a simple standalone program for the 3D model in Chapter 4.

The flexibility of this energy-based approach for solving cavity problems has successfully met the aims of this research by demonstrating it can be used for 3D problems as well as incorporating a wide range of material behaviour. Therefore these tools could be applied to a wide range of cavity problems, such as tunnelling problems, the design of underground storage caverns to hold hydrocarbons and nuclear waste (e.g. [3]), as well as problems outside the field of geomechanics.

7.3 Suggestions for further work

The tools developed in this thesis for cavity analysis have been programmed using MATLAB 7.9.0, but the performance could be improved greatly using a code such as FORTRAN. The current code could be investigated to see whether it could be written more efficiently so as to enable speed up. The run times of the models could then be compared with FE analysis in order to evaluate the performance. For example Basu et al. [2] developed a 3D model for piles using the energy-based method adopted in this thesis and compared run times of their model which used a FORTRAN code, with FE analysis. They found that their model required much less computation time. In particular the viscoplastic-damage constitutive models developed in Chapters 5 and 6 could be incorporated into a commercial FE code such as ABAQUS, used in this thesis, by writing user subroutines. The run times of the energy-based cavity models in Chapters 5 and 6 could then be compared with those obtained using FE analysis. Conducting these tests would also allow the viscoplastic-damage cavity displacements and stresses shown in Figures 5.13-5.16 and Figures 6.9-6.11 to be compared with FE analysis, thus providing a rigorous validation, rather than just a parametric study conducted in this thesis.

The 3D model developed in Chapter 4 currently uses viscoelastic material behaviour. This model could be extended to incorporate the viscoplastic-damage constitutive models developed in this thesis, and thus more accurately predict the response of creeping rock.

The frictional viscoplastic-damage constitutive model developed in Chapter 6 could be compared with a greater amount of experimental data in order to obtain the material parameters more accurately. Ideally an experimental program would be conducted in the laboratory

on samples of rock. Both short-term and long-term triaxial tests could be conducted under different levels of confining pressure and rates of loading in order to determine more accurate strength parameters.

It would be useful to investigate the effects of temperature on the response of the viscoplastic-damage constitutive models developed in Chapters 5 and 6. Significant temperatures can be present in deep cavities which may increase the creep deformation as shown in Figure 2.3. Temperature dependency could be easily incorporated within the theory of hyperplasticity as explained by Houlsby and Puzrin [7]. This involves modifying the dissipation potential which is used to derive a new constitutive model. These models could also be generalised by incorporating an appropriate Lode angle dependency function such as that suggested by Eekelen [4].

Finally, the models developed for cavity analysis could be compared to time-dependent field data to investigate their practical use. Many publications exist where models for cavities or tunnels are validated using *in situ* closure measurements (e.g. [1], [13]). This would provide an idea of how realistic the models developed in this thesis are and how useful they are to practically help the design of deeply embedded cavities in the early stages of the design process. Such a comparison could be used to evaluate the 3D viscoelastic cavity model developed in Chapter 4 and the 2D viscoplastic-damage models shown in Chapters 5 and 6.

7.4 References

1 Barla, G., Bonini, M. & Debernardi, D. (2010). Time Dependent Deformations in Squeezing Tunnels. *International Journal of Geoengineering Case Histories*, 2(1) p. 40-65.

2 Basu, D. & Salgado, R. & Prezzi, M. (2009). A continuum-based model for analysis of laterally loaded piles in layered soils. *Géotechnique*, 59(2) p. 127-140.

3 Bérest, P. & Brouard, B. (2003). Safety of salt caverns used for underground storage. *Oil & Gas Science and Technology - Rev IFP*, 58(3) p. 361-384.

4 Eekelen, H. A. M. (1980). Isotropic yield surface in three dimensions for use in soil mechanics. *International Journal for Numerical and Analytical Methods in Geomechanics*, 4 p. 89-101.

5 Fahimifar, A., Tehrani, F.M., Hedayat, A. & Vakilzadeh, A. (2010). Analytical solution for the excavation of circular tunnels in a visco-elastic Burger's material under hydrostatic stress field. *Tunnelling and Underground Space Technology*, 25(4) p. 297-304.

6 Ghaboussi, J. & Gioda, G. (1977). On the time dependent effects in advancing tunnels. *International Journal for Numerical and Analytical Methods in Geomechanics*, 1 p. 249-269.

7 Houlsby, G.T. & Puzrin, A.M. (2006). *Principles of hyperplasticity: an approach to plasticity theory based on thermodynamic principles*. Springer-Verlag, London.

8 Ladanyi, B. (1993). Time-dependent response of rock around tunnels. *Comprehensive Rock Engineering*, 2, Elsevier, Amsterdam, p. 77-112.

9 Panet, M. (1993). Understanding deformations in tunnels. *Comprehensive rock engineering*, 1, Pergamon Press, Oxford, p. 663-690.

10 Sakurai, S. (1978). Approximate time-dependent analysis of tunnel support structure considering progress of tunnel face. *International Journal for Numerical and Analytical Methods in Geomechanics*, 2 p. 159-175.

11 Schubert, W., Moritz, B. & Sellner, P. (2009). Tunnelling methods for squeezing ground. *9th International congress on rock mechanics*, 1-2 p. 233-236.

12 Sulem, J., Panet, M. & Guenot, A. (1987). An Analytical Solution for Time-dependent Displacements in a Circular Tunnel. *International Journal of Rock Mechanics and Mining Sciences and Geomechanics*, 24(3) p. 155-164.

13 Swift, G.M. & Reddish, D.J. (2005). Underground excavations in rock salt. *Geotechnical and Geological Engineering*, 23 p. 17-42.

14 Yang, S. & Jiang, Y. (2010). Triaxial mechanical creep behaviour of sandstone. *Mining Science and Technology*, 20 p. 0339-0349.

Bibliography

ABAQUS (2008). ABAQUS/Standard User's Manual, Version 6.8. Habbit, Karlsson and Sorenson Inc.

Afrouz, A. & Harvey, J.M. (1974). Rheology of rocks within the soft to medium strength range. *International Journal of Rock Mechanics and Mining Science and Geomechanics*, 11(7) p. 281-290.

Aiyer, A.K. (1969). An analytical study of the time-dependent behaviour of underground openings. Ph.D. thesis, University of Illinois at Urbana Champaign, Urbana, III.

Anandarajah, A. (2010). *Computational Methods in Elasticity and Plasticity, Solids and Porous Media*. Springer.

Bardet, J.P. & Choucair, W. (1991). Triaxial mechanical creep behaviour of sandstone. *International Journal for Numerical and Analytical Methods in Geomechanics*, 15 p. 1-19.

Barla, G. (1995). Squeezing rocks in tunnels. *ISRM News Journal*, 2(3-4) p. 44-49.

Barla, G., Bonini, M. & Debernardi, D. (2008). Time Dependent Deformations in Squeezing Tunnels. *International Journal of Geoengineering Case Histories*, 2(1) p. 40-65.

Basu, D. & Salgado, R. (2007). Elastic analysis of laterally loaded pile in multi-layered soil. *Geomechanics and Geoengineering*, 2(3) p. 183-196.

Basu, D. & Salgado, R. & Prezzi, M. (2009). A continuum-based model for analysis of laterally loaded piles in layered soils. *Géotechnique*, 59(2) p. 127-140.

Becker, R. (2011). An alternative approach to integrating plasticity relations. *International Journal of Plasticity*, 27 p.1224-1238.

Bérest, P. & Brouard, B. (2003). Safety of salt caverns used for underground storage. *Oil & Gas Science and Technology - Rev IFP*, 58(3) p. 361-384.

Bérest, P., Béraud, J.F., Brouard, B., Blum, P.A., Charpentier, J.P., de Greef, V., Gharbi, H. & Valès, F. (2010). Very slow creep tests on salt samples. EPJ Web of Conferences, 6.

Birchall, T.J. & Osman, A.S. (2011). Response of a tunnel deeply embedded in a viscoelastic medium. *International Journal for Numerical and Analytical Methods in Geomechanics*, Doi: 10.1002/nag.1069.

Bonini, M., Debernardi, D., Barla, M. & Barla G. (2007). The mechanical behaviour of clay shales and implications on the design of tunnels. *Rock Mech Rock Engng* 42(2) p. 361388.

Boresi, A.P. & Deere, D.U. (1963). Creep Closure of a Spherical Cavity in an Infinite Medium. *Report*, Holmes and Narver, Las Vegas, NV.

de Borst, R, Crisfield, M.A., Remmers, J.J.C. & Verhoosel, C.V. (2012). *Non-linear Finite Element Analysis of Solids and Structures*. 2nd Edition. John Wiley & Sons, Chichester, UK.

Bosman, J.D., Malan, D.F., & Drescher, K. (2000). Time-dependent tunnel deformation at Hartebeestfontein Mine. In:*Proceedings of the AITES-ITA 2000 World Tunnel Congress*, SAIMM, Durban, p.55-62.

Brekke, T.L. & Howard, T.R. (1973). Functional classification of gouge materials from seams and faults in relation to stability problem in underground openings. Rep. No. H0220022, U.S. Bureau of Mines (ARPA).

Campos De Orellana, A.J. (1996). Pressure solution creep and non associated plasticity in the mechanical behaviour of potash mine openings. *International Journal of Rock Mechanics and Mining Science in Geomechanics*, 33(4) p. 347-370.

Carranza-Torres, C. & Fairhurst, C. (2000). Application of the convergence-confinement method of tunnel design to rock masses that satisfy the Hoek-Brown failure criterion. *Tunneling and Underground Space Technology*, 15(2) p. 187-213, (Personal communication with Hoek).

Carter, J.P, Booker, J.R. & Yeung, S.K. (1986). Cavity expansion in cohesive frictional soils. *Géotechnique*, 36(3) p. 349-353.

Chern, J.C., Shiao, F.Y. & Yu, C.W. (1998). An empirical safety criterion for tunnel construction. In: *Proceedings of the Regional Symposium on Sedimentary Rock Engineering*, Taipei, Taiwan, p. 222-227.

Chin, H.P. & Rogers, J.D. (1987). Creep Parameters of Rocks on an Engineering Scale. *Rock Mechanics and Rock Engineering*, 20 p. 137-146.

Cividini, A., Gioda, G. & Carini, A. (1991). A finite element analysis of time-dependent behaviour of underground openings. In: Beer, Booker, Carter (Eds.), *Computer Methods and Advances in Geomechanics*.

Cleveland Potash Ltd. (2008). Ground Control at Boulby Mine. Internal Report.

Collins, I.F. & Houlsby, G.T. (1997). Application of thermomechanical principles to the modelling of geotechnical materials. In: *Proceedings of the Royal Society*, London, England, p. 1975-2001.

Coombs, W.M. (2011). Finite deformation of particulate geomaterials: frictional and anisotropic Critical State elasto-plasticity. Ph.D. Thesis, Durham University.

Corbetta, F., Bernaud, D. & Nguyen-Minh, D. (1991). Contribution a la methode convergence-confinement par le principe de la similitude. Rev Fr Geotech, 54 p. 5-11.

Coulomb, C.A.(1773). Sur une application des régles de Maximis et Minimis a quelques problémes de statique relatifs á l'Architecture. *Acad. Roy. des Sciences Memoires de math. et de physique par divers savans*, 7 p. 343-382.

Cristescu, N. (1989). *Rock Rheology*. Kluwer, Dordrecht.

Debernardi, D. (2008). Viscoplastic Behaviour and Design of Tunnels. Ph.D. Thesis, Politecnico di Torino, Torino.

Desai, C.S. & Christian, J.T. (eds.). (1977). *Numerical Methods in Geotechnical Engineering*. McGraw-Hill, New York.

Dreyer, W. (1973). Flow at a constant stress. In:*The science of rock mechanics*, Part 1, Clausthal:

Trans Tech Publications, p. 126-139.

Dunne, F. & Petrinic, N. (2005). *Introduction to Computational Plasticity.* Oxford University Press.

Dusseault, M. B. & Fordham, C. J. (1993). Time-dependent behaviour of rocks. In:*Comprehensive rock engineering*, 3 (edited by J.A. Hudson), Pergamon Press, p. 119-149.

Eekelen, H. A. M. (1980). Isotropic yield surface in three dimensions for use in soil mechanics. *International Journal for Numerical and Analytical Methods in Geomechanics*, 4 p. 89-101.

Einav, I., Houlsby, G.T. & Nguyen, G.D. (2007). Coupled damage and plasticity models derived from energy and dissipation potentials. *International Journal of Solids and Structures*, 44 p. 2487-2508.

Einav, I. (2005). Energy and variational principles for piles in dissipative soil. *Géotechnique*, 55(7) p. 515-525.

Einav, I. (2002). Applications of thermodynamical approaches to mechanics of soils. Ph.D. Thesis, Technion- Israel Institute of Technology, Haifa.

Fahimifar, A., Tehrani, F.M., Hedayat, A. & Vakilzadeh, A. (2010). Analytical solution for the excavation of circular tunnels in a visco-elastic Burger's material under hydrostatic stress field. *Tunnelling and Underground Space Technology*, 25(4) p. 297-304.

Fakhimi, A.A. (1992). The influence of time-dependent deformation of rock on the stability of underground excavations. Ph.D. Thesis, University of Minnesota, U.S.A.

Fakhimi, A.A. & Fairhurst, C. (1994). A model for the time-dependent behaviour of rock. *International Journal of Rock Mechanics and Mining Sciences*, 31 p. 117-126.

Febres-Cordero, E. (1974). Influence on testing conditions on creep behaviour of clay. Ph.D. Thesis, University of Illinois at Urbana Champaign, Urbana, III.

Forrest, J.A. & Hunt, H.E.M. (2006). A three-dimensional tunnel model for calculation of train-induced ground vibration. *Journal of Sound and Vibration*, 294 p. 678-705.

Fritz, P. (1984). An analytical solution for axisymmetric tunnel problems in elasto-viscoplastic media. *International Journal for Numerical and Analytical Methods in Geomechanics*, p. 325-342.

Ghaboussi, J. & Gioda, G. (1977). On the time dependent effects in advancing tunnels. *International Journal for Numerical and Analytical Methods in Geomechanics*, 1 p. 249-269.

Gioda, G. (1982). On the non linear squeezing effects around circular tunnels. *International Journal for Numerical and Analytical Methods in Geomechanics*, 6 p. 21-46.

Gioda, G. (1981). A finite element solution of non-linear creep problems in rocks. International Journal for Rock Mechanics and Mining Sciences and Geomechanics,18, pp. 34-46.

Gioda, G. & Cividini, A. (1996). Numerical methods for the analysis of tunnel performance in squeezing rocks. *Rock Mechanics and Rock Engineering*, 29 p. 171-193.

Gioda, G. & Swoboda, G. (1999). Developments and applications of the numerical analysis of tunnels in continuous media. *International Journal for Numerical and Analytical Methods in Geomechanics*, 23 p. 1393-1405.

Gnirk, P.F. & Johnson, R.E. (1964). The deformational behaviour of a circular mine shaft situated in a viscoelastic medium under hydrostatic stress. In:*Proceedings of the Sixth U.S. Symposium on Rock*

Mechanics, Rolla, p. 231-259.

Goodman, R.E. (1989). *Introduction to Rock Mechanics.* 2nd Edition, John Wiley & Sons, New York.

Griggs, D. (1939). Creep of Rocks. *The Journal of Geology*, 47(3) p. 225-251.

Guo, W.D., & Lee, F.H. (2001). Load transfer approach for laterally loaded piles. *International Journal for Numerical and Analytical Methods in Geomechanics*, 25(11) p. 1101-1129.

Hanafy, E.A., & Emery, J.J. (1979). Advancing face simulation of tunnel excavations and lining placements. In:*Proceedings of the 13th Canadian Rock Mechanics Symposium*, Underground Rock Engineering, Toronto, p. 119-125.

Hansen, F.D & Carter, N.L. (1984). Creep of Avery Island rocksalt. In:*Proceedings of the 1st Conference on Mechanical Behaviour of Salt*, Clausthal:Trans Tech Publications, p. 53-69.

Hill, R. (1950). *The Mathematical Theory of Plasticity.* Oxford University Press, London.

de Hoog, F.R., Knight, J.H. & Stokes, A.N. (1982). An improved method for numerical inversion of Laplace transforms. SIAM (Society for Industrial and Applied Mathematics). *Journal on Scientific and Statistical Computing*, 3(3) p. 357-366.

Houlsby, G.T. (1981). A study of plasticity theories and their applicability to soils. Ph.D. Thesis, University of Cambridge.

Houlsby, G.T. & Puzrin, A.M. (2006). *Principles of hyperplasticity: an approach to plasticity theory based on thermodynamic principles.* Springer-Verlag, London.

Jaeger, J.C., Cook, N.G.W. & Zimmerman, R.W. (2007). *Fundamentals of rock mechanics.* Fourth Edition. Blackwell, Oxford.

Jeremic, M.L. (1994). *Rock Mechanics in Salt Mining.* Balkema, Rotterdam.

Jaeger, J., Cook, N.G. & Zimmerman, R. (2007). *Fundamentals of Rock Mechanics.* 4th edition. Blackwell.

Kachanov, L.M. (1958). Time of the Rupture Process under Creep Condition. *Izv. Akad. Nauk. SSSR, Otd. Tekhn. Nauk.*, 8 p. 26-31.

Kirsch, G. (1898). Die Theorie der Elastizität und die Bedürfnisse der Festigkeitslehre. *Zeitschrift des Vereines deutscher Ingenieure*, 42 p. 797-807.

Kontogianni, V., Psimoulis, P. & Stiros, S. (2005). What is the contribution of time-dependent deformation in tunnel convergence? *Engineering Geology*, 82 p. 264-267.

Ladanyi, B. (1993). Time-dependent response of rock around tunnels. *Comprehensive Rock Engineering*, 2, Elsevier, Amsterdam, p. 77-112.

Langer, M. (1982). Geotechnical investigation methods for rock salt. *Bulletin of the International Association of Engineering Geology*, 25 p. 155-164.

Le Comte, P. (1965). Creep in Rock Salt. *Journal of Geology*, 73 p. 469-484.

Lemaitre, J. (1985). Coupled elasto-plasticity and damage constitutive equations. *Comput. Meth. Appl. Mech.Eng.*, 51 p. 31-49.

Lemaitre, J. (1971). Evaluation of dissipation and damage in metals. *In Proc. I.C.M., 1*, Kyoto, Japan.

Lemaitre, J. & Chaboche, J.L. (1996). Mécanique des matériaux solides. *Dunod*, 253-341.

Lemaitre, J. & Chaboche, J.L. (1990). *Mechanics of Solid Materials*. Cambridge University Press.

Lin, H.D., & Wang, C.C. (1998). Stress-strain time function of clay. *Liquid Crystal and Ordered Fluids*, 142(4) p. 289-296.

Malan, D.F. (1995). A viscoelastic approach to the modelling of transient closure behaviour of tabular excavations after blasting. *Journal of the South African Institute of Mining and Metallurgy*, 95 p. 211220.

Mesri, G., Febres-Cordero, E., Shield, D.R. & Castro, A. (1981). Shear-stress-strain behaviour of clays. *Géotechnique*, 31(4) p. 537-552.

Mirza, U.A. (1984). Prediction of creep deformations in rock salt pillars. In:*Proceedings of the 1st Conference on the Mechanical Behaviour of Salt*, Clausthal: Trans Tech Publications, p. 311-337.

Munson, D.E. & Dawson, P.R. (1984). Salt constitutive modelling using mechanism maps. In:*Proceedings of the 1st Conference on the Mechanical Behaviour of Salt*, Clausthal: Trans Tech Publications, p. 717-737.

Nguyen, G.D. (2005). A thermodynamic approach to constitutive modelling of concrete using damage mechanics and plasticity theory. D.Phil Thesis, Department of Engineering Science, Oxford University.

Nonaka, T. (1981). A time-independent analysis for the final state of an elasto-visco-plastic medium with internal cavities. *International Journal of Solids and Structures*, 17 p. 961-967.

Obert, L. (1965). Creep in mine pillars: Report of investigation. Rep. No. 6703, U.S. Bureau of Mines.

Pan, Y.W. & Dong, J.J. (1991). Time-dependent tunnel convergence I. Formulation of the model. *International Journal of Rock Mechanics and Mining Sciences*, 28 p. 469-475.

Panet, M. (1995). Le calcul des tunnels par la method convergence-confinement. *Presses de l'Ecole Nationale des Ponts et Chaussees*, Paris, France.

Panet, M. (1993). Understanding deformations in tunnels. *Comprehensive rock engineering*, 1, Pergamon Press, Oxford, p. 663-690.

Peila, D., Oreste, P., Rabajuli, G. & Trabucco, E. (1995). The pre-tunnel method, a new Italian technology for full-face tunnel excavation: a numerical approach to design. *Tunnelling and Underground Space Technology*, 10(3) p. 367-394.

Pender, M.J. (1980). Elastic solutions for a deep circular tunnel. *Géotechnique*, 30(2) p. 216-222.

Perry, J. & Aboudi, J. (2003). Elasto-Plastic Stresses in Thick Walled Cylinders. *Journal of Pressure Vessel Technology*, 125 p. 248-252.

Perzyna, P. (1966). Fundamental Problems in Viscoplasticity. *Advances in Applied Mechanics*, vol. 9. New York: Academic Press. p. 243-377.

Perzyna, P. (1971). Thermodynamic Theory of Viscoplasticity. *Advances in Applied Mechanics*, vol. 11. New York: Academic Press. p. 313-354.

Phienwej, N. (1987). Squeezing ground response of sheared shale of Steelwater tunnel. Ph.D. Thesis, University of Illinois at Urbana Champaign, Urbana, I11.

Phienwej, N., Thakur, P.K. & Cording, P.E. (2007). Time-Dependent Response of Tunnels Considering Creep Effect. *International Journal of Geomechanics*, 7(4) p. 296-306.

Phueakphum, D. & Fuenkajorn, K. (2010). Effects of cycling loading on mechanical properties of Maha Sarakhm salt.*Engineering Geology*, 112(14) p. 4352.

Potts, D.M. & Zdravkovic, L. (1999). *Finite element analysis in geotechnical engineering, theory.* Thomas Telford.

Puzrin, A.M. (2012). *Constitutive Modelling in Geomechanics: Introduction.* Springer.

Rabotnov, Y.N. (1963). On the equations of state for creep. *Page 307 of: Progress in Applied Mechanics, Prager Anniversary Volume.* New York: Macmillan.

Radoncic, N., Schubert, W. & Moritz, B. (2009). Ductile support design. Zur Auslegung duktiler Ausbauten. *Geomechanics and Tunnelling*, 2(5) p. 561-577.

Reddy, J.N. (2002). *Energy and Variational Methods in Applied Mechanics.* 2nd Edition, John Wiley & Sons.

Rutishauser, H. (1957). Der Quotienten-Differenzen-Algorithmus. *Mitt. Inst. Agnew. Math. ETH*, 7, Birkhauser Verlag, Basel.

Sadd, M.H. (2005). *Elasticity, Theory, Applications, and Numerics.* Elsevier.

Sakurai, S. (1978). Approximate time-dependent analysis of tunnel support structure considering progress of tunnel face. *International Journal for Numerical and Analytical Methods in Geomechanics*, 2 p. 159-175.

Salamon, M.D.G. (1974). Rock mechanics of underground excavations. In:*Proceedings of the Third Congress of the International Society of Rock Mechanics* 1 part B p. 994-1000.

Scott-Duncan, E.J. & Lajtai, E.Z. (1993). The creep of potash salt rocks from Saskatchewan. *Geotechnical and Geological Engineering*, 11 p. 159-184.

Schubert, W. (2008). Design of Ductile Tunnel Linings. *42nd U.S. Rock Mechanics Symposium (US-RMS)*, San Francisco, CA.

Schubert, W., Button, E.A., Sellner, P.J., & Solak, T. (2003). Analysis of time dependent displacements of tunnels. *FELSBAU*, 21(5) p. 96-103.

Schubert, W., Moritz, B. & Sellner, P. (2009). Tunnelling methods for squeezing ground. *9th International congress on rock mechanics*, 1-2 p. 233-236.

Semple, R.M. (1973). Effect of time-dependent properties of altered rocks on tunnel support requirements. Ph.D. Thesis, University of Illinois at Urbana Champaign, Urbana, I11.

Senseny, P.E. (1984). Specimen size and history effects on creep of salt. In:*Proceedings of the 1st Conference on the Mechanical Behaviour of Salt*, Clausthal: Trans Tech Publications, p. 369-379.

Shalabi, F.I. (2005). FE analysis of time-dependent behaviour of tunnelling in squeezing ground using two different creep models. *Tunnelling and Underground Space Technology*, 20 p. 271-279.

Shao, J.F., Zhu, Q.Z. & Su, K. (2003). Modeling of creep in rock materials in terms of material degradation. *Computers and Geotechnics*, 30(7) p. 549-555.

Shen, W.Y., Chow, Y.K. & Yong, K.Y. (1997). Variational approach for vertical deformation analysis of pile group. *International Journal for Numerical and Analytical Methods in Geomechanics*, 21(11) p. 741-752.

Simo, J.C. & Hughes, T.J.R. (1998). *Computational Inelasticity.* Volume 7. Springer.

Singh, D.P. (1975). A Study of Creep of Rocks. *International Journal of Rock Mechanics and Mining Sciences and Geomechanics*, 12 p. 271-276.

Singh, A. & Mitchell, J.K. (1968). General stress-strain time function for soils. *Journal of the Soil Mechanics and Foundations Division*, 94(1) p. 21-46.

de Souza Neto, E.A., Peric, D. & Owen, D.R.J. (2008). *Computational Methods for Plasticity: Theory and Applications.* John Wiley & Sons.

Sterpi, D. & Gioda, G. (2009). Visco-plastic behaviour around advancing tunnels in squeezing rock. *Rock Mechanics and Rock Engineering*, 42 p. 319-339.

Sulem, J., Panet, M. & Guenot, A. (1987). An Analytical Solution for Time-dependent Displacements in a Circular Tunnel. *International Journal of Rock Mechanics and Mining Sciences and Geomechanics*, 24(3) p.155-164.

Sulem, J., Panet, M. & Guenot, A. (1987). Closure Analysis in Deep Tunnels. *International Journal of Rock Mechanics and Mining Sciences and Geomechanics*, 24(3) p.145-154.

Sun, K. (1994). Laterally Loaded Piles in Elastic Media. *Journal of Geotechnical Engineering*, 120(8) p.1324-1344.

Swift, G.M. & Reddish, D.J. (2005). Underground excavations in rock salt. *Geotechnical and Geological Engineering*, 23 p. 17-42.

Terzaghi, K. (1946). Rock defects and loads on tunnel supports. *Rock tunneling with steel supports*, Proctor and White Ed., Commercial Shearing and Stamping Co., Youngstown, Ohio.

Timoshenko, S.P. & Goodier, J.N. (1987). *Theory of Elasticity.* 3rd Edition, McGraw-Hill.

United States Army Corps of Engineers. (1965). Project Dribble-Petrographic Examination and Physical Tests of Cores, Tatum Salt Dome, Mississippi, Technical Report No. 6-614, Vicksburg, Mississippi.

Unlu, T. & Gercek, H. (2003). Effect of Poisson's ratio on the normalised radial displacements occuring around the face of a circular tunnel. *Tunnelling and Underground Space Technology*, 18 p. 547-553.

Vlasov, V.Z. & Leontiev, U.N. (1966). Beams, plates and shells on elastic foundations. In:*Israel Program for Scientific Translations*, Jerusalem, translated from Russian.

Vouille, G., Tijani, F. & de Grenier, F. (1984). Experimental determination of the rheological behaviour of Tersanne rock salt. In:*Proceedings of the 1st Conference on the Mechanical Behaviour of Salt*, Clausthal: Trans Tech Publications, p. 407-420.

Vyalov, S.S. (1972). Creep in rock. *Power Technology and Engineering*, 6 p. 228-234.

Wynn, P. (1967). Transformations to accelerate the convergence of fourier series. Blanch Anniversary Volume. In: Mond, B. (Ed.), US Air Force, Washington DC, p. 339-379.

Yang, S. & Jiang, Y. (2010). Triaxial mechanical creep behaviour of sandstone. *Mining Science and Technology*, 20 p. 339-349.

Yu, C.W. (1998). Creep characteristics of Soft Rock and Modelling of Creep in Tunnel. Ph.D. thesis, University of Bradford, Bradford.

Yu, H.S. (2000). *Cavity Expansion Methods in Geomechanics*. Kluwer, Dordrecht.

Yu, Y.S., Ong, C.G. & Mottahed, P. (1988). Viscoelastic finite element analysis in design of potash mines. *Engineering Computations*, 5 p. 248-253.

Zhifa, Y., Zhiyin, W., Luqing, Z., Ruiguang, Z. & Nianxing, X. (2001). Back-analysis of viscoelastic displacements in a soft rock road tunnel. *International Journal of Rock Mechanics and Mining Sciences*, 38 p. 331-341.

Ziegler, H. (1983). *An introduction to thermomechanics*. 2nd Edition, North Holland Pub. Co, Amsterdam.

Zienkiewicz, O.C. (1977). *The Finite Element Method*. McGraw-Hill Book Company (UK) Limited.

MATLAB code

The MATLAB code written during this research is included on a CD below. The CD has a separate folder for each chapter, which contains the main programs, associated functions and a text file providing a description of each program.